Cooperative Interactions in Lattices of Atomic Dipoles

Robert James Bettles

Abstract

Coherent radiation by an ensemble of scatterers can dramatically modify the ensemble's optical response. This can include, for example, enhanced and suppressed decay rates (superradiance and subradiance respectively), energy level shifts, and highly directional scattering. This behaviour is referred to as *cooperative*, since the scatterers in the ensemble behave as a collective rather than independently. In this Thesis, we investigate the cooperative behaviour of one- and two-dimensional arrays of interacting atoms.

We calculate the extinction cross-section of these arrays, analysing how the cooperative eigenmodes of the ensemble contribute to the overall extinction. Typically, the dominant eigenmode if the atoms are driven by a uniform or Gaussian light beam is the mode in which the atomic dipoles oscillate in phase together and with the same polarisation as the driving field. The eigenvalues of this mode become strongly resonant as the atom number is increased. For a one-dimensional array, the location of these resonances occurs when the atomic spacing is an integer or half integer multiple of the wavelength, thus behaving analogously to a single atom in a cavity. The interference between this mode and additional eigenmodes can result in Fano-like asymmetric lineshapes in the extinction. We find that the kagome lattice in particular exhibits an exceptionally strong interference lineshape, like a cooperative analog of electromagnetically induced transparency.

Triangular, square and hexagonal lattices however are typically dominated by one single mode which, for lattice spacings of the order of a wavelength, can be highly subradiant. This can result in near-perfect extinction of a resonant driving field, signifying a significant increase in the atom-light coupling efficiency. We show that this extinction is robust to possible experimental imperfections.

Cooperative Interactions in Lattices of Atomic Dipoles

Robert James Bettles

A thesis submitted in partial fulfillment
of the requirements for the degree of
Doctor of Philosophy

Department of Physics
Durham University

June 6, 2016

Contents

List of Figures

List of Tables

Acknowledgements

This Thesis would not have been possible without the help, support, enthusiasm and encouragement of so many people. Whilst my thanks here may be brief, I hope that all those who have helped me over the last three and a half years will accept my heart-felt thanks and gratitude.

First and foremost, I would not even have a Thesis if it were not for my two supervisors, Charles Adams and Simon Gardiner. I was first introduced to atomic physics through a summer project with Charles in the second year of my undergraduate degree. Since then, he has guided me through a Masters project and now this PhD, and his infectious enthusiasm and passion for the subject are a large part of why I now study atomic physics. Simon's keen eye for detail and determination to get to the heart of a problem have turned me into a better physicist, and his constant approachability and (literal) open door policy have given me an example to aspire to. I have been extremely fortunate to be supported by two such excellent supervisors, who have patiently encouraged and guided me every week for the last three and a half years. I cannot thank them enough.

My time in AtMol has been all the more enjoyable thanks to the wonderful community of people that I have gotten to know here. My thanks go out to James, Christophe, David, Chris, Nikola, Hannes, Paul, Tom and many others for their stimulating and thought-provoking discussions about all things dipole-related and beyond. A special thanks to all those in Fatmol for keeping my spirits, and my sugar levels, on a weekly high. Thanks to Steven and Simon for sacrificing time and energy to proof-read this Thesis (although any remaining mistakes are entirely the fault of the author). Diolch hefyd i Ifan am f'atgoffa i o gartref.

I have received a huge amount of support and hospitality from so many people, not just in Durham but in many other places. Thank you in particular to Bea Olmos and Igor Lesanovsky, Janne Ruostekoski and Mark Lee, and Sebastian Krämer and Helmut Ritsch. Through visiting and spending time with these people and their groups I have learnt many valuable things and grown in many ways.

To my parents, Rick and Julia, thank you for always encouraging me in all I do. Thank you particularly for allowing to me go to a university on the other side of the country and for always selflessly supporting me. Thank you Rosie for so many fun adventures and putting me up on my way to conferences even when I have had to leave at such ungodly hours of the morning. Thank you also to my other family, my church, who have been a constant in the changing years of my time in Durham. And lastly, but most importantly, thank you Joy, for being the person I can always turn to every day, for looking after me, and for being my best friend (even if you're driven to despair when I keep talking to you about physics).

"The heavens are telling of the glory of God; And their expanse is declaring the work of His hands."

Psalm 19:1

Declaration

I confirm that no part of the material offered has previously been submitted by myself for a degree in this or any other University. Where material has been generated through joint work, the work of others has been indicated.

Robert J. Bettles
Durham, June 6, 2016

Notation

Throughout the Thesis we attempt to adhere to the following convention of notation:

Objects in 3-space:

- vectors $\mathbf{a} = (a_1, a_2, a_3)^{\mathrm{T}}$, where T stands for transpose
- unit vectors $\hat{\mathbf{b}} = \mathbf{b}/|\mathbf{b}|$
- tensors C with elements C_{ij}

Quantum mechanical (general N-space):

- state vectors $|d\rangle$
- operators e (scalar valued) and f (vector valued)

Numerical representations (linear algebra):

- vectors $\vec{\mathbf{g}}$
- matrices H

For Joy

Chapter 1

Introduction

1.1 Cooperativity

Understanding and manipulating the interaction of light with matter is one of the principal goals of modern science. It allows us to test our understanding of fundamental physics whilst also opening doors to many new and exciting applications.

The interaction of light with an ensemble of scatterers (such as electric dipoles) can be dramatically modified if the scatterers behave coherently (Sec. 1.2). The scatterers no longer behave independently but rather as an ensemble. This is known as *collective* or *cooperative* behaviour, and can lead to effects such as large frequency shifts and modified decay rates (Sec. 1.3). These have been realised experimentally in a number of different systems, including quantum dots [2], nuclei [3], ions [4, 5, 6], Bose-Einstein condensates [7], cold atoms [8, 9, 10, 11] and atoms at room-temperature [12]. Additional cooperative phenomena can include highly directional scattering [13], excitation localization [14, 15, 16], and modified optical transmission and scattering [17, 18, 19]. There is therefore considerable current interest in understanding these phenomena.

Interactions between the scatterers also play an important role in determining the cooperative behaviour, since the environment of each scatterer is determined by its neighbours. In this Thesis we will be considering atoms with electric dipole transitions (al-

though our treatment could also be applied to other types of electric dipole). The dipole–dipole interaction is both long range and anisotropic (Sec. 4.2), and therefore the cooperative response of the ensemble will depend closely on the geometry of the scatterers. The goal of this Thesis is to understand better how atomic configuration affects cooperativity, in particular focussing on atoms arranged in one-dimensional (1D) and two-dimensional (2D) periodic arrays (Sec. 1.5). We will find that for different geometries, many varied cooperative phenomena can be realised.

1.2 Dicke superradiance

One of the seminal works in attempting to predict the radiative behaviour of an ensemble of scatterers was by Dicke in 1954 [20]. He calculated that a cloud of N two-level atoms much smaller in size than a single wavelength and initially all prepared in their excited states will spontaneously decay N times faster than just a single atom. This revolutionary discovery was named *superradiance* and has been extensively studied both theoretically and experimentally over the past 60 years, in many different systems (see references in Sec. 1.1).

Dicke's approach was to consider the eigenstates of the system as a whole, treating the atomic ensemble as a single quantum system, rather than N independent atoms. Assuming that the atoms were prepared coherently, then the eigenstates can be characterised as angular momentum spin states. Depending on the values of this effective spin and projection for each state, its associated spontaneous decay might be faster (superradiant) or slower (subradiant) than the natural decay rate. The superradiant state in the previous paragraph is the maximally symmetric state. The symmetric nature of the state means the fields radiated from the atomic dipoles all interfere constructively, resulting in a much brighter, shorter decay pulse (the peak pulse intensity scales with N^2 and the length of the pulse with $1/N$) [21].

Dicke considered first an atomic cloud much smaller in extent than a single wavelength. It is easy to see that in this situation the atoms will all couple to the same mode of the electromagnetic (EM) field and be prepared in a fully symmetric state. Dicke had ignored the

resonant dipole–dipole interaction that would take place between atoms separated by so short a distance, and the superradiant decay is purely due to the coherent radiation of the individual atoms. Dicke [20] and later others [22] also considered ensembles where the atomic samples are less dense and interactions would therefore be weaker (and thus ignoring them is more valid an approximation). The eigenstates are now *timed* Dicke states, with each atomic state having a term proportional to $e^{i\mathbf{k}\cdot\mathbf{r}_i}$, where $\mathbf{k}$ is the wavevector of the initial preparation field and $\mathbf{r}_i$ is the position of atom i. Depending on the relative phases of the different eigenstate terms, the decay can still be superradiant, although the decay rate is never as large as in the small sample limit. Furthermore, because of the phased preparation, the spontaneous decay occurs preferentially in directions governed by the initial wavevector of the driving field and the geometry of the atomic ensemble [22].

1.3 Dipole–dipole interactions; superradiance and cooperative Lamb shifts

Even for extended diffuse samples however, including the dipole–dipole interaction proved to be necessary in order to correctly model what was being observed in experiment [21, 23, 24, 25, 26]. The presence of each atom modifies the effective EM mode environment experienced by every other atom, and therefore the local environment of each atom depends on the configuration of all other atoms in the ensemble. The dipole–dipole interaction [27] has both coherent and dissipative components. The interaction therefore introduces an energy shift for each atom and also modifies their spontaneous decay rates. For a *true* two-level atom (with three degenerate excited states, see Chap. 3), the interactions also correlate the dipole polarisations [26].

The modification of the mode environment is analogous to the effect of putting a quantum emitter inside an optical cavity [28].[a] In the so-called *strong coupling regime* of cavity quantum electrodynamics (QED) [29], the coherent matter–light interaction happens on a much faster time scale than the spontaneous decay of the matter and the loss from the

[a] An optical cavity can be formed, for example, between two highly reflecting mirrors.

cavity. The back action of the cavity field on the emitter therefore needs to be accounted for and a photon can be coherently absorbed and re-emitted many times before it leaves the cavity (vacuum Rabi oscillations [30]). An analogous strong coupling regime can be realised in a strongly interacting cooperative ensemble. In this case, it is the coherent interaction between emitters that dominates over spontaneous decay, resulting in multiple recurrent scattering between the emitters before the photon is decayed. For example, we show in Sec. 6.4.6 that the decay rate of an infinite 1D chain of atoms is identical to that of a single atom between two mirrors. The recurrent scattering between the atoms is equivalent to the recurrent scattering between the single atom and image dipoles induced in the mirror. The strict limit for being in the strong coupling regime is that the atom separation be much smaller than the wavelength of the radiation field. However, the dipole–dipole interaction is long range and cooperative behaviour can still exist for spacings much larger than a wavelength. This similarity between cavities and cooperative ensembles has the potential for realising cavity phenomena without the need of a cavity, for example cavity-free lasing [31].

There has been considerable recent interest in understanding the cross-over between different regimes in which cooperative phenomena can be realised. These regimes can be characterised by whether the emitters are dominated by homogeneous or inhomogeneous broadening [18, 32, 33, 34, 35]. In this Thesis, we will be considering ensembles of cold atoms trapped in their positions with no motion. In this situation, the recurrent radiation scattering between the atoms has to be treated fully self-consistently [17, 36, 37, 38, 39, 40]. If, however, the emitter linewidth becomes dominated by inhomogeneous broadening (e.g., Doppler broadening due to thermal motion), then the recurrent scattering can be significantly attenuated [32]. The ensemble of emitters can instead be treated as a continuous polarisable medium [24], meaning that each atom experiences a mean field which, depending on the geometry of the medium, can lead to modified decay rates and energy shifts. These shifts are historically known as *cooperative Lamb shifts*, referring to the exchange of photons responsible for the dipole–dipole interaction, and have recently been measured in high temperature atomic vapour cells [12] and nuclear x-ray optics [3]. In [32], the authors refer to a homogeneously broadened medium as *collective* and an inhomogeneously broadened medium as *cooperative*. However, as we shall only be considering the latter case, we shall in general use the two terms interchangeably.

1.4 Why atoms?

As mentioned in Sec. 1.1, cooperative behaviour such as superradiance, subradiance and energy shifts have been realised in many different systems. Indeed, the model that we employ throughout most of this Thesis simply treats the atoms as classical coupled electric dipoles, and so by changing the form of the electric polarisability (the constant of proportionality relating an applied electric field to the resulting driven electric dipole), the model can easily be applied to other systems, for example plasmonic nanoresonators and metamaterials [41, 42, 43]. These nanoresonators can often support magnetic and higher order multipolar resonances which can add to the complexity of the behaviour.

One advantage of using atoms over plasmonic dipoles is that atoms have very low non-radiative decay rates and very high Q-factors (ratio of the resonance frequency to the linewidth), making them ideal for quantum processing applications and memory storage. They are also highly reproducible, since other than differences in local environment, every atom of a particular species is exactly the same.

There are however disadvantages to atoms, which other systems such as metallic nanoresonators do not have. For example, precise control over atomic position is difficult, as we shall discuss in more detail in Sections 7.3.4 and 8.6. In addition, low temperatures are often needed (if wanting to trap individual atoms), and improvements in nanofabrication mean that nanostructures can be finely tuned to whatever resonance or behaviour is required.

1.5 Why lattices?

Many of the current atomic experiments investigating cooperative behaviour involve random atomic vapours [12, 18, 34, 35, 44]. Recent advances in technology however have made it possible to trap single atoms in large, arbitrary 1D and 2D geometries. These include, for example, optical lattices in the Mott-insulator phase [45, 46] or spatial light modulator dipole trap arrays [47]. Coherent scattering between two-level dipoles maps exactly onto a spin exchange description [48, 49, 50]; consequently, there is a unifying

crossover between cooperative light scattering and interacting spin systems. Spin lattices are a subject of widespread contemporary interest, and manifest in such diverse systems as quantum degenerate gases [51, 52], polar molecules [49, 53] and cold atoms [47, 54] in optical lattices, and electric and magnetic multipoles in plasmonic nanostructures [55, 56, 57, 58]. Understanding the cooperative behaviour in lattices[b] therefore has implications for a number of different applications, from predicting shifts and lifetimes in optical lattice clocks [59], use in narrow linewidth superradiant lasers [60, 61], subwavelength light control [14], to many body spin models [40, 49]) and simulation of condensed matter frustration and spin ice [58, 62, 63].

Simple Bragg scattering shows that the scattering from a periodic structured lattice can result in strong interference effects. The radiative nature of the dipole–dipole interaction (Sec. 4.2) also means that the interaction across the lattice has a strongly resonant behaviour. These two factors combined mean that periodically structured lattices of atoms can result in striking cooperative behaviour [5, 14, 40, 64, 65]. Reducing the dimensionality of the system also allows us to tailor the anisotropic dipole–dipole interaction, and the eigenmodes in lattices are typically much cleaner and more distinct than in random ensembles, exhibiting well defined patterns and structures. Lattice geometries therefore present us with a well-controlled testing ground for understanding some of the fundamental principles of cooperativity.

Two particular cooperative lattice effects we shall focus on in this Thesis are Fano resonances and optical extinction. In Chap. 7 we demonstrate that a kagome lattice supports simultaneously strong superradiant and subradiant modes which interfere, resulting in a characteristic Fano-like resonance lineshape. Steep dispersion lineshapes are a requirement of many applications including lasers, sensors, switching, and non-linear and slow-light devices. In Chap. 8 we then demonstrate that triangular, square, and hexagonal lattices can result in near-perfect extinction of an incident focussed Gaussian beam. The resulting enhanced atom–light coupling is also necessary for many applications, including quantum information and quantum processing.

[b] By *lattice* we will always mean a periodic array, rather than simply the atoms being trapped in space.

1.6 Structure of this Thesis

This Thesis is split into three parts. In Part I we derive the coupled dipole model that will be used throughout the later parts of the Thesis. We will also introduce the observables which we will be considering. In Part II, we apply this model first to pairs and then 1D arrays of atoms. We investigate in particular the patterns that emerge as the number of atoms increases, showing how an infinite atomic chain can behave like a single atom in a cavity. In Part III we will consider atoms in 2D arrays, considering both their eigenmode behaviour and also the extinction of an incident focused Gaussian beam through the array. Finally, in Chap. 9 we will present our conclusions and discuss the outlook for possible future directions.

1.7 Publications from this work

Some of the material in this Thesis has been published in the following publications:

- R.J. Bettles, S.A. Gardiner, and C.S. Adams, *Cooperative ordering in lattices of interacting two-level dipoles*, *Phys. Rev. A* **92**, 063822 (2015) [66]
- R.J. Bettles, S.A. Gardiner, and C.S. Adams, *Enhanced Optical Cross Section via Collective Coupling of Atomic Dipoles in a 2D Array*, Phys. Rev. Lett. **116**, 103602 (2016) [67]

Part I

Interacting Dipole Theory

Part I: Interacting Dipole Theory

In Chapters 2 and 3, we introduce the main models that will be used throughout the rest of this Thesis. In general, we will be treating the interacting atoms as classical dipoles coupled by and to the classical electromagnetic field. In Section 2.5 we show that this is no different to modeling the dipole as a driven, damped, simple harmonic oscillator.

Rather than simply stating this result, we first spend some time motivating why and in what regimes such a model is valid. We do this by first treating the atoms and electromagnetic field quantum mechanically. Then, taking various approximations including that the external driving field is a sufficiently weak coherent state, we show that the quantum model becomes equivalent to the classical model.

There are several approaches that we could take to doing this. Using quantum field theory, a hierarchy of correlation functions describing the recurrent scattering within an arbitrary atomic density can be derived, which can be solved exactly by numerically averaging over many atomic configurations [37, 38]. If the atomic positions are already well defined, then this is equivalent to calculating the electromagnetic field operator expectations using the Heisenberg equation [36, 68]. By treating this as a quantum scattering process, the same results can be derived by employing transfer matrix methods [17]. Integrating the Schrödinger equation dynamics can also allow this to be treated as an eigenvalue problem [39].

We shall follow the method outlined in the recent textbooks of Gardiner and Zoller [69, 70]. This method involves deriving the quantum master equation for the atomic dynamics via the quantum stochastic Schrödinger equation, allowing us to derive many-atom optical Bloch equations. Assuming the driving is weak and the excited state population negligible, the results are then the same as those mentioned previously.

The reason for choosing this method in particular is that it deals explicitly with the interaction of the atoms mediated by the electromagnetic field, allowing us to highlight important points such as how this field has the same form as the field radiated by a single classical dipole, and that a driving field in a coherent state is also equivalent to a classical electric field. Showing this equivalence between quantum and classical pictures is important for motivating our classical model but is also a subtle point, as it is easy to inad-

vertently credit an observed phenomenon as *quantum*, whilst it may be no less classical in behaviour than a mass on a spring [39, 71] (Sec. 2.5).

Whilst the majority of the material in the Part has appeared elsewhere, the inclusion of it here helps to motivate and explain the results of the later Parts. These Chapters are not intended as a substitute for the literature that has already been mentioned, but rather we will focus on the points of the arguments which best help to highlight our message. For a thorough and well written account, the reader is encouraged to look to [69, 70] or some of the many other excellent texts on the topic.

In Chapter 4 we introduce some of the observable quantities we can calculate with this coupled dipole model. This is by no means an exhaustive list, although the few observables we do consider are more than rich enough to give us much to investigate in the following Parts.

Chapter 2

Single two-level atom

2.1 Overview

We will start our discussion with the most simple system: a single two-level atom interacting with an electromagnetic field. The models used in later Chapters typically treat both the atom and the field classically. However, we will begin here by considering the quantum mechanics of the system, showing that when the electric field is in a sufficiently weak coherent state, the atomic dynamics can be fully described by a classical electric dipole interacting with a classical electric field. Spending some time looking at the quantum model will prove beneficial for understanding the limitations and strengths of the classical model.

The theory presented in this Chapter closely follows the discussions of Zoller and Gardiner which can be found in Chapter 12 of [69] and Chapters 9 and 14 of [70].

2.2 System Hamiltonian

2.2.1 Two-level atom

One of the simplest cases we can consider is that of a single two-level atom, with ground state $|g\rangle$ and excited state $|e\rangle$ (see Fig. 2.1). The energy difference between these two states is $E_e - E_g = \hbar\omega_0$, where $E_{g(e)}$ is the ground (excited) state energy and ω_0 is the resonant transition frequency. Assuming the two states form a closed transition, then the excited state decays solely to the ground state with decay rate $\Gamma_0 \equiv 2\gamma_0$,[a] corresponding to an excited state lifetime of $\tau_0 = 1/\Gamma_0$. We will show in Sec. 2.3.3 that this decay arises due to coupling between the atom and the quantum vacuum field.

In following Sections we will apply a light field to the atom which will couple the two electronic quantum states. In practice, real atoms have many states, some of which may be degenerate. This degeneracy can usually be broken by applying appropriate electric or magnetic fields to the atom (see Sec. 3.2.1), and so assuming that the frequency of the driving field ω is close to the resonant atomic frequency ω_0 (and far detuned from the transitions to all other states), then these other energy levels can be treated as a perturbation, resulting in Stark shifts of the ground and excited state energies (see Chap. 4 of [70]). These shifts are not important for the features we will be considering and so we shall ignore them.

The Hamiltonian describing the bare energies of the two energy levels can be written as

$$\mathsf{H}_0 = E_g |g\rangle\langle g| + E_e |e\rangle\langle e| . \tag{2.2.1}$$

Without loss of generality, we can set the ground state energy $E_g = 0$, in which case

$$\mathsf{H}_0 = \hbar\omega_0 |e\rangle\langle e| . \tag{2.2.2}$$

[a] For convenience, we will use both the decay rate Γ and half-decay rate γ at different points in this Thesis.

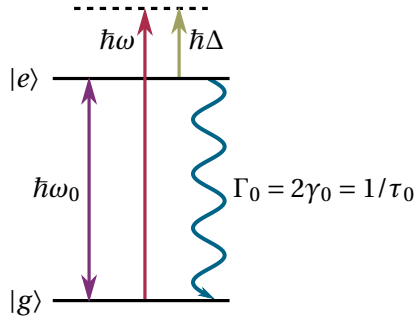

Figure 2.1: Ground $|g\rangle$ and excited $|e\rangle$ energy levels of a two-level atom. The energy levels are separated by an energy $E = \hbar\omega_0$. A driving field with frequency ω is detuned from the bare atomic transition by $\Delta = \omega - \omega_0$. The excited state decays to the ground state with decay rate $\Gamma_0 = 2\gamma_0 = 1/\tau_0$.

2.2.2 Vector notation

It can be convenient to represent $|g\rangle$ and $|e\rangle$ in vector notation,

$$|g\rangle = \begin{pmatrix} 1 \\ 0 \end{pmatrix}, \qquad |e\rangle = \begin{pmatrix} 0 \\ 1 \end{pmatrix}. \tag{2.2.3}$$

Note that other texts (e.g., [69, 70, 72]) will sometimes use the opposite notation $|g\rangle = (0,1)^{\mathrm{T}}$ and $|e\rangle = (1,0)^{\mathrm{T}}$, where T stands for transpose. We can define raising and lowering operators

$$\sigma^+ \equiv |e\rangle\langle g| = \begin{pmatrix} 0 \\ 1 \end{pmatrix}\begin{pmatrix} 1 & 0 \end{pmatrix} = \begin{pmatrix} 0 & 0 \\ 1 & 0 \end{pmatrix}, \qquad \sigma^- \equiv |g\rangle\langle e| = \begin{pmatrix} 1 \\ 0 \end{pmatrix}\begin{pmatrix} 0 & 1 \end{pmatrix} = \begin{pmatrix} 0 & 1 \\ 0 & 0 \end{pmatrix}. \tag{2.2.4}$$

In addition, the Pauli matrices present a convenient basis for describing two-level systems,

$$\sigma^x = \begin{pmatrix} 0 & 1 \\ 1 & 0 \end{pmatrix}, \qquad \sigma^y = \begin{pmatrix} 0 & -\mathrm{i} \\ \mathrm{i} & 0 \end{pmatrix}, \qquad \sigma^z = \begin{pmatrix} 1 & 0 \\ 0 & -1 \end{pmatrix}. \tag{2.2.5}$$

Using this notation, the bare Hamiltonian in Eq. (2.2.2) can be written as

$$\mathsf{H}_0 = \hbar\omega_0 \sigma^+\sigma^- = \begin{pmatrix} 0 & 0 \\ 0 & \hbar\omega_0 \end{pmatrix}. \tag{2.2.6}$$

2.2.3 Density matrix

A convenient representation for describing the behaviour of a quantum state with wavefunction $|\Psi\rangle$ is as a density operator, $\rho \equiv |\Psi\rangle\langle\Psi|$.[b] For the two-level atom, the corresponding density operator (density matrix) in bra-ket and matrix notation is

$$\rho = \big(a|g\rangle + b|e\rangle\big)\big(a^*\langle g| + b^*\langle e|\big) = \begin{pmatrix} \rho_{gg} & \rho_{ge} \\ \rho_{eg} & \rho_{ee} \end{pmatrix}, \tag{2.2.7}$$

where $\rho_{gg} = |a|^2$ and $\rho_{ee} = |b|^2$ are the ground and excited state *populations* respectively, and $\rho_{ge} = ab^*$ and $\rho_{eg} = ba^*$ are the *coherences*. The requirement that the total population be 1 means that the trace of ρ is $\mathrm{Tr}(\rho) = \rho_{gg} + \rho_{ee} = 1$, and the coherences are related by $\rho_{eg} = \rho_{ge}^*$. The expectation of an operator A for a state with density matrix ρ can be found by calculating the trace

$$\langle \mathsf{A} \rangle = \mathrm{Tr}\big(\rho \mathsf{A}\big). \tag{2.2.8}$$

In addition to a two-level atom, the total system also contains electromagnetic (EM) field modes (Sec. 2.2.5), and so the overall wavefunction $|\Psi_{\mathrm{sys}}\rangle$ describes the field as well as the atomic state. However, in Sec. 2.3.6, we will trace away the field parts of the density matrix, being left with just the atomic density matrix in Eq. (2.2.7).

2.2.4 Dipole operator

We assume the energy levels $|g\rangle$ and $|e\rangle$ are coupled via an electric dipole transition. The quantum operator for the dipole moment is

[b] A density operator can be used to describe a statistical mixed state of quantum states that cannot be described by one single state vector, $\rho = \sum_i p_i |\Psi_i\rangle\langle\Psi_i|$.

$$\mathbf{d} \equiv \mathbf{d}_{eg} |e\rangle \langle g| + \mathbf{d}_{ge} |g\rangle \langle e|, \tag{2.2.9}$$

where $\mathbf{d}_{ge} = \langle g| \mathbf{d} |e\rangle = e \langle g| \mathbf{s} |e\rangle = \mathbf{d}_{eg}^*$ is the dipole matrix element, e is the electron charge and $\mathbf{s}$ the electron displacement operator.[c] The expectation value of the dipole moment operator is given by

$$\langle \mathbf{d} \rangle = \mathrm{Tr}\left(\rho \mathbf{d}\right) = \mathbf{d}_{ge}\rho_{eg} + \mathbf{d}_{eg}\rho_{ge}. \tag{2.2.10}$$

The dipole expectation value is therefore related to the coherence ρ_{eg}.

In Sec. 3.2.1 of the next Chapter, we show that the vector polarisation of the dipole transition $\mathbf{d}$ is related to the nature of the ground and excited states. We leave further discussion of this topic to that Section, and for now assume that the transition between the two states results in a dipole polarisation identical to the polarisation of the driving field.

2.2.5 Electric field operator

In addition to the atomic states, the system also contains EM field modes $|\Lambda\rangle \equiv |\mathbf{k}, \hat{\boldsymbol{\epsilon}}_{\varepsilon_\mathbf{k}}\rangle$. The mode index Λ corresponds to a spatial mode with propagation wavevector $\mathbf{k}$ (in a plane wave basis) and polarisation $\hat{\boldsymbol{\epsilon}}_{\varepsilon_\mathbf{k}}$. For a given $\mathbf{k}$, there are two possible polarisations (with index $\varepsilon_\mathbf{k} \in \{1,2\}$), both of which are orthogonal to $\mathbf{k}$ and orthogonal to each other, $(\hat{\boldsymbol{\epsilon}}_{\varepsilon_\mathbf{k}})^* \cdot \hat{\boldsymbol{\epsilon}}_{\varepsilon'_\mathbf{k}} = \delta_{\varepsilon_\mathbf{k},\varepsilon'_\mathbf{k}}$. The wavevector $\mathbf{k} = k\hat{\mathbf{k}}$ has unit vector $\hat{\mathbf{k}}$ and wavenumber $k = |\mathbf{k}|$ with corresponding wavelength $\lambda = 2\pi/k$ and frequency $\omega_k = ck$.

The total electric field operator is (see Eqs. (11.1.43) and (11.1.48) in [69])

$$\mathsf{E}(\mathbf{r}) = \mathrm{i}\sum_\Lambda \sqrt{\frac{\hbar\omega_k}{2\varepsilon_0}} \left[\mathsf{a}_\Lambda \mathbf{u}_\Lambda(\mathbf{r}) - \mathsf{a}_\Lambda^\dagger \mathbf{u}_\Lambda^*(\mathbf{r})\right], \tag{2.2.11}$$

where $\sum_\Lambda = \sum_\mathbf{k} \sum_{\varepsilon_\mathbf{k}}$, the operator $\mathsf{a}^\dagger$ (a) creates (annihilates) a photon in mode Λ, ε_0 is the

[c] The mass of the positively charged atom core (nucleus plus core electrons) is very much larger than the electron and so is assumed to be unmoved by the electric field.

permittivity of free space, $\mathbf{u}_\Lambda(\mathbf{r})$ are the set of plane wave mode functions,

$$\mathbf{u}_\Lambda(\mathbf{r}) = \frac{1}{\sqrt{V}}\hat{\boldsymbol{\epsilon}}_{\varepsilon_\mathbf{k}}\, e^{i\mathbf{k}\cdot\mathbf{r}}, \tag{2.2.12}$$

and V is the quantisation mode volume. There is also a corresponding magnetic field $\mathbf{B}$ which can be related to the electric field via the vector potential operator $\mathbf{A}$ (see, e.g., Sec. 6.2 of [73]). In Sec. 2.3.5, we will show that if the electric field is in a coherent state, it can be treated as a classical electric field. The energy of the field modes is

$$H_{EM} = \sum_\Lambda \hbar\omega_k \left(a_\Lambda^\dagger a_\Lambda + \frac{1}{2}\right). \tag{2.2.13}$$

2.2.6 Atom–field coupling

An electric field couples the atomic ground and excited states, as shown in Fig. 2.1. This induces atomic coherences ρ_{eg} between the ground and excited states which as we saw in Sec. 2.2.4 results in a nonzero electric dipole moment in the atom. The interaction energy between an electric dipole and an electric field is

$$H_{int} = -\mathbf{d}\cdot\mathbf{E}(\mathbf{r}_0), \tag{2.2.14}$$

where $\mathbf{r}_0$ is the atom position. The size of the atom ($\sim 10^{-10}$ m) is much smaller than the wavelength of the driving light ($\lambda \sim 10^{-6}$ m), and so we can assume that the field is constant over the extent of the atom. This is known as the *dipole approximation* and also allows us to ignore higher order multipolar terms (see Sec. 4.2 of [72]).

Substituting in the electric dipole operator (2.2.9) and electric field operator (2.2.11), the interaction energy becomes

$$H_{int} = i\hbar\sigma^- \sum_\Lambda \left(a_\Lambda^\dagger \kappa_\Lambda^* e^{-i\mathbf{k}\cdot\mathbf{r}_0} - a_\Lambda \tilde{\kappa}_\Lambda^* e^{i\mathbf{k}\cdot\mathbf{r}_0}\right) - i\hbar\sigma^+ \sum_\Lambda \left(a_\Lambda \kappa_\Lambda e^{i\mathbf{k}\cdot\mathbf{r}_0} - a_\Lambda^\dagger \tilde{\kappa}_\Lambda e^{-i\mathbf{k}\cdot\mathbf{r}_0}\right), \tag{2.2.15}$$

where we have defined the coupling coefficients as[d]

$$\kappa_\Lambda \equiv \sqrt{\frac{\omega_k}{2\hbar\varepsilon_0}}\mathbf{d}_{eg}\cdot\mathbf{u}_\Lambda(0), \qquad \tilde{\kappa}_\Lambda \equiv \sqrt{\frac{\omega_k}{2\hbar\varepsilon_0}}\mathbf{d}_{eg}\cdot\mathbf{u}^*_\Lambda(0), \tag{2.2.16}$$

2.2.7 Interaction picture, rotating wave approximation

The dynamics we are interested in are those involving the coupling between the atom and the electric field modes. It is therefore convenient to transform into the *interaction picture*. Until now, we have been working in the *Schrödinger picture*, that is, the frame in which the operators H_S are time-*independent* and the state vectors $|\Psi_\mathrm{S}(t)\rangle$ are time-*dependent*. The evolution of the state vectors in the Schrödinger picture is governed by the Schrödinger equation,

$$\frac{\mathrm{d}}{\mathrm{d}t}|\Psi_\mathrm{S}(t)\rangle = -\frac{\mathrm{i}}{\hbar}\mathsf{H}_\mathrm{tot,S}\,|\Psi_\mathrm{S}(t)\rangle\,, \tag{2.2.17}$$

where the Hamiltonians $\mathsf{H}_\mathrm{tot,S} = \mathsf{H}_\mathrm{0,S} + \mathsf{H}_\mathrm{EM,S} + \mathsf{H}_\mathrm{int,S}$ were defined in (2.2.2), (2.2.13) and (2.2.14) respectively. In the *interaction picture*, the operators evolve in time due to the free Hamiltonian (as if there were no atom–field interaction), leaving the state vectors to evolve dependent only on the interaction Hamiltonian H_int. The interaction picture operators and state vectors are related to the Schrödinger picture by the following transformation:

$$\begin{aligned}
\mathsf{U}_I(t) &= \exp\left[-\frac{\mathrm{i}}{\hbar}\big(\mathsf{H}_\mathrm{0,S}+\mathsf{H}_\mathrm{EM,S}\big)t\right],\\
\mathsf{H}_I(t) &= \mathsf{U}_I^\dagger(t)\,\mathsf{H}_\mathrm{S}\,\mathsf{U}_I(t),\\
|\Psi_I(t)\rangle &= \mathsf{U}_I^\dagger(t)\,|\Psi_\mathrm{S}(t)\rangle\,.
\end{aligned} \tag{2.2.18}$$

[d] The signs of κ_Λ and $\tilde{\kappa}_\Lambda$ in Eq. (12.1.28) of [69] differ to those here. However, the quantities of interest are $|\kappa_\Lambda|^2$ and $|\tilde{\kappa}_\Lambda|^2$ and so a sign difference is not important.

Since both $\mathsf{H}_{0,\mathrm{S}}$ and $\mathsf{H}_{\mathrm{EM,S}}$ are diagonal in atomic and field operators respectively, U_I obeys the general rule for exponentials of diagonal matrices,

$$\exp\left(\mathsf{X}\right) = \exp\begin{pmatrix} \mathsf{X}_{11} & 0 & 0 & \dots \\ 0 & \mathsf{X}_{22} & 0 & \dots \\ 0 & 0 & \mathsf{X}_{33} & \dots \\ \vdots & \vdots & \vdots & \ddots \end{pmatrix} = \begin{pmatrix} \mathrm{e}^{\mathsf{X}_{11}} & 0 & 0 & \dots \\ 0 & \mathrm{e}^{\mathsf{X}_{22}} & 0 & \dots \\ 0 & 0 & \mathrm{e}^{\mathsf{X}_{33}} & \dots \\ \vdots & \vdots & \vdots & \ddots \end{pmatrix}. \tag{2.2.19}$$

The bare atomic Hamiltonian has the form (2.2.2)

$$\mathsf{H}_{0,\mathrm{S}} = 0\,|g\rangle\langle g| + \hbar\omega_0\,|e\rangle\langle e|\,. \tag{2.2.20}$$

Notice here that we have included the additional ground state term, even though we previously set the ground state energy to zero.[e] When we take the exponential of $\mathsf{H}_{0,\mathrm{S}}$, the ground state is still important:

$$\exp\left(-\frac{\mathrm{i}}{\hbar}\mathsf{H}_{0,\mathrm{S}}t\right) = \exp\left[-\frac{\mathrm{i}}{\hbar}\left(0\,|g\rangle\langle g| + \hbar\omega_0\,|e\rangle\langle e|\right)t\right] = |g\rangle\langle g|\,\mathrm{e}^{0} + |e\rangle\langle e|\,\mathrm{e}^{-\mathrm{i}\omega_0 t}. \tag{2.2.21}$$

The atomic raising operator in the interaction picture is then[f]

$$\begin{aligned} \sigma_I^+(t) =& \mathsf{U}_I^\dagger \sigma_{\mathrm{S}}^+ \mathsf{U}_I \\ =& \left(|g\rangle\langle g| + |e\rangle\langle e|\,\mathrm{e}^{\mathrm{i}\omega_0 t}\right)|e\rangle\langle g|\left(|g\rangle\langle g| + |e\rangle\langle e|\,\mathrm{e}^{-\mathrm{i}\omega_0 t}\right) \\ =& \mathrm{e}^{\mathrm{i}\omega_0 t}\,|e\rangle\langle g| = \mathrm{e}^{\mathrm{i}\omega_0 t}\sigma_{\mathrm{S}}^+, \end{aligned} \tag{2.2.22}$$

and the lowering operator is $\sigma_I^-(t) = [\sigma_I^+(t)]^\dagger = \mathrm{e}^{-\mathrm{i}\omega_0 t}\sigma_{\mathrm{S}}^-$. The exponential of the EM field Hamiltonian (2.2.13) has a similar form:

$$\exp\left(-\frac{\mathrm{i}}{\hbar}\mathsf{H}_{\mathrm{EM,S}}t\right) = \exp\left\{-\frac{\mathrm{i}}{\hbar}\left[\sum_\Lambda \hbar\omega_k\left(\mathsf{a}_\Lambda^\dagger\mathsf{a}_\Lambda + \frac{1}{2}\right)\right]t\right\}. \tag{2.2.23}$$

It is convenient here to express the creation and annihilation operators in the number

[e] The choice of ground state energy is arbitrary, since E_e is defined relative to E_g.

[f] The EM field part of the Hamiltonian has no effect on the atomic operator, and vice versa.

state basis,

$$a_\Lambda^\dagger = \sum_{n=0}^{\infty} \sqrt{n+1}\,|\Lambda, n+1\rangle\langle\Lambda, n|, \qquad a_\Lambda = \sum_{n=1}^{\infty} \sqrt{n}\,|\Lambda, n-1\rangle\langle\Lambda, n|, \tag{2.2.24}$$

where $|\Lambda, n\rangle$ is the EM field state with n photons in mode Λ. The exponential in Eq. (2.2.23) then becomes

$$\begin{aligned}\exp\left\{-\frac{\mathrm{i}}{\hbar}\left[\sum_\Lambda \hbar\omega_k\left(\frac{1}{2}+\mathsf{a}_\Lambda^\dagger\mathsf{a}_\Lambda\right)\right]t\right\} &= \exp\left\{-\frac{\mathrm{i}}{\hbar}\left[\sum_\Lambda \hbar\omega_k\left(\frac{1}{2}+\sum_{n=0}^{\infty} n\,|\Lambda, n\rangle\langle\Lambda, n|\right)\right]t\right\} \\ &= \sum_\Lambda \mathrm{e}^{-\mathrm{i}\omega_k t/2}\sum_{n=0}^{\infty}\mathrm{e}^{-\mathrm{i}n\omega_k t}\,|\Lambda, n\rangle\langle\Lambda, n|. \end{aligned}\tag{2.2.25}$$

An EM field creation operator in the interaction picture is therefore

$$\begin{aligned}\mathsf{a}_{\Lambda,I}^\dagger(t) =& \mathsf{U}_I^\dagger(t)\,\mathsf{a}_{\Lambda,\mathrm{S}}^\dagger\,\mathsf{U}_I(t) \\ =& \left(\sum_{\Lambda'}\mathrm{e}^{\mathrm{i}\omega_{k'}t/2}\sum_{n'=0}^{\infty}\mathrm{e}^{\mathrm{i}n'\omega_{k'}t}\,|\Lambda', n'\rangle\langle\Lambda', n'|\right)\sum_{n=0}^{\infty}\sqrt{n+1}\,|\Lambda, n+1\rangle\langle\Lambda, n| \\ &\times\left(\sum_{\Lambda''}\mathrm{e}^{-\mathrm{i}\omega_{k''}t/2}\sum_{n''=0}^{\infty}\mathrm{e}^{-\mathrm{i}n''\omega_{k''}t}\,|\Lambda'', n''\rangle\langle\Lambda'', n''|\right) \\ =& \sum_{\Lambda'\Lambda''}\mathrm{e}^{\mathrm{i}(\omega_{k'}-\omega_{k''})t/2}\sum_{n=0}^{\infty}\sum_{n'=0}^{\infty}\sum_{n''=0}^{\infty}\mathrm{e}^{\mathrm{i}(n'\omega_{k'}-n''\omega_{k''})t}\sqrt{n+1}\,|\Lambda', n'\rangle\langle\Lambda'', n''| \\ &\times\delta_{\Lambda',\Lambda}\delta_{\Lambda'',\Lambda}\delta_{n',n+1}\delta_{n,n''} \\ =& \mathrm{e}^{\mathrm{i}\omega_k t}\sum_{n=0}^{\infty}\sqrt{n+1}\,|\Lambda, n+1\rangle\langle\Lambda, n| \\ =& \mathrm{e}^{\mathrm{i}\omega_k t}\,a_{\Lambda,\mathrm{S}}^\dagger\,. \end{aligned}\tag{2.2.26}$$

The corresponding annihilation operator is $\mathsf{a}_{\Lambda,I}(t) = [\mathsf{a}_{\Lambda,I}^\dagger(t)]^\dagger = \mathrm{e}^{-\mathrm{i}\omega_k t}\,\mathsf{a}_{\Lambda,\mathrm{S}}$.

The bare atomic Hamiltonian and field Hamiltonian are therefore unchanged in the interaction picture,

$$\mathsf{H}_{0,\mathrm{S}} = \hbar\omega_0\,|e\rangle\langle e| = \hbar\omega_0\sigma_\mathrm{S}^+\sigma_\mathrm{S}^- = \hbar\omega_0\,\sigma_I^+(t)\,\sigma_I^-(t) = \mathsf{H}_{0,I}(t), \tag{2.2.27a}$$

$$\mathsf{H}_{\mathrm{EM,S}} = \sum_\Lambda \hbar\omega_k\left(a_\mathrm{S}^\dagger a_\mathrm{S}+\frac{1}{2}\right) = \sum_\Lambda \hbar\omega_k\left(a_I^\dagger(t)\,a_I(t)+\frac{1}{2}\right) = \mathsf{H}_{\mathrm{EM},I}(t). \tag{2.2.27b}$$

The interaction Hamiltonian (2.2.15) on the other hand becomes

$$\begin{aligned}\mathsf{H}_{\mathrm{int},I}(t) =& \mathrm{i}\hbar\sigma_{\mathrm{S}}^{-}\sum_{\Lambda}\left(\mathsf{a}_{\Lambda,\mathrm{S}}^{\dagger}\kappa_{\Lambda}^{*}\,\mathrm{e}^{\mathrm{i}(\omega_k-\omega_0)t-\mathrm{i}\mathbf{k}\cdot\mathbf{r}_0} - \mathsf{a}_{\Lambda,\mathrm{S}}\tilde{\kappa}_{\Lambda}^{*}\,\mathrm{e}^{-\mathrm{i}(\omega_k+\omega_0)+\mathrm{i}\mathbf{k}\cdot\mathbf{r}_0}\right)\\ &-\mathrm{i}\hbar\sigma_{\mathrm{S}}^{+}\sum_{\Lambda}\left(\mathsf{a}_{\Lambda,\mathrm{S}}\kappa_{\Lambda}\,\mathrm{e}^{-\mathrm{i}(\omega_k-\omega_0)t+\mathrm{i}\mathbf{k}\cdot\mathbf{r}_0} - \mathsf{a}_{\Lambda,\mathrm{S}}^{\dagger}\tilde{\kappa}_{\Lambda}\,\mathrm{e}^{\mathrm{i}(\omega_k+\omega_0)t-\mathrm{i}\mathbf{k}\cdot\mathbf{r}_0}\right).\end{aligned} \tag{2.2.28}$$

Notice that we have kept the atomic and field operators in their time-independent Schrödinger picture forms. By convention, we will omit the subscript S to refer to the Schrödinger picture and assume that unless stated explicitly, all operators and state vectors are in the Schrödinger picture.

Using these results, the Schrödinger equation in the interaction picture becomes

$$\begin{aligned}\frac{\mathrm{d}}{\mathrm{d}t}|\Psi_I(t)\rangle =& \frac{\mathrm{d}}{\mathrm{d}t}\mathsf{U}_I^{\dagger}(t)\,|\Psi_{\mathrm{S}}(t)\rangle\\ =& \left[\frac{\mathrm{d}}{\mathrm{d}t}\mathsf{U}_I^{\dagger}(t)\right]|\Psi_{\mathrm{S}}(t)\rangle + \mathsf{U}_I^{\dagger}(t)\left[\frac{\mathrm{d}}{\mathrm{d}t}|\Psi_{\mathrm{S}}(t)\rangle\right]\\ =& \left[\frac{\mathrm{i}}{\hbar}\left(\mathsf{H}_{0,\mathrm{S}}+\mathsf{H}_{\mathrm{EM,S}}\right)\right]\mathsf{U}_I^{\dagger}(t)\,|\Psi_{\mathrm{S}}(t)\rangle - \frac{\mathrm{i}}{\hbar}\mathsf{U}_I^{\dagger}(t)\left(\mathsf{H}_{0,\mathrm{S}}+\mathsf{H}_{\mathrm{EM,S}}+\mathsf{H}_{\mathrm{int,S}}\right)|\Psi_{\mathrm{S}}(t)\rangle\\ =& -\frac{\mathrm{i}}{\hbar}\left[\mathsf{U}_I^{\dagger}(t)\mathsf{H}_{\mathrm{int,S}}\mathsf{U}_I(t)\right]\left[\mathsf{U}_I^{\dagger}(t)\,|\Psi_{\mathrm{S}}(t)\rangle\right]\\ =& -\frac{\mathrm{i}}{\hbar}\mathsf{H}_{\mathrm{int},I}(t)\,|\Psi_I(t)\rangle.\end{aligned} \tag{2.2.29}$$

This is also known as the *Schwinger–Tomonaga equation*. As already mentioned, the evolution of $|\Psi_I(t)\rangle$ therefore only depends on the interaction Hamiltonian.

2.2.8 Rotating wave approximation

There are two different contributions to the atom–field interaction that we need to consider. Firstly, the atom interacts with an external driving field, which we will assume to be both monochromatic and close to resonance ($\omega \simeq \omega_0$). Secondly, the atom also interacts with the quantum vacuum field, spontaneously and randomly emitting and absorbing photons into and from all possible field modes. However, we can restrict the sum over modes Λ in (2.2.28) to a small range around ω_0, $|\omega_k - \omega_0| < \vartheta$, where ϑ is the *coupling*

bandwidth (see Sec. 9.1 of [70]).[g] This will allow us to set appropriate time scales for the Born–Markov approximations discussed later in Sec. 2.3.3.

With these two considerations, it becomes clear that the $\omega_k + \omega_0$ terms in Eq. (2.2.28) will oscillate very much faster than any of the other time scales involved, and these terms can thus be dropped from H_{int},

$$\mathsf{H}_{\text{int},I}(t) \simeq \mathrm{i}\hbar \sum_{|\omega_k-\omega_0|<\vartheta} \left(\sigma^- \mathsf{a}_\Lambda^\dagger \kappa_\Lambda^* \, \mathrm{e}^{\mathrm{i}(\omega_k-\omega_0)t - \mathrm{i}\mathbf{k}\cdot\mathbf{r}_0} - \sigma^+ \mathsf{a}_\Lambda \kappa_\Lambda \, \mathrm{e}^{-\mathrm{i}(\omega_k-\omega_0)t + \mathrm{i}\mathbf{k}\cdot\mathbf{r}_0}\right). \tag{2.2.30}$$

The two remaining terms correspond physically to the atom emitting a photon into mode Λ ($\sigma^- \mathsf{a}_\Lambda^\dagger$) and the atom absorbing a photon from mode Λ ($\sigma^+ \mathsf{a}_\Lambda$). The two terms that were discarded corresponded to the atom decaying and the field gaining a photon simultaneously and vice versa, which is clearly much less likely for the case of resonant driving. There are many situations in which these non-resonant terms are important [74, 75, 76], although that is beyond the scope of this Thesis.

2.3 Dissipation: Quantum Stochastic Schrödinger Equation and the Master Equation

2.3.1 Overview

We now have a Schrödinger equation (2.2.29) which describes the dynamics of the system in the interaction picture. If it were possible to follow the evolution of the EM field states, the evolution of the system would be coherent. However, in tracing over the EM field, the atomic evolution becomes noisy resulting in dissipation, i.e. loss of energy and information into the EM field from the atomic system. In this Section, we will employ one of the stochastic methods of modelling this dissipation: the *quantum stochastic Schrödinger equation* (again, following the discussion from Chapters 9 and 14 of [69]). From this we will derive a master equation which will describe the full dissipative system dynamics.

[g] It is still assumed that we sum over the two polarisations as well.

2.3.2 Noise operator

The atom–field interaction Hamiltonian in the interaction picture and the rotating wave approximation (2.2.30) can be written as

$$\mathsf{H}_{\mathrm{int},I}(t) = \mathrm{i}\hbar\left[\mathsf{f}^\dagger(t)\sigma^- - \sigma^+\mathsf{f}(t)\right], \tag{2.3.1}$$

where $\mathsf{f}(t)$ is a time-dependent noise operator

$$\mathsf{f}(t) \equiv \sum_{|\omega_k-\omega_0|<\vartheta} \kappa_\Lambda \mathsf{a}_\Lambda \, \mathrm{e}^{-\mathrm{i}(\omega_k-\omega_0)t+\mathrm{i}\mathbf{k}\cdot\mathbf{r}_0}. \tag{2.3.2}$$

These noise operators have the commutation relation

$$\left[\mathsf{f}(t),\mathsf{f}^\dagger(t')\right] = \gamma(t-t'), \tag{2.3.3}$$

where

$$\begin{aligned}\gamma(\tau) &= \sum_{|\omega_k-\omega_0|<\vartheta} |\kappa_\Lambda|^2 \mathrm{e}^{-\mathrm{i}(\omega_k-\omega_0)\tau}, \\ &\to \int_{\omega_0-\vartheta}^{\omega_0+\vartheta} \mathrm{d}\omega\, g(\omega)\,|\kappa(\omega)|^2\,\mathrm{e}^{-\mathrm{i}(\omega-\omega_0)\tau},\end{aligned} \tag{2.3.4}$$

where we have assumed the modes are a continuum with a density of states $g(\omega)$. We have also made use of the bosonic commutation relation $[\mathsf{a}_\Lambda, \mathsf{a}^\dagger_{\Lambda'}] = \delta_{\Lambda,k'}$. One of the requirements of the choice of coupling bandwidth ϑ is that $g(\omega)|\kappa(\omega)|$ varies smoothly over the range $(\omega_0 \pm \vartheta)$.

2.3.3 Born–Markov approximation

The interaction picture Schrödinger equation (2.2.29) is

$$\frac{\mathrm{d}}{\mathrm{d}t}|\Psi_I(t)\rangle = \left[\sigma^-\mathsf{f}^\dagger(t) - \sigma^+\mathsf{f}(t)\right]|\Psi_I(t)\rangle, \tag{2.3.5}$$

where we have assumed that the initial state is a product of the atomic and field states $|\Psi_I(0)\rangle = |\Psi_{0,I}(0)\rangle \otimes |\Psi_{\mathrm{EM},I}(0)\rangle$, and so the atomic ($\sigma^{\pm}$) and field ($f, f^{\dagger}$) operators commute. Integrating Eq. (2.3.5) from $t = 0$ to t gives[h]

$$|\Psi_I(t)\rangle = \left\{1 + \int_0^t \mathrm{d}t_1 \left[\sigma^- \mathrm{f}^\dagger(t_1) - \sigma^+ \mathrm{f}(t_1)\right]\right\} |\Psi_I(0)\rangle + \int_0^t \mathrm{d}t_1 \left[\sigma^- \mathrm{f}^\dagger(t_1) - \sigma^+ \mathrm{f}(t_1)\right] \int_0^{t_1} \mathrm{d}t_2 \left[\sigma^- \mathrm{f}^\dagger(t_2) - \sigma^+ \mathrm{f}(t_2)\right] |\Psi_I(t_2)\rangle . \tag{2.3.6}$$

Let us consider a time interval $0 < t_2 < \Delta t$. We can replace $|\Psi_I(t_2)\rangle \simeq |\Psi_I(0)\rangle$ in the second line of (2.3.6) if we assume that interaction is sufficiently weak. This is known as the *Born approximation*. If we also assume that the field is initially in the vacuum state such that $\mathrm{f}|\Psi_I(0)\rangle = 0$ and use the commutation relation from (2.3.3), then the state vector after the time interval Δt is

$$\begin{aligned} |\Psi_I(\Delta t)\rangle = &\left[1 - \sigma^+\sigma^- \int_0^{\Delta t} \mathrm{d}t_1 \int_0^{t_1} \mathrm{d}t_2 \gamma(t_1 - t_2)\right] |\Psi_I(0)\rangle \\ &+ \sigma^- \int_0^{\Delta t} \mathrm{d}t_1 \mathrm{f}^\dagger(t_1) |\Psi_I(0)\rangle \\ &+ \sigma^-\sigma^- \int_0^{\Delta t} \mathrm{d}t_1 \int_0^{t_1} \mathrm{d}t_2 \mathrm{f}^\dagger(t_1)\mathrm{f}^\dagger(t_2) |\Psi_I(0)\rangle . \end{aligned} \tag{2.3.7}$$

The three lines in Eq. (2.3.7) correspond respectively to states with zero, one and two photons. For sufficiently small Δt, the probability of the two-photon state is negligible (order Δt^2) and so only the first two lines need be considered.

If we further assume that $\Delta t \gg 1/\vartheta$, then we can approximate

$$\gamma(t_1 - t_2) \simeq 2\left(\frac{1}{2}\Gamma + \mathrm{i}\delta\omega\right)\delta(t_1 - t_2), \tag{2.3.8}$$

where $\delta(t_1 - t_2)$ is the Dirac delta function, and the damping constant Γ and line-shift $\delta\omega$

[h] If $\mathrm{d}y(t)/\mathrm{d}t = x(t)y(t)$ then $\int_0^t \dot{y}(t_1)\mathrm{d}t_1 = \int_0^t x(t_1)y(t_1)\mathrm{d}t_1 = \int_0^t x(t_1)y(0)\mathrm{d}t_1 + \int_0^t x(t_1)\left(\int_0^{t_1} \dot{y}(t_2)\mathrm{d}t_2\right)\mathrm{d}t_1$

are given by

$$\Gamma = 2\pi g(\omega_0)|\kappa(\omega_0)|^2, \tag{2.3.9a}$$

$$\delta\omega = -\mathrm{P}\int_{\omega_0-\vartheta}^{\omega_0+\vartheta} \mathrm{d}\omega \frac{g(\omega)|\kappa(\omega)|^2}{\omega-\omega_0}, \tag{2.3.9b}$$

where P is the principal value integral (Eq. (12.2.21) of [69] and Eq. B.2.7 in Appendix B). This is known as the *Markov approximation* and has the physical significance that the free system dynamics happen on a much faster time scale (ω_0, ω_k) than the evolution in the interaction picture $(\Gamma, \delta\omega)$. The double integral in the first line of Eq. (2.3.7) then becomes

$$\int_0^{\Delta t} \mathrm{d}t_1 \int_0^{t_1} \mathrm{d}t_2\, \gamma(t_1-t_2) \simeq \left(\frac{1}{2}\Gamma + \mathrm{i}\delta\omega\right)\Delta t. \tag{2.3.10}$$

Substituting in κ from (2.3.7) and integrating over the quantisation volume V, the damping constant Γ becomes (B.2.6)

$$\Gamma = \Gamma_0 = \frac{|\mathbf{d}_{eg}|^2 k_0^3}{3\pi\varepsilon_0\hbar}. \tag{2.3.11}$$

This is just the natural decay rate of the single two-level atom Γ_0 introduced in Sec. 2.2.1.

The line-shift $\delta\omega$ can also be determined, although this requires careful renormalisation of $(\omega-\omega_0)$ terms in the denominator. In full quantum electrodynamics, this line-shift is the *Lamb shift*. From now on we shall assume that $\delta\omega$ is included within the definition of ω_0 and so can be ignored.

2.3.4 Quantum stochastic Schrödinger equation

The one-photon term in (2.3.7) can be redefined as a *quantum Ito increment* (see Sec. 4.1 of [69] and Secs. 9.3 and 21.2.2 of [70])

$$\Delta\mathsf{B}(t) \equiv \frac{1}{\sqrt{\Gamma_0}}\int_t^{t+\Delta t} \mathsf{f}(t_1)\mathrm{d}t_1. \tag{2.3.12}$$

We cannot let $\Delta t \to 0$ (since $\Delta t \gg \vartheta$), although in the limit that the interaction strength $(\Gamma_0, \delta\omega)$ is very weak, (2.3.7) can be written as a differential equation

$$\mathrm{d}|\Psi_I(t)\rangle = \left[-\frac{\Gamma_0}{2}\sigma^+\sigma^-\mathrm{d}t + \sqrt{\Gamma_0}\sigma^-\mathrm{dB}^\dagger(t)\right]|\Psi_I(t)\rangle\,. \tag{2.3.13}$$

This is known as the *quantum stochastic Schrödinger equation.*

Ito stochastic differential equations were originally used to describe classical Brownian motion of particles in thermal systems. Collisions between particles in these systems result in each particle experiencing a random force acting on its motion. What we are considering here is the quantum analog of this, where the dynamics of the internal atomic quantum state are being influenced by a random noise term due to quantum vacuum fluctuations. The classical Ito term describes the differential change in particle velocity; the quantum Ito term describes the equivalent differential change in the state wavefunction. It is assumed that the noise terms in first order average to zero, and so using the calculus resulting from the Ito formalism (Sec. 2.3.6), the expectations resulting from the state dynamics can be expressed in a way that removes these fluctuating noise terms. What this means is that whilst the state vector itself evolves noisily, the expectation of the state vector evolves smoothly and deterministically. More details can be found in Chapters 3 and 4 of [69].

As an aside, one alternative method for solving the quantum stochastic Schrödinger equation directly is via the method of quantum jumps [77]. In this method, the wavefunction of the (atomic) system is allowed to evolve coherently with no dissipation. At random time intervals however, a decay event is assumed to occur, corrresponding to the detection of a spontaneous photon. When this happens, the atomic wavefunction is instantaneously projected onto the ground state, and then once more allowed to evolve coherently until another decay event occurs. The time between decay events is a random variable with some characteristic lifetime. This process is repeated over many realisations, and the average of these realisations then converges to the full dissipative dynamics of the system. One advantage of this type of approach over a master equation approach, which we shall discuss in Sec. 2.3.6, is that the wavefunction has the square root of the dimension of the density matrix, which for large systems can greatly reduce the computational complexity.

2.3.5 Classical driving field

In Section 9.5 of [70] the authors consider the case where the EM field modes are initially each in a coherent state. A coherent state $|\beta_\Lambda\rangle$ is the eigenstate of the field annihilation operator,

$$\mathsf{a}_\Lambda |\beta_\Lambda\rangle = \beta_\Lambda |\beta_\Lambda\rangle . \tag{2.3.14}$$

The noise operator acting on a coherent state $|\boldsymbol{\beta}\rangle = \bigotimes_\Lambda |\beta_\Lambda\rangle$, where $\bigotimes_\Lambda$ is the tensor product over all field modes, is then

$$\mathsf{f}(t)\,|\boldsymbol{\beta}\rangle = F(t)\,|\boldsymbol{\beta}\rangle , \tag{2.3.15}$$

where

$$F(t) = \sum_{|\omega_k-\omega_0|<\vartheta} \kappa_\Lambda \beta_\Lambda \mathrm{e}^{-\mathrm{i}(\omega_k-\omega_0)t+\mathrm{i}\mathbf{k}\cdot\mathbf{r}_0}, \tag{2.3.16}$$

is a complex-valued function of t (and $\mathbf{r}_0$). When we use this new state vector (the coherent field in addition to the vacuum field), we obtain a similar expression for $|\Psi_I(\Delta t)\rangle$ (2.3.7), with terms corresponding to zero, one and two photons,

$$\begin{aligned} |\Psi_I(\Delta t)\rangle = &\left[1-\sigma^+\sigma^- \int_0^{\Delta t} \mathrm{d}t_1 \int_0^{t_1} \mathrm{d}t_2 \gamma(t_1-t_2)\right] |\Psi_I(0)\rangle \\ &+ \int_0^{\Delta t} \mathrm{d}t_1 \left[\sigma^- \mathsf{f}^\dagger(t_1) + \sigma^- F^*(t_1) - \sigma^+ F(t_1)\right] |\Psi_I(0)\rangle \\ &+ \big(\text{two-photon terms}\big) . \end{aligned} \tag{2.3.17}$$

The zero-photon term has remained unchanged and the two-photon term can again be neglected since the probability scales with Δt^2.

The modified quantum stochastic Schrödinger equation (2.3.13) has the form

$$\mathrm{d}|\Psi_I(t)\rangle = \left[-\frac{\Gamma_0}{2}\sigma^+\sigma^-\,\mathrm{d}t + \Big(F^*(t)\sigma^- - F(t)\sigma^+\Big)\mathrm{d}t + \sqrt{\Gamma_0}\sigma^-\mathrm{d}\mathsf{B}^\dagger(t)\right] |\Psi_I(t)\rangle , \tag{2.3.18}$$

where we have subtracted the coherent part of the noise operator from the quantum Ito

increment,

$$\Delta \mathsf{B}(t) \equiv \frac{1}{\sqrt{\Gamma_0}} \int_t^{t+\Delta t} \Big[\mathsf{f}(t_1) - F(t_1) \Big] \mathrm{d}t_1. \tag{2.3.19}$$

Comparing the first two terms in (2.3.18), we can see that the coherent state adds an additional Hamiltonian-like term, which has the form

$$\begin{aligned} F^*(t)\sigma^- - F(t)\sigma^+ &= \sum_{|\omega_k - \omega_0| < \vartheta} \left(\kappa_\Lambda^* \beta_\Lambda^* \mathrm{e}^{\mathrm{i}(\omega_k - \omega_0)t - \mathrm{i}\mathbf{k}\cdot\mathbf{r}_0} \sigma^- - \kappa_\Lambda \beta_\Lambda \mathrm{e}^{-\mathrm{i}(\omega_k - \omega_0)t + \mathrm{i}\mathbf{k}\cdot\mathbf{r}_0} \sigma^+ \right) \\ &= -\frac{\mathrm{i}}{\hbar} \Big[-\mathbf{d} \cdot \mathscr{E}_0(\mathbf{r}_0) \Big], \end{aligned} \tag{2.3.20}$$

where $\mathbf{d} = \mathbf{d}_{ge}\sigma^- \mathrm{e}^{-\mathrm{i}\omega_0 t} + \mathbf{d}_{eg}\sigma^+ \mathrm{e}^{\mathrm{i}\omega_0 t}$ is the dipole operator and $\mathscr{E}_0$ is a classical electric field:

$$\begin{aligned} \mathscr{E}_0(\mathbf{r}, t) &= \mathbf{E}_0(\mathbf{r}, t)\mathrm{e}^{-\mathrm{i}\omega_k t} + \mathbf{E}_0^*(\mathbf{r}, t)\mathrm{e}^{\mathrm{i}\omega_k t} \\ &= 2\,\mathrm{Re}[\mathbf{E}_0(\mathbf{r}, t)]\,\cos\omega_k t + 2\,\mathrm{Im}[\mathbf{E}_0(\mathbf{r}, t)]\,\sin\omega_k t. \end{aligned} \tag{2.3.21}$$

We assume that the temporal profile function $\mathbf{E}_0(t)$ varies slowly on the optical time scale, $|\dot{\mathbf{E}}_0(t)| \ll \omega_k |\mathbf{E}_0(t)|$. In most of this Thesis we will just consider constant driving field amplitudes $\mathbf{E}_0(\mathbf{r}, t) = \mathbf{E}_0(\mathbf{r})$. The sum over modes has reduced to just a single mode with frequency ω_k (monochromatic) and polarisation $\hat{\boldsymbol{\epsilon}}$.

This is an important result: a coherent field state behaves the same as a classical electric field, with interaction Hamiltonian of the same form as $\mathsf{H}_{\mathrm{int}}$ (2.2.14).

2.3.6 Master equation

In its current form, the quantum stochastic Schrödinger equation

$$\mathrm{d}|\Psi_I(t)\rangle = \left[-\frac{\mathrm{i}}{\hbar} \mathsf{H}_{\mathrm{eff},I}\, \mathrm{d}t + \sqrt{\Gamma_0}\sigma^- \mathrm{d}\mathsf{B}^\dagger(t) \right] |\Psi_I(t)\rangle, \tag{2.3.22}$$

with effective (non-Hermitian) Hamiltonian

$$\mathsf{H}_{\text{eff},I} = -\mathrm{i}\hbar\frac{\Gamma_0}{2}\sigma^+\sigma^- - \mathbf{d}_{eg}\cdot\mathbf{E}_0(\mathbf{r}_0,t)\mathrm{e}^{-\mathrm{i}(\omega_k-\omega_0)t}\sigma^+ - \mathbf{d}_{ge}\cdot\mathbf{E}_0^*(\mathbf{r}_0,t)\mathrm{e}^{\mathrm{i}(\omega_k-\omega_0)t}\sigma^-, \tag{2.3.23}$$

is inconvenient to work with given the presence of the quantum Ito term $\mathrm{d}\mathsf{B}$. The advantage of the quantum Ito representation lies in the algebra rules that govern it (Eq. (9.3.21) in [70]):

$$\begin{aligned}\mathrm{d}\mathsf{B}(t)\,\mathrm{d}\mathsf{B}^\dagger(t) &= \mathrm{d}t,\\ \mathrm{d}\mathsf{B}^\dagger(t)\,\mathrm{d}\mathsf{B}(t) = \mathrm{d}\mathsf{B}(t)^2 = \mathrm{d}\mathsf{B}^\dagger(t)^2 &= 0,\\ \mathrm{d}\mathsf{B}(t)\mathrm{d}t = \mathrm{d}t\mathrm{d}\mathsf{B}(t) = \mathrm{d}\mathsf{B}^\dagger(t)\mathrm{d}t = \mathrm{d}t\mathrm{d}\mathsf{B}^\dagger(t) = \mathrm{d}t^2 &= 0.\end{aligned} \tag{2.3.24}$$

The calculus of two quantum Ito terms B and C also contains additional terms compared with the conventional calculus,

$$\mathrm{d}(\mathsf{BC}) = (\mathrm{d}\mathsf{B})\mathsf{C} + \mathsf{B}(\mathrm{d}\mathsf{C}) + (\mathrm{d}\mathsf{B})(\mathrm{d}\mathsf{C}). \tag{2.3.25}$$

A solution to (2.3.22) can be found using a method like that described in Sec. 2.3.4, involving many numerical stochastic realisations. It can, however, be convenient to consider the density matrix $\rho(t) \equiv |\Psi(t)\rangle\langle\Psi(t)|$ defined in Sec. (2.2.3), as opposed to just the wavefunction $|\Psi(t)\rangle$ (for example, if considering a mixed state). Converting the quantum stochastic Schrödinger equation into a master equation will allow us to obtain equations of motion for the individual elements in the density matrix, rather than relying on numerical stochastic realisations. For particular limits, we will even be able to obtain analytic solutions to these equations of motion.

We are not concerned with the behaviour of the field part of the wavefunction and so we can extract just the atomic part of the density matrix by calculating the *reduced atomic density matrix*,

$$\rho_0(t) \equiv \mathrm{Tr}_{\mathrm{EM}}\Big(|\Psi(t)\rangle\langle\Psi(t)|\Big), \tag{2.3.26}$$

where $\mathrm{Tr}_{\mathrm{EM}}$ is a trace over the field parts of the density matrix. Transforming back into the *Schrödinger picture*[i] and using the quantum Ito calculus rules in (2.3.24) and (2.3.25),

[i] We do not remove the oscillation of the EM field as this is no longer operator-valued.

the nonzero terms left when considering a differential element of $\mathrm{d}\rho_0(t)$ give us the single atom master equation [70],

$$\dot{\rho}_0(t) = -\frac{\mathrm{i}}{\hbar}\left[\mathsf{H}_{\mathrm{sys,S}}, \rho_0(t)\right] + \frac{\Gamma_0}{2}\left(2\sigma^- \rho(t)\sigma^+ - \sigma^+\sigma^-\rho(t) - \rho(t)\sigma^+\sigma^-\right), \tag{2.3.27}$$

where $[a,b] \equiv ab - ba$ is a commutator and the coherent dynamics are included in $\mathsf{H}_{\mathrm{sys}}$,

$$\mathsf{H}_{\mathrm{sys,S}} = \hbar\omega_0 \sigma^+\sigma^- - \mathbf{d}_{eg}\cdot\mathbf{E}_0(\mathbf{r}_0,t)\,\mathrm{e}^{-\mathrm{i}\omega_k t}\sigma^+ - \mathbf{d}_{ge}\cdot\mathbf{E}_0^*(\mathbf{r}_0,t)\,\mathrm{e}^{\mathrm{i}\omega_k t}\sigma^-. \tag{2.3.28}$$

The dissipation is now included in the three terms outside the commutator. The terms $(-\sigma^+\sigma^-\rho - \rho\sigma^+\sigma^-)$ come from the imaginary part of $\mathsf{H}_{\mathrm{eff}}$. The quantum Ito term $(\sigma^-\rho\sigma^+)$ is known as the *recycling term* because it recycles population, conserving the trace of ρ.

The master equation in (2.3.27) can be expressed in terms of the well known *optical Bloch equations* for a single two-level atom,

$$\dot{\rho}_{ee} = -\dot{\rho}_{gg} = -\rho_{ee}\Gamma_0 - \frac{\mathrm{i}}{\hbar}\left(\mathbf{d}_{ge}\cdot\mathbf{E}_0^*\,\mathrm{e}^{\mathrm{i}\omega_k t}\rho_{eg} - \mathbf{d}_{eg}\cdot\mathbf{E}_0\,\mathrm{e}^{-\mathrm{i}\omega_k t}\rho_{ge}\right), \tag{2.3.29a}$$

$$\dot{\rho}_{eg} = \dot{\rho}_{ge}^* = -\left(\mathrm{i}\omega_0 + \frac{\Gamma_0}{2}\right)\rho_{eg} - \frac{\mathrm{i}}{\hbar}\left(\rho_{ee} - \rho_{gg}\right)\mathbf{d}_{eg}\cdot\mathbf{E}_0\,\mathrm{e}^{-\mathrm{i}\omega_k t}. \tag{2.3.29b}$$

These can be calculated from the many-atom optical Bloch equations (C.5.4) and (C.5.6) in Appendix C by ignoring the many-atom terms and just considering a single excited energy level.

2.4 Dipole moment

2.4.1 Equations of motion

We have written the oscillating (classical) electric field in the form (2.3.21)

$$\begin{aligned}\mathscr{E}_0(\mathbf{r},t) =& \mathbf{E}_0(\mathbf{r},t)\,\mathrm{e}^{-\mathrm{i}\omega_k t} + \mathbf{E}_0^*(\mathbf{r},t)\,\mathrm{e}^{\mathrm{i}\omega_k t} \\ =& 2\,\mathbf{E}_0^{\Re}(\mathbf{r},t)\,\cos\omega_k t + 2\,\mathbf{E}_0^{\Im}(\mathbf{r},t)\,\sin\omega_k t. \end{aligned} \tag{2.4.1}$$

We have constructed this in such a way that the real and imaginary parts of $\mathbf{E}_0 = \mathbf{E}_0^{\Re} + \mathrm{i}\mathbf{E}_0^{\Im}$ correspond to the two different quadratures of the oscillating total field, oscillating $\pi/2$ out of phase with respect to each other.[j] $\mathbf{E}_0$ itself is not oscillating but rather is in a rotating frame with frequency ω.

We can express the dipole operator (in the Schrödinger picture) in a similar manner,

$$\begin{aligned}\langle \mathbf{d} \rangle = \mathrm{Tr}\left(\rho \mathbf{d}\right) =& \mathbf{d}_{ge}\rho_{eg} + \mathbf{d}_{eg}\rho_{ge} \\ =& \left(\mathbf{d}_{ge}\rho_{eg}\mathrm{e}^{\mathrm{i}\omega_k t}\right)\mathrm{e}^{-\mathrm{i}\omega_k t} + \left(\mathbf{d}_{eg}\rho_{ge}\mathrm{e}^{-\mathrm{i}\omega_k t}\right)\mathrm{e}^{\mathrm{i}\omega_k t} \\ \equiv& \mathbf{d}\,\mathrm{e}^{-\mathrm{i}\omega_k t} + \mathbf{d}^*\,\mathrm{e}^{\mathrm{i}\omega_k t} \\ =& 2\,\mathbf{d}^{\Re}\cos\omega_k t + 2\,\mathbf{d}^{\Im}\sin\omega_k t, \end{aligned} \tag{2.4.2}$$

where $\mathbf{d} \equiv \mathbf{d}_{ge}\rho_{eg}\mathrm{e}^{\mathrm{i}\omega_k t}$. As with the electric field, this is therefore a way of representing a real dipole moment $\langle \mathbf{d} \rangle$, which oscillates with the same frequency as the driving field ω_k, as a complex vector $\mathbf{d}$ whose real and imaginary parts correspond to the two different quadratures of oscillation. For example, if $\mathbf{E}_0^{\Im} = 0$, i.e. $\mathscr{E}_0$ oscillates with $\cos\omega_k t$, then the real and imaginary parts of $\mathbf{d}$ correspond to the parts of $\langle \mathbf{d} \rangle$ oscillating in phase and out of phase respectively with the driving field.

Using the optical Bloch equations (2.3.29), the equation of motion for the dipole moment

[j] $\sin(\omega t) = \cos(\omega t - \pi/2)$

$\mathbf{d}$ is

$$\begin{aligned}\frac{\mathrm{d}}{\mathrm{d}t}\mathbf{d} &= \frac{\mathrm{d}}{\mathrm{d}t}\left(\mathbf{d}_{ge}\rho_{eg}\mathrm{e}^{\mathrm{i}\omega_k t}\right)\\ &= \mathrm{i}\omega_k\left(\mathbf{d}_{ge}\rho_{eg}\mathrm{e}^{\mathrm{i}\omega_k t}\right) + \mathbf{d}_{ge}\frac{\mathrm{d}\rho_{eg}}{\mathrm{d}t}\mathrm{e}^{\mathrm{i}\omega_k t}\\ &= \mathrm{i}\omega_k\mathbf{d} - \left(\mathrm{i}\omega_0 + \frac{\Gamma_0}{2}\right)\mathbf{d} - \mathbf{d}_{ge}\frac{\mathrm{i}}{\hbar}\left(\rho_{ee}-\rho_{gg}\right)\mathbf{d}_{eg}\cdot\mathbf{E}_0\\ &= \left(\mathrm{i}\Delta - \frac{\Gamma_0}{2}\right)\mathbf{d} - \mathrm{i}\frac{|\mathbf{d}_{ge}|^2}{\hbar}\left(\rho_{ee}-\rho_{gg}\right)\left(\hat{\mathbf{d}}_{ge}\cdot\hat{\boldsymbol{\epsilon}}_0\right)E_0\,\hat{\mathbf{d}}_{ge},\end{aligned} \tag{2.4.3}$$

where $\Delta = \omega_k - \omega_0$ is the detuning of the driving field from the atomic transition frequency, and $\hat{\mathbf{d}}_{eg}$ and $\hat{\boldsymbol{\epsilon}}_0$ are the polarisation unit vectors for the dipole ($\mathbf{d}_{eg} = d_{eg}\hat{\mathbf{d}}_{eg}$) and field [$\mathbf{E}_0(\mathbf{r},t) = E_0(\mathbf{r},t)\hat{\boldsymbol{\epsilon}}_0$] respectively. Assuming that $\hat{\mathbf{d}}_{ge} = \hat{\boldsymbol{\epsilon}}_0$, then $\dot{\mathbf{d}}$ becomes

$$\dot{\mathbf{d}} = \left(\mathrm{i}\Delta - \frac{\Gamma_0}{2}\right)\mathbf{d} - \mathrm{i}\frac{|\mathbf{d}_{ge}|^2}{\hbar}\left(\rho_{ee}-\rho_{gg}\right)\mathbf{E}_0, \tag{2.4.4}$$

where the equation of motion for $\dot{\rho}_{ee}$ is

$$\dot{\rho}_{ee} = -\rho_{ee}\Gamma_0 - 2\frac{\mathrm{i}}{\hbar}\mathrm{Im}\left(\mathbf{d}\cdot\mathbf{E}_0^*\right), \tag{2.4.5}$$

and $\rho_{gg}(t) = 1 - \rho_{ee}(t)$.

2.4.2 Atomic polarisability and the weak-driving steady state

If we assume weak driving (see Sec. 2.4.3), then we can set $(\rho_{ee} - \rho_{gg}) \simeq -1$, resulting in just one equation of motion,

$$\dot{\mathbf{d}} \simeq \left(\mathrm{i}\Delta - \frac{\Gamma_0}{2}\right)\mathbf{d} + \mathrm{i}\frac{|\mathbf{d}_{ge}|^2}{\hbar}\mathbf{E}_0. \tag{2.4.6}$$

This has a linear steady-state solution

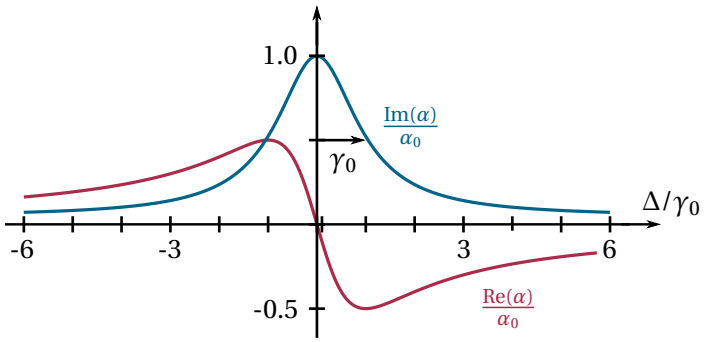

Figure 2.2: Real (red) and imaginary (blue) parts of the single-atom polarisability, α (2.4.10), normalised by α_0. The blue line is a Lorentzian with halfwidth γ_0.

$$\mathbf{d} = \alpha\, \mathbf{E}_0, \tag{2.4.7}$$

where we have introduced the atomic polarisability,

$$\alpha = -\alpha_0 \frac{\gamma_0}{\Delta + \mathrm{i}\gamma_0}, \tag{2.4.8}$$

where [using Eq. (2.3.11)]

$$\alpha_0 \equiv \frac{|\mathbf{d}_{ge}|^2}{\hbar} = \frac{6\pi\varepsilon_0}{k_0^3}, \qquad \text{and} \qquad \gamma_0 = \frac{\Gamma_0}{2} = \frac{|\mathbf{d}_{eg}|^2 k_0^3}{6\pi\varepsilon_0\hbar}. \tag{2.4.9}$$

This complex polarisabilty α describes the resonance behaviour of the atomic dipole to the driving field. In Fig. 2.2 we plot the real and imaginary parts of α,

$$\frac{\alpha}{\alpha_0} = -\frac{\gamma_0\Delta}{\Delta^2+\gamma_0^2} + \mathrm{i}\frac{\gamma_0^2}{\Delta^2+\gamma_0^2}. \tag{2.4.10}$$

The imaginary part (blue line) is a Lorentzian lineshape with halfwidth-at-half-maximum (HWHM) γ_0 and centered on $\Delta = 0$ (i.e. it is a maximum when the driving frequency ω is resonant with the natural frequency of the atomic transition ω_0).

2.4.3 Transient and steady-state solutions

Let us now consider how quickly the system settles into the steady-state solution. Substituting α back into the equations of motion (2.4.4) and (2.4.5), we get

$$\dot{d} = \left(\mathrm{i}\Delta - \frac{\Gamma_0}{2}\right) d - \mathrm{i}\left(\rho_{ee} - \rho_{gg}\right) \frac{\Gamma_0}{2} \alpha_0 E_0, \tag{2.4.11a}$$

$$\dot{\rho}_{ee} = -\Gamma_0 \rho_{ee} - \Gamma_0 \,\mathrm{Im}\left(\frac{d^* \alpha_0 E_0}{|\mathbf{d}_{ge}|^2}\right), \tag{2.4.11b}$$

where $\mathbf{d} = d\hat{\boldsymbol{\epsilon}}_0$. Looking at these two equations, the characteristic time scale is the natural decay rate Γ_0, the characteristic dipole moment magnitude is $|\mathbf{d}_{ge}|$, and the characteristic electric field magnitude is $|\mathbf{d}_{ge}|/\alpha_0$. We can therefore define new dimensionless variables,

$$\tilde{t} \equiv \Gamma_0 t = \frac{t}{\tau_0}, \qquad \tilde{\Delta} \equiv \frac{2\Delta}{\Gamma_0} \qquad \tilde{d} \equiv \frac{d}{|\mathbf{d}_{ge}|}, \qquad \tilde{E}_0 \equiv \frac{\alpha_0 E_0}{|\mathbf{d}_{ge}|}, \tag{2.4.12}$$

resulting in the dimensionless equations of motion

$$\frac{\mathrm{d}}{\mathrm{d}\tilde{t}}\tilde{d} = \left(\mathrm{i}\tilde{\Delta} - 1\right)\frac{\tilde{d}}{2} - \mathrm{i}\left(\rho_{ee} - \frac{1}{2}\right)\tilde{E}_0, \tag{2.4.13a}$$

$$\frac{\mathrm{d}}{\mathrm{d}\tilde{t}}\rho_{ee} = -\rho_{ee} - \mathrm{Im}\left(\tilde{d}^* \tilde{E}_0\right). \tag{2.4.13b}$$

Note also that the normalised dipole-moment is equivalent to ρ_{eg} in the rotating frame, $\tilde{d} = \bar{\rho}_{eg} \mathrm{e}^{\mathrm{i}\omega_k t}$.

In Fig. 2.3 (a–f) we plot the time evolution of $\tilde{d}$ and ρ_{gg} for different driving field strengths, $\tilde{E}_0 = 0.1, 1, 10$. For all three driving strengths, after around 10 natural lifetimes ($\tilde{t} \equiv t/\tau_0 \simeq 10$), the evolution has settled into a steady state. This steady-state solution is plotted in Fig. 2.3 (g,h) as a function of driving strength. For weak driving ($\tilde{E}_0 \ll 1$), the full solution can be well approximated by assuming that $\rho_{gg} = 1$, as we did for Eq. (2.4.7). Once the driving strength increases past $\tilde{E}_0 \simeq 1$ however, this is no longer a good approximation as there is now appreciable population in the excited state. For strong driving, the linear response of $\tilde{d}$ to $\tilde{E}_0$ breaks down and the nonlinearities in (2.4.13) significantly attenuate the dipole moment.

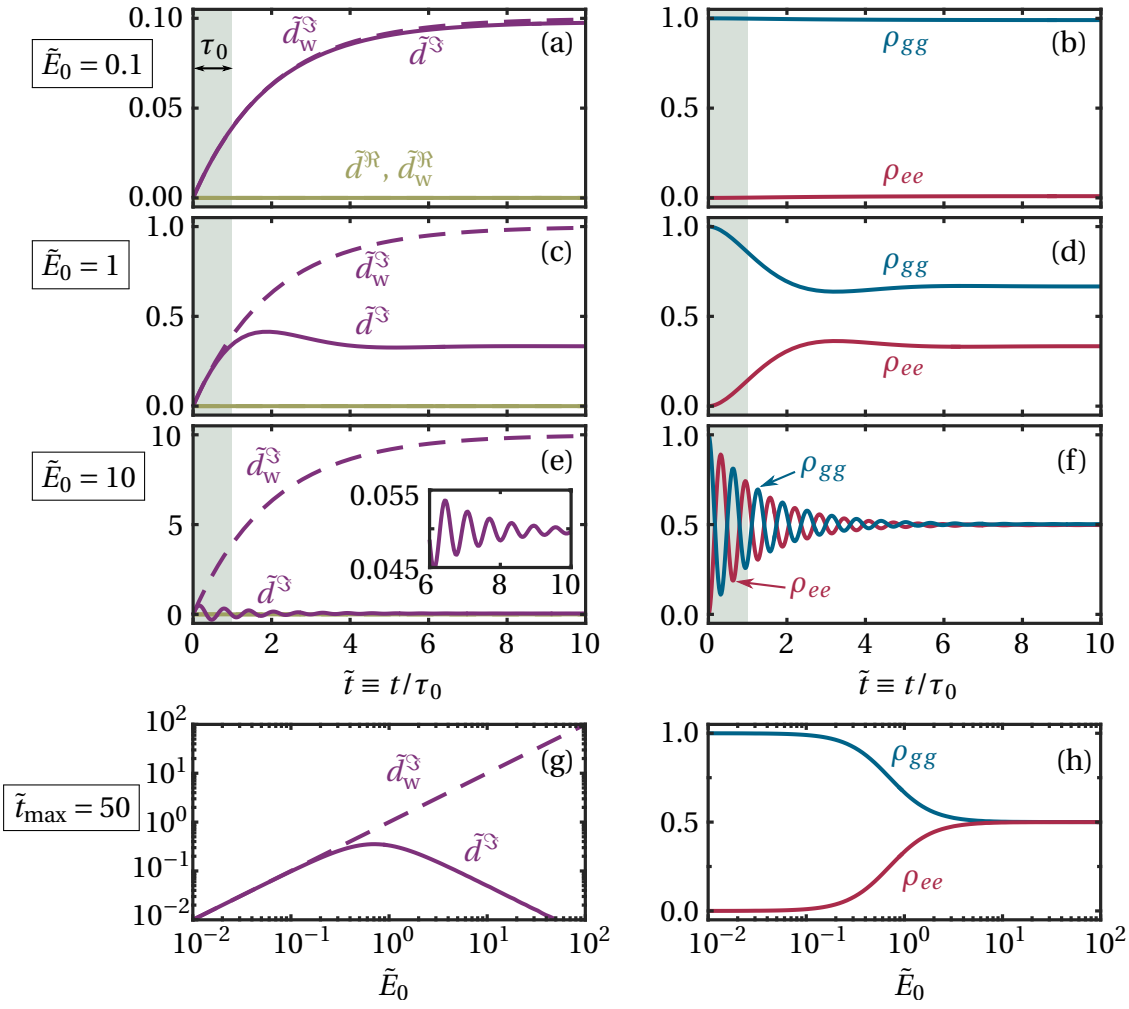

Figure 2.3: Solutions to the single-atom two-level optical Bloch equations with dimensionless parameters (2.4.13). (a,c,e) The time evolution of the real (olive) and imaginary (purple) dipole moments $\tilde{d} \equiv d/|\mathbf{d}_{ge}|$. The dashed lines are the solutions in the weak-driving approximation (setting $\rho_{gg} = 1$). (b,d,f) The evolution of the ground (blue) and excited (red) state populations. The driving fields $\tilde{E}_0 \equiv E_0\alpha_0/|\mathbf{d}_{ge}|$ are 0.1 (a,b), 1 (c,d) and 10 (e,f) and are resonant with the atomic frequency ($\Delta = 0$). The steady-state solutions for the dipole moments and populations after $\tilde{t} = 50$ are plotted in (g) and (h) respectively, as a function of driving field strength. For $\tilde{E}_0 \ll 1$, the weak-driving model is a good approximation for the full behaviour. For $\tilde{E}_0 \gtrsim 1$ however, the full behaviour deviates from the weak-driving approximation.

In most of this Thesis, we will use the weak-driving approximation as this allows us to calculate a linear steady-state solution with minimal computational effort. What we have seen in this Section is that this approximation is valid provided that

$$E_{0,\text{weak}} \ll \frac{|\mathbf{d}_{ge}|}{\alpha}. \tag{2.4.14}$$

2.5 Classical dipole — simple harmonic oscillator

In Sec. 2.3.5, we showed that when the field is in a coherent state, we can treat it as a classical electric field. In this Section, we will show (as has already been shown in, e.g., [39, 78]) that the behaviour of the weakly-driven electric dipole in Sec. 2.4.2 is identical to that of a damped driven simple harmonic oscillator.

As before, let us assume that the driving field has the form

$$\mathscr{E}_0(\mathbf{r},t) = \mathbf{E}_0(\mathbf{r})\,\mathrm{e}^{-\mathrm{i}\omega t} + \mathbf{E}_0^*(\mathbf{r})\,\mathrm{e}^{\mathrm{i}\omega t} = 2\,\mathbf{E}_0^{\Re}(\mathbf{r})\cos\omega t + 2\,\mathbf{E}_0^{\Im}(\mathbf{r})\sin\omega t. \tag{2.5.1}$$

We are assuming that the only time dependence in $\mathscr{E}_0$ is the rotation with frequency ω. The equation of motion for the displacement $\mathbf{s}(t) = s(t)\hat{\boldsymbol{\epsilon}}_0$ of an electron in this external electric field is

$$\frac{\mathrm{d}^2 s^2}{\mathrm{d}t^2} + \Gamma\frac{\mathrm{d}s}{\mathrm{d}t} + \omega_0^2 s = \frac{2e}{m}\left[E_0^{\Re}(\mathbf{r}_0)\cos\omega t + E_0^{\Im}(\mathbf{r}_0)\sin\omega t\right], \tag{2.5.2}$$

where motion is damped by Γ, the natural frequency of oscillation is ω_0, e is the electron charge and m is the electron mass. Again we assume the *dipole approximation*, i.e. the maximum electron displacement is very much smaller than the field wavelength.

2.5.1 Steady-state solution

Let us first look for a solution of the form

$$s(t) = \bar{s}\,\mathrm{e}^{-\mathrm{i}\omega t} + \bar{s}^*\,\mathrm{e}^{\mathrm{i}\omega t} = 2\,\bar{s}^{\Re}\cos\omega t + 2\,\bar{s}^{\Im}\sin\omega t. \tag{2.5.3}$$

By substituting (2.5.3) into (2.5.2) and comparing coefficients of cos and sin, we arrive at the solutions (see Appendix A.1)

$$\bar{s}^{\Re} = \frac{e}{m}\frac{(\omega_0^2-\omega^2)\,E_0^{\Re} - \omega\Gamma E_0^{\Im}}{(\omega_0^2-\omega^2)^2+\omega^2\Gamma^2}, \tag{2.5.4a}$$

$$\bar{s}^{\Im} = \frac{e}{m}\frac{(\omega_0^2-\omega^2)\,E_0^{\Im} + \omega\Gamma E_0^{\Re}}{(\omega_0^2-\omega^2)^2+\omega^2\Gamma^2}, \tag{2.5.4b}$$

$$\Rightarrow \qquad \bar{s} \;=\; \bar{s}^{\Re} + \mathrm{i}\,\bar{s}^{\Im} = \frac{e}{m}\frac{(\omega_0^2-\omega^2)+\mathrm{i}\omega\Gamma}{(\omega_0^2-\omega^2)^2+\omega^2\Gamma^2}E_0. \tag{2.5.4c}$$

Again assuming that $|\omega_0-\omega| \ll (\omega_0+\omega)$ (*rotating wave approximation*), we can approximate

$$(\omega_0^2-\omega^2) = (\omega_0+\omega)(\omega_0-\omega) \simeq 2\omega_0(\omega_0-\omega), \tag{2.5.5}$$

resulting in a steady-state dipole moment (in the rotating frame) $d = e\bar{s}$,

$$\begin{aligned} d &\simeq \frac{e^2}{m}\frac{2\omega_0(\omega_0-\omega)+\mathrm{i}\omega_0\Gamma}{4\omega_0^2(\omega_0-\omega)^2+\omega_0^2\Gamma^2}E_0 \\ &= \frac{e^2}{2m\omega_0}\frac{-\Delta+\mathrm{i}(\Gamma/2)}{\Delta^2+(\Gamma/2)^2}E_0 \\ &= -\alpha_0\frac{\gamma}{\Delta^2+\gamma^2}E_0. \end{aligned} \tag{2.5.6}$$

This has the same form as Eq. (2.4.7) where the steady-state solution to the dipole moment is $d = \alpha E_0$. Comparing the two, we can see that the dissipation rate Γ is equivalent to the

natural decay rate of the atomic excited state Γ_0 (2.4.9),

$$\Gamma \equiv 2\gamma = \frac{\mathscr{D}_0^2 k_0^3}{3\pi\varepsilon_0\hbar}, \qquad \alpha_0 = \frac{6\pi\varepsilon_0}{k_0^3}, \tag{2.5.7}$$

where we have chosen the characteristic dipole element $\mathscr{D}_0 = ea_0$ with characteristic length $a_0 = \sqrt{(\hbar/m\omega_0)}$.

2.5.2 Transient solution

In addition to this steady-state solution, Eq. (2.5.2) also has a transient solution (Appendix A.1),

$$s_t(t) = s(0)\,\mathrm{e}^{-\gamma t}\cos\left(\sqrt{\omega_0^2-\gamma^2}\,t\right), \tag{2.5.8}$$

where $s(0)$ is the initial state of $s(t)$ (if we assume the driving field is switched on at $t = 0$). The amplitude of these oscillations decays away with lifetime γ, after which the steady-state solution (2.5.4c) dominates.

Chapter Summary

- The interaction between a 2-level atom and an EM field can be described using the master equation
- A weak EM field in a coherent state, such as from a laser, can be treated as an oscillating classical EM field
- For a weak driving field, the atomic electric dipole has a steady-state solution
- This steady-state solution can also be derived from the behaviour of a classical driven damped simple harmonic oscillator

Chapter 3

Multiple four-level atoms

3.1 Overview

In Chap. 2, we discussed the interaction between a single two-level atom and an electromagnetic (EM) field. In this Chapter, we extend this model to include multiple atoms, each with a single ground state and three degenerate excited states. Again, we closely follow the discussion of [69, 70], although extend their treatment to multiple excited states. The resulting many-atom master equation in Sec. 3.3 can be found in many references, e.g., [26, 35, 40, 79]. In Sec. 3.5 we discuss methods of solving the weak-driving coupled equations, focussing on the eigenmodes of the system.

3.2 Four-level atom

3.2.1 Energy levels of a four-level atom

In Chap. 2, we considered the simple case of a 2-level atom with a single excited state $|e\rangle$. The resulting dipole moment had just a single polarisation determined by the polarisation of the driving field. With multiple atoms however, the local field experienced by each atom need not necessarily have the same polarisation as the driving field, but will depend on

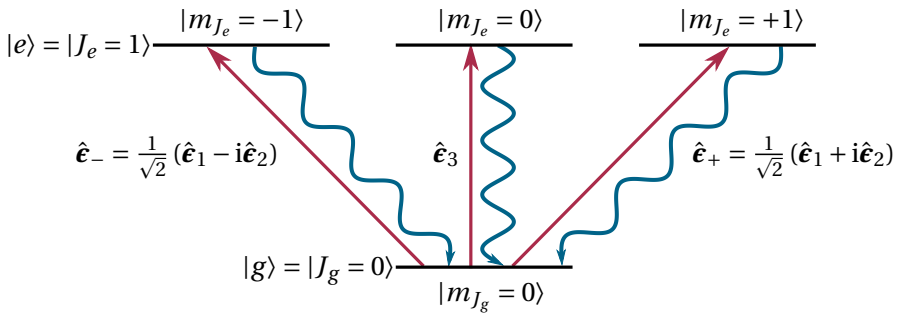

Figure 3.1: Ground $|g\rangle$ and excited $|e\rangle$ energy levels with angular momentum quantum numbers $J_g = 0$ and $J_e = 1$ respectively. In the absence of an external magnetic field, the three excited state angular momentum projections $m_{J_e} = \{-1, 0, +1\}$ are degenerate. A transition between $|g\rangle$ and $|e\rangle$ is associated with the absorption or emission of a photon with polarisation $\boldsymbol{\epsilon}$ dependent on the value of m_{J_e}.

the relative positions of the other atoms. Adding more energy levels means that we will be able to drive dipole moments with different polarisations, resulting in a richer cooperative behaviour.

One of the simplest electric dipole transitions we can consider[a] is between states with total angular momentum[b] $J = 0$ and $J = 1$. For the triplet $J = 1$ state there exist three quantum states $m_J \in \{-1, 0, +1\}$ which correspond to different projections of the angular momentum ($m_J\hbar$) onto a quantization axis $\hat{\boldsymbol{\epsilon}}_3$. In the absence of any external magnetic fields these three states are degenerate.

A transition between the $|J = 0, m_J = 0\rangle$ state and a $|J' = 1, m_{J'}\rangle$ state involves the absorption or emission of a photon with polarisation dependent on the difference in m_J and m'_J [26]. This is because the transition between two different states results in an oscillating transitionary electric dipole (which we came across previously in Sec. 2.2.4). The $J = 0$ state has a spherical s orbital wavefunction, and (we can choose the basis such that) each $J = 1$ state has a p orbital wavefunction, which has the form of two lobes of opposite sign, aligned along a particular axis. If the atom is in a superposition of the two states, as

[a] The selection rules for electric dipole transitions are described in [80].

[b] The total angular momentum vector is $\mathbf{J} = \mathbf{L} + \mathbf{S}$ where $\mathbf{L}$ is the orbital angular momentum and $\mathbf{S}$ is the spin angular momentum.

happens when it is undergoing a transition from one to the other, then the overall wavefunction is a combination of the two different wavefunctions. Because of the opposite signs of the two lobes of the p wavefunction, one lobe interferes constructively with the s wavefunction whilst the other interferes destructively. The total wavefunction therefore ends up skewed in one direction, resulting in a separation of the negative (electron) and positive (core) centres of charge in the atom. This produces a dipole, the polarisation of which depends on the quantization axis of the p orbital. Alternatively, as we saw in Sec. 2.5, treating the electron and nuclear core as classical point charges under the influence of an external electric field, the nuclear core, being much more massive than the electron, is unmoved, whilst the electron becomes displaced by the electric field, resulting in a dipole.

The $m_J \in \{-1, 0, +1\}$ basis results in two circular polarisations and one linear polarisation,

$$\hat{\boldsymbol{\epsilon}}_+ = \frac{\hat{\boldsymbol{\epsilon}}_1 + \mathrm{i}\hat{\boldsymbol{\epsilon}}_2}{\sqrt{2}}, \qquad \hat{\boldsymbol{\epsilon}}_- = \frac{\hat{\boldsymbol{\epsilon}}_1 - \mathrm{i}\hat{\boldsymbol{\epsilon}}_2}{\sqrt{2}}, \qquad \hat{\boldsymbol{\epsilon}}_3, \tag{3.2.1}$$

where $\hat{\boldsymbol{\epsilon}}_{1,2,3}$ are three orthogonal unit vectors (typically the three Cartesian coordinates $\{x, y, z\}$), and $\hat{\boldsymbol{\epsilon}}_+$ and $\hat{\boldsymbol{\epsilon}}_-$ are often referred to respectively as left and right circular polarisation. In Sec. 3.2.3 we describe how to transform between this basis and the linear $\hat{\boldsymbol{\epsilon}}_{1,2,3}$ basis described in the previous paragraph.

Since m_J is a projection of the total angular momentum in the $\hat{\boldsymbol{\epsilon}}_3$ direction, a change in m_J of $\Delta m_J = \pm 1$ corresponds to a change in angular momentum projection of $\pm\hbar$. The two polarisations $\hat{\boldsymbol{\epsilon}}_+$ and $\hat{\boldsymbol{\epsilon}}_-$ carry momentum of $+\hbar$ and $-\hbar$ respectively. To increase m_J by 1 would therefore either require absorbing a photon with polarisation $\hat{\boldsymbol{\epsilon}}_+$ or emitting a photon with polarisation $\hat{\boldsymbol{\epsilon}}_-$, and vice versa for $\Delta m_J = -1$. If there is no change in m_J (going between $m_J = 0$ states), then the corresponding absorbed or emitted photon has polarisation $\hat{\boldsymbol{\epsilon}}_3$.

If we chose to have a ground state with $J_g = 1$ and an excited state with $J_e = 0$, then it is possible that population could become trapped in one of the m_{J_g} levels. We will typically be considering a driving field with one dominant polarisation which might only couple one pair of m_J states as discussed above. Decay from the excited state can occur into any

of the different polarisations (assuming decay into free space[c]) and so population will be transfered into all three of the m_{J_g} states, although will only be pumped out of the one (or more) states that are allowed by the driving field polarisation. Considering instead a single ground state $J_g = 0$ and excited state with $J_e = 1$ (see Fig. 3.1) avoids this problem since even if the driving field only excites one of the three excited states, once the atom decays, it will always end up back in the same single ground state.

3.2.2 Possible experimental realisations

A $|J = 0\rangle \rightarrow |J = 1\rangle$ triplet-triplet transition can be realised in an atomic species with two valent electrons, for example the alkaline earth metals [40, 81] or Yb [82, 83]. Mott-Insulator states have been demonstrated in Sr [84] and Yb [83] for which there also exist magic wavelength lattices [40, 81, 82].[d] Whilst state-selective excitation can be achieved with a narrow linewidth resonant driving field, care needs to be taken when considering the possible decay channels of the excited state. For example, the ${}^3D_1$ state in Sr considered in [40] decays into the states $({}^3P_0, {}^3P_1, {}^3P_2)$ with respective decay rates of $\Gamma = (290, 187, 9) \times 10^3\,\mathrm{s}^{-1}$ [81]. The decay into ${}^3P_0$ may be the dominant decay pathway, although for a more complete description, decay into the additional channels needs to be included in the model (in addition to repumping to avoid population loss into dark states).

Alternatively, the atomic Hamiltonians can, under certain circumstances, be reduced from 4-level systems to 2-level systems, as in Chap. 2. For example, the degeneracy of the $|J = 1, m_J\rangle$ states can be broken by applying an external magnetic field, allowing us to address just a single excited state. As well as $|J = 0\rangle \rightarrow |J = 1\rangle$ systems, we can also consider more complex state transitions such as the D1 and D2 transitions in alkali metal atoms (this proposal was suggested in the Supplemental Material of [14]). Setting the ground state as $|5^2S_{1/2}; F_g, m_g = F_g\rangle$ where F is the hyperfine quantum number and the excited state as $|5^2P_{1/2(3/2)}; F_e = F_g + 1, m_e = F_e\rangle$, all the other transitions can be detuned

[c] If we restrict the possible decay modes by, e.g., placing the atom in a cavity, then the excited state might only decay with a particular polarisation.

[d] A *magic wavelength* is a wavelength which will generate an optical lattice with identical trapping potentials for both the ground and excited states.

from this one by again applying a magnetic field. This leaves a closed cycling transition between these two states with circular polarisation.

In addition to applying external magnetic fields to shift different states off resonance, we shall see in later Chapters that for particular geometries, we can ignore one (Chaps. 7,8) or two (Chaps. 5,6) or the three possible dipole polarisations, reducing the effective atomic Hamiltonians to 3-level or 2-level systems respectively.

3.2.3 xyz basis

For brevity, let us write

$$\begin{aligned} |J_g = 0, m_{J_g} = 0\rangle &\equiv |g\rangle\,, \\ |J_e = 1, m_{J_e} = \pm 1\rangle &\equiv |\pm\rangle = \frac{|1\rangle \pm \mathrm{i}|2\rangle}{\sqrt{2}}, \\ |J_e = 1, m_{J_e} = 0\rangle &\equiv |3\rangle\,. \end{aligned} \tag{3.2.2}$$

It is going to be convenient later on to work in the $\{|1\rangle, |2\rangle, |3\rangle\}$ orthogonal basis. The inverse transformation of (3.2.2) can be done using the matrix U_{123},

$$\mathsf{U}_{123} = \begin{pmatrix} \frac{1}{\sqrt{2}} & \frac{1}{\sqrt{2}} & 0 \\ -\frac{\mathrm{i}}{\sqrt{2}} & \frac{\mathrm{i}}{\sqrt{2}} & 0 \\ 0 & 0 & 1 \end{pmatrix}, \qquad \begin{pmatrix} |1\rangle \\ |2\rangle \\ |3\rangle \end{pmatrix} = \mathsf{U}_{123} \begin{pmatrix} |+\rangle \\ |-\rangle \\ |3\rangle \end{pmatrix}. \tag{3.2.3}$$

The three dipole moment vectors associated with transitions between $|g\rangle$ and $\{|1\rangle, |2\rangle, |3\rangle\}$ are therefore aligned along the $\{\hat{\boldsymbol{\epsilon}}_1, \hat{\boldsymbol{\epsilon}}_2, \hat{\boldsymbol{\epsilon}}_3\}$ directions respectively (Sec. 2.2.4).

From now on, we will align the $\hat{\boldsymbol{\epsilon}}_{1,2,3}$ directions along the three Cartesian coordinates

$$\begin{aligned} \hat{\boldsymbol{\epsilon}}_1 &= \hat{\mathbf{x}} & |1\rangle &= |x\rangle\,, \\ \hat{\boldsymbol{\epsilon}}_2 &= \hat{\mathbf{y}} & |2\rangle &= |y\rangle\,, \\ \hat{\boldsymbol{\epsilon}}_3 &= \hat{\mathbf{z}} & |3\rangle &= |z\rangle\,. \end{aligned} \tag{3.2.4}$$

3.2.4 Single-atom Hamiltonian

Assuming the excited states are degenerate, the Hamiltonian for a single 4-level atom in the xyz basis is (shifting the ground state energy to $E_g = -\hbar\omega_0/2$)

$$\mathsf{H}_0 = \frac{\hbar\omega_0}{2}\left(-|g\rangle\langle g| + |x\rangle\langle x| + |y\rangle\langle y| + |z\rangle\langle z|\right). \tag{3.2.5}$$

3.3 Many-atom master equation

3.3.1 Many-atom density matrix

The many-atom wavefunction has the general form

$$|\Psi_N\rangle = \sum_{\alpha_1}\sum_{\alpha_2}\cdots\sum_{\alpha_N} a_{\alpha_1\alpha_2\ldots\alpha_N}|\alpha_1\alpha_2\ldots\alpha_N\rangle, \tag{3.3.1}$$

where $\alpha_i \in \{g, x, y, z\}$ is the internal state of atom i and $\{a\}$ are the set of coefficients. $|\Psi_N\rangle$ has 4^N elements. The corresponding many-atom density matrix $\rho_N \equiv |\Psi_N\rangle\langle\Psi_N|$ therefore has size 4^{2N}. This very quickly becomes computationally intractable. To get round this, many different approximations can be made to reduce the dimension of ρ_N. The one that we shall employ is the *mean field approximation* as used in [79]. In this approximation, we assume that the density matrix can be factorised into a product state of single-atom density matrices,

$$\rho_N \simeq \bigotimes_i \rho_i, \tag{3.3.2}$$

where

$$\rho_i = \sum_{\alpha,\beta}\rho^{(i)}_{\alpha\beta}|\alpha_i\rangle\langle\beta_i| = \begin{pmatrix} \rho^{(i)}_{gg} & \rho^{(i)}_{gx} & \rho^{(i)}_{gy} & \rho^{(i)}_{gz} \\ \rho^{(i)}_{xg} & \rho^{(i)}_{xx} & \rho^{(i)}_{xy} & \rho^{(i)}_{xz} \\ \rho^{(i)}_{yx} & \rho^{(i)}_{yx} & \rho^{(i)}_{yy} & \rho^{(i)}_{yz} \\ \rho^{(i)}_{zg} & \rho^{(i)}_{zy} & \rho^{(i)}_{zy} & \rho^{(i)}_{zz} \end{pmatrix}, \tag{3.3.3}$$

is the density matrix of the ith atom, $\bigotimes_i$ is the tensor product over all atoms i and

$$\rho^{(i)}_{\alpha\beta} = (\rho^{(i)}_{\beta\alpha})^* = a^{(i)}_{\alpha}(a^{(i)}_{\beta})^* \left|\alpha_i\right\rangle \left\langle\beta_i\right|. \tag{3.3.4}$$

As with the two-level atom, the total population is 1, and so $\mathrm{Tr}(\rho_i) = \rho^{(i)}_{gg} + \rho^{(i)}_{xx} + \rho^{(i)}_{yy} + \rho^{(i)}_{zz} = 1$. The mean field approximation is valid either for weak driving (which is what we shall be assuming), or for strong driving but with weak interactions (e.g., a dilute gas, [85]).

Again we are only concerned with the atomic part of the density matrix and so will use the reduced density matrix $\rho_N = \mathrm{Tr}_{\mathrm{EM}}(\rho_{\mathrm{sys}})$.

3.3.2 Many-atom spin operators

We can define spin operators, as in Sec. 2.2.2, that act on a single atom within the ensemble, leaving the other atomic states unchanged. For example, the raising operator acting on the ith atom is

$$\sigma^+_{i\alpha} \equiv \mathbb{1}_1 \otimes \mathbb{1}_2 \otimes \cdots \otimes (\sigma^+_{\alpha})_i \otimes \cdots \otimes \mathbb{1}_N, \tag{3.3.5}$$

where $\mathbb{1}_j$ is the 4×4 identity matrix acting on the jth atom and $\sigma^+_{\alpha} = \left|\alpha_i\right\rangle \left\langle g_i\right|$ is the single-atom raising operator exciting atom i from $\left|g_i\right\rangle$ to $\left|\alpha_i\right\rangle$.

The state vectors in this basis are

$$\left|g_i\right\rangle = \begin{pmatrix} 1 \\ 0 \\ 0 \\ 0 \end{pmatrix}_i, \qquad \left|x_i\right\rangle = \begin{pmatrix} 0 \\ 1 \\ 0 \\ 0 \end{pmatrix}_i, \qquad \left|y_i\right\rangle = \begin{pmatrix} 0 \\ 0 \\ 1 \\ 0 \end{pmatrix}_i, \qquad \left|z_i\right\rangle = \begin{pmatrix} 0 \\ 0 \\ 0 \\ 1 \end{pmatrix}_i, \tag{3.3.6}$$

with single-atom raising operators

$$\sigma_{ix}^{+} = |x_i\rangle\langle g_i| = \begin{pmatrix} 0 & 0 & 0 & 0 \\ 1 & 0 & 0 & 0 \\ 0 & 0 & 0 & 0 \\ 0 & 0 & 0 & 0 \end{pmatrix}_i, \qquad \sigma_{iy}^{+} = |y_i\rangle\langle g_i| = \begin{pmatrix} 0 & 0 & 0 & 0 \\ 0 & 0 & 0 & 0 \\ 1 & 0 & 0 & 0 \\ 0 & 0 & 0 & 0 \end{pmatrix}_i,$$

$$\sigma_{iz}^{+} = |z_i\rangle\langle g_i| = \begin{pmatrix} 0 & 0 & 0 & 0 \\ 0 & 0 & 0 & 0 \\ 0 & 0 & 0 & 0 \\ 1 & 0 & 0 & 0 \end{pmatrix}_i. \tag{3.3.7}$$

The lowering operators are $\sigma_{\alpha}^{-} = (\sigma_{\alpha}^{+})^{\mathrm{T}}$.

3.3.3 Vector dipole operator

The dipole operator acting on atom i now has three independent dipole vector components, $\mathbf{d}_i^{\alpha} = \mathbf{d}_{\alpha g}\sigma_{i\alpha}^{+} + \mathbf{d}_{g\alpha}\sigma_{i\alpha}^{-}$, where $\mathbf{d}_{\alpha g} = \langle\alpha|\,\mathbf{d}\,|g\rangle = d_{\alpha g}\hat{\boldsymbol{\epsilon}}_{\alpha}$ is the dipole matrix element in direction $\alpha \in \{x, y, z\}$. There are then three corresponding expectation values

$$\langle \mathbf{d}_i^{\alpha} \rangle = \mathbf{d}_i^{\alpha} \mathrm{e}^{-\mathrm{i}\omega t} + (\mathbf{d}_i^{\alpha})^{*} \mathrm{e}^{\mathrm{i}\omega t}, \tag{3.3.8}$$

where $\mathbf{d}_i^{\alpha} = d_i^{\alpha}\hat{\boldsymbol{\epsilon}}_{\alpha} = \mathbf{d}_{g\alpha}\rho_{\alpha g}^{(i)}\mathrm{e}^{\mathrm{i}\omega t}$. The total vector dipole moment of the atom is the sum of the three Cartesian dipole moments

$$\langle \mathbf{d}_i \rangle = \left(d_i^{x}\hat{\mathbf{x}} + d_i^{y}\hat{\mathbf{y}} + d_i^{z}\hat{\mathbf{z}}\right)\, \mathrm{e}^{-\mathrm{i}\omega t} + \text{c.c.} \;=\; \mathbf{d}_i\, \mathrm{e}^{-\mathrm{i}\omega t} + \text{c.c.}, \tag{3.3.9}$$

where c.c. stands for complex conjugate. The time derivative of each component of the dipole moment is

$$\dot{d}_i{}^{\alpha} = d_{g\alpha}\mathrm{e}^{\mathrm{i}\omega t}\left(\dot{\rho}_{\alpha g}^{(i)} + \mathrm{i}\omega\rho_{\alpha g}^{(i)}\right). \tag{3.3.10}$$

3.3.4 Dipole–dipole interactions

In Sec. 2.2.6 we introduced the Hamiltonian describing the interaction between a single 2-level atom and the EM field modes, H_{int}. In the interaction picture and rotating wave approximation, the total interaction Hamiltonian is simply the sum of the interactions of each individual atom with the field (2.2.30),

$$\begin{aligned}\mathsf{H}_{\text{int},I}(t) =& \mathrm{i}\hbar \sum_{i=1}^{N} \sum_{\alpha} \sum_{|\omega_k-\omega_0|<\vartheta} \left(\sigma_{i\alpha}^{-} \mathsf{a}_{\Lambda}^{\dagger} \kappa_{\Lambda\alpha}^{*} \, \mathrm{e}^{\mathrm{i}(\omega_k-\omega_0)t - \mathrm{i}\mathbf{k}\cdot\mathbf{r}_i} - \sigma_{i\alpha}^{+} \mathsf{a}_{\Lambda} \kappa_{\Lambda\alpha} \, \mathrm{e}^{-\mathrm{i}(\omega_k-\omega_0)t + \mathrm{i}\mathbf{k}\cdot\mathbf{r}_i} \right), \\ =& \mathrm{i}\hbar \sum_{i} \sum_{\alpha} \left[f_{i\alpha}^{\dagger}(t) \sigma_{i\alpha}^{-} - \sigma_{i\alpha}^{+} f_{i\alpha}(t) \right], \end{aligned} \tag{3.3.11}$$

where $\mathbf{r}_i$ is the position of the ith atom, N is the number of atoms in the ensemble, Λ is the field mode index (as in Sec. 2.2.5), the new coupling coefficient $\kappa_{\Lambda\alpha}$ is (2.2.16)

$$\kappa_{\Lambda\alpha} \equiv \sqrt{\frac{\omega_k}{2\hbar\varepsilon_0}} \mathbf{d}_{\alpha g} \cdot \mathbf{u}_{\Lambda}(0), \tag{3.3.12}$$

and the noise operators are defined in the same manner as in (2.3.2):

$$\mathsf{f}_{i\alpha}(t) \equiv \sum_{|\omega_k-\omega_0|<\vartheta} \kappa_{\Lambda\alpha} \mathsf{a}_{\Lambda} \, \mathrm{e}^{-\mathrm{i}(\omega_k-\omega_0)t + \mathrm{i}\mathbf{k}\cdot\mathbf{r}_i}. \tag{3.3.13}$$

The new commutation relation for $f_{i\alpha}$ is

$$\left[f_{i\alpha}(t), f_{j\beta}^{\dagger}(t') \right] = \gamma_{ij}^{\alpha\beta}(t-t'), \tag{3.3.14}$$

with

$$\gamma_{ij}^{\alpha\beta}(\tau) = \sum_{|\omega_k-\omega_0|<\vartheta} \left(\kappa_{\Lambda\alpha} \kappa_{j\beta}^{*} \right) \mathrm{e}^{-\mathrm{i}(\omega_k-\omega_0)\tau + \mathrm{i}\mathbf{k}\cdot(\mathbf{r}_i-\mathbf{r}_j)}. \tag{3.3.15}$$

If the energy levels of the three excited states were different, then we would have to replace ω_0 with $\omega_{g\alpha}$ and $\omega_{g\beta}$.

The zero photon term in Eq. (2.3.7) becomes

$$\int_0^{\Delta t} \mathrm{d}t_1 \int_0^{t_1} \mathrm{d}t_2 \, \gamma_{ij}^{\alpha\beta}(t_1-t_2) \equiv \left(\frac{1}{2}\Gamma_{ij}^{\alpha\beta} + \mathrm{i}\Omega_{ij}^{\alpha\beta} \right), \tag{3.3.16}$$

where the cooperative decay rate

$$\Gamma_{ij}^{\alpha\beta} = \frac{|d_{eg}|^2 k_0^3}{3\pi\varepsilon_0\hbar}\Big\{\delta_{\alpha,\beta}\left[j_0(k_0 r_{ij}) + \frac{1}{2}\left(3|\hat{\mathbf{r}}_{ij}\cdot\hat{\mathbf{d}}_{\alpha g}|^2 - 1\right) j_2(k_0 r_{ij})\right] + \frac{3}{2}(1-\delta_{\alpha,\beta})\, j_2(k_0 r_{ij})\left(\hat{\mathbf{d}}_{\alpha g}\cdot\hat{\mathbf{r}}_{ij}\right)\left(\hat{\mathbf{d}}_{g\beta}\cdot\hat{\mathbf{r}}_{ij}\right)\Big\}, \tag{3.3.17}$$

and the cooperative shift

$$\Omega_{ij}^{\alpha\beta} = \frac{\Gamma_0}{2}\Big\{\delta_{\alpha,\beta}\left[y_0(k_0 r_{ij}) + \frac{1}{2}\left(3|\hat{\mathbf{r}}_{ij}\cdot\hat{\mathbf{d}}_{\alpha g}|^2 - 1\right) y_2(k_0 r_{ij})\right] + \frac{3}{2}(1-\delta_{\alpha,\beta})\, y_2(k_0 r_{ij})\left(\hat{\mathbf{d}}_{\alpha g}\cdot\hat{\mathbf{r}}_{ij}\right)\left(\hat{\mathbf{d}}_{g\beta}\cdot\hat{\mathbf{r}}_{ij}\right)\Big\}, \tag{3.3.18}$$

are derived in Appendix B. j_ℓ (B.2.5) and y_ℓ (B.2.11) are the spherical Bessel function and spherical Neumann functions respectively. We refer to (3.3.17) and (3.3.18) as the cooperative decay rate and shift because for $N = 2$ in Sec. 5.2.2 they modify the decay rate and shift the eigenmodes respectively. In fact, these expressions are nothing more than the real and imaginary parts of the interaction between a dipole matrix element, $\mathbf{d}_{\alpha g}$ at $\mathbf{r}_i$, and the classical electric field radiated from a second dipole matrix element, $\mathbf{d}_{g\beta}$ at $\mathbf{r}_j$ (B.2.13). Using the definition of $\mathsf{H}_{\text{int}} = -\mathsf{d}\cdot\mathsf{E}$ from Eq. (2.2.14), we find that

$$\mathsf{H}_{\text{int}} = -\mathbf{d}_{\alpha g}\cdot\mathsf{G}(\mathbf{r}_i - \mathbf{r}_j)\,\mathbf{d}_{g\beta} = \hbar\Omega_{ij}^{\alpha\beta} - \frac{\mathrm{i}}{2}\hbar\Gamma_{ij}^{\alpha\beta}. \tag{3.3.19}$$

where the classical electric field radiated by a classical electric dipole is shown later in Eq. (4.2.4),

$$\begin{aligned}\mathbf{E}_j(\mathbf{r}_i) \equiv& \mathsf{G}(\mathbf{r}_{ij})\,\mathbf{d}_j \\ =& \frac{k^3}{4\pi\varepsilon_0}\mathrm{e}^{\mathrm{i}kr_{ij}}\Big[\left(\frac{1}{kr_{ij}} + \frac{\mathrm{i}}{(kr_{ij})^2} - \frac{1}{(kr_{ij})^3}\right)\mathbf{d}_j \\ & - \left(\frac{1}{kr_{ij}} + \frac{3\mathrm{i}}{(kr_{ij})^2} - \frac{3}{(kr_{ij})^3}\right)(\hat{\mathbf{r}}_{ij}\cdot\mathbf{d}_j)\,\hat{\mathbf{r}}_{ij}\Big],\end{aligned} \tag{3.3.20}$$

where $\mathbf{r}_{ij} \equiv \mathbf{r}_i - \mathbf{r}_j$.

3.3.5 Many-atom master equation

From this we can determine a many-atom quantum stochastic Schrödinger equation, (as we did for the single 2-level atom in Sec. 2.3.4),

$$\mathrm{d}\left|\Psi_{\mathrm{sys},I}(t)\right\rangle = \left[-\frac{i}{\hbar}\mathsf{H}_{\mathrm{eff},I}\,\mathrm{d}t + \sum_i \sum_\alpha \sigma^-_{i\alpha}\mathrm{d}\mathsf{B}^\dagger_{i\alpha}(t)\right]\left|\Psi_{\mathrm{sys},I}(t)\right\rangle\,, \tag{3.3.21}$$

where the effective (non-Hermitian) Hamiltonian is

$$\mathsf{H}_{\mathrm{eff},I}(t) = \mathsf{H}_{\mathrm{sys},I}(t) + \hbar\sum_{i,j}\sum_{\alpha,\beta}\left(\Omega^{\alpha\beta}_{ij} - \frac{1}{2}\mathrm{i}\Gamma^{\alpha\beta}_{ij}\right)\sigma^+_{i\alpha}\sigma^-_{j\beta}, \tag{3.3.22}$$

and the quantum Ito increment is

$$\Delta\mathsf{B}_{i\alpha}(t) = \int_t^{t+\Delta t}\mathsf{f}_{i\alpha}(t), \tag{3.3.23}$$

$$\left[\Delta\mathsf{B}_{i\alpha}(t)\,,\,\Delta\mathsf{B}^\dagger_{j\beta}(t)\right] = \frac{1}{2}\left(\Gamma^{\alpha\beta}_{ij} + \Gamma^{\alpha\beta}_{ij}\right)\Delta t. \tag{3.3.24}$$

Finally, the equation of motion for the reduced atomic many-atom density matrix, $\rho_N(t) \equiv \mathrm{Tr}_{\mathrm{EM}}\left(\left|\Psi_{\mathrm{sys}}(t)\right\rangle\left\langle\Psi_{\mathrm{sys}}(t)\right|\right)$, is given by the *many-atom master equation* [26, 35, 40, 79],

$$\begin{aligned}\dot{\rho}_N(t) = &-\frac{\mathrm{i}}{\hbar}\Big[\sum_i \mathsf{H}_{\mathrm{sys},i} + \sum_{\substack{i,j\\ i\neq j}}\sum_{\alpha,\beta}\hbar\Omega^{\alpha\beta}_{ij}\sigma^+_{i\alpha}\sigma^-_{j\beta}\,,\,\rho_N(t)\Big] \\ &+\frac{1}{2}\sum_{i,j}\sum_{\alpha,\beta}\Gamma^{\alpha\beta}_{ij}\Big(2\sigma^-_{i\alpha}\rho_N(t)\sigma^+_{j\beta} - \sigma^+_{j\beta}\sigma^-_{i\alpha}\rho_N(t) - \rho_N(t)\sigma^+_{j\beta}\sigma^-_{i\alpha}\Big),\end{aligned} \tag{3.3.25}$$

where

$$H_{\mathrm{sys},i} = -\frac{\hbar\omega_0}{2}\left(|g_i\rangle\langle g_i| - |x_i\rangle\langle x_i| - |y_i\rangle\langle y_i| - |z_i\rangle\langle z_i|\right) - \sum_\alpha \left[\mathbf{d}_{\alpha g}\cdot\mathbf{E}_0(\mathbf{r}_i)\mathrm{e}^{-\mathrm{i}\omega t}\sigma^+_{i\alpha} + \mathbf{d}_{g\alpha}\cdot\mathbf{E}_0^*(\mathbf{r}_i)\mathrm{e}^{\mathrm{i}\omega t}\sigma^-_{i\alpha}\right], \tag{3.3.26}$$

and α and β sum over $\{x, y, z\}$. We have transformed back into the Schrödinger picture.

3.3.6 Many-atom optical Bloch equations

From this many-atom master equation, we can calculate (see Appendix C) the equations of motion for the single-atom density matrices, $\{\dot\rho_\ell\}$. There are three types of matrix element that will need considering: $\dot\rho_{\mu\mu}$ [$\mu \neq g$, Eq. (C.5.4)], $\dot\rho_{\mu g}$ [$\mu \neq g$, Eq. (C.5.6)] and $\dot\rho_{\mu\nu}$ [$\mu \neq \nu \neq g$, Eq. (C.5.7)] [35, 79],

$$\dot\rho^{(\ell)}_{\mu\mu}\Big|_{\mu\neq g} = -\Gamma_0\rho^{(\ell)}_{\mu\mu} - \frac{2}{\hbar}\mathrm{Im}\left[\rho^{(\ell)}_{g\mu}\mathbf{d}_{\mu g}\cdot\left(\mathbf{E}^{(+)}_{0,\ell} + \sum_{i\neq\ell}\sum_\alpha^{\{x,y,z\}}\rho^{(i)}_{\alpha g}\mathsf{G}_{i\ell}\mathbf{d}_{g\alpha}\right)\right], \tag{3.3.27a}$$

$$\dot\rho^{(\ell)}_{\mu g}\Big|_{\mu\neq g} = -\left(\mathrm{i}\omega_0 + \frac{\Gamma_0}{2}\right)\rho^{(\ell)}_{\mu g} + \frac{\mathrm{i}}{\hbar}\left(\rho^{(\ell)}_{gg}\mathbf{d}_{\mu g} - \sum_\alpha^{\{x,y,z\}}\rho^{(\ell)}_{\mu\alpha}\mathbf{d}_{\alpha g}\right)\cdot\left(\mathbf{E}^{(+)}_{0,\ell} + \sum_{i\neq\ell}\sum_\beta^{\{x,y,z\}}\rho^{(i)}_{\beta g}\mathsf{G}_{i\ell}\mathbf{d}_{g\beta}\right), \tag{3.3.27b}$$

$$\dot\rho^{(\ell)}_{\mu\nu}\Big|_{\mu\neq\nu\neq g} = -\Gamma_0\rho^{(\ell)}_{\mu\nu} + \frac{\mathrm{i}}{\hbar}\rho^{(\ell)}_{g\nu}\mathbf{d}_{\mu g}\cdot\left(\mathbf{E}^{(+)}_{0,\ell} + \sum_{i\neq\ell}\sum_\alpha^{\{x,y,z\}}\rho^{(i)}_{\alpha g}\mathsf{G}_{i\ell}\mathbf{d}_{g\alpha}\right) - \frac{\mathrm{i}}{\hbar}\rho^{(\ell)}_{\mu g}\mathbf{d}_{g\nu}\cdot\left(\mathbf{E}^{(-)}_{0,\ell} + \sum_{i\neq\ell}\sum_\alpha^{\{x,y,z\}}\rho^{(i)}_{g\alpha}\mathsf{G}^*_{i\ell}\mathbf{d}_{\alpha g}\right), \tag{3.3.27c}$$

where $\mathbf{E}^{(+)}_{0,i} = \left(\mathbf{E}^{(-)}_{0,i}\right)^* = \mathbf{E}_0(\mathbf{r}_i)\mathrm{e}^{-\mathrm{i}\omega t}$. Notice that $\rho^{(\ell)}_{\mu\nu}$ in (3.3.27c) behaves like the population

terms in (3.3.27a) rather than like the coherences in (3.3.27b). Discarding the many-atom terms and only considering a single excited level, these then become the optical Bloch equations for a single 2-level atom as were given in Eq. (2.3.29). To account for limitations in the density matrix factorisation approximation (3.3.2), higher order correlation terms can be added, resulting in further equations of motion [37, 79]. However, we are only concerned with weak-driving, and so this is sufficient for our purposes.

3.4 Dipole moments

3.4.1 Time dynamics

In Sec. 2.4, we used the optical Bloch equations for a single 2-level atom to calculate the equations of motion for the expectation value of the electric dipole operator. In Sec. 3.3.3, we generalised the dipole operator to account for three possible excited states. The expectation of this vector operator has the form (3.3.9)

$$\langle \mathbf{d}_\ell \rangle = \left(d_\ell^x \hat{\mathbf{x}} + d_\ell^y \hat{\mathbf{y}} + d_\ell^z \hat{\mathbf{z}} \right) \mathrm{e}^{-\mathrm{i}\omega t} + \text{c.c.} \;=\; \mathbf{d}_\ell \, \mathrm{e}^{-\mathrm{i}\omega t} + \text{c.c.}, \tag{3.4.1}$$

where $\mathbf{d}_\ell^\mu = d_\ell^\mu \, \hat{\boldsymbol{\epsilon}}_\mu = \mathbf{d}_{g\mu} \, \rho_{\mu g}^{(\ell)} \, \mathrm{e}^{\mathrm{i}\omega t}$ is the dipole moment in the rotating frame. The equation of motion for $\mathbf{d}_\ell^\mu$ is therefore

$$\dot{\mathbf{d}}_\ell^\mu = \mathbf{d}_{g\mu} \mathrm{e}^{\mathrm{i}\omega t} \left(\dot{\rho}_{\mu g}^{(\ell)} + \mathrm{i}\omega \rho_{\mu g}^{(\ell)} \right). \tag{3.4.2}$$

Substituting in the solution for $\dot{\rho}_{\mu g}^{(\ell)}$ from Eq. (3.3.27b), this becomes

$$\begin{aligned}\dot{\mathbf{d}}_\ell^\mu &= -\left(\mathrm{i}\omega_0 + \frac{\Gamma_0}{2}\right)\mathbf{d}_{g\mu}\,\rho_{\mu g}^{(\ell)}\,\mathrm{e}^{\mathrm{i}\omega t} \;+\; \mathrm{i}\omega\,\mathbf{d}_{g\mu}\,\rho_{\mu g}^{(\ell)}\,\mathrm{e}^{\mathrm{i}\omega t} \\ &\quad + \mathbf{d}_{g\mu}\,\mathrm{e}^{\mathrm{i}\omega t}\frac{\mathrm{i}}{\hbar}\left(\rho_{gg}^{(\ell)}\mathbf{d}_{\mu g} - \sum_\alpha^{\{x,y,z\}}\rho_{\mu\alpha}^{(\ell)}\,\mathbf{d}_{\alpha g}\right)\cdot\left(\mathbf{E}_0(\mathbf{r}_\ell)\,\mathrm{e}^{-\mathrm{i}\omega t} + \sum_{i\neq\ell}\sum_\beta^{\{x,y,z\}}\rho_{\beta g}^{(i)}\,\mathsf{G}_{i\ell}\,\mathbf{d}_{g\beta}\right) \\ &= \left(\mathrm{i}\Delta - \frac{\Gamma_0}{2}\right)\mathbf{d}_\ell^\mu \\ &\quad + \mathrm{i}\,\hat{\mathbf{d}}_{g\mu}\frac{|\mathbf{d}_{eg}|^2}{\hbar}\left(\rho_{gg}^{(\ell)}\hat{\mathbf{d}}_{\mu g} - \sum_\alpha^{\{x,y,z\}}\rho_{\mu\alpha}^{(\ell)}\,\hat{\mathbf{d}}_{\alpha g}\right)\cdot\left(\mathbf{E}_0(\mathbf{r}_\ell) + \sum_{i\neq\ell}\sum_\beta^{\{x,y,z\}}\mathsf{G}_{i\ell}\,\mathbf{d}_i^\beta\right).\end{aligned} \tag{3.4.3}$$

where $\Delta = \omega - \omega_0$ is the detuning of the driving field from the atomic resonance and $\dot{\rho}_{\mu\mu}^{(\ell)}$ and $\dot{\rho}_{\mu\nu}^{(\ell)}$ are given by Eqs. (3.3.27a) and (3.3.27c) respectively. If we ignore the sums over α and the other atoms i, then this is the same as the result for the single 2-level atom in Eq. (2.4.4).

3.4.2 Weak-driving steady-state solution

Assuming a weak driving field (for a single 2-level atom we found the requirement for this was that the driving field amplitude $E_0 \ll |\mathbf{d}_{ge}|/\alpha_0$), then we can approximate the population of each atom to be entirely in the ground state, $\rho_{gg}^{(\ell)} \simeq 1$, $\rho_{\mu\mu\neq g}^{(\ell)} \simeq 0$. Similarly, the terms $\rho_{\mu\nu}^{(\ell)}$ ($\mu \neq \nu \neq g$) in (3.3.27c) behave like the populations in (3.3.27a), and so we can approximate these too as being zero. The only terms we are left with are therefore the coherences which give the dipole moments in (3.4.3). The weak-driving dipole moments are then

$$\dot{\mathbf{d}}_\ell^\mu \simeq \left(\mathrm{i}\Delta - \frac{\Gamma_0}{2}\right)\mathbf{d}_\ell^\mu \;+\; \mathrm{i}\frac{|\mathbf{d}_{eg}|^2}{\hbar}\hat{\mathbf{d}}_{\mu g}\cdot\left(\mathbf{E}_0(\mathbf{r}_\ell) \;+\; \sum_{i\neq\ell}\sum_\beta^{\{x,y,z\}}\mathsf{G}_{i\ell}\,\mathbf{d}_i^\beta\right)\hat{\mathbf{d}}_{g\mu}. \tag{3.4.4}$$

By setting $\dot{\mathbf{d}}_\ell^\mu = 0$, we can find the steady-state solution to this equation,

$$\mathbf{d}_\ell^\mu = \alpha\,\hat{\mathbf{d}}_{\mu g}\cdot\left(\mathbf{E}_0(\mathbf{r}_\ell) + \sum_{i\neq\ell}\sum_{\beta}^{\{x,y,z\}} \mathsf{G}_{i\ell}\,\mathbf{d}_i^\beta\right)\hat{\mathbf{d}}_{g\mu}, \tag{3.4.5}$$

where α is the atomic polarisability defined in (2.4.8) and (2.4.9):

$$\alpha = -\alpha_0\frac{\gamma_0}{\Delta + \mathrm{i}\gamma_0}, \qquad\qquad \alpha_0 \equiv \frac{|\mathbf{d}_{ge}|^2}{\hbar\gamma_0}. \tag{3.4.6}$$

We can combine the three components $\mathbf{d}_\ell^\mu$ into a single 3-component vector,

$$\mathbf{d}_\ell \equiv \sum_{\mu}^{\{x,y,z\}} \mathbf{d}_\ell^\mu = \alpha\,\mathbf{E}_0(\mathbf{r}_\ell) + \alpha\sum_{i\neq\ell}\mathsf{G}_{i\ell}\,\mathbf{d}_i. \tag{3.4.7}$$

The steady-state behaviour of an ensemble of weakly-driven dipoles depends therefore only on the configuration of the dipole positions $\{\mathbf{r}_\ell\}$ (and the driving field at these positions) and can be described by a set of coupled linear equations (3.4.7). In the next Section we will discuss how to solve these coupled equations. In the remainder of the Thesis, we will typically consider weakly-driven steady-states such as these, in a variety of different geometries and configurations.

3.5 Solution to steady state using complex symmetric matrices

3.5.1 Coupled linear equations

The coupled dipole equations (3.4.7) can be written in terms of vectors and matrices (see [17] for similar methods):

$$\vec{\mathbf{E}}_0 = \mathsf{M}\vec{\mathbf{d}}, \tag{3.5.1}$$

which written out element by element is

$$\begin{pmatrix} E_0^x(\mathbf{r}_1) \\ E_0^y(\mathbf{r}_1) \\ E_0^z(\mathbf{r}_1) \\ E_0^x(\mathbf{r}_2) \\ E_0^y(\mathbf{r}_2) \\ E_0^z(\mathbf{r}_2) \\ \vdots \end{pmatrix} = \begin{pmatrix} \alpha^{-1} & 0 & 0 & -\mathsf{G}_{12}^{xx} & -\mathsf{G}_{12}^{xy} & -\mathsf{G}_{12}^{xz} & \\ 0 & \alpha^{-1} & 0 & -\mathsf{G}_{12}^{xy} & -\mathsf{G}_{12}^{yy} & -\mathsf{G}_{12}^{yz} & \dots \\ 0 & 0 & \alpha^{-1} & -\mathsf{G}_{12}^{xz} & -\mathsf{G}_{12}^{yz} & -\mathsf{G}_{12}^{zz} & \\ -\mathsf{G}_{21}^{xx} & -\mathsf{G}_{21}^{xy} & -\mathsf{G}_{21}^{xz} & \alpha^{-1} & 0 & 0 & \\ -\mathsf{G}_{21}^{xy} & -\mathsf{G}_{21}^{yy} & -\mathsf{G}_{21}^{yz} & 0 & \alpha^{-1} & 0 & \dots \\ -\mathsf{G}_{21}^{xz} & -\mathsf{G}_{21}^{yz} & -\mathsf{G}_{21}^{zz} & 0 & 0 & \alpha^{-1} & \\ & \vdots & & & \vdots & & \ddots \end{pmatrix} \begin{pmatrix} d_1^x \\ d_1^y \\ d_1^z \\ d_2^x \\ d_2^y \\ d_2^z \\ \vdots \end{pmatrix}, \tag{3.5.2}$$

where $\mathsf{G}_{ij}^{\mu\nu}$ is the shorthand for the (μ,ν)th matrix element of $\mathsf{G}(\mathbf{r}_i-\mathbf{r}_j)$ [see Eq. (4.2.6)] and $\{\mu,\nu\}\in\{x,y,z\}$. The general form for an element in M is $\left[\delta_{\mu,\nu}\delta_{i,j}\,\alpha^{-1}-(1-\delta_{i,j})\,\mathsf{G}_{ij}^{\mu\nu}\right]$. This can be solved by finding the inverse matrix of M,

$$\vec{\mathbf{d}} = \mathsf{M}^{-1}\,\vec{\mathbf{E}}_0. \tag{3.5.3}$$

Numerically calculating the inverse matrix can be slow and prone to error, and so typically a method based on Gaussian elimination is used when solving sets of linear equations such as this. We use the mldivide function in MATLAB[e] which implements LU decomposition for the type of matrix given by M.

We shall use the convention that a vector $\vec{\mathbf{v}}$ has dimension $3N$ with elements $(v_1^x, v_1^y, v_1^z, v_2^x, \dots)^{\mathrm{T}}$. The size of M scales $\propto N^2$, which is far more favourable than the full density matrix ($\propto 2^{4N}$) and therefore allows us to consider ensembles with atom numbers up to the order $\sim 10^4$ [17, 32, 86].

3.5.2 Complex-symmetric matrices and left-right eigenvectors

Whilst an analytic solution to (3.5.1) is only possible and helpful for small N (Chap. 5) or atoms arranged in very particular configurations (e.g., 1D chains, Chap. 6), we can learn a lot about the system behaviour by considering the eigenmodes of M. Let us define the

[e] http://uk.mathworks.com/help/matlab/ref/mldivide.html

pth eigenvector $\vec{\mathbf{m}}_p$ and eigenvalue μ_p,

$$\mathsf{M}\vec{\mathbf{m}}_p = \mu_p \vec{\mathbf{m}}_p. \tag{3.5.4}$$

M can be separated into a diagonal matrix containing the driving field terms $\mathbb{1}/\alpha$ and a matrix describing the coupling between dipoles G,

$$\begin{aligned}\mathsf{M}\vec{\mathbf{m}}_p &= \left(\frac{1}{\alpha}\mathbb{1} - \mathsf{G}\right)\vec{\mathbf{m}}_p \\ &= \left(\frac{1}{\alpha} - g_p\right)\vec{\mathbf{m}}_p \\ &= \mu_p \vec{\mathbf{m}}_p,\end{aligned} \tag{3.5.5}$$

giving

$$\mu_p = \frac{1}{\alpha} - g_p, \tag{3.5.6}$$

where g_p is the pth eigenvalue of G.

The off-diagonal terms in M are all contained within G. G in turn depends only on the separation between pairs of dipoles $|\mathbf{r}_i - \mathbf{r}_j|$ and not on the vector direction. It is therefore symmetric under exchange of i and j, and so is a symmetric matrix. A coupling matrix that is dependent only on the particle spacing is known as a *Euclidean* matrix and is common within many physical models.

Since the elements of G are complex, M is *complex-symmetric* rather than *Hermitian* (Sec. 7.11.1 of [87]). Non-Hermitian Euclidean matrices [88] appear in many different physical models, including Anderson localisation in light [89] and matter waves [90], light propagation in nonlinear disordered media [91] and, in our case, collective behaviour in atomic systems [17, 32, 39, 86, 92]. The non-Hermitian nature of M means that the eigenvalues μ_p are complex (the significance of which we shall examine in Sec. 3.5.4) and the eigenvectors can be non-orthogonal. In addition, complex symmetric matrices are not necessarily diagonalisable. For example, the matrix

$$\begin{pmatrix} 1 & \mathrm{i} \\ \mathrm{i} & -1 \end{pmatrix}, \tag{3.5.7}$$

is not diagonalisable. Such a matrix is known as *defective*.[f] A matrix is diagonalisable if there exists an invertible matrix P such that $\mathsf{P}^{-1}\mathsf{M}\mathsf{P}$ is diagonal. The columns of P are the right eigenvectors of M and the rows of P^{-1} are the left eigenvectors of M (see next paragraph). The resulting elements in the diagonal matrix are the corresponding eigenvalues of M. It is not immediately clear whether there may exist a physical atomic configuration for which M is defective (non-diagonalisable), since for every configuration tested so far, we have found the matrix to be diagonalisable. A general proof of whether this is always the case is left for later work.

As well as right eigenvectors $\vec{\mathbf{m}}_p$, the matrix M also has a set of left eigenvectors $\vec{\mathbf{n}}_q$ (see, e.g., p. 185 of [93]), each of them row vectors:

$$\vec{\mathbf{n}}_q \mathsf{M} = \vec{\mathbf{n}}_q \nu_q, \tag{3.5.8}$$

Combining the left and right eigenvectors into one expression, we get

$$\vec{\mathbf{n}}_q \mathsf{M} \vec{\mathbf{m}}_p = \nu_q \vec{\mathbf{n}}_q \cdot \vec{\mathbf{m}}_p = \mu_p \vec{\mathbf{n}}_q \cdot \vec{\mathbf{m}}_p. \tag{3.5.9}$$

This is only true if either $\nu_q = \mu_q$ or if $\vec{\mathbf{n}}_q \cdot \vec{\mathbf{m}}_p = 0$. The left and right eigenvectors are therefore mutually orthogonal and share the same eigenspectrum. Furthermore, we can use the fact that the complex symmetric matrix M is unchanged under a transpose T to show that

$$\left(\vec{\mathbf{n}}_q \mathsf{M}\right)^{\mathrm{T}} = \mathsf{M}^{\mathrm{T}} \vec{\mathbf{n}}_q^{\mathrm{T}} = \mathsf{M} \vec{\mathbf{n}}_q^{\mathrm{T}} = \nu_q \vec{\mathbf{n}}_q^{\mathrm{T}}. \tag{3.5.10}$$

Since $\nu_q = \mu_p$, then $\vec{\mathbf{n}}_q^{\mathrm{T}} = \vec{\mathbf{m}}_p$. This is an important rule for complex symmetric matrices: the left eigenvectors are simply the transpose of the right eigenvectors.

The conventional Euclidean inner product for a pair of complex vectors is defined as $\vec{\mathbf{a}} \cdot \vec{\mathbf{b}} \equiv \sum_i a_i^* b_i$. Eigenvectors of a Hermitian matrix are orthogonal under this inner product, i.e. the left eigenvectors of a Hermitian matrix are the conjugate transpose of the right eigenvectors. However, because the left eigenvectors of a complex symmetric matrix are just the transpose and not the conjugate transpose of the right eigenvectors, they require a different definition of the inner product. As a convention, we will therefore include

[f] The definition of a defective matrix is that its eigenvectors do not form a complete basis (see Sec. 3.5.5), which is true if and only if the matrix is not diagonalisable.

either the transpose operator T or the conjugate transpose (adjoint) operator † in the dot product definition to make it clear whether the left vector is the conjugate of the right vector or not:

$$\vec{\mathbf{a}}^{\mathrm{T}} \cdot \vec{\mathbf{b}} \equiv \sum a_i b_i, \tag{3.5.11a}$$

$$\vec{\mathbf{a}}^{\dagger} \cdot \vec{\mathbf{b}} \equiv \sum a_i^* b_i = \vec{\mathbf{a}} \cdot \vec{\mathbf{b}}. \tag{3.5.11b}$$

If we do not include either type of transpose operator [as in the final term in Eq. (3.5.11)], then the conventional conjugate transpose definition is assumed.

So whilst the eigenvectors of a complex symmetric matrix are orthogonal under the transpose inner product $\vec{\mathbf{m}}_p^{\mathrm{T}} \cdot \vec{\mathbf{m}}_q = \delta_{p,q}$,[g] they are not necessarily orthogonal under the adjoint inner product $\vec{\mathbf{m}}_p^{\dagger} \cdot \vec{\mathbf{m}}_q \neq \delta_{p,q}$. This will have consequences when calculating the extinction or scattering from a cooperative ensemble, allowing different eigenmodes to couple and interfere with one another (Sec. 4.6.3). It should be noted that there do exist complex vectors $\vec{\mathbf{a}}$ such that $\vec{\mathbf{a}}^{\mathrm{T}} \cdot \vec{\mathbf{a}} = 0$ for $\vec{\mathbf{a}} \neq 0$, e.g., $\vec{\mathbf{a}} = (\mathrm{i}, 1)^{\mathrm{T}}$. This, however, has not occurred for any of the configurations considered in this Thesis.

3.5.3 Vector decomposition

Let us next decompose the vectors $\vec{\mathbf{E}}_0$ and $\vec{\mathbf{d}}$ into sums of the right eigenvectors $\vec{\mathbf{m}}_p$. We will start with $\vec{\mathbf{E}}_0$ as this does not depend on the detuning Δ,

$$\vec{\mathbf{E}}_0 = \sum_p b_p \vec{\mathbf{m}}_p. \tag{3.5.12}$$

If we take the dot product of this with the left eigenvector $\vec{\mathbf{m}}_q^{\mathrm{T}}$, we can determine the complex expansion coefficients b_q (3.5.11a)

$$\vec{\mathbf{m}}_q^{\mathrm{T}} \cdot \vec{\mathbf{E}}_0 = \sum_p b_p \vec{\mathbf{m}}_q^{\mathrm{T}} \cdot \vec{\mathbf{m}}_p = \sum_p b_p \delta_{p,q} = b_q. \tag{3.5.13}$$

This is assuming that the eigenvectors are normalised such that $\vec{\mathbf{m}}_q^{\mathrm{T}} \cdot \vec{\mathbf{m}}_p = \delta_{q,p}$.

[g] To normalise $\vec{\mathbf{m}}_p$ such that $\vec{\mathbf{m}}_p^{\mathrm{T}} \cdot \vec{\mathbf{m}}_p = 1$, we can calculate $\vec{\mathbf{m}}_{p,\mathrm{norm}} = \vec{\mathbf{m}}_p / (|m_{pp}|^{0.5} \mathrm{e}^{\mathrm{i}\phi_{pp}/2})$, where $m_{pp} \equiv \vec{\mathbf{m}}_p^{\mathrm{T}} \cdot \vec{\mathbf{m}}_p = |m_{pp}| \mathrm{e}^{\mathrm{i}\phi_{pp}}$ is a complex number with magnitude $|m_{pp}|$ and phase $\mathrm{e}^{\mathrm{i}\phi_{pp}}$.

We could instead use the conjugate transpose dot product (3.5.11b) to calculate b_q. Taking the dot product of $\vec{\mathbf{E}}_0$ with $\vec{\mathbf{m}}_q$ gives

$$\begin{aligned} b_q^* \vec{\mathbf{m}}_q^\dagger \cdot \vec{\mathbf{E}}_0 &= \sum_p b_q^* b_p \vec{\mathbf{m}}_q^\dagger \cdot \vec{\mathbf{m}}_p \\ &= |b_q|^2 + \sum_{p \neq n} b_q^* b_p \vec{\mathbf{m}}_q^\dagger \cdot \vec{\mathbf{m}}_p. \end{aligned} \tag{3.5.14}$$

This is now assuming the $\vec{\mathbf{m}}_p$ is normalised such that $\vec{\mathbf{m}}_p^\dagger \cdot \vec{\mathbf{m}}_p = 1$, and therefore the values of b_p calculated in (3.5.14) will be different to those calculated in (3.5.13). This does not matter provided we are consistent with our choice of method. The non-orthogonality of the eigenvectors now means that the terms $\vec{\mathbf{m}}_p^\dagger \cdot \vec{\mathbf{m}}_q \neq \delta_{p,q}$ are not necessarily zero so we are therefore required to solve a set of coupled linear equations (3.5.14).

Once we have calculated the expansion coefficients $\{b_p\}$ we can also expand $\vec{\mathbf{d}}$ in terms of the eigenvectors $\vec{\mathbf{m}}_p$ as follows:

$$\mathsf{M}\vec{\mathbf{d}} = \vec{\mathbf{E}}_0 = \sum_p b_p \vec{\mathbf{m}}_p = \sum_p \frac{b_p}{\mu_p} \left(\mu_p \vec{\mathbf{m}}_p\right) = \sum_p \frac{b_p}{\mu_p} \left(\mathsf{M}\vec{\mathbf{m}}_p\right) = \mathsf{M} \sum_p \frac{b_p}{\mu_p} \vec{\mathbf{m}}_p, \tag{3.5.15}$$

resulting in

$$\vec{\mathbf{E}}_0 = \sum_p b_p \vec{\mathbf{m}}_p, \qquad \text{and} \qquad \vec{\mathbf{d}} = \sum_p \frac{b_p}{\mu_p} \vec{\mathbf{m}}_p. \tag{3.5.16}$$

Note that b_p, like $\vec{\mathbf{E}}_0$, does not depend on Δ and therefore is only dependent on the atomic configuration. This method could be used as an alternative means of solving Eq. (3.5.3). Once the eigenvalues and eigenvectors of M have been calculated and b_p have been determined, it is then trivial to calculate $\vec{\mathbf{d}}$. We only need do this for a single detuning, since the eigenvalues change linearly in detuning (3.5.17), which means we can avoid having to solve the full coupled equations for every different detuning (provided the atomic configuration remains unchanged from detuning to detuning).

3.5.4 Complex eigenvalues

Let us now expand on the functional form of the eigenvalues μ_p from Eq. (3.5.6):

$$\begin{aligned}\mu_p = \frac{1}{\alpha} - g_p &= -\frac{1}{\alpha_0}\frac{\Delta + \mathrm{i}\gamma_0}{\gamma_0} - g_p \\ &= -\frac{1}{\alpha_0\gamma_0}\left[(\Delta + \mathrm{i}\gamma_0) + g_p\alpha_0\gamma_0\right] \\ &= -\frac{1}{\alpha_0\gamma_0}\left[(\Delta - \Delta_p) + \mathrm{i}(\gamma_0 + \gamma_p)\right], \end{aligned} \tag{3.5.17}$$

where we have defined the eigenvalue shift and decay rate respectively as

$$\Delta_p \equiv -\alpha_0\gamma_0\,\mathrm{Re}(g_p) \qquad \text{and} \qquad \gamma_p \equiv \alpha_0\gamma_0\,\mathrm{Im}(g_p). \tag{3.5.18}$$

The dipole moment therefore has the functional form

$$\vec{\mathbf{d}} = \sum_p b_p\vec{\mathbf{m}}_p \frac{-\alpha_0\gamma_0}{(\Delta - \Delta_p) + \mathrm{i}(\gamma_0 + \gamma_p)} = \sum_p \alpha_p b_p \vec{\mathbf{m}}_p, \tag{3.5.19}$$

where the effective *collective* polarisability of the pth mode is

$$\alpha_p \equiv \frac{1}{\mu_p} = \frac{-\alpha_0\gamma_0}{(\Delta - \Delta_p) + \mathrm{i}(\gamma_0 + \gamma_p)}, \tag{3.5.20}$$

and $b_p\vec{\mathbf{m}}_p$ is similar to pth component of the electric field [comparing with Eq. (3.5.16)]. This collective polarisability has a similar form to the single atom polarisability, but is now shifted off resonance by Δ_p and broadened/narrowed by γ_p (an example lineshape is shown in Fig. 3.2). Note also that the peak amplitude of $\mathrm{Im}(\alpha)$ scales as $\gamma_0/(\gamma_0 + \gamma_p)$.

3.5.5 Complete eigenbasis

To be able to expand the vectors $\vec{\mathbf{E}}_0$ and $\vec{\mathbf{d}}$ onto the eigenbasis in Sec. 3.5.3, a requirement is that the eigenbasis is *complete*. This means that the set of N eigenvectors for a $N \times N$ matrix are all linearly independent. The condition that the coupling matrix M be

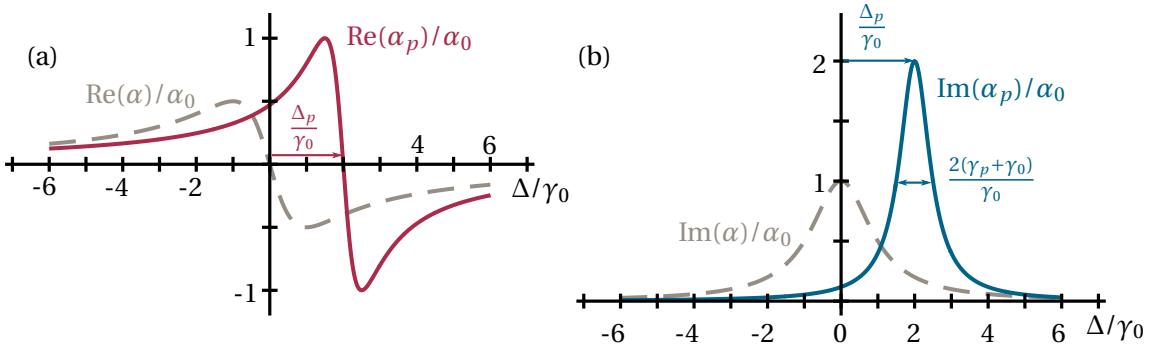

Figure 3.2: Real (a) and imaginary (b) parts of the collective polarisability of the pth eigenmode, α_p, normalised by α_0 (solid lines). The lineshape is shifted by $\Delta_p = 2\gamma_0$ and has total collective halfwidth $\gamma_0 + \gamma_p = 0.5\gamma_0$. These are contrasted with the grey dashed lines showing the single atom polarisability with halfwidth γ_0 and centred on $\Delta = 0$.

diagonalisable, i.e. non-defective, is true if and only if the eigenvectors form a complete, linearly independent basis (p.77 [94]), and so provided that M is diagonalisable, there will always exist a complete eigenbasis. As mentioned in Sec. 3.5.2 however, it is not yet clear whether they may exist a physical atomic configuration for which M is defective, since until now we have found M to always be diagonalisable. If a defective M did exist, then a complete basis could still be formed by supplementing the set of eigenvectors with *generalised* eigenvectors [95]. Such a discussion is left for later work.

3.5.6 Degenerate eigenmodes

The form of the coupling matrix G (3.5.2) means that spatial symmetries in the lattice can produce eigenmodes with degenerate eigenvalues. For example, if the dipoles of an eigenmode of a 1D chain of atoms separated along the x axis are all polarised in the yz plane, then we can uniformly rotate the dipole polarisations around the x axis without changing the eigenvalue. Similarly, for a square lattice in the xy plane, any eigenmode with dipoles polarised just in x will be degenerate with the same eigenmode rotated into y. We do not consider any geometries with three axes of symmetry and so there will only ever be degenerate pairs. However, these need to be treated with care.

Typically, literature treatments of the eigenbasis of complex symmetric matrices in physical problems consider systems with little or no ordering in the system configuration [39, 75, 96], and as such degeneracies are rare and, if present, not important. However, in our highly ordered symmetric configurations, not only are we going to obtain degenerate eigenmodes, but they are going to be significant in describing the overall system behaviour and so cannot be ignored.

In Sec. 3.5.5, we discuss how our vector decompositions of $\vec{\mathbf{E}}_0$ and $\vec{\mathbf{d}}$ require that the eigenvectors form a complete basis. One way in which the set of eigenvectors might not be complete is if there exists an *exceptional point* [97], that is, a pair of eigenmodes with identical eigenvalues AND eigenvectors. This means, obviously, that the eigenvectors are not linearly independent and not a complete set. Whilst typically the MATLAB eigenvector algorithm avoids returning exceptional points, care needs to be taken when modifying the degenerate eigenmodes, which leads to the question of what can be done to deal with mode degeneracies.

For a pair of eigenvalues $\vec{\mathbf{m}}_1$ and $\vec{\mathbf{m}}_2$ with degenerate eigenvalues μ, any linear superposition of the two eigenvectors is also an eigenvector with eigenvalue μ,

$$\mathsf{M}\left(a\vec{\mathbf{m}}_1 + b\vec{\mathbf{m}}_2\right) = \mu\left(a\vec{\mathbf{m}}_1 + b\vec{\mathbf{m}}_2\right). \tag{3.5.21}$$

We can therefore define two new eigenvectors $\vec{\mathbf{m}}_3$ and $\vec{\mathbf{m}}_4$ composed of linear superpositions of $\vec{\mathbf{m}}_1$ and $\vec{\mathbf{m}}_2$. Provided we ensure that $\vec{\mathbf{m}}_3$ and $\vec{\mathbf{m}}_4$ are still linearly independent with each other and the remaining eigenvectors then this changes nothing about the overall behaviour, although it may make determining which modes are populated for particular configurations easier. For example, we might choose $\vec{\mathbf{m}}_3$ and $\vec{\mathbf{m}}_4$ to maximise and minimise the overlap with $\vec{\mathbf{E}}_0$ respectively. However, this has not proved overly beneficial and typically we have not done this.

A more effective but not always possible solution has been to simplify the Hamiltonian if the configuration allows it. For example, if the atoms are all separated along the x axis and the driving field is polarised in y, then there will be degenerate pairs of eigenmodes with polarisation in the yz plane. However, the dipole solution will have no polarisation in z given the driving and separation vectors, and so we can ignore the z excited state, turning

each atom into a 3-level atom. In practice we could further simplify this Hamiltonian since there will only be polarisation in y and therefore we can ignore the x excited state also. The overall behaviour is unchanged, although there are no longer degenerate modes, and there is the added advantage that the computation is faster. Because of these reasons, we employ this method where possible.

Chapter Summary

- We generalise the master equation to account for multiple 4-level atoms interacting via the electromagnetic field
- The dipole–dipole interaction can be described by the scattering of classical electric fields between the dipoles
- The weak-driving steady-state solution is described by a set of coupled linear equations
- The eigenspectrum of the steady-state solution tells us about the cooperative decays and shifts experienced by the different eigenmodes of the system
- The coupling matrix is complex symmetric rather than Hermitian, resulting in non-orthogonal eigenvectors

Chapter 4

Observables

4.1 Overview

In the previous Chapter, we discussed how to calculate the steady-state behaviour of an ensemble of atomic dipoles driven by a weak classical electric field [see Eq. (3.5.3)]. Just knowing the dipole moment vectors $\mathbf{d}_i$ has limited utility. In this Chapter we will discuss how to calculate observable quantities from the dipole moment solutions, including scattered fields (Sec. 4.2), the scattering cross-section (Sec. 4.4), and the extinction cross-section (Sec. 4.6).

4.2 Dipole radiation

Classical electrodynamics shows that an oscillating electric dipole $\mathbf{d}$ radiates an oscillating electromagnetic (EM) field with electric field $\mathbf{E}(\mathbf{r})$ and magnetic field $\mathbf{H}(\mathbf{r})$ [73],

$$\mathbf{E}(\mathbf{r}) = \frac{k^3}{4\pi\varepsilon_0} e^{ikr} \left\{ (\hat{\mathbf{r}} \times \mathbf{d}) \times \hat{\mathbf{r}} \frac{1}{kr} + [3\hat{\mathbf{r}}(\hat{\mathbf{r}} \cdot \mathbf{d}) - \mathbf{d}] \left(\frac{1}{(kr)^3} - \frac{i}{(kr)^2} \right) \right\}, \tag{4.2.1a}$$

$$\mathbf{H}(\mathbf{r}) = \frac{ck^2}{4\pi} (\hat{\mathbf{r}} \times \mathbf{d}) \frac{e^{ikr}}{r} \left(1 + \frac{i}{kr} \right), \tag{4.2.1b}$$

where $\mathbf{r} = r\hat{\mathbf{r}}$ is the distance from the dipole, assumed to be positioned at the origin. The form of these fields is the same regardless of whether derived classically from Maxwell's equations [73] or quantum mechanically by considering the back-action of the dipole on the quantum vacuum field (see [70] and Appendix B). If the dipole $\mathbf{d}$ is in the rotating frame then so are the fields, which are rotating with frequency ω_k (see Sec. 2.4.1).

The magnetic field is always transverse to the position vector $\hat{\mathbf{r}}$, whereas the electric field has components parallel to both $\mathbf{d}$ and $\hat{\mathbf{r}}$. This can be seen by using the vector cross product identity

$$(\mathbf{a} \times \mathbf{b}) \times \mathbf{c} = (\mathbf{a} \cdot \mathbf{c})\mathbf{b} - (\mathbf{b} \cdot \mathbf{c})\mathbf{a}. \tag{4.2.2}$$

The first term in Eq. (4.2.1) becomes

$$(\hat{\mathbf{r}} \times \mathbf{d}) \times \hat{\mathbf{r}} = (\hat{\mathbf{r}} \cdot \hat{\mathbf{r}})\,\mathbf{d} - (\mathbf{d} \cdot \hat{\mathbf{r}})\,\hat{\mathbf{r}} = -\hat{\mathbf{r}}\,(\hat{\mathbf{r}} \cdot \mathbf{d}) + \mathbf{d}, \tag{4.2.3}$$

meaning Eq. (4.2.1) can be rewritten as

$$\mathbf{E}(\mathbf{r}) = \frac{k^3}{4\pi\varepsilon_0} e^{ikr} \left\{ \left(\frac{1}{kr} + \frac{i}{(kr)^2} - \frac{1}{(kr)^3} \right) \mathbf{d} + \left(-\frac{1}{kr} - \frac{3i}{(kr)^2} + \frac{3}{(kr)^3} \right) (\hat{\mathbf{r}} \cdot \mathbf{d})\,\hat{\mathbf{r}} \right\}. \tag{4.2.4}$$

We can write this as a matrix equation, where the vectors $\mathbf{E}(\mathbf{r})$ and $\mathbf{d}$ are related by

$$\mathbf{E}(\mathbf{r}) = \mathsf{G}(\mathbf{r})\,\mathbf{d}. \tag{4.2.5}$$

G is a 3×3 matrix with elements

$$\mathsf{G}^{p,q}(u) \equiv \frac{k^3}{4\pi\varepsilon_0} e^{iu} \left[\delta_{p,q}\, g_1(u) + \frac{u_p u_q}{u^2} g_2(u) \right], \tag{4.2.6}$$

where $\{p,q\} \in \{x,y,z\}$, $u \equiv kr$, $\delta_{p,q}$ is the Kronecker delta function, u_p is the p component of u (e.g., $u_x = kx$) and

$$g_1(u) = \frac{1}{u} + \frac{\mathrm{i}}{u^2} - \frac{1}{u^3}\,, \qquad g_2(u) = -\frac{1}{u} - \frac{3\mathrm{i}}{u^2} + \frac{3}{u^3}\,. \tag{4.2.7}$$

This is expressed in a similar form in [17].

4.2.1 Near-field and far-field

In the far-field (FF) of the dipole ($kr \gg 1$), the electric and magnetic fields have the form

$$\mathbf{E}_{\mathrm{FF}}(\mathbf{r}) = \frac{k^2}{4\pi\varepsilon_0}[(\hat{\mathbf{r}}\times\mathbf{d})\times\hat{\mathbf{r}}]\frac{\mathrm{e}^{\mathrm{i}kr}}{r} \tag{4.2.8a}$$

$$\mathbf{H}_{\mathrm{FF}}(\mathbf{r}) = \frac{ck^2}{4\pi}(\hat{\mathbf{r}}\times\mathbf{d})\frac{\mathrm{e}^{\mathrm{i}kr}}{r}. \tag{4.2.8b}$$

In this limit, the two fields are related by $\mathbf{E}_{\mathrm{FF}} = Z_0(\mathbf{H}_{\mathrm{FF}}\times\hat{\mathbf{r}})$, where $Z_0 = 1/(c\varepsilon_0) \simeq 400\Omega$ is the free-space impedance.

In the near-field (NF, $kr \ll 1$), the fields have the form

$$\mathbf{E}_{\mathrm{NF}}(\mathbf{r}) = \frac{1}{4\pi\varepsilon_0}[3\hat{\mathbf{r}}(\hat{\mathbf{r}}\cdot\mathbf{d}) - \mathbf{d}]\frac{1}{r^3} + \mathrm{i}\frac{k^3}{6\pi\varepsilon_0}\mathbf{d}, \tag{4.2.9a}$$

$$\mathbf{H}_{\mathrm{NF}}(\mathbf{r}) = \frac{\mathrm{i}ck}{4\pi}(\hat{\mathbf{r}}\times\mathbf{d})\frac{1}{r^2}. \tag{4.2.9b}$$

$\mathbf{E}_{\mathrm{NF}}$ has both a divergent part (corresponding to $\mathrm{Re}[\mathsf{G}(\mathbf{r}\to 0)]$) and a convergent part (corresponding to $\mathrm{Im}[\mathsf{G}(\mathbf{r}\to 0)]$). The magnitude $|\mathbf{E}_{\mathrm{NF}}|$ is approximately $Z_0/(kr)$ times larger than $|\mathbf{H}_{\mathrm{NF}}|$, which because $kr \ll 1$, again means $|\mathbf{E}_{\mathrm{NF}}| \gg |\mathbf{H}_{\mathrm{NF}}|$. At all lengths therefore, the magnetic field magnitude is much smaller than the electric field, and so in this Thesis we will only consider the behaviour of the electric field. The near-field electric field (4.2.9a) is equivalent to the field produced by a static (non-oscillating, $k = 0$) electric dipole. Such a dipole radiates no magnetic field. The imaginary part of $\mathsf{G}(\mathbf{r}\to 0)$ is the *radiative reaction*, the interaction energy of a dipole with the field it radiates.

4.3 Poynting vectors, power flow and cross-sections

Using the radiation fields calculated in Sec. 4.2, it is possible to determine the flow of energy through the system, thus calculating how much energy is scattered, absorbed and dissipated from the driving field by the atomic scatterers. The concepts outlined in this and the following Sections are given a more detailed treatment in Sections 6.7, 6.9, 9.2 and 10.1 of [73], as well as [98, 99].

4.3.1 Poynting vector, S

The energy flux density (rate of energy transfer per unit area) of an EM field is given by its *Poynting vector*

$$\mathbf{S}(\mathbf{r},t) = \mathscr{E}(\mathbf{r},t) \times \mathscr{H}(\mathbf{r},t), \tag{4.3.1}$$

where $\mathscr{E}$ and $\mathscr{H}$ are the full time-dependent electric and magnetic fields [see Eq. (2.3.21)]. If the only time dependence is a rotation with frequency ω_k, then these can be written in the rotating frame,

$$\begin{aligned}\mathscr{E}(\mathbf{r},t) =& \mathbf{E}(\mathbf{r})\,\mathrm{e}^{-\mathrm{i}\omega_k t} + \mathbf{E}^*(\mathbf{r})\,\mathrm{e}^{\mathrm{i}\omega_k t} \\ =& 2\,\mathrm{Re}[\mathbf{E}(\mathbf{r})]\cos\omega_k t + 2\,\mathrm{Im}[\mathbf{E}(\mathbf{r})]\sin\omega_k t, \end{aligned} \tag{4.3.2a}$$

$$\begin{aligned}\mathscr{H}(\mathbf{r},t) =& \mathbf{H}(\mathbf{r})\,\mathrm{e}^{-\mathrm{i}\omega_k t} + \mathbf{H}^*(\mathbf{r})\,\mathrm{e}^{\mathrm{i}\omega_k t} \\ =& 2\,\mathrm{Re}[\mathbf{H}(\mathbf{r})]\cos\omega_k t + 2\,\mathrm{Im}[\mathbf{H}(\mathbf{r})]\sin\omega_k t. \end{aligned} \tag{4.3.2b}$$

More commonly, these fields are defined such that $\mathscr{E} = \mathrm{Re}[\mathbf{E}]\cos\omega_k t + \mathrm{Im}[\mathbf{E}]\sin\omega_k t$. The reason our definition differs by a factor of 2 is so that they are consistent with the other Chapters in this Thesis. The physics is unchanged, as long as care is taken to be consistent. Substituting these fields into the Poynting vector gives

$$\begin{aligned}\mathbf{S}(\mathbf{r},t) =& \left[\mathbf{E}(\mathbf{r})\,\mathrm{e}^{-\mathrm{i}\omega_k t} + \mathbf{E}^*(\mathbf{r})\,\mathrm{e}^{\mathrm{i}\omega_k t}\right] \times \left[\mathbf{H}(\mathbf{r})\,\mathrm{e}^{-\mathrm{i}\omega_k t} + \mathbf{H}^*(\mathbf{r})\,\mathrm{e}^{\mathrm{i}\omega_k t}\right] \\ =& 2\mathrm{Re}\left[\mathbf{E}(\mathbf{r}) \times \mathbf{H}^*(\mathbf{r})\right] \;+\; 2\mathrm{Re}\left[\mathbf{E}(\mathbf{r}) \times \mathbf{H}(\mathbf{r})\,\mathrm{e}^{-2\mathrm{i}\omega_k t}\right]. \end{aligned} \tag{4.3.3}$$

When we take the time average of this, the second term in the equation above averages to zero, leaving just

$$\langle \mathbf{S}(\mathbf{r},t)\rangle_t = 2\mathrm{Re}\left[\mathbf{E}(\mathbf{r})\times\mathbf{H}^*(\mathbf{r})\right]. \tag{4.3.4}$$

4.3.2 Power, P

The time-averaged power passing through a differential unit area $\mathrm{d}\mathbf{A}$ is

$$\mathrm{d}P = \langle \mathbf{S}\rangle \cdot \mathrm{d}A, \tag{4.3.5}$$

where $\mathrm{d}\mathbf{A} = \hat{\mathbf{n}}\,\mathrm{d}A$ and $\hat{\mathbf{n}}$ is the unit vector normal to the surface $\mathrm{d}A$. To calculate the total power exchange in this system, we need to integrate $\mathrm{d}P$ over some closed surface S which fully encloses the atomic scatterers. For mathematical convenience, we will choose this surface to be a sphere with radius r centered on the centre of mass of the atomic system, and where $r > \{r_i\}_{\max}$ (so that all the atoms are within the surface). The differential area element subtended by some solid angle $\mathrm{d}\Omega$ over the surface of this sphere is then

$$\mathrm{d}\mathbf{A} = \hat{\mathbf{r}}\,r^2\,\mathrm{d}\Omega = \hat{\mathbf{r}}\,r^2\sin\theta\,\mathrm{d}\theta\,\mathrm{d}\phi, \tag{4.3.6}$$

where $\hat{\mathbf{r}}$ is the unit vector in the direction of $\mathrm{d}\Omega$ and θ and ϕ are the spherical polar angles. The differential power $\mathrm{d}P/\mathrm{d}\Omega$ is therefore

$$\frac{\mathrm{d}P}{\mathrm{d}\Omega} = r^2\,\langle \mathbf{S}\rangle \cdot \hat{\mathbf{r}}, \tag{4.3.7}$$

which describes the angular dependence of the power flow through the surface. The total power flowing through the surface S is

$$P \;=\; r^2 \oint_S \langle \mathbf{S}\rangle \cdot \hat{\mathbf{r}}\,\mathrm{d}\Omega \;=\; r^2 \int_{\theta=0}^{\pi}\int_{\phi=0}^{2\pi} \langle \mathbf{S}\rangle \cdot \hat{\mathbf{r}}\sin\theta\,\mathrm{d}\theta\,\mathrm{d}\phi. \tag{4.3.8}$$

The integral calculation in (4.3.8) can prove problematic once we consider multiple atoms. An alternative method of calculating the integral of the Poynting vector over some arbitrary closed surface is to use the *Poynting theorem* [99, 100],

$$-\frac{\partial u(\mathbf{r},\mathbf{t})}{\partial t} = \nabla\cdot\mathbf{S}(\mathbf{r},t) + \mathbf{J}(\mathbf{r},t)\cdot\mathscr{E}(\mathbf{r},t), \tag{4.3.9}$$

where u is the energy density of the EM field, $\nabla\cdot\mathbf{S}$ is the divergence of the Poynting vector and $\mathbf{J}$ is the free current density. This result is due to the conservation of energy, and states that the rate of change of the EM field energy in a region of unit volume equals the energy flux leaving the region plus the rate of work done on the charge distribution within the region. In free space, the energy density is [using the field expressions in (4.3.2)][a]

$$\begin{aligned}
u(\mathbf{r},t) =& \frac{1}{2}\left[\varepsilon_0\mathscr{E}^\dagger(\mathbf{r},t)\cdot\mathscr{E}(\mathbf{r},t) + \mu_0\mathscr{H}^\dagger(\mathbf{r},t)\cdot\mathscr{H}(\mathbf{r},t)\right] \\
=& \frac{1}{2}\varepsilon_0\left[\mathbf{E}^\dagger(\mathbf{r})\,\mathrm{e}^{\mathrm{i}\omega t} + \mathbf{E}^{\mathrm{T}}(\mathbf{r})\,\mathrm{e}^{-\mathrm{i}\omega t}\right]\cdot\left[\mathbf{E}(\mathbf{r})\,\mathrm{e}^{-\mathrm{i}\omega t} + \mathbf{E}^*(\mathbf{r})\,\mathrm{e}^{\mathrm{i}\omega t}\right] \\
&+ \frac{1}{2}\mu_0\left[\mathbf{H}^\dagger(\mathbf{r})\,\mathrm{e}^{\mathrm{i}\omega t} + \mathbf{H}^{\mathrm{T}}(\mathbf{r})\,\mathrm{e}^{-\mathrm{i}\omega t}\right]\cdot\left[\mathbf{H}(\mathbf{r})\,\mathrm{e}^{-\mathrm{i}\omega t} + \mathbf{H}^*(\mathbf{r})\,\mathrm{e}^{\mathrm{i}\omega t}\right] \\
=& \frac{1}{2}\varepsilon_0\left\{2|\mathbf{E}(\mathbf{r})|^2 + 2\mathrm{Re}\left[\mathbf{E}(\mathbf{r})^{\mathrm{T}}\cdot\mathbf{E}(\mathbf{r})\,\mathrm{e}^{-2\mathrm{i}\omega t}\right]\right\} \\
&+ \frac{1}{2}\mu_0\left\{2|\mathbf{H}(\mathbf{r})|^2 + 2\mathrm{Re}\left[\mathbf{H}(\mathbf{r})^{\mathrm{T}}\cdot\mathbf{H}(\mathbf{r})\,\mathrm{e}^{-2\mathrm{i}\omega t}\right]\right\}.
\end{aligned} \tag{4.3.10}$$

When we take the time average of this, the fast rotating terms $\mathrm{e}^{\pm 2\mathrm{i}\omega t}$ average to zero. The remaining terms are time independent and so the total time derivative of $\langle u\rangle$ is zero. In Sec. 6.9 of [73], Jackson shows that this is true provided the medium is a lossless dielectric or perfect conductor.

The current density $\mathbf{J}(\mathbf{r})$ is just the time derivative of the electric dipoles within the ensemble,

$$\begin{aligned}
\mathbf{J}(\mathbf{r},t) =& \sum_i \delta(\mathbf{r}-\mathbf{r}_i)\,\frac{\mathrm{d}}{\mathrm{d}t}\langle \mathrm{d}_i(t)\rangle \\
=& \sum_i \delta(\mathbf{r}-\mathbf{r}_i)\left(-\mathrm{i}\omega\,\mathbf{d}_i\mathrm{e}^{-\mathrm{i}\omega t} + \mathrm{i}\omega\,\mathbf{d}_i^*\mathrm{e}^{\mathrm{i}\omega t}\right),
\end{aligned} \tag{4.3.11}$$

[a] For clarity, we here use our own explicit definitions for the inner dot product given in (3.5.11).

using the dipole definition from Sec. 3.3.3. The time average of the final term in (4.3.9) is then

$$\begin{aligned}\left\langle \mathbf{J}(\mathbf{r},t)\cdot\mathscr{E}(\mathbf{r},t)\right\rangle =& \mathrm{i}\omega\sum_i \delta(\mathbf{r}-\mathbf{r}_i)\left\langle \left[-\mathbf{d}_i\,\mathrm{e}^{-\mathrm{i}\omega t}+\mathbf{d}_i^*\,\mathrm{e}^{\mathrm{i}\omega t}\right]\cdot\left[\mathbf{E}(\mathbf{r})\mathrm{e}^{-\mathrm{i}\omega t}+\mathbf{E}^*(\mathbf{r})\mathrm{e}^{\mathrm{i}\omega t}\right]\right\rangle \\ =& \mathrm{i}\omega\sum_i \delta(\mathbf{r}-\mathbf{r}_i)\left[-\mathbf{d}_i\cdot\mathbf{E}^*(\mathbf{r}_i)+\mathbf{d}_i^*\cdot\mathbf{E}(\mathbf{r}_i)\right] \\ =& 2ck\sum_i \delta(\mathbf{r}-\mathbf{r}_i)\,\mathrm{Im}\left[\mathbf{d}_i\cdot\mathbf{E}^*(\mathbf{r}_i)\right]. \end{aligned} \tag{4.3.12}$$

The full time-averaged Poynting theorem is then

$$\nabla\cdot\langle\mathbf{S}(\mathbf{r},t)\rangle = -2ck\sum_i \mathrm{Im}\left[\mathbf{d}_i\cdot\mathbf{E}^*(\mathbf{r}_i)\right]. \tag{4.3.13}$$

Using the divergence theorem, we can relate the integral over the surface S for the power in (4.3.8) to an integral over the volume V enclosed by S,

$$\begin{aligned} P =& \oint_S \langle\mathbf{S}(\mathbf{r},t)\rangle\cdot\mathrm{d}\mathbf{A} \\ =& \int_V \nabla\cdot\langle\mathbf{S}(\mathbf{r},t)\rangle\,\mathrm{d}V \\ =& -\int_V 2ck\sum_i \delta(\mathbf{r}-\mathbf{r}_i)\,\mathrm{Im}\left[\mathbf{d}_i\cdot\mathbf{E}^*(\mathbf{r}_i)\right]\mathrm{d}V \\ =& -2ck\sum_i \mathrm{Im}\left[\mathbf{d}_i\cdot\mathbf{E}^*(\mathbf{r}_i)\right]. \end{aligned} \tag{4.3.14}$$

Note that this is a factor of 4 larger than similar expressions from [73], due to the difference in our definitions of the field (Sec. 4.3.1). However, in the next Section we consider the cross-section which is normalised by the field amplitude, and so the expressions will be the same whichever convention is being used.

4.3.3 Cross-section, σ

A common way of quantifying a scattering process is through use of a *cross-section*, σ. The cross-section for a given process (e.g., scattering, extinction, absorption) is the power resulting from that process per incident field intensity and has units of area,

$$\mathrm{d}\sigma = \frac{\langle \mathbf{S}(\mathbf{r},t)\rangle \cdot \mathrm{d}\mathbf{A}}{\hat{\mathbf{k}}_0 \cdot \langle \mathbf{S}_0(\mathbf{r},t)\rangle}, \tag{4.3.15}$$

where $\mathbf{S}_0$ and $\hat{\mathbf{k}}_0$ are the Poynting vector and unit wavevector of the incident field respectively.

For a *uniform incident plane wave*

$$\mathbf{E}_0(\mathbf{r}) = \hat{\boldsymbol{\epsilon}}_0 E_0 \mathrm{e}^{\mathrm{i}\mathbf{k}_0\cdot\mathbf{r}}, \tag{4.3.16a}$$

$$\mathbf{H}_0(\mathbf{r}) = c\varepsilon_0 \hat{\mathbf{k}}_0 \times \mathbf{E}_0(\mathbf{r}), \tag{4.3.16b}$$

the incident intensity has the form

$$\begin{aligned}\hat{\mathbf{k}}_0 \cdot \langle \mathbf{S_0}(\mathbf{r})\rangle &= 2c\varepsilon_0 \hat{\mathbf{k}}_0 \cdot \mathbf{E}_0(\mathbf{r}) \times \left[\hat{\mathbf{k}}_0 \times \mathbf{E}_0^*(\mathbf{r})\right] \\ &= 2c\varepsilon_0 \left[|\mathbf{E}_0(\mathbf{r})|^2 - |\hat{\mathbf{k}}_0 \cdot \mathbf{E}_0(\mathbf{r})|^2\right] \\ &= 2c\varepsilon_0 |E_0|^2. \end{aligned} \tag{4.3.17}$$

The differential cross-section is then

$$\frac{\mathrm{d}\sigma}{\mathrm{d}\Omega} = \frac{1}{2c\varepsilon_0|E_0|^2}\frac{\mathrm{d}P}{\mathrm{d}\Omega} = \frac{r^2}{c\varepsilon_0|E_0|^2}\hat{\mathbf{r}} \cdot \mathrm{Re}\left[\mathbf{E}_N(\mathbf{r}) \times \mathbf{H}_N^*(\mathbf{r})\right], \tag{4.3.18}$$

and the total cross-section is

$$\sigma = \frac{P}{2c\varepsilon_0|E_0|^2} = -\frac{k}{\varepsilon_0|E_0|^2}\sum_i \mathrm{Im}\left[\mathbf{d}_i \cdot \mathbf{E}^*(\mathbf{r}_i)\right]. \tag{4.3.19}$$

4.4 Scattering

The first process we shall consider is the scattering from the radiating dipoles. In Sec. 4.2 we showed that an oscillating electric dipole radiates an EM field. In Fig. 4.1 we consider two such electric dipoles $\mathbf{d}_i$ and $\mathbf{d}_j$ located at positions $\mathbf{r}_i$ and $\mathbf{r}_j$ respectively. Let us consider a closed spherical surface S centred on the origin with radius r. It is assumed the power flowing through the surface S is the same regardless of our choice of r, so for convenience we assume that r is in the far-field of all the dipoles, $\{R_i\} \gg \lambda/(2\pi)$, where $\mathbf{R}_i \equiv \mathbf{r} - \mathbf{r}_i$. The total electric and magnetic fields at some point $\mathbf{r}$ on this surface are the sum of the fields produced by each of the dipoles,

$$\mathbf{E}_N(\mathbf{r}) = \sum_i^N \mathbf{E}_i(\mathbf{R}_i), \qquad \mathbf{H}_N(\mathbf{r}) = \sum_i^N \mathbf{H}_i(\mathbf{R}_i), \tag{4.4.1}$$

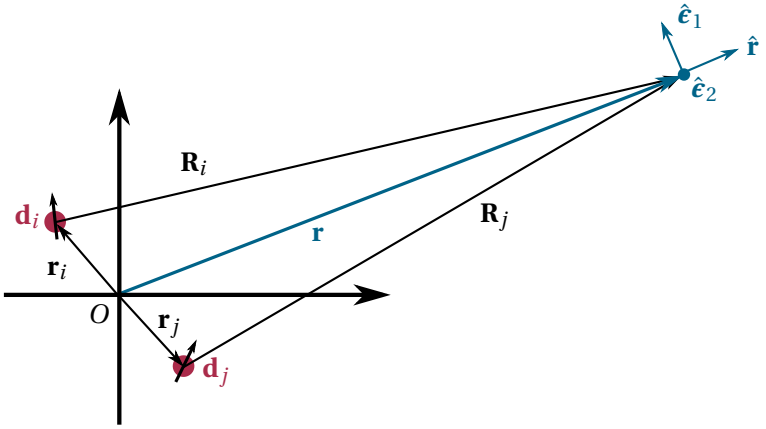

Figure 4.1: Diagram showing two dipoles $\mathbf{d}_i$ and $\mathbf{d}_j$ positioned at $\mathbf{r}_i$ and $\mathbf{r}_j$ respectively with respect to the origin O. In Eq. (4.3.7) we consider the energy flux in a direction $\mathbf{r}$ from the origin. $\hat{\boldsymbol{\epsilon}}_1$ and $\hat{\boldsymbol{\epsilon}}_2$ are two orthogonal polarisation vectors orthogonal to a wave vector propagating in direction $\hat{\mathbf{r}}$.

where the fields radiated by dipole i have the far-field form (4.2.8),

$$\mathbf{E}_i(\mathbf{R}_i) \simeq \frac{k^2}{4\pi\varepsilon_0}\frac{\mathrm{e}^{\mathrm{i}kR_i}}{R_i}\Big[\mathbf{d}_i - (\hat{\mathbf{R}}_i\cdot\mathbf{d}_i)\hat{\mathbf{R}}_i\Big], \tag{4.4.2a}$$

$$\mathbf{H}_i(\mathbf{R}_i) \simeq c\varepsilon_0\,\hat{\mathbf{R}}_i\times\mathbf{E}_i(\mathbf{R}_i). \tag{4.4.2b}$$

4.4.1 Differential scattering cross-section $\mathrm{d}\sigma_{\mathbf{sc}}/\mathrm{d}\Omega$

Let us start by considering the differential scattering cross-section, which describes the angular distribution of the scattering. The differential scattering cross-section is (4.3.18)

$$\begin{aligned}
\frac{\mathrm{d}\sigma_{\mathrm{sc}}}{\mathrm{d}\Omega} &= \frac{r^2}{c\varepsilon_0|E_0|^2}\,\hat{\mathbf{r}}\cdot\mathrm{Re}\big[\mathbf{E}_N(\mathbf{r})\times\mathbf{H}_N^*(\mathbf{r})\big] \\
&= \frac{r^2}{|E_0|^2}\mathrm{Re}\left\{\hat{\mathbf{r}}\cdot\sum_i\mathbf{E}_i(\mathbf{R}_i)\times\sum_j\Big[\hat{\mathbf{R}}_j\times\mathbf{E}_j^*(\mathbf{R}_j)\Big]\right\} \\
&= \frac{r^2}{|E_0|^2}\mathrm{Re}\left\{\hat{\mathbf{r}}\cdot\sum_{ij}\Big(\hat{\mathbf{R}}_j\big[\mathbf{E}_i(\mathbf{R}_i)\cdot\mathbf{E}_j^*(\mathbf{R}_j)\big] - \mathbf{E}_j^*(\mathbf{R}_j)\big[\mathbf{E}_i(\mathbf{R}_i)\cdot\hat{\mathbf{R}}_j\big]\Big)\right\} \\
&= \frac{r^2}{|E_0|^2}\mathrm{Re}\sum_{ij}\Big\{\big[\hat{\mathbf{r}}\cdot\hat{\mathbf{R}}_j\big]\big[\mathbf{E}_i(\mathbf{R}_i)\cdot\mathbf{E}_j^*(\mathbf{R}_j)\big] - \big[\hat{\mathbf{r}}\cdot\mathbf{E}_j^*(\mathbf{R}_j)\big]\big[\mathbf{E}_i(\mathbf{R}_i)\cdot\hat{\mathbf{R}}_j\big]\Big\}.
\end{aligned} \tag{4.4.3}$$

Since r is very much larger than all r_i, then we can approximate

$$R_i \;=\; |\mathbf{r}-\mathbf{r}_i| \;=\; \left(r^2 - 2\mathbf{r}\cdot\mathbf{r}_i + r_i^2\right)^{1/2} \;\simeq\; r - \hat{\mathbf{r}}\cdot\mathbf{r}_i\,, \tag{4.4.4}$$

and

$$\hat{\mathbf{R}}_i \;=\; \frac{\mathbf{R}_i}{R_i} \;\simeq\; \frac{\mathbf{r}-\mathbf{r}_i}{r-\hat{\mathbf{r}}\cdot\mathbf{r}_i} \;\simeq\; \frac{\mathbf{r}}{r} - \frac{\mathbf{r}_i}{r} \;\simeq\; \hat{\mathbf{r}}\,, \tag{4.4.5}$$

giving

$$\frac{\mathrm{d}\sigma_{\mathrm{sc}}}{\mathrm{d}\Omega} \simeq \frac{r^2}{|E_0|^2}\mathrm{Re}\sum_{ij}\Big\{\mathbf{E}_i(\mathbf{R}_i)\cdot\mathbf{E}_j^*(\mathbf{R}_j) - \big[\hat{\mathbf{r}}\cdot\mathbf{E}_j^*(\mathbf{R}_j)\big]\big[\mathbf{E}_i(\mathbf{R}_i)\cdot\hat{\mathbf{r}}\big]\Big\}. \tag{4.4.6}$$

Substituting in the far-field radiation field (4.4.2) this becomes

$$\begin{aligned}\frac{\mathrm{d}\sigma_{\mathrm{sc}}}{\mathrm{d}\Omega} &= \frac{k^4}{(4\pi\varepsilon_0|E_0|)^2}\mathrm{Re}\sum_{ij}\frac{r^2}{R_iR_j}\mathrm{e}^{\mathrm{i}k(R_i-R_j)}\left[\mathbf{d}_i\cdot\mathbf{d}_j^* - (\hat{\mathbf{r}}\cdot\mathbf{d}_i)(\hat{\mathbf{r}}\cdot\mathbf{d}_j^*)\right] \\ &\simeq \frac{k^4}{(4\pi\varepsilon_0|E_0|)^2}\mathrm{Re}\sum_{ij}\mathrm{e}^{-\mathrm{i}k(\hat{\mathbf{r}}\cdot\mathbf{r}_i-\hat{\mathbf{r}}\cdot\mathbf{r}_j)}\left[\mathbf{d}_i\cdot\mathbf{d}_j^* - (\hat{\mathbf{r}}\cdot\mathbf{d}_i)(\hat{\mathbf{r}}\cdot\mathbf{d}_j^*)\right] \\ &= \frac{k^4}{(4\pi\varepsilon_0|E_0|)^2}\left(\left|\sum_i\mathbf{d}_i\mathrm{e}^{-\mathrm{i}k\hat{\mathbf{r}}\cdot\mathbf{r}_i}\right|^2 - \left|\sum_i\hat{\mathbf{r}}\cdot\mathbf{d}_i\mathrm{e}^{-\mathrm{i}k\hat{\mathbf{r}}\cdot\mathbf{r}_i}\right|^2\right). \end{aligned} \tag{4.4.7}$$

If the dipole ensemble is thin and diffuse such that multiple scattering between the dipoles can be ignored, then each dipole has a phase due to the phase of the plane wave incident field

$$\mathbf{d}_i = \alpha E_0\hat{\boldsymbol{\epsilon}}_0\mathrm{e}^{\mathrm{i}\mathbf{k}_0\cdot\mathbf{r}_i}. \tag{4.4.8}$$

The sums in (4.4.7) then just become a sum over the phases

$$\mathscr{F}(\mathbf{q}) = \left|\sum_i\mathrm{e}^{\mathrm{i}\mathbf{q}\cdot\mathbf{r}_i}\right|^2, \tag{4.4.9}$$

where $\mathscr{F}(\mathbf{q})$ is the *structure factor* for an incident field wavevector $\mathbf{k}_0$ scattered into the mode with wavevector $\mathbf{k}_{\mathrm{sc}} = k\hat{\mathbf{r}}$ and $\mathbf{q} \equiv (\mathbf{k}_0 - \mathbf{k}_{\mathrm{sc}})$ (see Sec. 10.1 of [73]). If the atom positions are distributed randomly, the phases sum incoherently resulting in $\mathscr{F}(\mathbf{q}) = N$. However, if the atoms are arranged in some periodic ordered configuration, then, other than in the forward $\mathbf{q} = 0$ direction, $\mathscr{F}(\mathbf{q})$ is nonzero only in particular directions allowed by the Bragg scattering condition.

In this Thesis, we are not considering a diffuse but rather a very dense medium, in which recurrent scattering between the dipoles results in cooperative rather than independent behaviour. As such, we have to keep the sum in its general form (4.4.7).

4.4.2 Total scattering cross-section σ_{sc}
Whilst the differential scattering cross-section can give information about the directionality of the scattering, performing the surface integral over (4.4.7) to calculate the total

scattering cross-section is only practical in specific cases such as when there is only one dipole or many non-interacting dipoles. To calculate $\sigma_{\rm sc}$ for a general ensemble configuration let us therefore use the Poynting theorem described in Sec. 4.3.2 and Equations (4.3.2) and (4.5.1):

$$\begin{aligned}\sigma_{\rm sc} &= -\frac{k}{\varepsilon_0|E_0|^2}\sum_i \mathrm{Im}\left[\mathbf{d}_i\cdot\mathbf{E}_N^*(\mathbf{R}_{ij})\right]\\ &= -\frac{k}{\varepsilon_0|E_0|^2}\mathrm{Im}\left\{\sum_i \mathbf{d}_i\cdot\left[\mathbf{E}_i^*(0)+\sum_{j\neq i}\mathbf{E}_j^*(\mathbf{R}_{ij})\right]\right\},\\ &= -\frac{k}{\varepsilon_0|E_0|^2}\sum_i \mathbf{d}_i\cdot\mathrm{Im}\left[\mathsf{G}^*(0)\right]\mathbf{d}_i^* \;-\; \frac{k}{\varepsilon_0|E_0|^2}\mathrm{Im}\left[\sum_i \mathbf{d}_i\cdot\sum_{j\neq i}\mathbf{E}_j^*(\mathbf{R}_{ij})\right]\end{aligned} \tag{4.4.10}$$

where $\mathbf{R}_{ij}\equiv\mathbf{r}_i-\mathbf{r}_j$ and we have substituted $\mathbf{E}_i^*(0)=\mathsf{G}(0)\,\mathbf{d}_i^*$. This radiative reaction term accounts for the interaction of a dipole with the field it scatters and using Eq. (4.2.6) it has the form $\mathrm{Im}\left[\mathsf{G}^*(0)\right]=-k^3/(6\pi\varepsilon_0)=-1/\alpha_0$. We can also make the substitution $\sum_{j\neq i}\mathbf{E}_j^*(\mathbf{R}_{ij})=\mathbf{d}_i^*/\alpha^*-\mathbf{E}_0^*(\mathbf{r}_i)$ which we know from the steady-state coupled equations for an ensemble of dipoles, (3.4.7). Doing this, the scattering cross-section becomes

$$\sigma_{\rm sc}=\frac{k}{\varepsilon_0|E_0|^2}\sum_i \mathbf{d}_i\cdot\mathbf{d}_i^*\left[\frac{1}{\alpha_0}-\mathrm{Im}\left(\frac{1}{\alpha^*}\right)\right]+\frac{k}{\varepsilon_0|E_0|^2}\sum_i\mathrm{Im}\left[\mathbf{d}_i\cdot\mathbf{E}_0^*(\mathbf{r}_i)\right]. \tag{4.4.11}$$

For an *atomic* dipole, the polarisability α has the form given in Eq. (2.4.8)

$$\mathrm{Im}\left(\frac{1}{\alpha^*}\right)=-\mathrm{Im}\left(\frac{\Delta-\mathrm{i}\gamma_0}{\alpha_0\gamma_0}\right)=\frac{1}{\alpha_0}. \tag{4.4.12}$$

The first term in (4.4.11) therefore cancels, leaving just

$$\sigma_{\rm sc}=\frac{k}{\varepsilon_0|E_0|^2}\sum_i\mathrm{Im}\left[\mathbf{d}_i\cdot\mathbf{E}_0^*(\mathbf{r}_i)\right]. \tag{4.4.13}$$

4.4.3 Single atom scattering power and cross-section

Substituting in $\mathbf{d} = \alpha \mathbf{E}_0(\mathbf{r}_i)$, the scattering cross-section for a single atom has a Lorentzian lineshape:

$$\sigma_{\mathrm{sc}}^{(1)} = \frac{k}{\varepsilon_0}\mathrm{Im}(\alpha) = \frac{\sigma_{\mathrm{sc},0}^{(1)}}{1+(\Delta/\gamma_0)^2}, \tag{4.4.14}$$

where

$$\sigma_{\mathrm{sc},0}^{(1)} = \frac{6\pi}{k_0^2} = \frac{3\lambda_0^2}{2\pi}, \tag{4.4.15}$$

is the resonant ($\Delta = 0$) cross-section. Using (4.5.1), the power scattered from a single resonant dipole is

$$P_{\mathrm{sc},0}^{(1)} = 2c\varepsilon|E_0|^2\sigma_{\mathrm{sc},0}^{(1)} = \frac{3\lambda_0^2 c\varepsilon_0|E_0|^2}{\pi} = \frac{3\lambda_0^2 c\varepsilon_0|\mathscr{E}_0|^2}{4\pi}, \tag{4.4.16}$$

where we have also included it in terms of the total field $\mathscr{E}_0$ as this is the form often quoted [101].

4.5 Absorption

For some types of driven electric dipole, there are also non-radiative decay mechanisms which result in light being absorbed rather than scattered [100], such as phonon excitation in plasmonic nanoresonators [102]. We can calculate this absorption by considering the total energy flux flowing into the closed surface S. Unlike when considering the scattering, we now need to consider both the driving field and the scattered fields.

Substituting $\mathbf{E}(\mathbf{r}_i) = \mathbf{E}_0(\mathbf{r}_i) + \sum_j \mathbf{E}_j(\mathbf{R}_{ij})$ into (4.5.1) gives

$$\sigma_{\text{abs}} = \frac{k}{\varepsilon_0 |E_0|^2} \sum_i \text{Im}\left\{ \mathbf{d}_i \cdot \left[\mathbf{E}_0^*(\mathbf{r}_i) + \sum_j \mathbf{E}_j^*(\mathbf{R}_{ij}) \right] \right\}, \tag{4.5.1}$$

The sign is now positive because we are considering the flux flowing *into* rather than *out of* the surface S, which flips the sign of $d\mathbf{A}$. The $\sum_j \mathbf{E}_j(\mathbf{R}_{ij})$ term is just the scattered cross-section from the previous Section [c.f. Eq. (4.4.10)]. The full general absorption cross-section is therefore

$$\begin{aligned} \sigma_{\text{abs}} &= \frac{k}{\varepsilon_0 |E_0|^2} \sum_i \text{Im}\left[\mathbf{d}_i \cdot \mathbf{E}_0^*(\mathbf{r}_i) \right] - \sigma_{\text{sc}} \\ &= \frac{k}{\varepsilon_0 |E_0|^2} \sum_i \mathbf{d}_i \cdot \mathbf{d}_i^* \left[\frac{1}{\alpha_0} - \text{Im}\left(\frac{1}{\alpha^*} \right) \right]. \end{aligned} \tag{4.5.2}$$

For atomic dipoles there is no non-radiative decay and therefore,

$$\sigma_{\text{abs}} = 0. \tag{4.5.3}$$

4.6 Extinction

4.6.1 Energy conservation

The final process that we shall consider is extinction. So far we have considered how much energy is scattered by the dipoles and how much energy is absorbed. By conservation of energy, the sum of these two terms is equal to the total energy that is removed from the driving field by the dipoles. This is called the *extinction*.

Trivially, we can use our already known expressions for the scattering (4.4.11) and absorption (4.5.2) cross-sections to determine the extinction,

$$\sigma_{\text{ext}} = \sigma_{\text{sc}} + \sigma_{\text{abs}} = \frac{k}{\varepsilon_0 |E_0|^2} \sum_i \text{Im}\left[\mathbf{d}_i \cdot \mathbf{E}_0^*(\mathbf{r}_i)\right]. \tag{4.6.1}$$

For atomic dipoles, because there is no absorption, the extinction cross-section is equal to the scattering cross-section. That is, all the radiation energy that is removed from the incident field is scattered by the dipoles.

We could however have derived the extinction cross-section directly. By comparison with Eq. (4.5.1) we see that the extinction is equivalent to the integrated power of just the driving beam flowing inward through the surface S. In the absence of any dipoles inside the surface, the flux of the driving field flowing in balances the flux flowing out and $\sigma_{\text{ext}} = 0$. The presence of dipoles however means that energy is lost from the driving field and so the net flow in is greater than the net flow out.

4.6.2 Optical Theorem

An alternative direct derivation of the extinction cross-section can be made using the *optical theorem* (see Sec. 10.11 of [73]). The extinction cross-section is shown to be related to the field scattered by the dipoles into the same forward-propagating mode as the incident driving field,

$$\sigma_{\text{ext}} = \frac{4\pi}{k|E_0|^2} \text{Im}\left[\mathrm{e}^{-\mathrm{i}\mathbf{k}_0 \cdot \mathbf{r}_i} E_0^* \, \hat{\boldsymbol{\epsilon}}_0^* \cdot \sum_i \mathbf{F}_i(\mathbf{k} = \mathbf{k}_0) \right], \tag{4.6.2}$$

where the field scattered into mode $\mathbf{k}$ is

$$\mathbf{E}_{\text{sc}}(\mathbf{r}) = \frac{\mathrm{e}^{\mathrm{i}kr}}{r} \mathbf{F}(\mathbf{k}, \mathbf{k_0}). \tag{4.6.3}$$

For a point electric dipole, $\mathbf{F}$ has the form

$$\mathbf{F}_i(\mathbf{k} = \mathbf{k}_0) = \frac{k^2}{4\pi\varepsilon_0} \left[\mathbf{d}_i - (\hat{\mathbf{k}}_0 \cdot \mathbf{d}_i) \hat{\mathbf{k}}_0 \right], \tag{4.6.4}$$

and so the extinction cross-section ends up being the same as we found in Eq. (4.6.1).

4.6.3 Eigenmode expansion

Substituting the eigenmode decompositions of $\mathbf{E}_0$ and $\mathbf{d}_i$ from (3.5.16) into the extinction cross-section (4.6.1) gives[b]

$$\begin{aligned}\sigma_{\text{ext}} &= \frac{k}{\varepsilon_0 |E_0|^2} \text{Im}\left[\vec{\mathbf{E}}_0^\dagger \cdot \vec{\mathbf{d}}\right] \\ &= \frac{k}{\varepsilon_0 |E_0|^2} \sum_{p,q} \text{Im}\left[b_p^* \vec{\mathbf{m}}_p^\dagger \cdot \alpha_q \, b_q \vec{\mathbf{m}}_q\right] \\ &= \frac{k}{\varepsilon_0 |E_0|^2} \sum_p |b_p|^2 \,\text{Im}(\alpha_p) \;+\; \frac{k}{\varepsilon_0 |E_0|^2} \sum_{p,q} \text{Im}\left[\alpha_q \, (b_p^* b_q) \, (\vec{\mathbf{m}}_p^\dagger \cdot \vec{\mathbf{m}}_q)\right]. \end{aligned} \tag{4.6.5}$$

In the first term, we have assumed that the eigenmodes have unit magnitude ($\vec{\mathbf{m}}_p^\dagger \cdot \vec{\mathbf{m}}_p = 1$). The contribution from each individual mode is proportional to the imaginary part of its collective eigenmode, $\text{Im}(\alpha_p)$. This is similar to the single atom cross-section behaviour $\sigma_{\text{sc}}^{(1)} = \text{Im}[\alpha](k/\varepsilon_0)$ (4.4.14). However, because in general the eigenmodes are not orthogonal (see Sec. 3.5), then there is also an interference term $\vec{\mathbf{m}}_p^\dagger \cdot \vec{\mathbf{m}}_q$ which, as we shall see in Sec. 6.3.4, results in characteristic Fano-like resonances. An equivalent eigenmode decomposition of the extinction cross-section has also been carried out for an ensemble of plasmonic resonators [42].

An aspect of the single mode terms that will be important for our understanding of the enhanced extinction discussed in Chap. 8 is how the peak cross-section depends on the collective decay rate. For a given eigenmode p, the collective polarisability has the form given in Eq. (3.5.20)

$$\alpha_p = \frac{-\alpha_0 \gamma_0}{(\Delta - \Delta_p) + \text{i}(\gamma_0 + \gamma_p)}, \tag{4.6.6}$$

where Δ_p and $(\gamma_0 + \gamma_p)$ are the collective shift and decay rate respectively. The imaginary part of α_p is

$$\text{Im}\left(\alpha_p\right) = \text{Im}\left[-\alpha_0 \gamma_0 \frac{(\Delta - \Delta_p) - \text{i}(\gamma_0 + \gamma_p)}{(\Delta - \Delta_p)^2 + (\gamma_0 + \gamma_p)^2}\right] = \frac{\alpha_0 \gamma_0 (\gamma_0 + \gamma_p)}{(\Delta - \Delta_p)^2 + (\gamma_0 + \gamma_p)^2}, \tag{4.6.7}$$

which on resonance ($\Delta = \Delta_p$) is

[b] For clarity, we here use our own explicit definitions for the inner dot product given in (3.5.11).

$$\mathrm{Im}\left(\alpha_{p,\Delta_p}\right) = \alpha_0 \frac{\gamma_0}{\gamma_0 + \gamma_p}. \tag{4.6.8}$$

The peak of the extinction cross-section for a single eigenmode is therefore inversely proportional to the total collective width $(\gamma_0 + \gamma_p)$ of the eigenmode polarisability.[c] The enhanced cross-section in Chap. 8 is therefore due to subradiant behaviour, i.e. $\gamma_0 + \gamma_p < \gamma_0$.

[c] This has a similar form to the resonant collective polarisability in Sec. 3.5.4.

Chapter Summary

- Solutions for the coupled dipole behaviour from previous Chapters can be used to calculate various observables
- We present the electric and magnetic fields radiated from a classical oscillating electric dipole
- From these fields, it is possible to calculate the radiation power flowing through the atomic system
- Using the Poynting theorem, we derive the scattering, absorption and extinction cross-sections for an ensemble of dipoles
- For atomic dipoles, the non-radiative decay (absorption) is zero, meaning the extinction cross-section is equal to the scattering cross-section

Part II

Cooperative Behaviour in One-Dimensional Arrays

Part II: Cooperative Behaviour in 1D Arrays

Now that we have introduced our model, we will begin to look at this cooperative behaviour in different atomic configurations. In this Part, we will confine the atomic positions to one dimension (although still assuming three-dimensional field modes).

We start in Chapter 5 with the simple case of just two atoms. For two atoms, it is possible to solve the master equation for the full quantum atomic density matrix. We can therefore compare this with the weak-driving model and observe which features are maintained and which are lost, as well as limits on the validity of the weak-driving model for multiple atom systems. It is also possible with two atoms to obtain analytic solutions for the weak driving steady-state, giving insight into this behaviour.

In Chapter 6 we will extend the ensemble to N atoms regularly spaced along a 1D chain. We will investigate the eigenmode behaviour of the weak-driving steady-state solutions and their contribution to the extinction cross-section of the atom chain. In particular we will see that whilst the number of eigenmodes increases with increasing N, these eigenmodes follow specific patterns and can be characterised by correlation functions measuring the phase difference between neighbouring dipoles. As $N \to \infty$, some of the modes behave equivalently to a single atom between two mirrors.

These simple configurations present a relatively clean system in which to investigate cooperative effects. For example, the first experimental demonstration of superradiance and subradiance for an ensemble of microscopically resolvable particles was for a pair of ions separated with varying separation [4]. Similar recent studies have measured cooperative shifts in ion chains up to $N = 8$ [5], superradiance for $0.19 \lesssim \langle N \rangle \lesssim 2.6$ atoms coupled along a 1D waveguide [10], and excitation hopping along 1D atoms chains ($N = 3$ [50]) which may also exhibit subradiance ($N = 20$ [40]).

Chapter 5

Two atoms

5.1 Overview

For the two atom system, we will first calculate analytic solutions for the weakly-driven coupled dipole steady state (Sec. 5.2), focussing particularly on the behaviour of the eigenvectors and eigenvalues for different atom configurations. In Sec. 5.3 we will then compare this weak driving solution with the full optical Bloch solutions to the quantum master equation, analysing the different time scales of the system dynamics.

5.2 Two-level, weak-driving steady-state

In Chapter 3, we derived the coupled equations of motion for an ensemble of driven atomic dipoles. For weak driving ($E_0 \ll |\mathbf{d}_{ge}|/\alpha_0$), the steady-state solution for the ℓth dipole has the form (3.4.7)

$$\mathbf{d}_\ell \equiv \sum_{\mu}^{\{x,y,z\}} \mathbf{d}_\ell^\mu = \alpha \mathbf{E}_0(\mathbf{r}_\ell) + \alpha \sum_{i\neq\ell} \mathsf{G}_{i\ell}\,\mathbf{d}_i. \tag{5.2.1}$$

For simplicity, let us first assume that only a single dipole polarisation is excited (the conditions for realising an effective two-level atom are discussed in Sec. 3.2.2). Assuming that

this dipole polarisation is the same as that of the driving field, we can rewrite (5.2.1) as

$$d_\ell \quad = \quad \alpha E_0^{(\ell)} + \alpha \sum_{i\neq\ell} G_{i\ell}\, d_i, \tag{5.2.2}$$

where $G_{i\ell} \equiv \hat{\mathbf{d}}_{ge} \cdot \mathsf{G}_{i\ell}\, \hat{\mathbf{d}}_{ge}$ and we have used the shorthand $E_0(\mathbf{r}_\ell) \equiv E_0^{(\ell)}$.

5.2.1 Recurrent scattering

Substituting d_2 into $d_1 = \alpha E_0^{(1)} + \alpha G_{12} d_2$, we obtain a recurrent solution for the two coupled dipoles [32],

$$\begin{aligned}
d_1 =& \alpha E_0^{(1)} + \alpha G_{12}\left(\alpha E_0^{(2)} + \alpha G_{12} d_1\right) \\
=& \alpha E_0^{(1)} + \alpha G_{12}\left[\alpha E_0^{(2)} + \alpha G_{12}\left(\alpha E_0^{(1)} + \alpha G_{12} d_2\right)\right] \\
=& \alpha E_0^{(1)} + \alpha G_{12}\left\{\alpha E_0^{(2)} + \alpha G_{12}\left[\alpha E_0^{(1)} + \alpha G_{12}\left(\alpha E_0^{(2)} + \alpha G_{12} d_1\right)\right]\right\} \\
&\vdots \\
=& \left(\alpha E_0^{(1)}\right) + (\alpha G_{12})\left(\alpha E_0^{(2)}\right) + (\alpha G_{12})^2\left(\alpha E_0^{(1)}\right) + (\alpha G_{12})^3\left(\alpha E_0^{(2)}\right) + \ldots
\end{aligned} \tag{5.2.3}$$

The total dipole moment corresponds to the infinite set of possible scattering events between the pair of dipoles, shown pictorially in Fig. 5.1. This *recurrent* scattering is characteristic of a homogeneously broadened ensemble where the time for a sufficient number of recurrent events is short compared to decay and decoherence timescales and the strength of each successive scattering event is not negligible. If the medium experiences inhomogeneous broadening, the strength of each successive scattering event becomes vanishingly small (proportional to powers of α) and only the first or second order terms need be included. This results in a mean field behaviour which is qualitatively different to the behaviour described in this thesis [32].

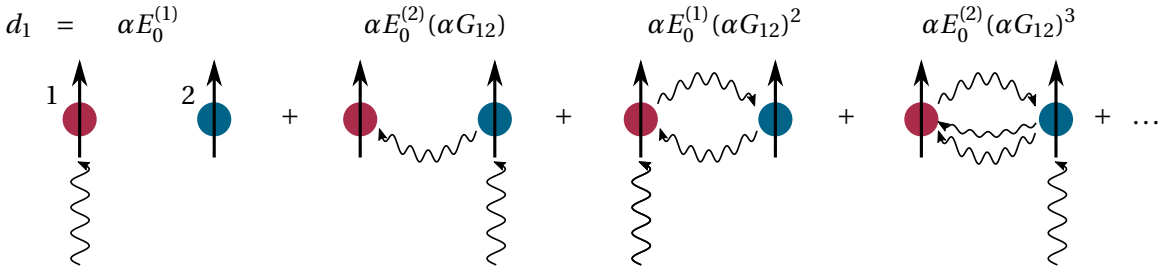

Figure 5.1: Recurrent scattering between two atoms. The scalar dipole moment of dipole 1 (red) is due to the infinite sum of recurrent scattering events between it and dipole 2 (blue) described by Eq. (5.2.3). Each time the photon hops from one dipole to the other, an additional term of (αG_{12}) is added. The first term $(\alpha E_0^{(1)})$ corresponds to the event where a photon is just absorbed from the driving field by dipole 1. The second term corresponds to dipole 2 absorbing a photon $(\alpha E_0^{(2)})$ and scattering it to dipole 1 (αG_{12}). The next term involves a photon being absorbed by dipole 1 $(\alpha E_0^{(1)})$, scattered to dipole 2 (αG_{12}) and then scattered back to dipole 1 again.

5.2.2 Eigenmode solution

As we did in Sec. 3.5, we can also write this as a matrix equation $\vec{\mathbf{E}} = \mathsf{M}\vec{\mathbf{d}}$, which for a pair of 2-level atoms has the form

$$\begin{pmatrix} E_0^{(1)} \\ E_0^{(2)} \end{pmatrix} = \begin{pmatrix} 1/\alpha & -G_{12} \\ -G_{12} & 1/\alpha \end{pmatrix} \begin{pmatrix} d_1 \\ d_2 \end{pmatrix}. \tag{5.2.4}$$

The normalised eigenvectors of M are

$$\vec{\mathbf{m}}_+ = \frac{1}{\sqrt{2}} \begin{pmatrix} 1 \\ 1 \end{pmatrix}, \qquad \vec{\mathbf{m}}_- = \frac{1}{\sqrt{2}} \begin{pmatrix} 1 \\ -1 \end{pmatrix}, \tag{5.2.5}$$

which have corresponding eigenvalues

$$\mu_+ = \frac{1}{\alpha} - G_{12}, \qquad \mu_- = \frac{1}{\alpha} + G_{12}. \tag{5.2.6}$$

We have labeled the two modes + and − to refer to the relative sign between the vector components of $\vec{\mathbf{m}}_\pm$. In the + mode, the two dipoles oscillate *in phase* with each other, whilst in the − mode, the two dipoles oscillate *out of phase* with each other. These are analogous to the symmetric and antisymmetric Dicke states discussed in Sec. 1.2.

Notice that for this special case, the eigenvectors $\vec{\mathbf{m}}_\pm$ are orthogonal. As we explained in Sec. 3.5.2, the matrix M is complex symmetric which means that the eigenvectors need not be orthogonal ($\vec{\mathbf{m}}_i^\dagger \cdot \vec{\mathbf{m}}_j \neq \delta_{ij}$), but rather are transpose orthogonal ($\vec{\mathbf{m}}_i^{\mathrm{T}} \cdot \vec{\mathbf{m}}_j = \delta_{ij}$). Because the eigenvectors are real however, the two cases are equivalent.

Using the vector decompositions in Sec. 3.5.3, both $\vec{\mathbf{E}}_0$ and $\vec{\mathbf{d}}$ can be decomposed into sums of $\vec{\mathbf{m}}_+$ and $\vec{\mathbf{m}}_-$,

$$\begin{pmatrix} E_0^{(1)} \\ E_0^{(2)} \end{pmatrix} = b_+\vec{\mathbf{m}}_+ + b_-\vec{\mathbf{m}}_- = \frac{E_0^{(1)}+E_0^{(2)}}{2}\begin{pmatrix}1\\1\end{pmatrix} + \frac{E_0^{(1)}-E_0^{(2)}}{2}\begin{pmatrix}1\\-1\end{pmatrix}, \tag{5.2.7}$$

$$\begin{pmatrix} d_1 \\ d_2 \end{pmatrix} = \frac{b_+}{\mu_+}\vec{\mathbf{m}}_+ + \frac{b_-}{\mu_-}\vec{\mathbf{m}}_- = \frac{1}{2}\frac{E_0^{(1)}+E_0^{(2)}}{\alpha^{-1}-G_{12}}\begin{pmatrix}1\\1\end{pmatrix} + \frac{1}{2}\frac{E_0^{(1)}-E_0^{(2)}}{\alpha^{-1}+G_{12}}\begin{pmatrix}1\\-1\end{pmatrix}. \tag{5.2.8}$$

As in Sec. 3.5.4, we can define two effective polarisabilites

$$\alpha_\pm \equiv -\frac{\alpha_0\gamma_0}{(\Delta-\Delta_\pm)+\mathrm{i}(\gamma_0+\gamma_\pm)}, \tag{5.2.9}$$

where the polarisability lineshapes are shifted by $\Delta_\pm$ and broadened or narrowed by $\gamma_\pm$,

$$\Delta_\pm = \mp\alpha_0\gamma_0\,\mathrm{Re}(G_{12}), \qquad \gamma_\pm = \pm\alpha_0\gamma_0\,\mathrm{Im}(G_{12}). \tag{5.2.10}$$

An example lineshape for an effective polarisability for a given Δ_{12} and γ_{12} was plotted in Fig. 3.2. The vector $\vec{\mathbf{d}}$ is now

$$\begin{pmatrix} d_1 \\ d_2 \end{pmatrix} = \frac{E_0^{(1)}+E_0^{(2)}}{2}\alpha_+\begin{pmatrix}1\\1\end{pmatrix} + \frac{E_0^{(1)}-E_0^{(2)}}{2}\alpha_-\begin{pmatrix}1\\-1\end{pmatrix}. \tag{5.2.11}$$

The relative contribution of each mode is governed by the symmetry of the driving field E_0 across the two atomic positions. If $E_0^{(1)} = E_0^{(2)}$, then only the first mode $\vec{\mathbf{m}}_+$ will contribute. Conversely, if $E_0^{(1)} = -E_0^{(2)}$ then only the second mode will contribute. Otherwise, the total

dipole behaviour will be a combination of the two modes. In general, the symmetry of the two dipoles matches the symmetry of the field. This will become clearer when considering the extinction of different atom orientations in Sec. 5.2.4.

5.2.3 Two-atom eigenvalues

The two collective polarisabilities $\alpha_\pm$ that determine the dipolar behaviour of each mode depend on the eigenvalues of these two modes $\mu_\pm = \alpha^{-1} \mp G_{12}$ (5.2.6). For a pair of 2-level atoms, we can write the interaction G_{12} in terms of the angle θ between the dipole vectors $\mathbf{d}_{1,2}$ and the separation vector $\hat{\mathbf{r}}_{12}$:

$$G_{12} = \frac{3}{2\alpha_0} e^{ikr_{12}} \left[\frac{1}{kr_{12}} \sin^2\theta + \left(\frac{i}{(kr_{12})^2} - \frac{1}{(kr_{12})^3} \right) \left(1 - 3\cos^2\theta\right) \right]. \tag{5.2.12}$$

In Fig. 5.2 we plot $\mathrm{Re}(G_{12})$ and $\mathrm{Im}(G_{12})$ for $\theta = 0$ and $\theta = \pi/2$. The real part, which gives a shift $\Delta_{1,2} = \mp\alpha_0\gamma_0\,\mathrm{Re}(G_{12})$, is divergent for $kr \to 0$, with the sign of this divergence depending on the orientation between the dipoles. The imaginary part, which gives a change in the decay rate $\gamma_{1,2} = \pm\alpha_0\gamma_0\,\mathrm{Im}(G_{12})$, tends to 1 as $kr \to 0$, regardless of the dipole orientation.

The in-phase eigenmode $\vec{\mathbf{m}}_+$ has a half decay rate of $\gamma = \gamma_0 + \gamma_1 = \gamma_0 + \alpha_0\gamma_0\mathrm{Im}(G_{12})$. As

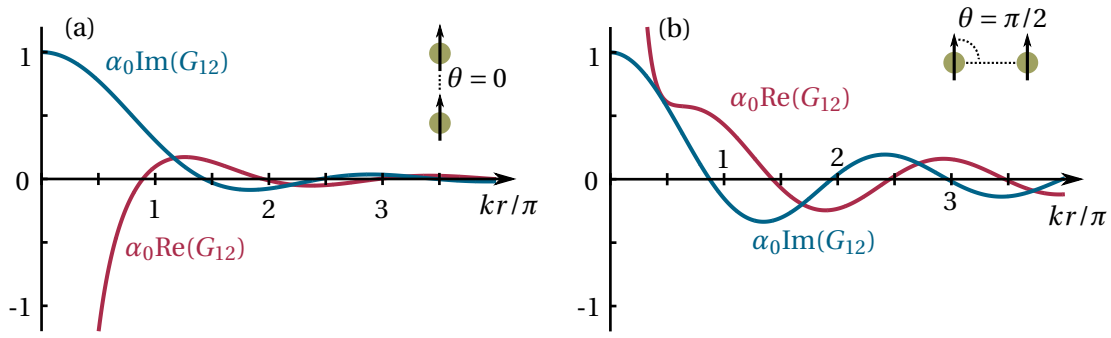

Figure 5.2: Real and imaginary parts of the dipole–dipole interaction G_{12} between a pair of dipoles oriented with $\theta = 0$ (a) and $\theta = \pi/2$ (b), as a function of kr.

$kr \to 0$, this therefore tends to $\gamma \to 2\gamma_0$, i.e. the decay rate is doubled. An enhancement of the decay rate like this is often referred to as *superradiance*. In his seminal work on the subject, Dicke [20] found that an ensemble of N atoms much smaller than the wavelength in extent (the $kr \to 0$ limit) experienced an N-fold enhancement in the decay rate (Sec. 1.2). The small sample size allowed him to assume that the atoms were in the N-wise symmetric state, equivalent, in the two-atom case, to the eigenstate $\vec{\mathbf{m}}_+$ in which the atoms all radiate in phase.

The out-of-phase eigenmode $\vec{\mathbf{m}}_-$ however experiences a reduction in the decay rate as $kr \to 0$: $\gamma = \gamma_0 + \gamma_2 = \gamma_0 - \alpha_0\gamma_0 \mathrm{Im}(G_{12}) \to 0$. This reduced decay rate is referred to as *subradiance*. In order to populate such an eigenmode, Eq. (5.2.11) shows us that there must be a difference in driving field between the two atom positions, $E_0^{(1)} - E_0^{(2)} \neq 0$. If $kr \ll 1$ however, the field is the same across the two atoms (dipole approximation), meaning we will only populate the $\vec{\mathbf{m}}_+$ eigenstate. To realise subradiance in this limit would therefore require some other method of initially preparing the atoms in the $\vec{\mathbf{m}}_-$ state.

The oscillatory behaviour of $\alpha_0 \mathrm{Im}(G_{12})$ in Fig. 5.2 means that $\vec{\mathbf{m}}_+$ and $\vec{\mathbf{m}}_-$ both oscillate between superradiant and subradiant behaviour as a function of kr. This was first demonstrated by DeVoe and Brewer in 1996 [4], where they measured both enhancement (subradiance) and reduction (superradiance) in the spontaneous emission lifetime of a pair of ions separated by $kr/\pi = \{5.6, 6, 6.2\}$. The corresponding energy shift has also been measured as a function of spacing between ions in chains from $N = 2$ to $N = 8$ [5].

For $kr \gtrsim \pi$, the real and imaginary parts of G_{12} are approximately periodic in kr/π (integer multiples of $r = \lambda/2$). This periodicity derives from the phase of the radiated field between the dipoles e^{ikr}. We will see in the Chap. 6 that this periodicity is enhanced for a 1D chain of dipoles, resulting in similar behaviour manifested by both a 1D chain of dipoles and a single dipole between two mirrors. In Part III we will then find that in 2D arrays, the competing incommensurate distance scales between pairs of dipoles results in a breaking down of this regular periodicity.

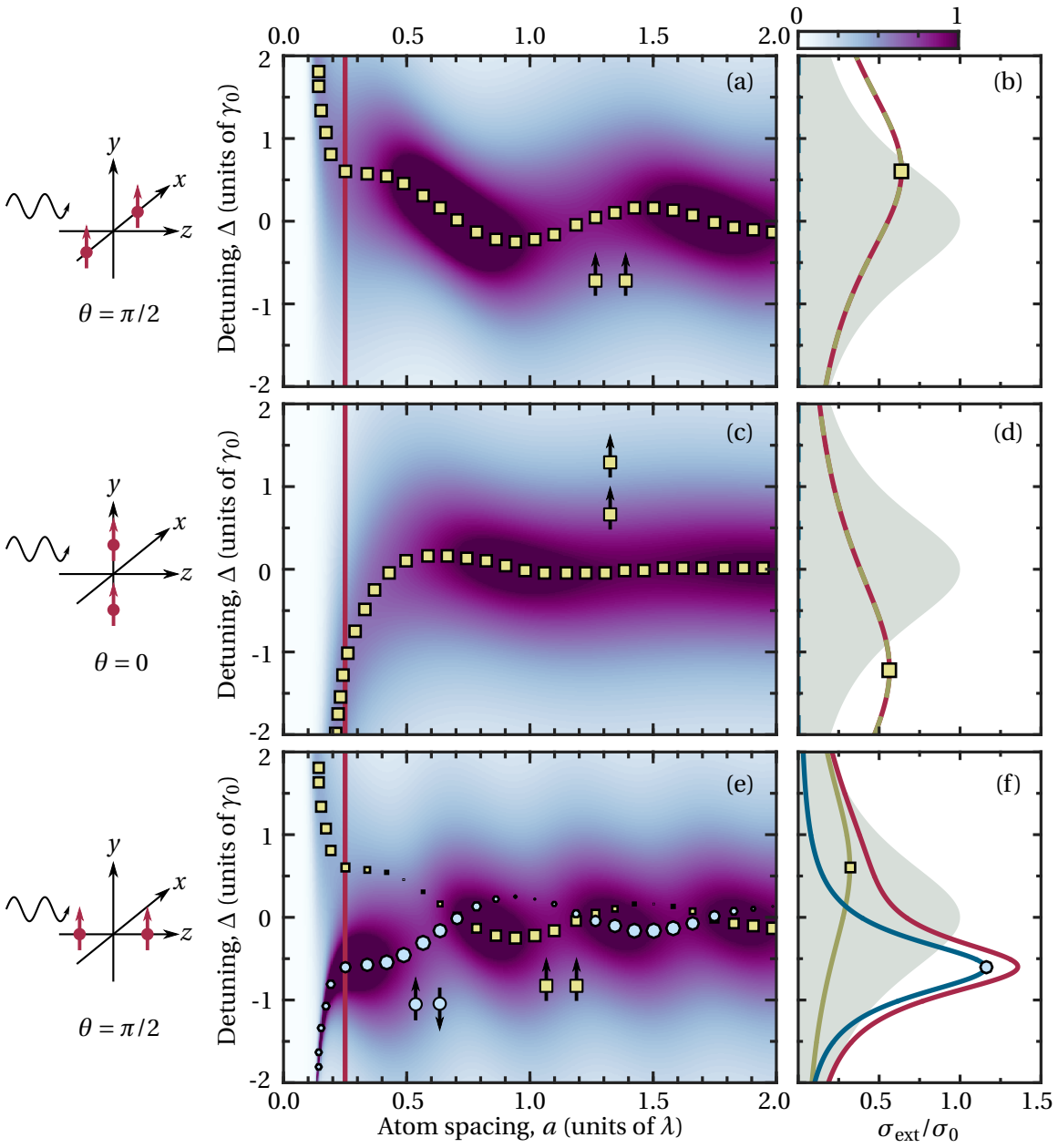

Figure 5.3: (a,c,e) Extinction cross-section σ_{ext} of a uniform plane wave electric field $\mathbf{E}(\mathbf{r}) = E_0\hat{\mathbf{y}}e^{ikz}$ due to a pair of 2-level atoms, as a function of atom spacing a and detuning of the driving field Δ. (b,d,f) Total cross-section (red line) and individual mode cross-sections $|b_\pm|^2\text{Im}(\alpha_\pm)$ for the $\vec{\mathbf{m}}_+$ (yellow line) and $\vec{\mathbf{m}}_-$ (blue line) modes in Eq. (5.2.5), as a function of detuning for $a = \lambda/4$ [indicated by red lines in (a,c,e)]. The grey background shows the single non-interacting atom lineshape. The yellow squares ($\vec{\mathbf{m}}_+$) and blue circles ($\vec{\mathbf{m}}_-$) indicate the mode shifts $\Delta_\pm$ and are proportional in size to the relative mode amplitudes $|b_\pm|^2$. The atoms are separated in x (a,b), y (c,d), and z (e,f).

5.2.4 Two-atom extinction cross-section

In Fig. 5.3 we plot the extinction cross-section for a pair of atoms separated in x, y, or z. The driving field is a uniform plane wave propagating in z and linearly polarised in y. For separation in x and y, the field is identical across both atoms and so only couples to the in-phase mode $\vec{\mathbf{m}}_+$. Depending on the orientation, this mode is either blue shifted or red shifted as $kr \to 0$. If the atoms are separated in z however, because of the propagation phase e^{ikz} in the driving field, depending on the spacing there can be both symmetric and antisymmetric components in the driving field across the two atoms. We see therefore in Fig. 5.3 (e) that the behaviour alternates between the two modes as a function of kr. Taking a cross-section at $kr = \pi/2$ in Fig. 5.3(f), the in-phase mode $\vec{\mathbf{m}}_+$ is blue shifted and superradiant ($\gamma > \gamma_0$) whilst the out-of-phase mode $\vec{\mathbf{m}}_-$ is red shifted and subradiant ($\gamma < \gamma_0$). The total extinction is the sum of the two mode contributions as there is no interference between the modes in this system.

5.3 Time dynamics

In addition to the weak-driving steady-state solution, we can also solve the time dynamics for the full two-atom master equation (3.3.25), as we did for a single atom in Sec. 2.4.3. Doing this allows us to determine the characteristic time scales associated with both the natural atomic dynamics as well as the interaction dynamics.

In Fig. 5.4 we plot the time dynamics of the single atom density matrix elements for one of a pair of atomic dipoles, driven by a uniform driving field and separated in the direction of (linear) polarisation [$\theta = 0$, this is equivalent to the configuration in Fig. 5.3(c,d)]. These single atom density matrix elements can be calculated by taking the trace of the single atom spin operators acting on the many-body density matrix, $\rho^{(\ell)}_{\mu\nu} = \mathrm{Tr}(\rho_N |\nu_\ell\rangle\langle\mu_\ell|)$, c.f. Eq. (C.5.7). As in Sec. 2.4.3, we define dimensionless variables

$$\tilde{t} \equiv \Gamma_0 t = \frac{t}{\tau_0}, \qquad \tilde{E}_0 \equiv \frac{\alpha_0 E_0}{|\mathbf{d}_{ge}|}, \qquad \tilde{G}_{12} \equiv \frac{\alpha G_{12}}{2}. \tag{5.3.1}$$

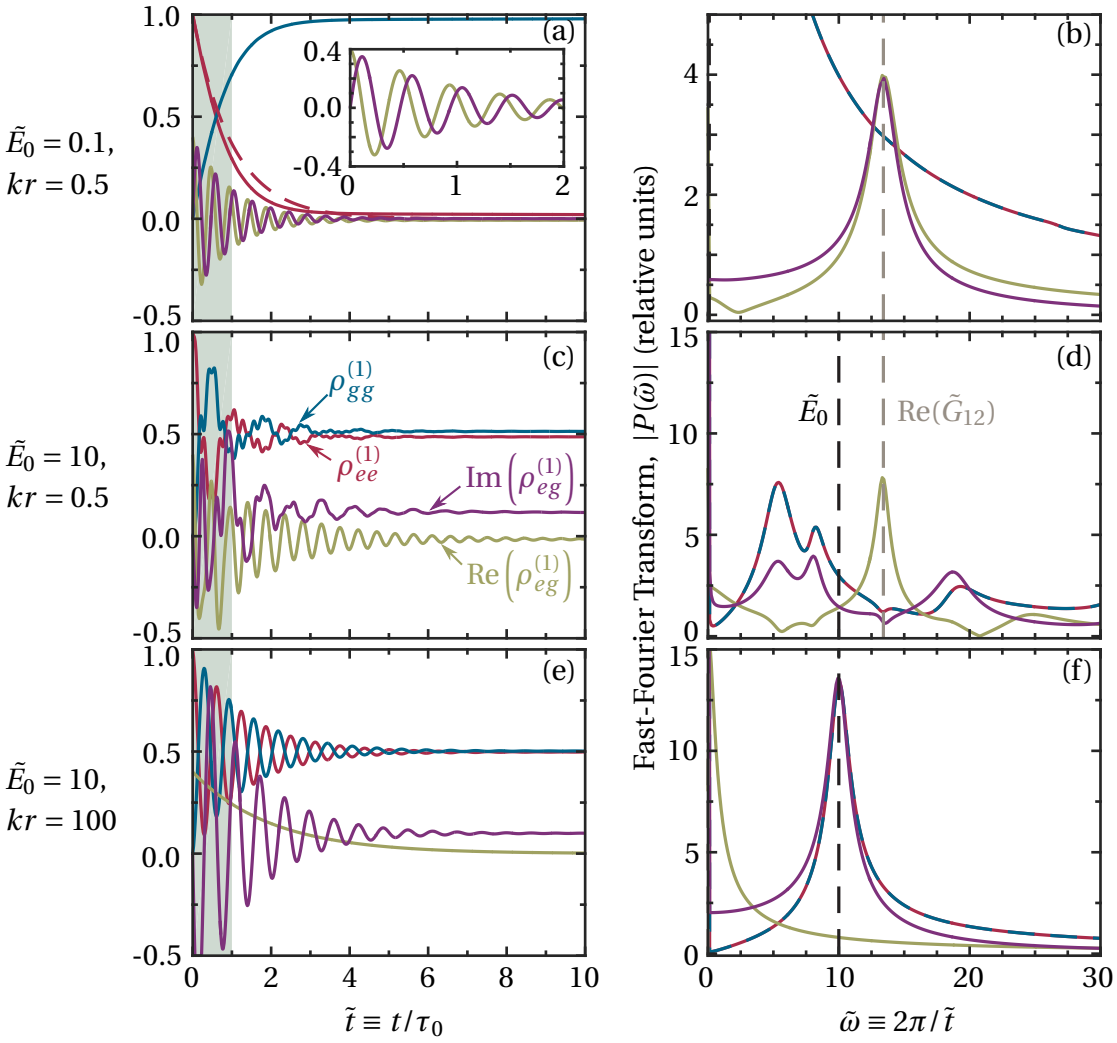

Figure 5.4: (a,c,e) Time dynamics of the single atom density matrix elements calculated from the two atom coupled master equation (3.3.25). (b,d,f) Fourier transforms of the solutions in (a,c,e). The atoms are separated along the direction of polarisation ($\theta = 0$) and experience the same electric field, which is driving on resonance ($\Delta = 0$). In (a)–(d) the dipole–dipole interaction is strong (atoms are closely spaced, $kr = 0.5$) resulting in a strong oscillation with frequency $\mathrm{Re}(\tilde{G}_{12})$. In (c)–(f), the driving is strong ($\tilde{E}_0$) resulting in a strong contribution with frequency $\tilde{E}_0$. Starting in the initial product state ($\rho_e^{(1,2)} = 1$, $\rho^{(1)}_{ge} = 0.2$, $\rho^{(2)}_{ge} = -0.2$), the time dynamics are calculated over a time $\tilde{t} = 50$. The red dashed line in (a) shows the natural decay rate (γ_0).

We choose an initial state where both atoms are in the excited state with a small and opposite coherence ($\rho_e^{(1,2)} = 1$, $\rho_{ge}^{(1)} = 0.2$, $\rho_{ge}^{(2)} = -0.2$).[a] In (a,b), the interactions dominate over the (weak) driving and the excited state decays into the ground state with a slightly enhanced decay rate. The coherences rapidly decay whilst oscillating with frequency $\mathrm{Re}(\tilde{G}_{12})$. If, instead, the driving is strong and the interaction is weak (e,f), then the populations and $\mathrm{Im}(\rho_{eg}^{(1)})$ oscillate with frequency $\tilde{E}_0$. If both driving and interactions are strong (c,d), then we see a number of different frequencies contributing.

Typically we will be working in the weak driving limit and so the two characteristic rates we need to consider are the new collective decay rate $\gamma_0+\gamma_\pm$, and the oscillation frequency of the interaction $\mathrm{Re}(\tilde{G}_{12})$.

[a] A different initial state would result in slightly different dynamical behaviour. We are not concerned with these specific differences as we just want to demonstrate a typical dynamical solution.

Chapter Summary

- For a pair of weakly-driven coupled 2-level atoms, there exist two orthogonal eigenmodes which correspond to the two dipoles oscillating in phase and out of phase with each other.
- The symmetry of the driving field determines the contribution from each mode
- The two modes alternate between superradiant and subradiant as a function of atom spacing
- For weak driving, the atomic dynamics are determined by the collective decay rate and oscillation frequency, which depend on the interaction strength

Chapter 6

One-dimensional atom array

6.1 Overview

In this Chapter, we move beyond considering just a pair of atoms to considering N atoms arranged in a one-dimensional chain. We calculate the extinction cross-section behaviour for different relative orientations of the atomic chain and driving field polarisation, investigating how this changes with N. For $N > 2$, the eigenmodes are not all orthogonal, resulting in interferences in the cross-section lineshapes. We also investigate the eigenvector and eigenvalue behaviour of these chains, showing the dependence as $N \to \infty$.

6.2 Effective two-level atom

Let us work in the xyz polarisation basis. Considering the form of the coupling described by the matrix M in Eq. (3.5.2), if the atoms are separated along one of the x, y, or z axes, then the only nonzero off-diagonal elements of M are G_{ij}^{xx}, G_{ij}^{yy}, and G_{ij}^{zz} [see Eq. (4.2.6)]. This means that there is no coupling between different polarisations. The polarisation of the dipoles will therefore be equal to the polarisation of the driving field. If this driving field is linearly polarised in y, then the dipoles will also be polarised in y and, as was

discussed in Sec. 3.2.2, this means we can treat the atoms as effective two-level systems. This both speeds up the computation and avoids the issue of degenerate eigenmodes.

Note, however, that if the vector separating the atoms is in some general direction (x, y, z), then the different polarisations can couple through nonzero $G_{ij}^{\alpha\beta}$ terms resulting in potential dipole polarisations in any direction. For this reason, we shall limit our discussion to atoms only separated in x, y, or z.

6.3 Extinction cross-section and mode behaviour, 3 atoms

In Sec. 5.2.3 we calculated the extinction cross-section for a pair of two-level atoms. For the case where the driving field was identical across the two atoms, the only mode to be driven was the mode in which both dipoles oscillated in phase with one another. If the dipoles were separated downstream of one another such that the driving field differed in phase by e^{ikz}, then in addition to this *in-phase* mode $\vec{\mathbf{m}}_+$, we could also drive an *out-of-phase* mode $\vec{\mathbf{m}}_-$ where the two dipoles oscillated π out of phase with each other. The total extinction lineshape was simply the sum of the two different mode contributions. We will now see how this behaviour changes with the addition of a third atom.

6.3.1 Symmetric modes

In Fig. 6.1, we plot the extinction cross-section, σ_{ext} (4.6.1), as a function of detuning of the driving field, Δ, and nearest-neighbour atom spacing, a, for three atoms regularly spaced along x (a), y (b), and z (c). The addition of a third atom introduces several changes to the mode behaviour compared with the two atom case (see Fig. 5.3). Firstly, there are now more eigenmodes (the number of modes scales with atom number N). As in the two atom case, when the atoms are separated in x or y (meaning each atom experiences the same driving field), there is one dominant mode, $\vec{\mathbf{m}}_1$, which we label with yellow squares.[a] In addition there is now also a much weaker mode which we label with blue circles ($\vec{\mathbf{m}}_2$).

[a] By *dominant* we mean that the magnitude or *population* of the expansion coefficient of mode 1, $|b_1|^2$ (3.5.16), is much greater than that of any other mode.

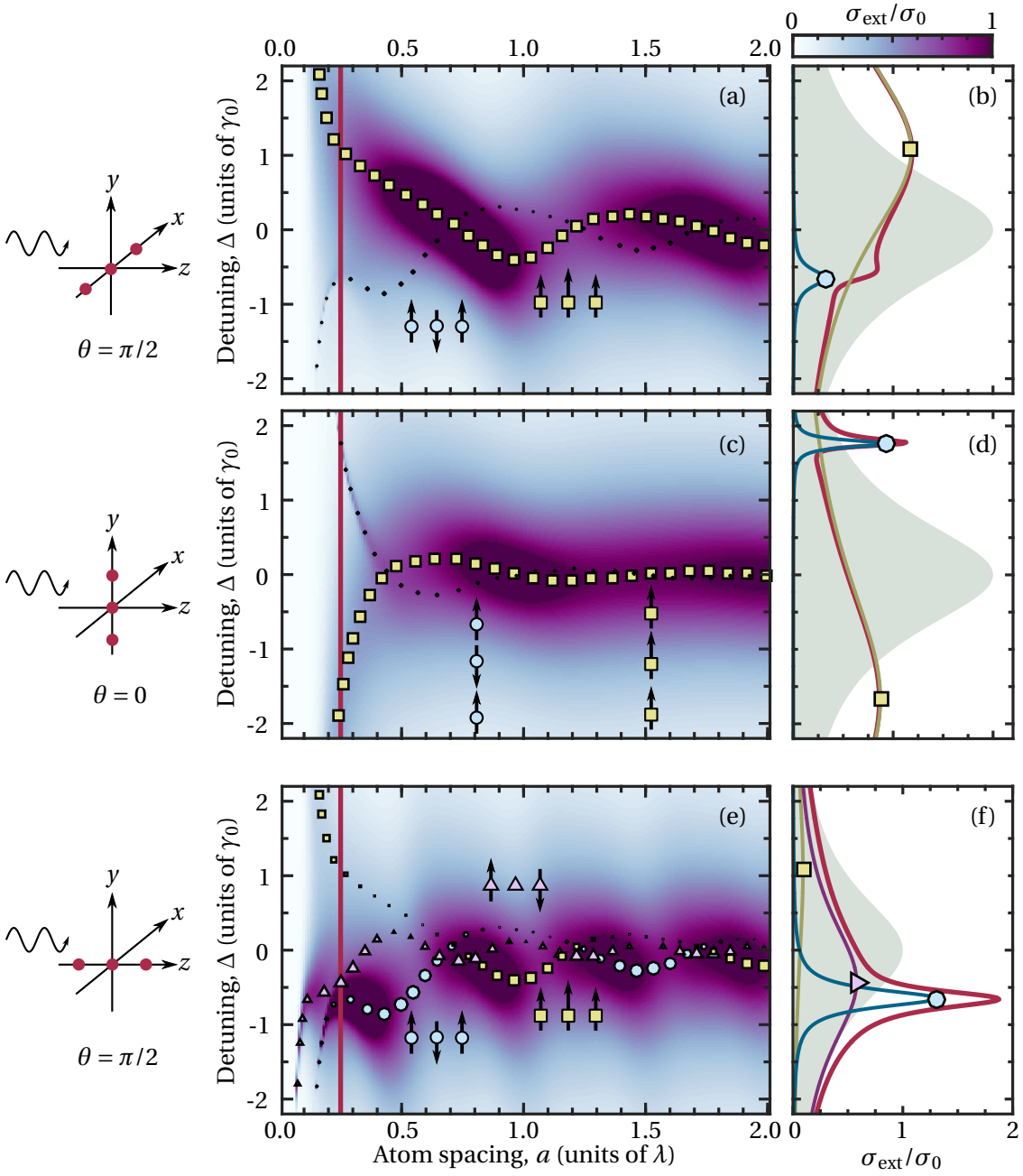

Figure 6.1: (a,c,e) Extinction cross-section σ_{ext} of a uniform plane wave incident electric field $\mathbf{E}(\mathbf{r}) = E_0\hat{\mathbf{y}}e^{ikz}$ due to three 2-level atoms, as a function of atom spacing a and detuning of the driving field Δ. The driving field is linearly polarised in y and propagating in the $+z$ direction. (b,d,f) Total cross-section (red line) and individual mode cross-sections $|b_p|^2\text{Im}(\alpha_p)$, as a function of detuning for $a = \lambda/4$. The grey background shows the single non-interacting atom lineshape. The yellow squares, blue circles, and pink triangles indicate the mode shifts Δ_p, and for (a,c,e) they are proportional in size to the mode amplitudes $|b_p|^2$. The atoms are aligned in a chain in x (a,b), y (c,d), and z (e,f).

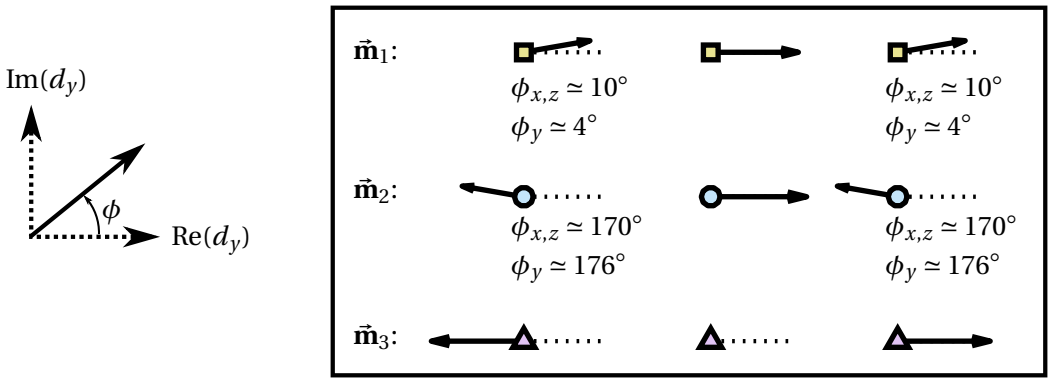

Figure 6.2: Phasors of the three dominant modes from Fig. 6.1, $\{\vec{\mathbf{m}}_1, \vec{\mathbf{m}}_2, \vec{\mathbf{m}}_3\}$. Each mode is polarised in y. The magnitude of each phasor is proportional to the eigenvector magnitude for that dipole.

In Fig. 6.2 we plot the phasors of the dipole vectors in each eigenmode. The polarisation of each dipole is linear in y. But for a small phase difference,[b] the dipoles in mode $\vec{\mathbf{m}}_1$ all oscillate in phase with one another. In contrast to this, the dipoles in mode $\vec{\mathbf{m}}_2$ are almost π out of phase with their nearest neighbours. However, the mode is still symmetric about the central atom, and so it has nonzero overlap with the (uniform) driving field.

6.3.2 Anti-symmetric mode

When the atoms are aligned along the z axis [Fig. 6.1(c)], because of the propagation phase of the driving field e^{ikz}, the driving field can now have nonzero overlap with a third eigenmode $\vec{\mathbf{m}}_3$, which we label with pink triangles. In Fig. 6.2, we see that this mode has anti-symmetry about the central atom; the atoms on either end are equal in magnitude and exactly π out of phase with each other, whilst the central atom has zero amplitude. The anti-symmetry of this mode is similar to the $\vec{\mathbf{m}}_-$ mode in the two atom system (Fig. 5.3).[c] Unlike in Fig. 6.1(a) or (b), the relative population of each mode $|b_p|^2$ in Fig. 6.1(c) changes significantly with changing atomic spacing due to the changing phase of the driving field

[b] For atoms separated in x and z, the phase difference between neighbouring atoms is $\cos\varphi_{i,i+1} \simeq 10°$; for atoms separated in y, $\cos\varphi_{i,i+1} \simeq 4°$.

[c] In Fig. 5.3 $\vec{\mathbf{m}}_-$ is labeled with blue circles because it also has similarities with the mode $\vec{\mathbf{m}}_2$ in that each atom is π out of phase with its nearest neighbours.

experienced by each atom.

6.3.3 Mode interferences and asymmetric lineshapes

In the cross-section lineshapes in Fig. 6.1(b,d), we can see that where the two modes $\vec{\mathbf{m}}_1$ and $\vec{\mathbf{m}}_2$ overlap, the total cross-section (red line) is not simply the sum of the two mode contributions, as was the case for two atoms, but rather now also depends on an interference between the two modes. To look at this in more detail, in Fig. 6.3 we again plot the extinction cross-section lineshapes for three atoms, separated now by $a = 0.2\lambda$ along either the x (a,c) or z (b,d) axes. As in Fig. 6.1(b,f), we plot both the total cross-section as well as the contributions from each individual mode (4.6.5),[d]

$$\sigma_p = \frac{k}{\varepsilon_0 |E_0|^2} |b_p|^2 \, \mathrm{Im}(\alpha_p). \tag{6.3.1}$$

For the atoms separated in x in Fig. 6.3(a,c), mode $\vec{\mathbf{m}}_1$ is superradiant and blue shifted. As already noted, it is also much stronger in amplitude than $\vec{\mathbf{m}}_2$ ($|b_1|^2/|b_2|^2 \simeq 44$), which is subradiant and red shifted. The difference in amplitude is not the same as the difference in the maxima of σ_1 and σ_2 because $\vec{\mathbf{m}}_2$ has a much narrower linewidth than $\vec{\mathbf{m}}_1$, which increases its relative resonant cross-section (see Sec. 4.6.3). The overall cross-section (red line) closely follows the broad stronger mode $\vec{\mathbf{m}}_1$ over most detunings. However, when it passes through resonance with the narrow weaker mode, it becomes distorted. The grey line in Fig. 6.3(c) shows that the total cross-section is not simply the sum of the two modes, but rather it also includes an interference term [black solid line in Fig. 6.3(c)],

$$\sigma_{pq} = \frac{k}{\varepsilon_0 |E_0|^2} \mathrm{Im}\left[\alpha_q \, (b_p^* b_q) \, (\vec{\mathbf{m}}_p^\dagger \cdot \vec{\mathbf{m}}_q)\right]. \tag{6.3.2}$$

6.3.4 Fano resonance

The overall resulting lineshape is similar to a Fano resonance [103]. A Fano resonance describes a scattering event relating to the transition from a discrete quantum state to a

[d] Assuming the eigenvectors are normalised $\vec{\mathbf{m}}_p^\dagger \cdot \vec{\mathbf{m}}_p = 1$, using the inner product notation defined in (3.5.11).

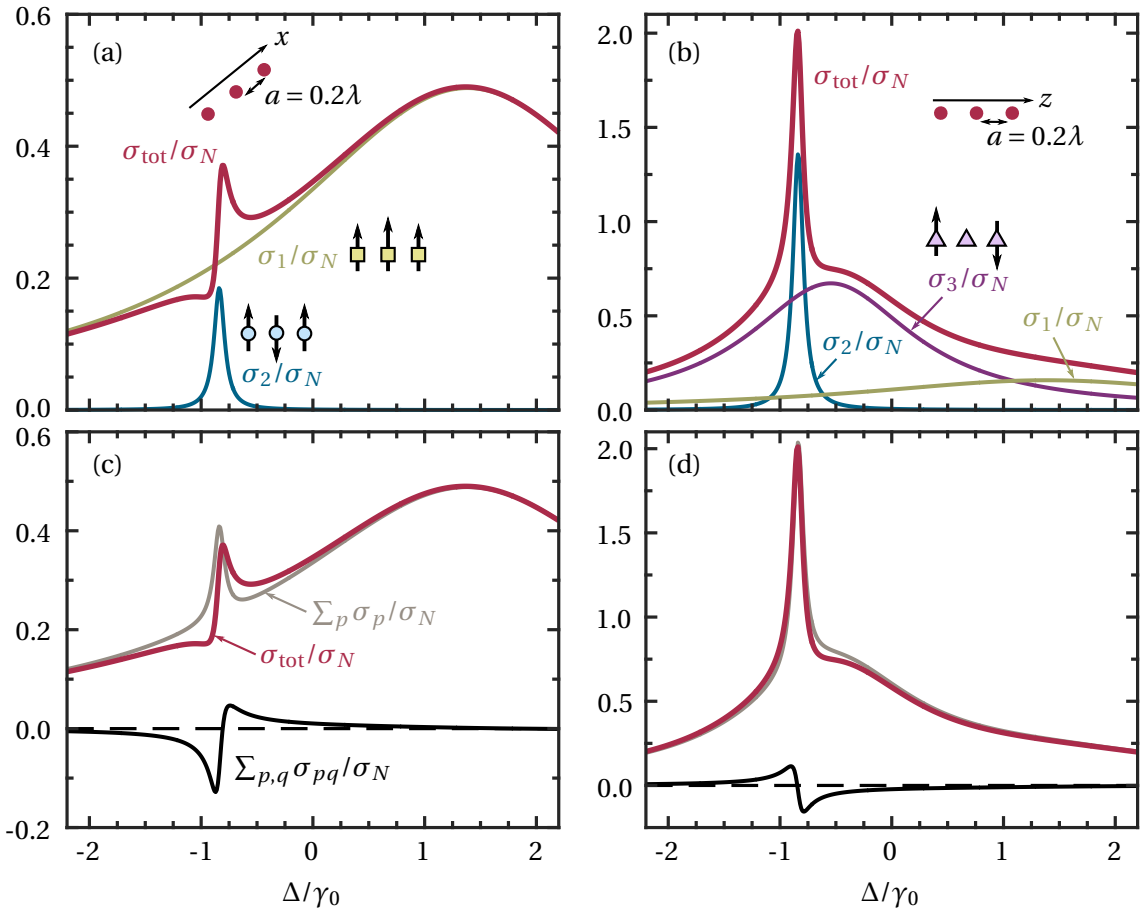

Figure 6.3: Extinction cross-section (red lines) due to three atoms arranged in a chain along x (a,c) or z (b,d), driven by a uniform electric field propagating in z and linearly polarised in y. (a,b) The total extinction cross-section σ_{tot} is compared with the single-mode cross-sections due to the two dominant modes, σ_1 (olive) and σ_2 (blue). (c,d) The sum of the single-mode cross-sections (grey) and the interference terms (black). The spacing between neighbouring atoms is $a = 0.2\lambda$.

quantum state within a continuum of states. This can either happen directly, or via an intermediate discrete quantum state, the energy of which sits within the energy manifold of the continuum of states. The two possible pathways interfere, resulting in the overall scattering lineshape. However, the sign of the interference changes rapidly by π as the energy of the scattered photon goes through resonance with the discrete intermediate state, meaning if the photon energy is less than the resonance energy the pathways interfere destructively, whilst a photon energy greater than the resonance energy results in constructive interference. This produces a characteristic asymmetric lineshape around this resonance, described by

$$\sigma(\epsilon) = \sigma_a \frac{(q+\epsilon)^2}{(1+\epsilon^2)} + \sigma_b, \tag{6.3.3}$$

where $\epsilon = (E - E_a)/\gamma$, E is the photon energy, E_a is the energy of state a, the index q characterises the line profile, and σ_a and σ_b are the values of the cross-sections of modes a and b at $E = E_a$ respectively.

Fano originally applied his model to the ionisation spectrum of He, although this type of interference resonance appears in many areas of physics. There has been particular recent interest in the field of nanoplasmonics and metamaterials [42, 43, 56, 104] as well as the interaction between plasmonic and atomic resonances [105]. In these systems, the interference might be between different mode resonances of the same emitter [56, 104], or between collective states of an ensemble of emitters [42, 43] (as is the case with our coupled atomic ensembles). The steep dispersion of the line Fano resonance could have value in many applications including lasers, sensors, switching, and non-linear and slow-light devices.

As we already know, our atomic ensembles contain many cooperative eigenmodes $\vec{\mathbf{m}}_p$. The transition from a discrete state to a continuum of states is now equivalently a transition from the ground state to a broad superradiant state, which on the scale of some of the narrower subradiant states, appears quasi-continuous. Because the different eigenvectors are non-orthogonal, we can get to this superradiant state either directly or via another state [43]. Again, the two possible pathways interfere, resulting in an asymmetric resonance lineshape, like a Fano resonance. The expressions in (6.3.1) and (6.3.2) do not exactly match the Fano resonance formula (6.3.3) from [103], although the nature of the interference is very similar.

Not all the modes result in interferences however. For the atoms separated along z in Fig. 6.3(b,d), mode $\vec{\mathbf{m}}_2$ now has the largest amplitude of the three modes $\vec{\mathbf{m}}_{1,2,3}$, with $|b_2|^2/|b_1|^2 \simeq 2$ and $|b_2|^2/|b_3|^2 \simeq 8$. We might expect a very strong interference lineshape because of this highly narrow mode overlapping two very broad modes. However, $\vec{\mathbf{m}}_3$ is orthogonal to modes $\vec{\mathbf{m}}_1$ and $\vec{\mathbf{m}}_2$ and so the only mode interference occurs between modes $\vec{\mathbf{m}}_1$ and $\vec{\mathbf{m}}_2$. Since σ_1 is relatively weak at the point of overlap with $\vec{\mathbf{m}}_2$ the resulting interference is very weak, and the overall lineshape is effectively just the sum of the individual modes.

6.4 N atom chain — extinction cross-section

6.4.1 Increasing atom number

Introducing a third atom modifies the system behaviour by increasing the number of eigenmodes and allowing these eigenmodes to interfere with one another, resulting in asymmetric interferences in the cross-section lineshapes. We shall now investigate the behaviour of the eigenvectors and eigenvalues for even larger atom numbers. Whilst the relative complexity increases with the number of atoms, we shall see that certain patterns and structures begin to emerge.

In Fig. 6.4 we plot the extinction cross-section as a function of detuning and atom spacing for $N \in \{3, 10, 50\}$ atoms equally separated along the x axis. In each case, the eigenmode behaviour is dominated by a single eigenmode, $\vec{\mathbf{m}}_1$, which we label with yellow squares. As N increases, the number of additional weaker modes which are present increases also, shown by the small blue circles. Some of these modes are very narrow [see, e.g., the insets of Fig. 6.4(d,f)], resulting in weak interferences in the total cross-section, as we saw in $N = 3$. Some of the weak modes are also very broad however and so contribute significantly to the total cross-section. As N increases, the number of these weak modes increases, however the effect of the narrow modes has less and less effect on the overall lineshape, which can be approximated well as the sum of a few of the broader modes.

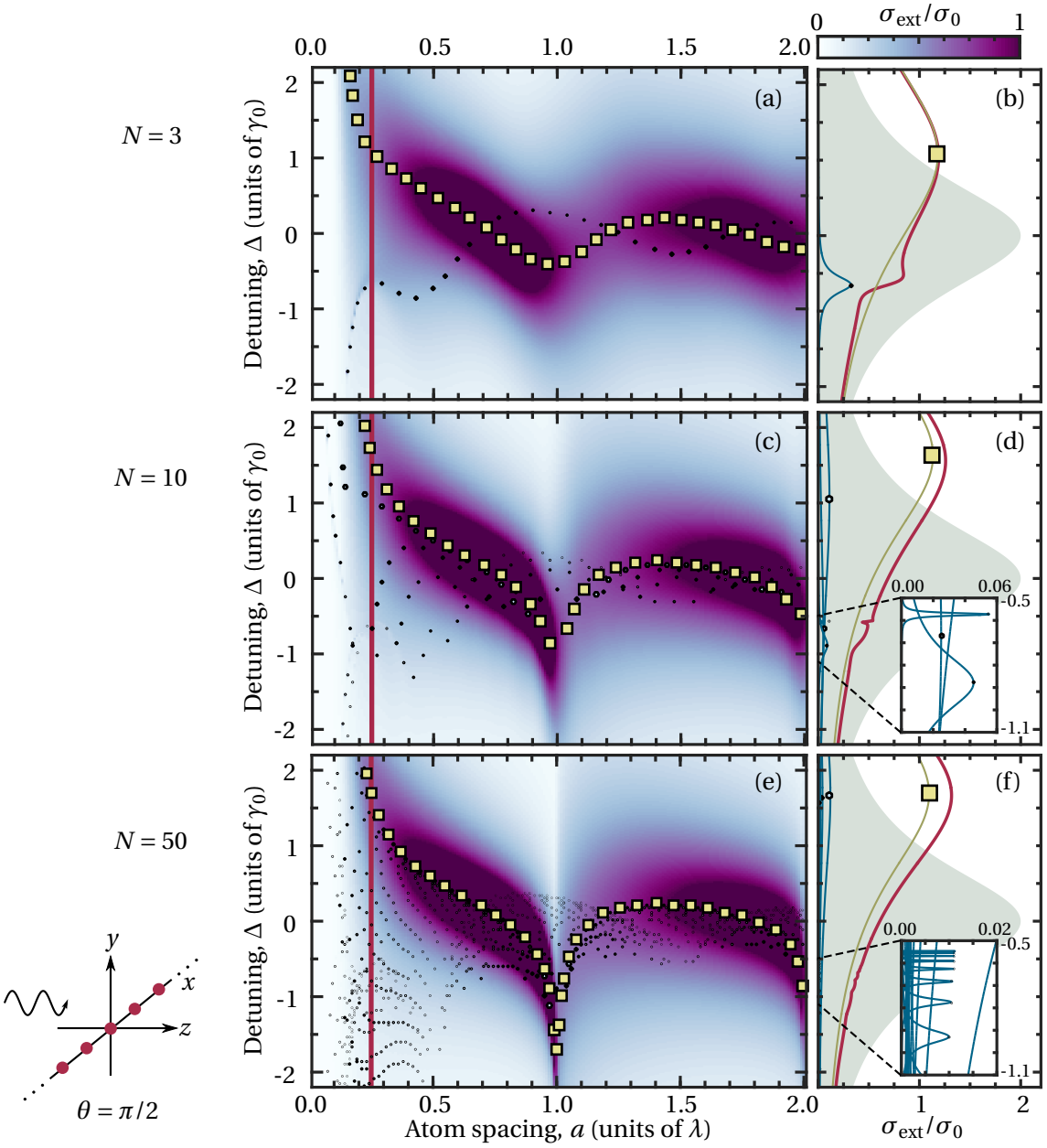

Figure 6.4: (a,c,e) Extinction cross-section σ_{ext} of a uniform plane wave electric field $\mathbf{E}(\mathbf{r}) = E_0\hat{\mathbf{y}}e^{ikz}$ due to a chain of $N = 3$ (a,b), $N = 10$ (c,d) and $N = 50$ (e,f) 2-level atoms separated along x as a function of atom spacing a and detuning of the driving field Δ. (b,d,f) Total cross-section (red line) and individual mode cross-sections $|b_p|^2\text{Im}(\alpha_p)$ (blue and yellow lines), as a function of detuning for $a = \lambda/4$. The grey background shows the single non-interacting atom lineshape. The yellow squares and blue circles indicate the mode shifts Δ_p are proportional in size to the mode amplitudes $|b_p|^2$. The insets in (d,f) highlight some of the weaker, narrower eigenmodes.

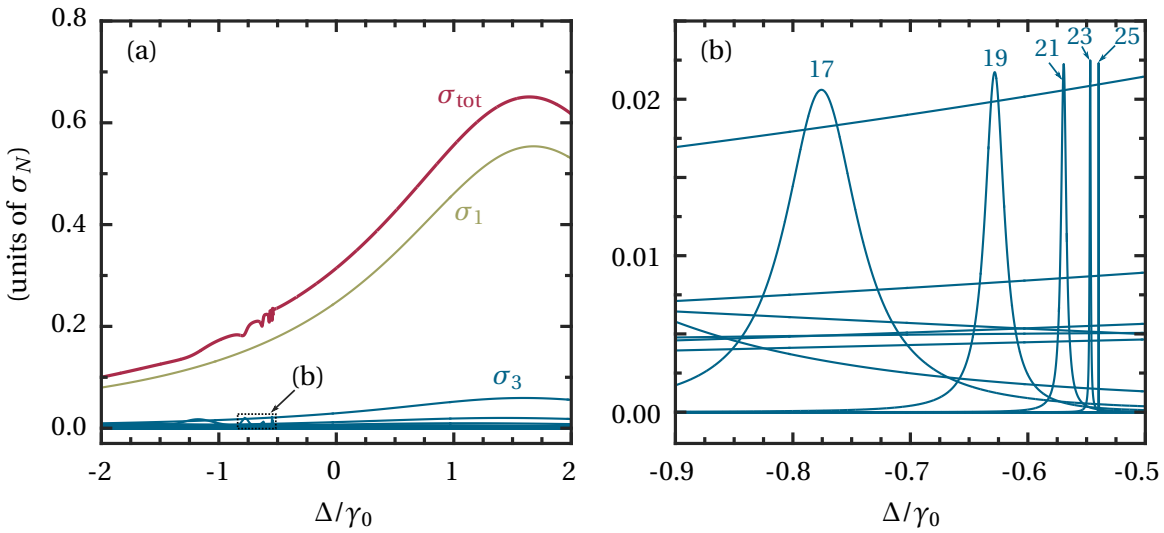

Figure 6.5: Individual mode contributions σ_p to the extinction cross-section σ_{tot} of a chain of $N = 25$ atoms separated in x with nearest-neighbour spacing $a = 0.25\lambda$. The modes are numbered as in Fig. 6.6 and the driving field is the same as in Fig. 6.4.

6.4.2 Eigenvalues

In Fig. 6.5, we examine more closely these different modes and their contribution to the overall lineshapes (for $N = 25$). Looking at the narrow modes in Fig. 6.5(b), it appears that these particular modes are following some pattern of shifting from red towards blue detuning and decreasing in linewidth. By plotting the eigenvalues (shifts and widths) for all 25 modes, irrespective of their overlap with the driving field, we see in Fig. 6.6 that indeed the modes are following some curved trajectory around ($\Delta_p = 0, \gamma_p = 0$). A similar behaviour has recently been shown in [106]. By numbering the modes from 1 to 25 in order of their distance around the loop, starting with the dominant (yellow squares) mode $\vec{\mathbf{m}}_1$, we see from Fig. 6.5 only the odd numbered modes have been coupled into for this particular configuration. Let us therefore look at the eigenvectors associated with these modes to determine if there is some pattern or structure related to this ordering.

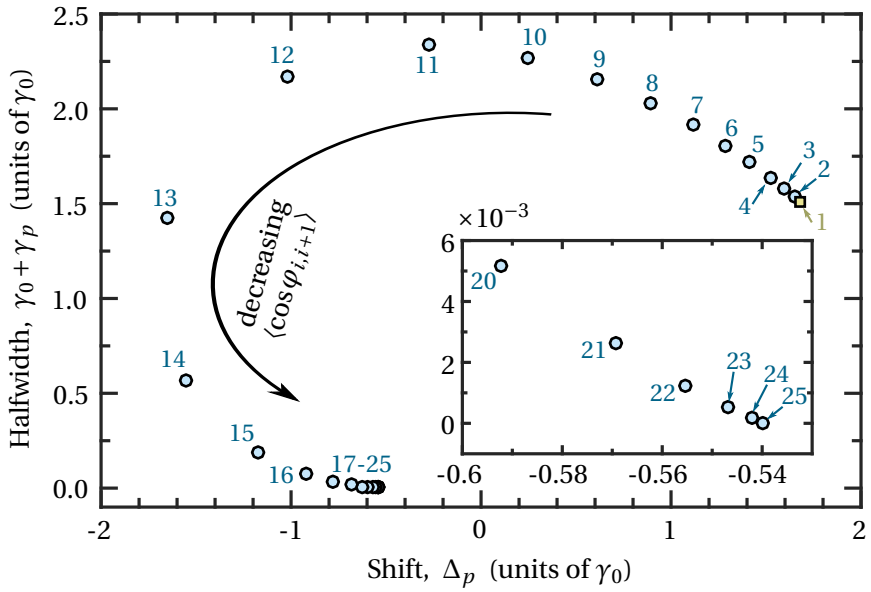

Figure 6.6: Mode eigenvalues for the eigenmodes of a chain of $N = 25$ atoms separated in x or z ($\theta = \pi/2$) with nearest-neighbour spacing $a = 0.25\lambda$. The modes are numbered according to their position around the spiral. The correlation function $\langle\cos\varphi_{i,i+1}\rangle$ is defined in Eq. (6.4.1).

6.4.3 Eigenvectors

In Fig. 6.7 we plot the phasors of the 25 atomic dipoles for a selection of the eigenvectors from Figs. 6.4, 6.5, and 6.6. Each dipole is polarised in y. As in the 3 atom system in Fig. 6.2, the dominant mode that we have called $\vec{\mathbf{m}}_1$ is the mode in which all dipoles oscillate in phase with one another. In addition to this, the amplitudes of the vectors peak in the middle of the chain and disappear off towards either end. If the envelope describing these phasors were the first harmonic of the chain, then the next two modes $\vec{\mathbf{m}}_2$ and $\vec{\mathbf{m}}_3$ appear to be the next two harmonics, with the number of antinodes increasing by one with each eigenmode. Working from the other extreme however, $\vec{\mathbf{m}}_{25}$ has a similar amplitude envelope to $\vec{\mathbf{m}}_1$, but each dipole is now approximately π out of phase with its neighbours. Similarly, the amplitude envelopes of $\vec{\mathbf{m}}_{24}$ and $\vec{\mathbf{m}}_{23}$ could, like $\vec{\mathbf{m}}_2$ and $\vec{\mathbf{m}}_3$, be described by the second and third harmonics, although with alternating signs between neighbouring dipoles.

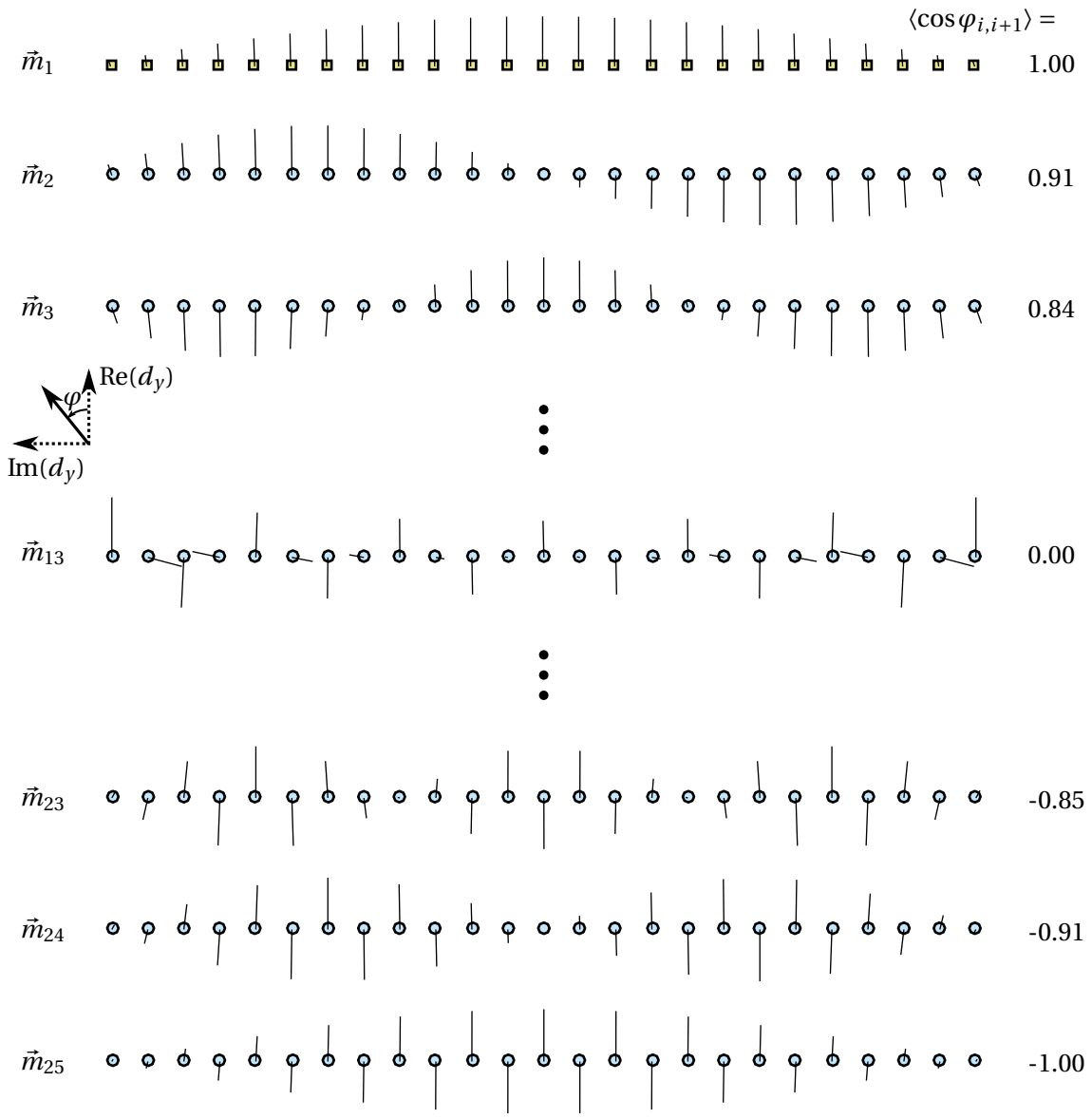

Figure 6.7: Phasors of each dipole in a chain of $N = 25$ atoms for a selection of eigenmodes. The atoms are separated in x or z ($\theta = \pi/2$) with nearest-neighbour spacing $a = 0.25\lambda$. The nearest-neighbour phase correlation function $\langle \cos\varphi_{i,i+1} \rangle$ decreases with increasing mode index. The magnitude of each phasor is proportional to the eigenvector magnitude for that dipole.

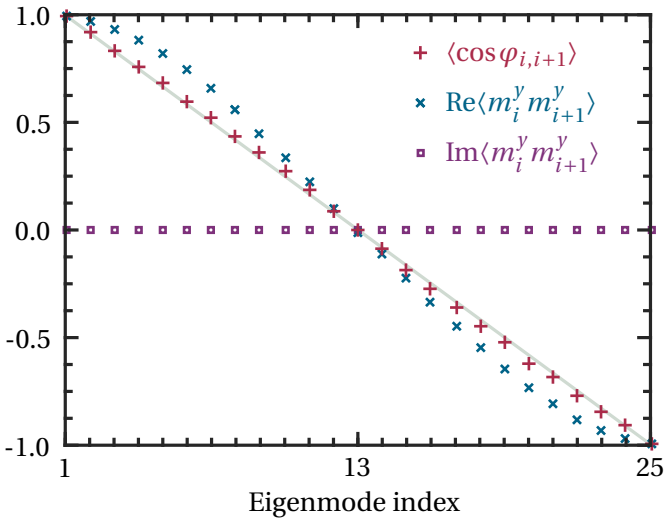

Figure 6.8: Correlation functions between phasors for a $N = 25$ atom chain separated along x or z ($\theta = \pi/2$).

The difference between even and odd numbered modes is that odd modes are symmetric about the central atom whereas even modes are antisymmetric about the central atom. In Figs. 6.4 and 6.5 the driving field is uniform in phase and amplitude across the atoms and so only couples to the symmetric (odd numbered) modes.

For each atom i, the eigenvector $\vec{\mathbf{m}}_p$ has three vector components, two of which we can ignore for this atomic configuration, leaving just the y polarisation component, $m_{p,i}^y = |m_{p,i}^y| e^{i\varphi_{p,i}}$. Fig. 6.7 seems to suggest that with increasing mode index, the phase between neighbouring dipoles increases. We can quantify this difference by defining the correlation function[e]

$$\langle\cos\varphi_{i,i+1}\rangle = \frac{1}{N-1}\sum_{i=1}^{N-1}\cos(\varphi_i - \varphi_{i+1}). \tag{6.4.1}$$

This is a measure of the phase difference between neighbouring dipoles. In addition, we

[e]We drop the p index for brevity.

can take into account the dipole amplitudes by defining a second correlation function

$$\langle m_i^y m_{i+1}^y \rangle = \frac{1}{N-1} \sum_{i=1}^{N-1} \frac{m_i^y m_{i+1}^y}{|\alpha_0 E_0|^2} = \frac{1}{N-1} \sum_{i=1}^{N-1} \frac{|m_i^y||m_{i+1}^y|}{|\alpha_0 E_0|^2} e^{i(\phi_i - \phi_{i+1})}, \tag{6.4.2}$$

These two correlation functions are plotted in Fig. 6.8 as a function of mode index for the atom chain in Figs. 6.4–6.7. Both $\langle \cos\varphi_{i,i+1} \rangle$ and $\mathrm{Re}\langle m_i^y m_{i+1}^y \rangle$ decrease from 1 to -1 as the mode index increases from 1 to 25. This quantifies what we had previously observed: as the eigenmode index increases, the degree of phase difference between neighbouring dipoles increases. $\mathrm{Im}\langle m_i^y m_{i+1}^y \rangle$ is zero for all modes. If the atoms are separated in y ($\theta = 0$) rather than x or z ($\theta = \pi/2$), then the difference in $\langle \cos\varphi_{i,i+1} \rangle$ compared with Fig. 6.8 is only a few percent. The difference now between symmetric (odd numbered) and antisymmetric (even numbered) modes is that if we sum the phase differences $\varphi_i - \varphi_{i+1}$ for all pairs of nearest neighbours in the chain, the total sum for the symmetric (odd numbered) modes is an integer multiple of 2π whereas the sum for the antisymmetric (even numbers) modes is $(2n+1)\pi$, where n is an integer.

6.4.4 Eigenvalue dependence on atom spacing

In Fig. 6.4 we saw that the eigenvalues of the modes change as the atom spacing increases. In Fig. 6.9 we plot the eigenvalues for all the eigenmodes in an atomic chain with $N = 25$ and oriented with $\theta = \pi/2$ (e.g., separated in x or z) or $\theta = 0$ (e.g., separated in y).

For small spacings [$a \to 0$, see insets in Fig. 6.9(c,d)], for both orientations there is one strongly superradiant mode with decay rate $\gamma_0 + \gamma_p \simeq 22\gamma_0$, one other superradiant mode with $\gamma_0 + \gamma_p \simeq 2\gamma_0$, and the remaining modes are all subradiant ($\gamma_0 + \gamma_p < \gamma_0$). Notice that this is slightly less than the small sample decay rate $N\gamma_0$ predicted by Dicke [20]. The reason for this discrepancy is that the superradiant mode $\vec{\mathbf{m}}_1$ in Fig. 6.7 is only an approximation to the fully symmetric mode considered by Dicke. In the Dicke model, the enhanced superradiant decay rate is a result of the total dipole moment of the system being N times larger. However, in Fig. 6.7, the dipole moments are not all equal and the

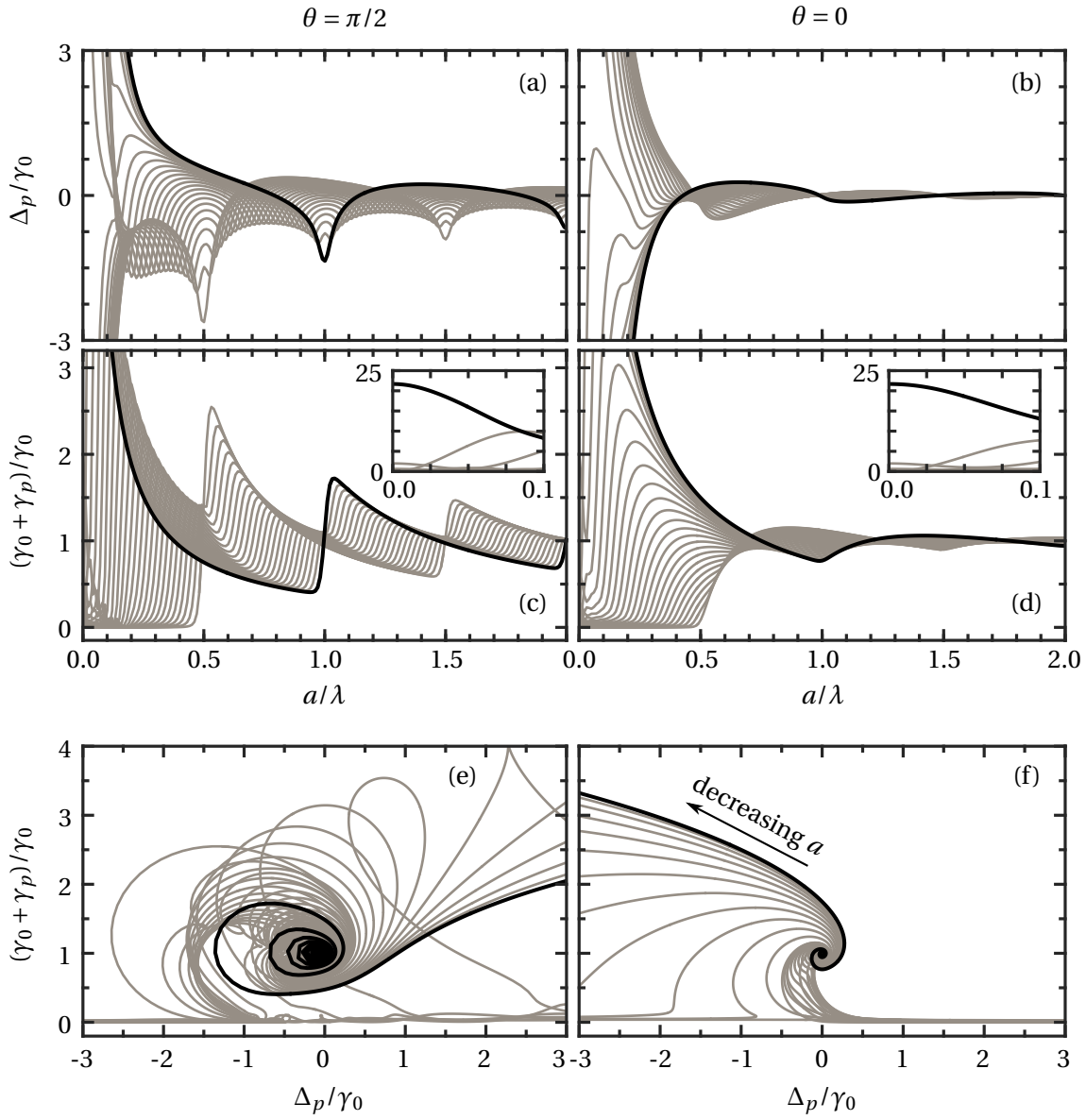

Figure 6.9: Eigenvalue dependence on atomic spacing for a chain of $N = 25$ atoms. The angle between the atomic separation and the polarisation vector is $\theta = \pi/2$ (a,c,e) and $\theta = 0$ (b,d,f). In (a–d) the eigenvalue shifts (a,b) and decay rates (c,d) are plotted separately as a function of atom spacing. In (e,f) the same eigenvalues are plotted together, starting at the centre with large atomic spacing and spiralling out with decreasing atomic spacing. Mode $\vec{\mathbf{m}}_1$ is highlighted in black.

sum of the dipoles is only around 23 ($N = 25$) times larger than a single dipole. To exactly reproduce the Dicke result, we would either need $N = 2$ or $N = \infty$, both of which would produce a *fully symmetric* eigenvector with every dipole equal and in phase.

Despite the seeming increase in complexity of the eigenmode behaviour due to increasing mode number, there are clear patterns which begin to emerge. For example, in Fig. 6.9(a,c) there are strong resonances in both the shifts and decay rates of the eigenmodes when ka/π is an integer (when a is an integer multiple of $\lambda/2$). Furthermore, the spiral behaviour of the eigenvalue plots in Fig. 6.9(e,f) is strongly reminiscent of the spherical Bessel functions that appear in the dipole–dipole interaction G (Sec. 4.2). By highlighting mode $\vec{\mathbf{m}}_1$ (black lines), we also see that, as in Fig. 6.6, the eigenvalues of this mode place it at the edge of the set of eigenvalues.

Similar phase space plots as in Fig. 6.9(e,f) have been calculated in [92, 107] for random ensembles. For random ensembles, the eigenvalues typically fill some solid area of eigenspace, with two or more branches of eigenmodes exciting the areas. The regular arrays here have much cleaner eigenmode behaviours, making it easier to compare how they all behave.

6.4.5 N-dependence of eigenvalues

In Fig. 6.10 we plot the eigenvalues for chains with increasing atom numbers with a fixed lattice spacing $a = 0.25\lambda$. We see that as the atom number increases, the magnitude of the eigenvalues tends to grow also. We can see this very clearly by plotting the eigenvalues of individual eigenmodes as a function of both atom number and lattice spacing.

In Fig. 6.11(a,c) we plot the eigenvalues for the maximally out-of-phase mode, $\vec{\mathbf{m}}_N$, for atoms separated in x, and in (b,d) we plot the eigenvalues for the maximally in-phase mode, $\vec{\mathbf{m}}_1$, for atoms separated in y. Firstly we see that as we add more atoms, the resonances in the eigenvalues become more extreme, with near-discontinuities appearing in Fig. 6.11(c). In addition to this however, ignoring the $a \to 0$ limit for the time-being, as $N \to \infty$ the eigenvalues appear to reach some limiting behaviour.

This limiting behaviour can be described by the modeling the infinite atom chain as a

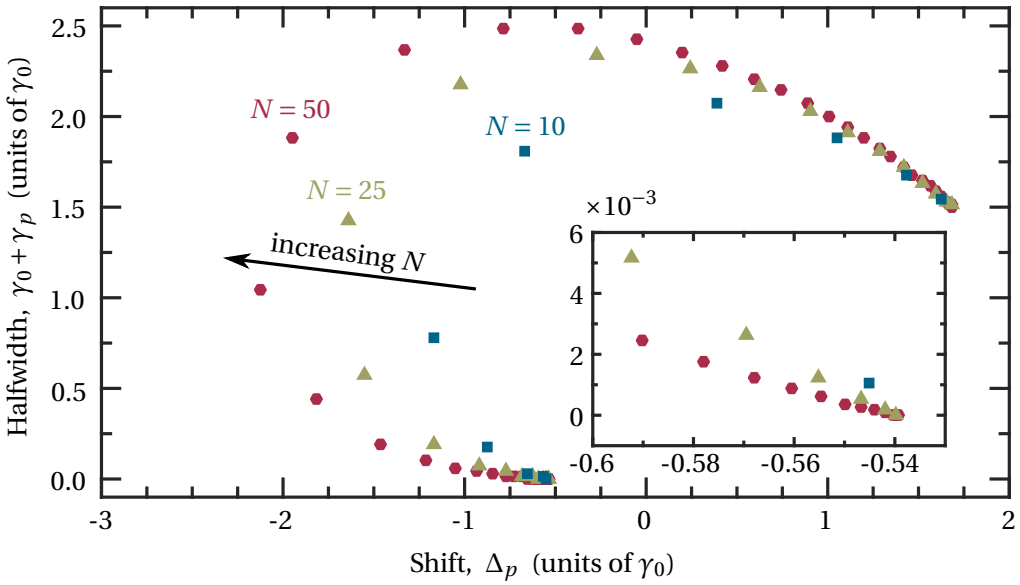

Figure 6.10: Eigenvalues for the eigenmodes of a chain of atoms separated in x or z ($\theta = \pi/2$) with nearest-neighbour spacing $a = 0.25\lambda$. The different markers correspond to atom numbers $N = 10$ (blue squares), $N = 25$ (olive triangles), and $N = 50$ (red circles).

single atom between two mirrors. An electric dipole near a conductive surface induces an effective *image* dipole in the surface (Chap. 2 [73]). This image dipole behaves in such a way as to cancel the electric field across the conductive surface. This is equivalent to if there were a real dipole behind the mirror, an equal distance from the mirror as the real dipole. If the real dipole is polarised parallel to the plane of the mirror, then the image dipole will be anti-aligned with the real dipole [diagram in Fig. 6.11(c)]. If the real dipole is polarised perpendicular to the plane of the mirror, then the image dipole will be aligned with the real dipole [diagram in Fig. 6.11(d)]. This is the reason why we chose the mode $\vec{\mathbf{m}}_N$ for the dipoles separated perpendicular to the polarisation axis and the mode $\vec{\mathbf{m}}_1$ for the dipoles separated parallel to the polarisation axis.

If there are two mirrors, one on either side of the dipole, then this results in an effective infinite chain of image dipoles with which the real dipole interacts. The spontaneous decay of a real dipole between two mirrors was calculated in [108]. For a dipole polarised

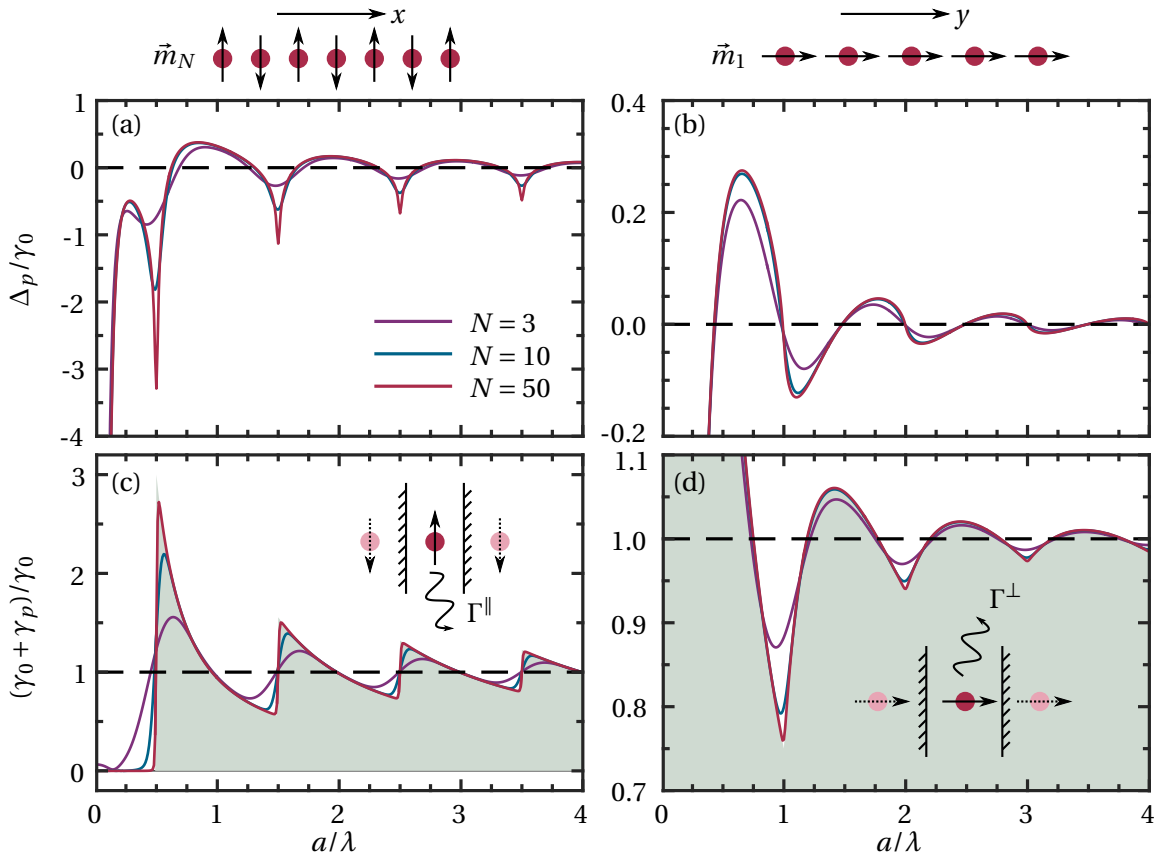

Figure 6.11: (a,b) Cooperative shifts and (c,d) decay rates for the main in-phase mode for a chain of $N \in \{3, 10, 50\}$ atoms. (a,c) Atoms separated in x in mode $\vec{\mathbf{m}}_N$. (b,d) Atoms separated in y in mode $\vec{\mathbf{m}}_1$.

parallel to the mirror planes, the decay rate is

$$\frac{\Gamma^{\parallel}}{\Gamma_0} = \frac{3\pi}{2k_0L}\sum_{n=1}^{k_0L/\pi}\left(1+\frac{n^2\pi^2}{k_0^2L^2}\right)\sin^2\left(\frac{n\pi}{2}\right), \tag{6.4.3}$$

where the dipole is assumed to be positioned midway between the two mirrors which are separated by distance L. For a dipole polarised perpendicular to the mirror planes, the decay rate is

$$\frac{\Gamma^{\perp}}{\Gamma_0} = \frac{3\pi}{k_0L}\left[\frac{1}{2}+\sum_{n=1}^{k_0L/\pi}\left(1-\frac{n^2\pi^2}{k_0^2L^2}\right)\cos^2\left(\frac{n\pi}{2}\right)\right]. \tag{6.4.4}$$

Notice in both expressions the sum over cavity modes $n < k_0 L/\pi$. These cavity modes originate from the radiation term of the dipole–dipole interaction in $\mathsf{G}(R_{ij})$ (4.2.6), $\mathrm{e}^{\mathrm{i}kr}$. If $kL = n\pi$ where $n \in \mathbb{Z}$, then $\mathrm{e}^{\mathrm{i}kL} = (-1)^n$. The dipoles in the mode $\vec{\mathbf{m}}_N$ in Fig. 6.11(a,c) are π out of phase with their neighbours and so the interaction between them hits a resonance when $\mathrm{e}^{\mathrm{i}kL} = -1$, i.e. when $(2n+1) \in \mathbb{Z}$. For $kL < \pi$, no modes are allowed between the mirrors and so in the infinite limit, there is no decay (subradiance). For mode $\vec{\mathbf{m}}_1$ the dipoles are in phase and the resonances are at integer multiples of $2kL/\pi$, i.e. when $\mathrm{e}^{\mathrm{i}kL} = 1$. Unlike the previous case, when $kL \ll \pi$ the mode condition is still satisfied and so the atom decays very rapidly (superradiant).

In the $N \to \infty$ limit, we can use a mean field approach to calculate the eigenvalues. Assuming that the dipoles are all equal in magnitude and either all aligned as in $\vec{\mathbf{m}}_1$ or antialigned as in $\vec{\mathbf{m}}_N$, we can take $\mathbf{d}_i \equiv (\pm 1)^j \mathbf{d}$ out of the sum over atoms in Eq. (3.4.7), and therefore calculate (numerically) the eigenvalues as just the sum of the coupling matrix $\sum_{j=-\infty}^{\infty} \mathsf{G}_{1j}$ [59], obtaining the same results as (6.4.4) and (6.4.3). In the $a \to 0$ limit, the infinite atom chain in the in-phase mode $\vec{\mathbf{m}}_1$ is equivalent to the Dicke model for which all atoms are in a symmetric state and the decay rate is enhanced N-fold (see discussion in Sec. 6.4.4).

6.4.6 Infinite limit and reduction in complexity

Initially, it appeared that increasing the number of atoms simply increased the complexity of the dipolar behaviour. However, in Fig. 6.4 we saw the contribution from most of the modes is increasingly weak, leaving just a few remaining significant modes and one dominant mode which, for particular configurations, behaves just the same as a single atom between two mirrors (Fig. 6.11). In the next Part, we will consider two-dimensional arrays of atoms, thus increasing the complexity of the mode behaviour again. However, the concepts we have come across in investigating one-dimensional chains will prove useful in our understanding of these more complex systems.

Chapter Summary

- We have calculated the extinction cross-section for a range of different atom numbers arranged in one-dimensional arrays
- The number of eigenmodes scales with atom number N
- Non-orthogonality between eigenvectors results in interference lineshapes in the extinction, similar to Fano resonances
- The eigenmodes can be characterised by correlation functions measuring the average phase difference between neighbouring dipoles
- As N increases, the eigenvalues become increasingly resonant at atom spacings of integer multiples of $\lambda/2$
- As $N \to \infty$, the decay of particular modes becomes the same as the decay from a single atom between two mirrors

Part III

Cooperative Behaviour in Two-Dimensional Arrays

Part III: Cooperative Behaviour in 2D Arrays

In this Part, we increase the dimensionality of the system by considering atoms arranged in two-dimensional lattices. Whilst this understandably increases the complexity of the cooperative behaviour, it also produces several features that would not have been possible in just one dimension. There are still many similarities between the cooperative behaviour of one- and two-dimensional arrays, such as the nature of the eigenvectors, cavity-like resonances in the eigenvalues, and interferences in the extinction. The things we learnt in Part II will therefore aid us in our understanding of these more complex systems.

In Chapter 7 we investigate the eigenvector and eigenvalue behaviour of different two-dimensional lattices. We find that different lattice geometries can produce strikingly different mode behaviours. For example, strong mode interferences in a kagome lattice result in distinctive extinction lineshapes, like a cooperative analog of electromagnetically induced transparency. This work was published in [66].

From optical lattice clocks to quantum simulation, understanding the cooperative behaviour of such two-dimensional lattices is of crucial importance (Sec. 1.5). In Chapter 8, we consider one such potential application: a perfect atomic mirror. By calculating the scattered electric field across output and input collection lenses, we measure directly the extinction of a single monolayer of atoms, showing that at particular lattice spacings, an incident light beam is almost completely reflected. This work was published in [67].

In both of these Chapters, we pay particular attention to considering how these features might be realised in an experiment and what limitations there may be. For example, in Chapter 8 we employ a detailed numerical model to calculate the effect of strong focusing on the incident light beam. In both Chapters we also simulate the effects of imperfect localisation of the atomic positions.

Chapter 7

Eigenmodes in a two-dimensional atomic monolayer

7.1 Overview

In Sec. 7.2 we calculate the extinction cross-section and eigenmode behaviour for 2D ensembles of just a few atoms. As in Chaps. 5 and 6, the dipoles in the dominant eigenvector are typically aligned and in phase, resulting in superradiant linewidths for small spacings. Increasing the atom number in Sec. 7.3, we find that in all but the kagome lattice, the eigenmode behaviour is dominated by just a single eigenmode. In the kagome lattice however there is a strong interference resonance between two modes that is relatively robust to lattice imperfections (Sec. 7.3.4).

Some of the figures and text in this Chapter have been taken, with permission, from [66].

7.2 Extinction of small two-dimensional lattices

7.2.1 Extinction eigenmodes

We begin our investigation of the cooperative behaviour of 2D lattices by considering small arrays of just a few atoms. In Fig. 7.1 we plot the extinction cross-section as a function of lattice spacing and detuning for small arrays of $N = 3-6$ atoms. Each of these geometries represents a sublattice of a larger lattice structure (not necessarily the same as the unit cell, but similar): Fig. 7.1(a,c) triangular lattice; (b,d) square lattice; (e,g) kagome lattice (see Sec. 7.3.3); (b,d) hexagonal lattice. As in Figs. 6.1 and 6.4, we assume the driving field is a linearly polarised uniform plane wave $\mathbf{E}_0(\mathbf{r}) = E_0 \mathrm{e}^{\mathrm{i}kz}\hat{\mathbf{y}}$.

For the 1D arrays in Part II, we could avoid the issue of mode degeneracies by restricting the number of excited states, since the configurations chosen only resulted in dipole polarisation in one direction. However, the atoms in these two-dimensional arrays will, in general, have polarisation components in both $\hat{\mathbf{x}}$ and $\hat{\mathbf{y}}$, which means that we cannot ignore degenerate modes in the x and y plane. These degeneracies do not cause issues with expanding the electric field and dipole vectors in the eigenvector basis (we always check that the eigenvector basis is complete, see Sec. 3.5.5). The b_p expansion coefficients however can result in very large interferences between degenerate eigenmodes, which can be misleading when plotting the individual mode contributions to the extinction cross-section. This can be seen in Fig. 7.2 where we plot the contribution to the extinction from each mode independently. For clarity therefore, in Fig 7.1, whenever there is a pair of degenerate modes, we shall plot as one line the sum of the two mode contributions *as well as* their interference. That is, instead of plotting σ_p and σ_q for degenerate p and q, we plot $\sigma_p + \sigma_q + \sigma_{pq} + \sigma_{qp}$ as one line. We do not do this in Fig. 7.2 as there we want to consider the individual eigenvectors.

There is a similar behaviour in the cross-section lineshapes for the configurations in Fig. 7.1 as there was for three atoms separated in a chain in x or y in Fig. 6.1. In Fig. 7.1(e,b,f), there is typically one (or a pair of degenerate) stronger broader mode(s) which dominates the lineshape over most detunings. In addition, there is a weaker narrow mode (or pair of degenerate modes) which overlaps and interferes with the broader mode, resulting in

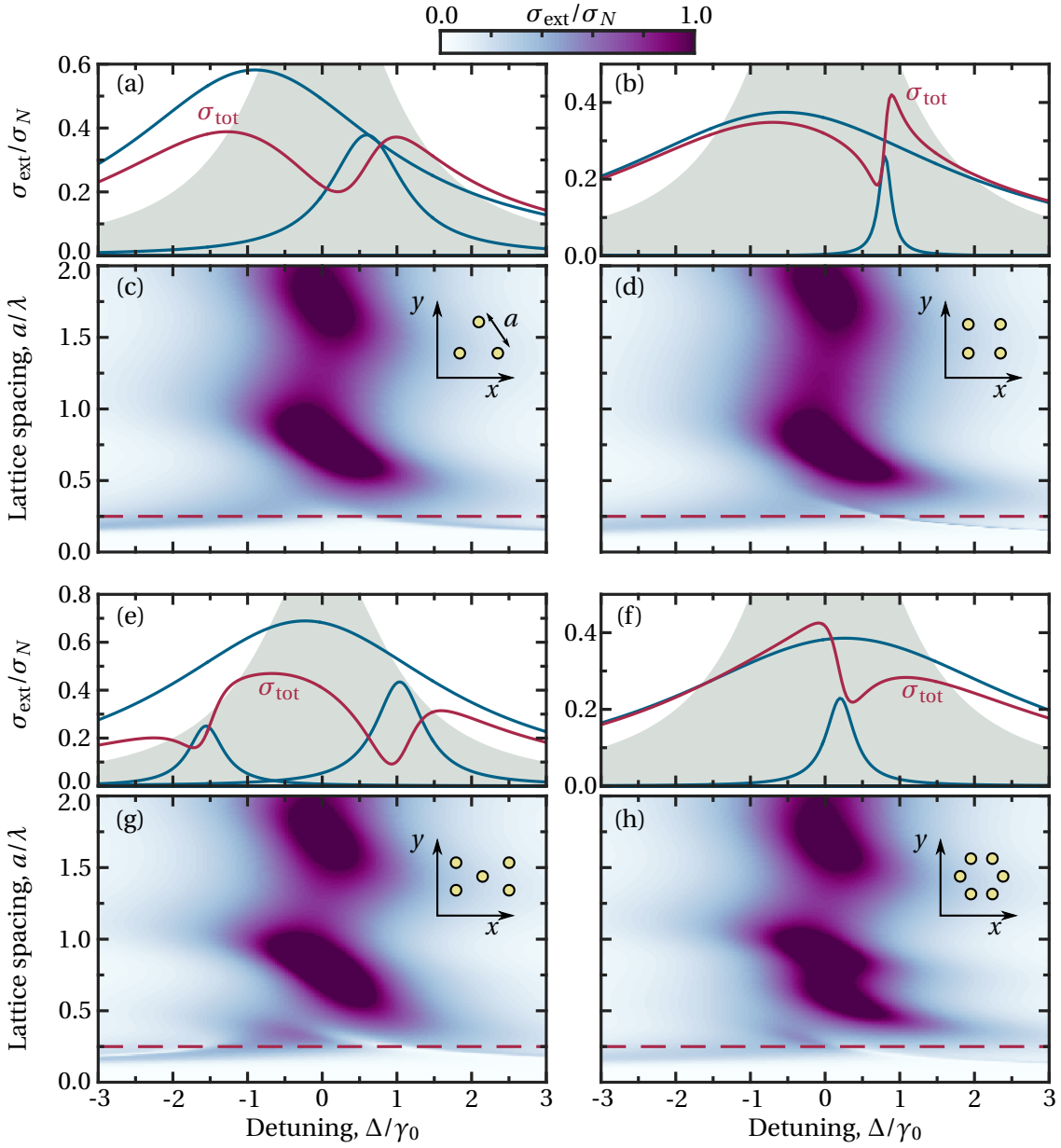

Figure 7.1: Extinction cross-section σ_{ext} of a uniform plane wave $\mathbf{E}_0(\mathbf{r}) = E_0 e^{ikz}\hat{\mathbf{y}}$ due to small ensembles of $N = 3$ (a,c), $N = 4$ (b,d), $N = 5$ (e,g), and $N = 6$ (f,h) atoms. The diagrams indicate the configuration of each array in the xy plane. (a,b,e,f) The total cross-section (red lines) as well as individual mode cross-sections σ_p (blue lines) are plotted as a function of detuning Δ, for nearest-neighbour lattice spacing $a = 0.25\lambda$. (c,d,g,h) The total cross-section is plotted as a function of detuning and atom spacing.

interference lineshapes. In Fig. 7.2, we see that the main modes in the triangle and square configurations actually each consist of two pairs of degenerate modes. In the bow-tie configuration in Fig. 7.1(e) however, there is an additional narrow mode which also interferes with the broader mode, resulting in two strong dips in the lineshape, with strong cancellation of the extinction at around $\Delta = \gamma_0$.

7.2.2 Eigenvectors

In Fig. 7.2, as well as plotting the contributions of the dominant eigenmodes to the extinction, we also plot the mode eigenvectors. For three atoms in a chain, we saw in Fig. 6.2 that the broader dominant mode ($\vec{\mathbf{m}}_1$) corresponded to all the dipoles oscillating in phase whilst the narrow weaker mode ($\vec{\mathbf{m}}_2$) corresponded to the dipoles oscillating π out of phase with their nearest neighbours. Unlike in 1D, the dipoles are now polarised in both x and y, and so we plot separately the real and imaginary parts of the dipole vectors in the xy plane. However, we still see some similarities between the 1D and 2D eigenvectors. The stronger, broader modes in Fig. 7.2 typically involve the real components of each dipole vector being aligned along a similar direction. The same is true for the imaginary components in Fig. 7.2(a,b), although in Fig. 7.2(c,d) the imaginary components are much smaller in amplitude. Conversely, the vectors in the narrower modes are typically anti-aligned with their nearest neighbours to some degree. This is especially clear in modes $\vec{\mathbf{m}}_3$ and $\vec{\mathbf{m}}_4$ of the square lattice (b).

The eigenvectors $\vec{\mathbf{m}}_2$ and $\vec{\mathbf{m}}_3$ in the bow-tie configuration in Fig. 7.2(c) have a similar appearance to each other, with the central atom of both being aligned in y and the four atoms either side being some symmetric configuration of vectors in x and y. This may help to explain why there are two narrow non-degenerate modes contributing to the extinction cross-section rather than just one, as is the case in the other configurations. In particular, the configuration of the dipole vectors in $\vec{\mathbf{m}}_3$ is reminiscent of the spin orientations of spin-ice in a kagome lattice [109] (see Sec. 7.3.3).

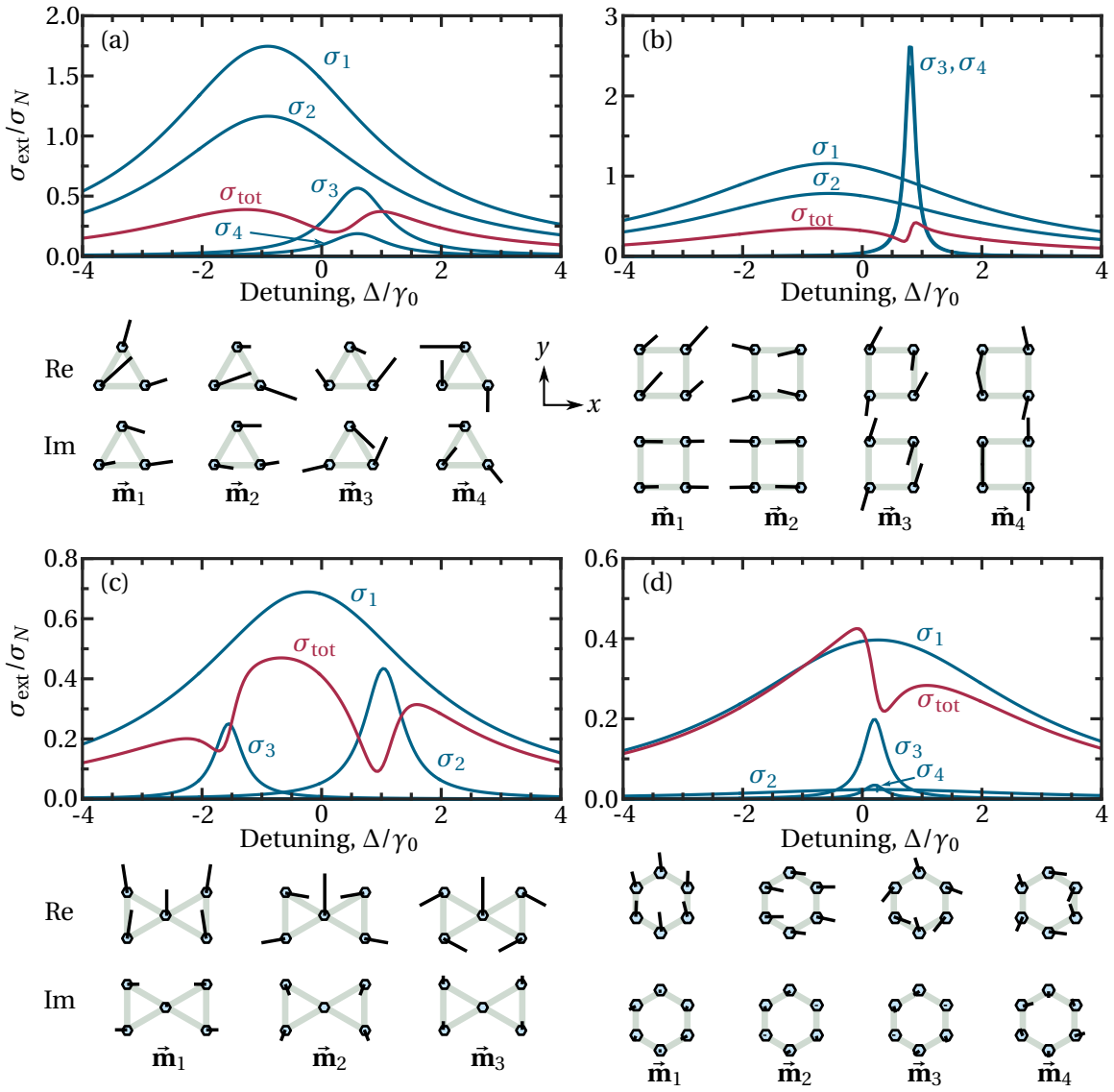

Figure 7.2: Extinction cross-section σ_{ext} of a uniform plane wave $\mathbf{E}_0(\mathbf{r}) = E_0 e^{ikz}\hat{\mathbf{y}}$ due to small ensembles of $N = 3$ (a), $N = 4$ (b), $N = 5$ (c), and $N = 6$ (d) atoms. The total cross-section (red lines) as well as individual mode cross-sections σ_p (blue lines) are plotted as a function of detuning Δ, for atomic spacing $a = 0.25\lambda$. Below the cross-section plots, we plot the real and imaginary x and y components of the main eigenvectors for each atom within the ensembles.

7.3 Large two-dimensional lattices

7.3.1 Extinction, cooperative EIT

Already for small 2D ensembles of atoms, interesting mode behaviour is beginning to appear, facilitated by the additional dimensionality not possible in just 1D. In the previous Chapter we found that increasing the number of atoms in a 1D lattice resulted in resonance behaviour in the eigenvalues and phase winding in the eigenvectors. We will therefore now extend our investigation of 2D ensembles to large periodic arrays of many atoms.

In Fig. 7.3 we plot the extinction cross-section as a function of detuning and lattice spacing for lattice geometries based on the configurations from Fig. 7.1[(a) triangular, (b) square, (c) kagome, and (d) hexagonal]. The extinction lineshapes at $a = 0.25\lambda$ for all but the kagome lattice [Fig. 7.3(a,b,f)] are dominated by a single (or pair of degenerate) eigenmode(s), with many other modes only producing small perturbations to the overall lineshape. In the kagome lattice however, an additional strong narrow mode interferes significantly with this broader dominant mode, resulting, as with the bow-tie configuration in Fig. 7.1(c), in a suppression of the cross-section.

This is similar to the Fano-like interferences we observed in 1D. However, the suppression of the extinction is so significant that it is almost like the recently proposed cooperative and dipolar analogs of electromagnetically induced transparency (EIT) [55, 110, 111, 112, 113]. In conventional EIT, destructive interference between different excitation pathways in a single multi-level atom results in a suppression of the extinction of an incident resonant driving field over a narrow spectral window. In these systems however, interferences between different cooperative states of the entire ensemble result in a similar transparency window, even though in general the atoms can be just two-level systems. This interference lineshape in the kagome lattice has also been predicted by [114].

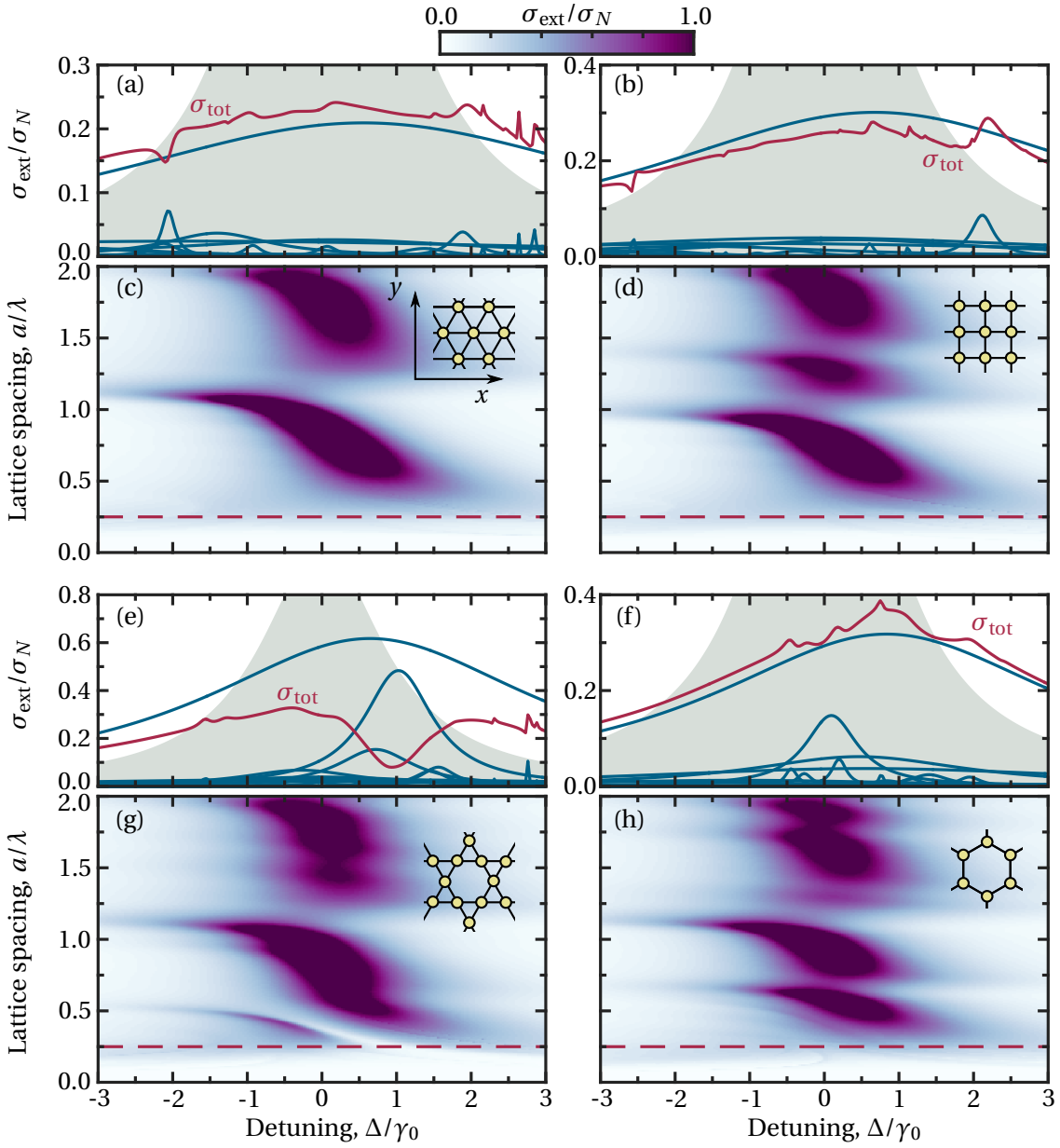

Figure 7.3: Extinction cross-section σ_{ext} of a uniform plane wave $\mathbf{E}_0(\mathbf{r}) = E_0 e^{ikz}\hat{\mathbf{y}}$ due to (a,c) $N = 52$ atoms in a triangular lattice, (b,d) $N = 49$ atoms in a square lattice, (e,g) $N = 47$ atoms in a kagome lattice, and (f,h) $N = 54$ atoms in a hexagonal lattice. (a,b,e,f) The total cross-section (red lines) as well as individual mode cross-sections σ_p (blue lines) are plotted as a function of detuning Δ, for atomic spacing $a = 0.25\lambda$. (c,d,g,h) The total cross-section is plotted as a function of detuning and atom spacing.

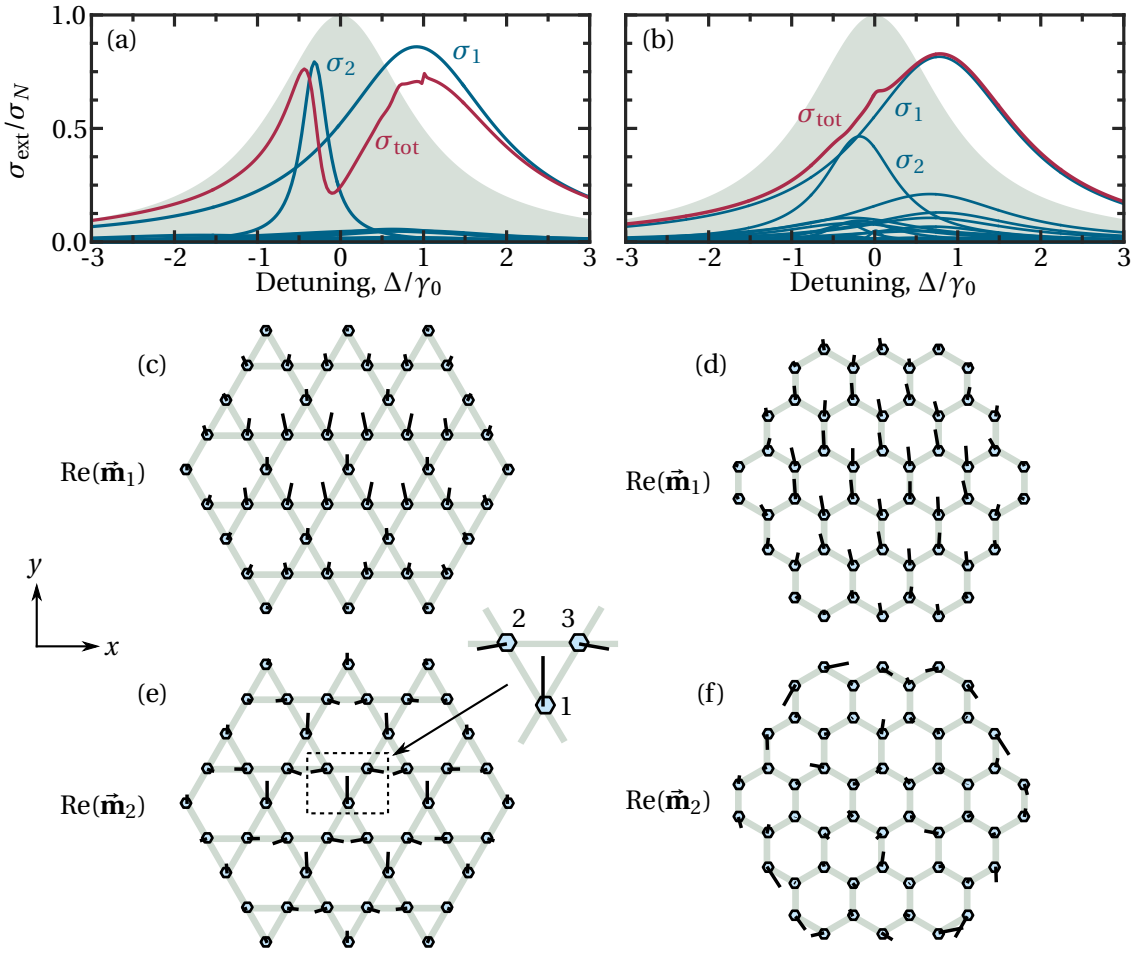

Figure 7.4: (a,b) Extinction cross-section $\sigma_{\rm ext}$ of a uniform plane wave electric field $\mathbf{E}(\mathbf{r}) = E_0\, e^{ikz}\hat{\mathbf{y}}$ due to (a) $N = 47$ atoms in a kagome lattice and (b) $N = 54$ atoms in a hexagonal lattice, with nearest-neighbour lattice spacing $a = 0.4\lambda$. The total cross-section (red lines) as well as individual mode cross-sections σ_p (blue lines) are plotted as a function of detuning Δ. (c–f) The real x and y components of the eigenvectors $\vec{\mathbf{m}}_1$ and $\vec{\mathbf{m}}_2$ in the kagome (c,e) and hexagonal (d,f) lattices.

7.3.2 Lattice eigenvectors

It is striking that among the four lattice structures considered, the kagome is the only one to exhibit a strong interference lineshape. Indeed, the hexagonal lattice also supports a

strong narrow mode [Fig. 7.3(f)], although the interference between this and the dominant mode is minimal. To investigate the origin of the strong narrow mode in the kagome lattice resulting in what we shall call *cooperative EIT*, we plot in Fig. 7.4 the mode vectors for each atom in the two dominant modes for both the kagome lattice and, for comparison, the hexagonal lattice. We use a slightly different lattice spacing here to highlight these modes ($a = 0.4\lambda$) although they are the same dominant modes as in Fig. 7.3.

As with every other uniformly driven atomic ensemble we have considered so far, the dominant (and at this lattice spacing, superradiant) eigenmode is that for which the dipoles all oscillate in phase and are aligned with one another (which we label $\vec{\mathbf{m}}_1$). In Fig. 7.4 we plot just the real components of the eigenvectors since the imaginary components are negligible in comparison. As with the one-dimensional array in Fig. 6.7, the amplitudes of the vectors peak in the centre of the lattice and disappear off towards the edges. A similar mode also exists with all vectors aligned along x, but the coupling with the field polarisation (linear in y) is much weaker. A similar mode to mode $\vec{\mathbf{m}}_1$ was observed in a kagome lattice of magnetic dipoles [63]. We call this mode *ferroelectric*, since it is similar to a ferromagnetic ensemble of aligned magnetic dipoles.

Looking now at the second modes $\vec{\mathbf{m}}_2$, the dipoles in the centre of the kagome lattice have a very similar configuration to those in mode $\vec{\mathbf{m}}_2$ of the bow-tie configuration from Fig. 7.1. This mode behaviour can be separated into alternating rows of dipoles. Starting at the bottom of the lattice, the dipoles in the odd-numbered rows are all aligned along the direction of the driving field y (ferroelectric). The dipoles in the even numbered rows however are anti-aligned along the x axis (anti-ferroelectric). Explaining the origin of this vector configuration is challenging given the long range nature of the dipole–dipole interaction combined with the non-trivial kagome geometry. We can, however, gain insight through considering the individual contributions of different dipoles. Considering first the dipole at the lattice site labeled 1 in Fig. 7.4(e), the dipole vectors of the nearest neighbours at sites 2 and 3 are symmetric in x, meaning that the sum of the electric fields they radiate onto site 1 has only a y component (the x components cancel). The same is true for the remaining dipoles along row 2-3 and other rows of that type: for every dipole there is an equal and opposite mirror dipole along the same row cancelling all the x field components experienced at site 1. The dipoles along the same row as dipole 1 contribute fields along y as does the driving field, resulting in an overall dipole orientation along

y for dipole 1. Similar symmetries can be used to explain the behaviour of the dipoles at sites 2 and 3, however what is striking is the stripe-like behaviour of these alternating rows.

Note that this mode behaviour we describe is only valid in the centre of the lattice, since the vector amplitudes die off towards the edges (for $\vec{\mathbf{m}}_1$ and $\vec{\mathbf{m}}_2$ at least). As the lattice increases in atom number, this bulk mode vector behaviour extends further and further, and seems to be responsible for this interference. Note that if the driving field was different to a uniform plane wave, then the overlap with the modes would be different and we would expect a different set of modes to contribute.

7.3.3 Semiregular kagome lattices

The kagome lattice can be constructed by removing a triangular lattice with lattice period $2a$ from a triangular lattice with period a [115] and this double periodicity is manifest in mode $\hat{\mathbf{m}}_2$ (a spacing between antiferroelectric dipoles; $2a$ spacing between ferroelectric dipoles). This suggests the mode is related to this double periodicity, which does not exist in the other *regular* lattices. A regular lattice is one in which the tiles surrounding each lattice vertex are the same. This is the case for the triangular, square, and hexagonal lattices. The kagome lattice, however, is *semiregular*, meanings its tiling consists of different types of tiles (triangles and hexagons) surrounding common vertices, and so even though it shares the same common base unit tiles as the triangular and hexagonal lattices, its behaviour can be significantly different.

There are many interesting phenomena that can be observed in kagome lattices, some relating to this semiregular lattice structure. These include photonic flat bands [116, 117, 118] and spin ice and geometric frustration [62, 63]. Investigating further similarities between our kagome spin lattices and these other kagome lattices could allow these phenomena to be realised in different systems, as well as improving understanding of how these spin systems manifest such behaviour. For example, the orientation of the dipoles in mode $\vec{\mathbf{m}}_2$ is similar to that in spin-ice [62, 63], suggesting there may be some underlying features connecting these fields.

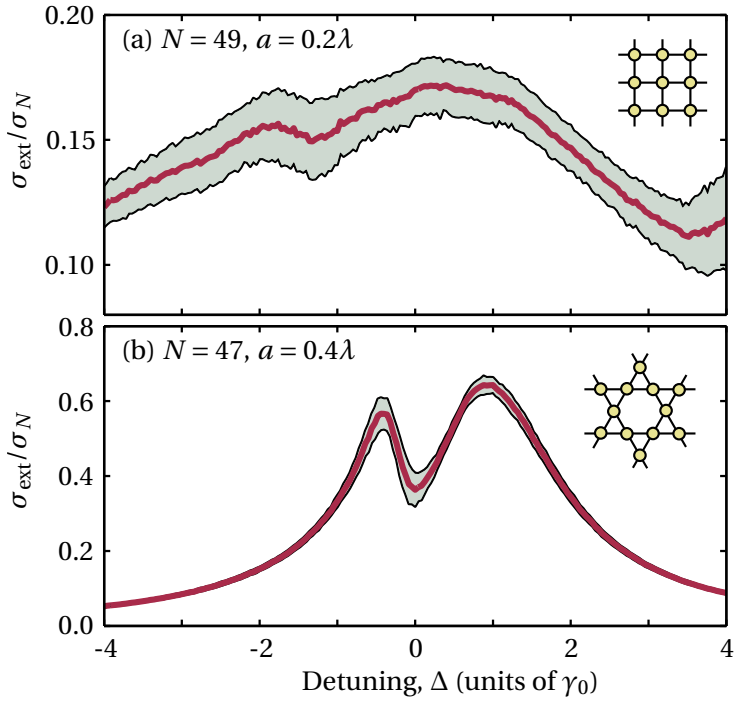

Figure 7.5: The effect of experimental imperfections on extinction cross-section, σ_{ext}, through (a) a square lattice with $N = 49$ sites and lattice spacing $a = 0.2\lambda_0$ and (b) a kagome lattice with $N = 47$ sites and lattice spacing $a = 0.4\lambda_0$. The red solid lines show the average over several hundred realisations; the black solid lines bounding the shaded areas represent the standard deviation. In each realisation (and at each detuning), we remove at random 5 atoms from both lattices and sample the individual atom positions using a Gaussian distribution, modeling the effect of finite trap depth ($V_0 = 750E_R$, where E_R is the lattice recoil energy).

7.3.4 Lattice imperfections

So far we have considered perfect systems in which every lattice site is occupied by one atom centred exactly on that lattice site (i.e. assuming an infinite trapping potential). Here we calculate how the interference lineshape in the kagome lattice deteriorates if the lattice filling is not perfect (not all of the lattice sites are occupied) and the trapping depth confining the atoms to the lattice is of finite magnitude (introducing uncertainty in the atomic positions). To model the finite trap depth, we assume the trapping potential is a

standing wave of amplitude V_0 (considered to be approximately harmonic at the minima). The atomic wavefunctions are assumed to be those of ground state harmonic oscillators, centred on each lattice site. Each realisation of the position is therefore determined according to a Gaussian probability distribution, $\rho_i \propto \exp(-[(x-x_i)^2+(y-y_i)^2]/\ell^2)$, where $\ell = (a/\pi)(E_R/V_0)^{1/4}$ and E_R is the lattice recoil energy (see Sec. 8.6 for further details). For relatively high filling factors (90% occupation) and significant trap depths $V_0 = 750E_R$, we see in Fig. 7.5(a) that the narrow subradiant modes responsible for the weak Fano resonances are washed out, leaving contributions from the broader, stronger modes only. Using the same lattice parameters in the kagome lattice however [Fig. 7.5(b)], the interference lineshape is still very clear to see. 90% filling has recently been realized for a 2×2 array [119] and trap depths of $10^3 E_R$ are possible in, e.g., optical lattices [51] where high filling factors are possible via the Mott-insulator phase and algorithmic cooling [120].

Chapter Summary

- Similar to atoms arranged in one-dimension, the extinction behaviour of two-dimensional lattices is dominated by a single ferroelectric mode with mode resonances appearing aperiodically as a function of lattice spacing
- In the kagome lattice, interference between a pair of strong modes results in a region of near transparency in the extinction, similar to a cooperative analog of EIT
- The mode responsible for this interference is thought to exist due to the semi-regular nature of the kagome lattice
- This mode interference is relatively robust to lattice imperfections

Chapter 8

Extinction in a two-dimensional atomic monolayer

8.1 Overview

In the Chap. 7 we investigated the eigenmode behaviour of different 2D lattices and the resulting extinction cross-section. In this Chapter, we consider how this extinction might be measured experimentally. In Sec. 8.2 we begin by calculating the transmission of a strongly focussed Gaussian beam incident on a single atom. For such strong focussing, it is necessary to model the Gaussian beam propagation beyond the paraxial approximation. This is discussed in Sec. 8.3. In Sec. 8.4 we replace the single atom with a random 2D ensemble of atoms, finding that at high number densities, strong dipole–dipole interactions between the atoms reduce the extinction of the driving field. By confining the atoms to periodic 2D lattices in Sec. 8.5, we discover ranges of lattice spacings and detunings over which the transmission through the lattices drops to close to zero. To address the question of how these extinctions might be realised experimentally, in Sec. 8.6 we determine the dependence of this extinction on experimental imperfections such as finite trap depths and finite filling factors.

Some of the figures and text in this Chapter have been taken, with permission, from [67].

8.2 Single atom extinction

As discussed in the Introduction (Chap. 1), achieving an efficient coupling between light and matter is a fundamental goal in many fields of physics. The ultimate limit would be to obtain perfect coupling between a single photon of light and a single quantum scatterer (such as an atom, quantum dot, plasmonic nanoresonator etc.). If such a perfect coupling were possible then that would open the door to a wealth of applications including single photon transistors [121, 122], quantum memory storage [123], and optical phase gates [124, 125].

8.2.1 Previous experiments

In Table D.1 in Appendix D, we outline some of the recent experimental progress towards realising efficient coupling between a single quantum emitter and light. This includes atoms, ions, molecules, quantum dots, and artificial superconducting atoms.

As discussed in Sec. 1.3, optimising the coupling between light and a scatterer requires matching the mode of the incident light with the mode of the scattered light. If the scatterer is an electric dipole, then the form of the radiated field in free space was given in Sec. 4.2,

$$\mathbf{E}_i(\mathbf{r}) = \frac{k^3}{4\pi\varepsilon_0}\mathrm{e}^{\mathrm{i}kR_i}\left\{(\hat{\mathbf{R}}_i\times\mathbf{d}_i)\times\hat{\mathbf{R}}_i\frac{1}{kR_i}+[3\hat{\mathbf{R}}_i(\hat{\mathbf{R}}_i\cdot\mathbf{d}_i)-\mathbf{d}_i]\left[\frac{1}{(kR_i)^3}-\frac{\mathrm{i}}{(kR_i)^2}\right]\right\}. \tag{8.2.1}$$

As we shall see in Sec. 8.2.3, this has the same form as that of a focussed Gaussian beam. Placing a single emitter (such as an atom, ion, molecule or quantum dot) into the focus of a high numerical aperture lens [$0.4 \lesssim \mathrm{NA} \lesssim 0.6$, where NA is given in Eq. (8.3.1)] has therefore enabled extinctions of an incident laser beam of up to around 20% [126, 127] (see Table D.1). Alternatively, the emitter can be placed in the focus of a deep parabolic lens, focussing and capturing almost all 4π solid angle of the emitted radiation [128]. Another approach again is to change the mode into which the emitter radiates, for example coupling it to a waveguide or an optical cavity, enabling large phase shifts [125, 129]

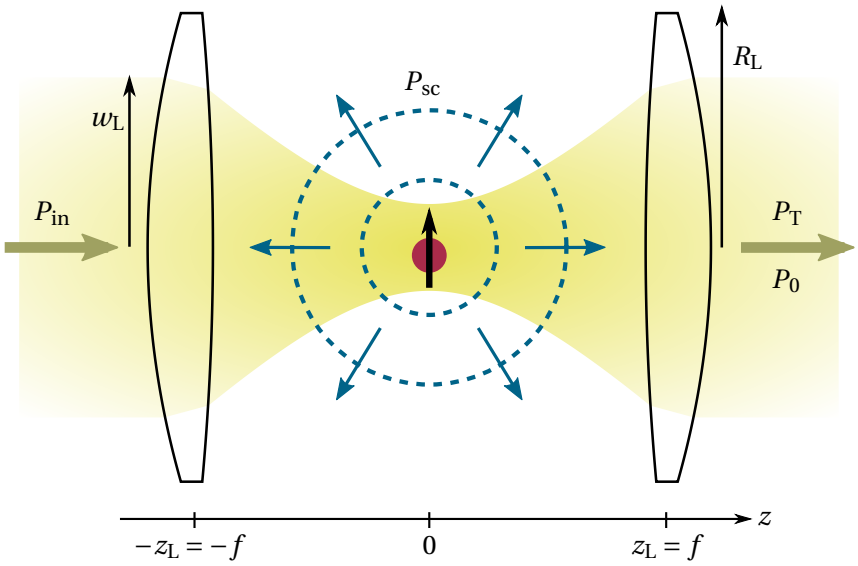

Figure 8.1: An incident laser beam with beam radius w_L is focussed onto a single atom through a focussing lens at position $z = -z_L = -f$ with radius R_L. The laser beam power across the focussing lens is P_{in} and the atomic dipole scatters a total power of P_{sc}. A second lens is placed at $z = z_L = f$ through which flows a total power P_T in the presence of an atom or P_0 if there is no atom.

and change in reflection of up to 25% [130]. An interesting recent twist on the single quantum emitter coupling problem has been the creation of artificial superconducting atoms [131] which couple through one-dimensional superconducting channels, resulting in near-perfect extinction.

In this work, we will consider the case of a high numerical aperture lens focussing a laser beam onto an atomic ensemble (Fig. 8.1), as this can be described well using our current model. This has been studied theoretically for single atoms and ions [101, 128, 132]. In addition to spatial mode matching, it is also necessary to match the temporal profile of the driving field or pulse with that of the emitted radiation [133]. However, we shall be considering a continuous driving field and therefore assume this condition is satisfied.

8.2.2 Gaussian beam - paraxial solution

Let us look more closely at the form of the mode matching between a focussed Gaussian beam and a single atom. The time-independent Maxwell equations in free space have the form of a Helmholtz equation

$$(\nabla^2 + k^2)\, E_{\hat{\boldsymbol{\epsilon}}}(x, y, z) = 0, \tag{8.2.2}$$

where ∇ is the differential operator and $E_{\hat{\boldsymbol{\epsilon}}}$ is the electric field component with $\hat{\boldsymbol{\epsilon}}$ polarisation. In the paraxial approximation ($\rho = \sqrt{x^2 + y^2} \ll z$), a solution to this equation is the Gaussian beam (here we just consider the first-order Laguerre Gaussian mode),

$$\mathbf{E}_0(x, y, z) = E_0 \frac{w_0}{w}\, \mathrm{e}^{\mathrm{i}[k(z+\rho^2/2R)-\zeta(z)]}\, \mathrm{e}^{-\rho^2/w^2}\, \hat{\boldsymbol{\epsilon}}, \tag{8.2.3}$$

where w_0 and $w = w_0\sqrt{1 + z^2/z_\mathrm{R}^2}$ are the $1/\mathrm{e}$ width at $z = 0$ (beam waist) and z (beam radius) respectively, $z_\mathrm{R} = \pi w_0^2/\lambda$ is the Rayleigh range, $R = z + z_\mathrm{R}^2/z$ is the beam curvature, and $\zeta(z) = \arctan(z/z_\mathrm{R})$ is the Gouy phase.

8.2.3 Extinction

The total field is the sum of the scattered dipole field (8.2.1) and the driving field (8.2.3), $\mathbf{E}(\mathbf{r}) = \mathbf{E}_i(\mathbf{r}) + \mathbf{E}_0(\mathbf{r})$. In the far field of the atom ($|z| \gg \{\lambda_0, z_\mathrm{R}\}$), the total field along the z axis has the form

$$\mathbf{E}(z) = \mathbf{E}_i(z) + \mathbf{E}_0(z) \simeq \mathrm{i}\frac{3E_0\mathrm{e}^{\mathrm{i}kz}}{2kz}\left[1 - \mathrm{sgn}(z)\frac{k^2 w_0^2}{3}\right]\hat{\boldsymbol{\epsilon}}, \tag{8.2.4}$$

where $\mathrm{sgn}(z)$ is the sign of z and we are assuming the driving field is resonant with the dipolar resonance frequency ($\Delta = 0$).[a]. The only difference between the two fields is a numerical factor, $k^2 w_0^2/3$, indicating that in the condition when $w_0 \simeq 0.28\lambda$, the two fields will efficiently cancel in the $+z$ direction, resulting in extinction of the two fields. The

[a] We have replaced the dipole moment in $\mathbf{E}_i$ with $\mathbf{d}_i = \alpha_0 \mathbf{E}_0(0)$.

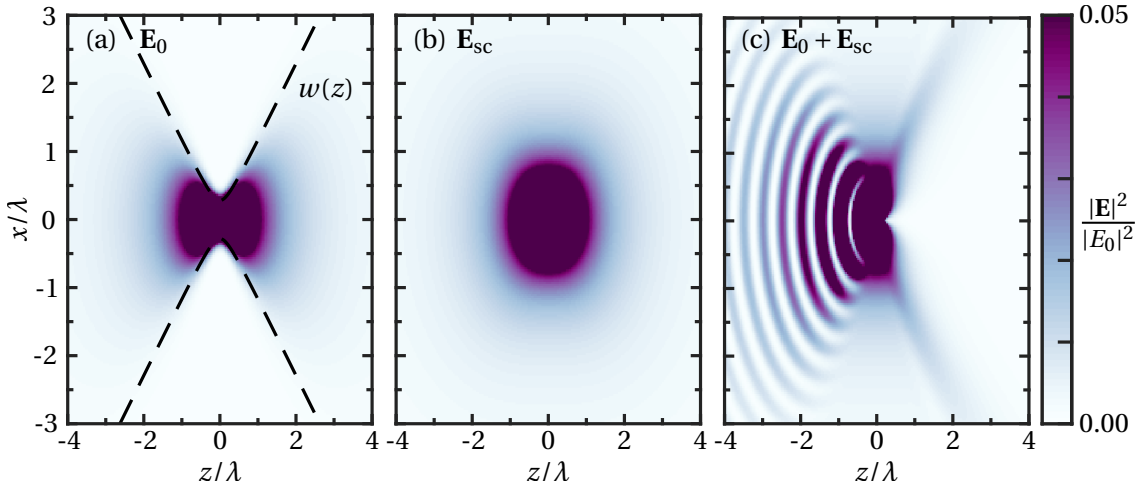

Figure 8.2: Extinction of a Gaussian by a single atom. Plotted are the electric field intensities of the Gaussian beam (a), the scattered dipole field (b) and the total field (c) in the xz plane. The Gaussian beam has beam radius $w_0 = 0.28\lambda$ and has circularly polarisation $\hat{\boldsymbol{\epsilon}}_+$.

opposite is true in the $-z$ direction, where the fields will add, resulting in reflection. This extinction and reflection can be seen by plotting the field intensities in Fig. 8.2.

In Fig. 8.3(a) we plot the transmission through a lens a distance $z_L = 150\lambda$ downstream of the atom and with radius $R_L = 10\lambda$. The power flowing through the lens is calculated using the methods described in Chapter 4.[b] Rather than defining the transmission as a ratio of the total output power P_{tot} with the total inpur power P_{in} (see Fig. 8.1), we define it as the difference in power over the output lens with and without the presence of an atom,

$$T = \frac{P_{tot}}{P_0}. \tag{8.2.5}$$

This way we can assume we have an infinite focussing lens whilst only a finite collection lens. Having a small collection lens optimises this difference in powers because the extinction is optimised close to the optical axis [notice the bright fringes scattered in the $+z$ direction off axis in Fig. 8.2(c)]. We see that, as predicted in Eq. (8.2.4), the maximal

[b] We assume that the wavevector of the Gaussian beam points away from the origin (the focus), $\hat{\mathbf{k}}_0 = \hat{\mathbf{r}}$.

extinction, which we define now as

$$\epsilon \equiv 1 - T, \tag{8.2.6}$$

occurs when $w_0 = 0.28\lambda$ and is $\epsilon > 99\%$.

8.3 Realistic beam focussing

By modelling the driving field as a Gaussian beam as in Eq. (8.2.3), we are assuming that the beam is in the paraxial limit, that the focussing lens is large enough such that it collects the entire beam, and that the focussing lens is perfect and has no aberrations or imperfections. If we want to model a realistic system however, we need to go beyond these various approximations.

We will leave dealing with lens aberrations and imperfections to later works. However, we will now consider the effects of finite lens size and non-paraxial beam propagation. We will be following the approaches taken in [101, 134]. See as well our paper [67] and the corresponding Supplemental Material.

8.3.1 Finite lens radius

The focussing strength of a lens can be characterised by its *numerical aperture*:

$$\mathrm{NA} = \eta \sin\theta = \frac{R_\mathrm{L}}{\sqrt{f^2 + R_\mathrm{L}^2}}, \tag{8.3.1}$$

where η is the refractive index of the medium in which the lens is working and θ is half the angle of the maximum possible light cone that can be focussed by the lens.

The beam radius at the focus w_0 and at the focussing lens $w_\mathrm{L} = w_{z=-z_\mathrm{L}}$ are inversely related, $w_\mathrm{L} \simeq z_\mathrm{L}\lambda/\pi w_0$ (assuming $z \gg z_\mathrm{L}$ for a paraxial Gaussian beam, Sec. 8.2.2). If we assume that the lens radius is $R_\mathrm{L} = w_\mathrm{L}$, then this would correspond to a numerical aperture of $\mathrm{NA} \simeq 0.75$. Realistically we would want the lens radius to be much larger than w_L, otherwise light will be lost around the edge of the lens and diffraction of the finite size

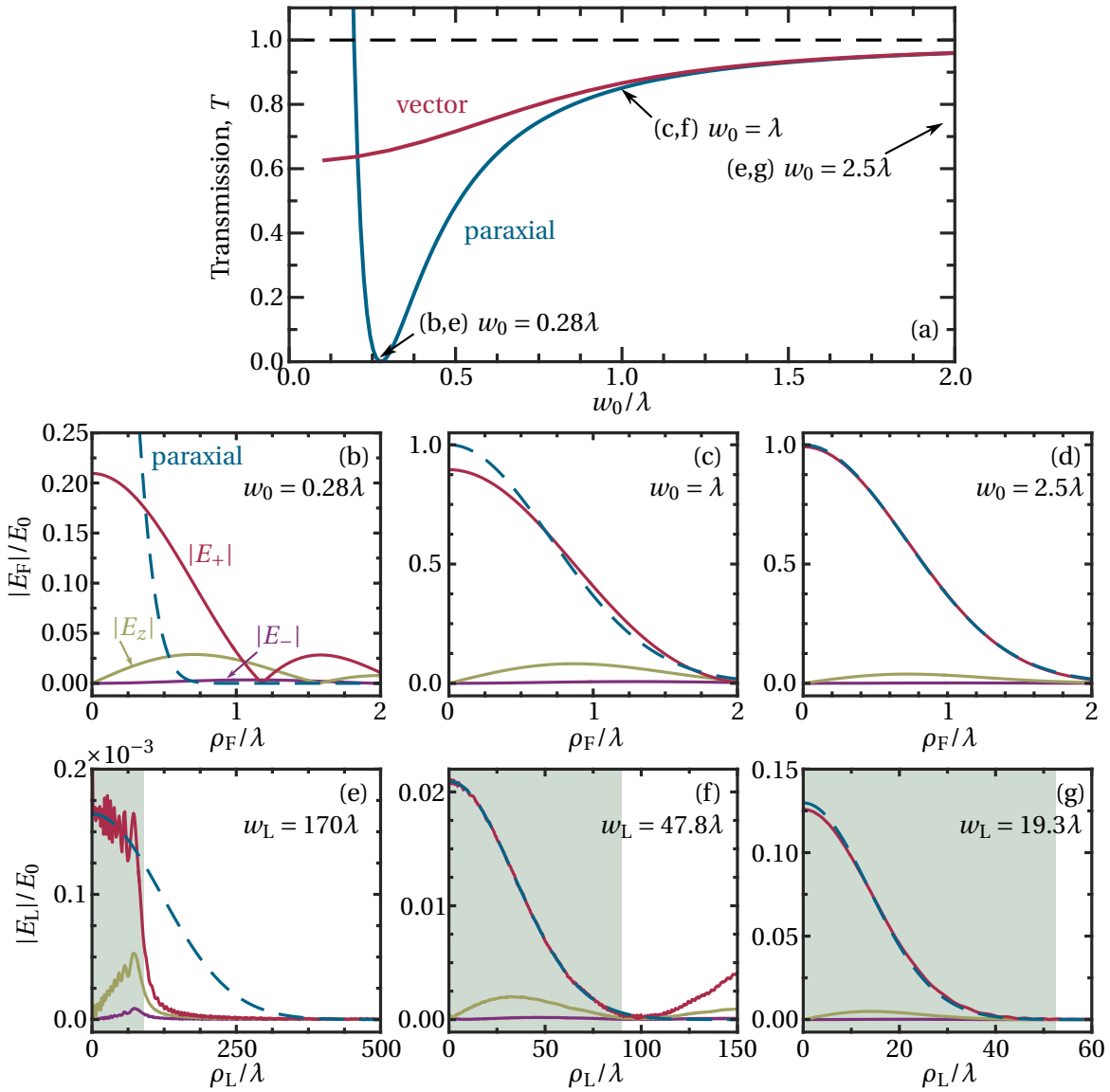

Figure 8.3: (a) The calculated transmission $T = P_{\text{tot}}/P_0$ of a focussed laser beam through a lens with radius $R_L = 10\lambda$ a distance $z_L = 150\lambda$ downstream of the atom. The blue line models the driving field as a paraxial Gaussian beam (8.2.3) with varying beam waist w_0 and circular polarisation $\hat{\boldsymbol{\epsilon}}_+$ focussed through a perfect lens of infinite radius at $-z_L$. The red line models the full vector field propagation (8.3.5), assuming the same incident field as the blue line but focused by a lens with radius $R_L = 90\lambda$. (b-g) The different polarisation components of the full vector field in the focal plane $z = 0$ (b,c,d) and output lens plane $z = f$ (e,f,g) for different beam sizes. Blue dashed lines show the paraxial field. Grey boxes indicate the extent of the lens.

will distort the focal image. In free space, typical high numerical apertures lens values lie in the range $0.5 \lesssim \mathrm{NA} \lesssim 0.7$ [126]. Higher numerical apertures are possible by immersing the lens system in a high refractive index medium [135, 136] or using novel diffractive elements [137](FWHM spot size of 0.57λ). However, the current limits on how tightly and efficiently light can be focused onto a single spot mean that reaching the predicted near-perfect extinction for a single atom is still out reach.

In the following Sections we will show that, using 2D atomic ensembles, it should be possible to realise near-perfect extinction with much larger spot sizes than for a single atom, meaning the requirements for tight focussing are much less demanding. For the size of atomic ensembles we consider, the extinction is optimised for a beam waist of around $w_0 \simeq 2.5\lambda$. The corresponding Rayleigh range is $z_\mathrm{R} \simeq 20\lambda$. For the lens to be in the far-field of the atom, we require that $z_\mathrm{L} \gg z_\mathrm{R}$ and so we shall choose a focal length $f = z_\mathrm{L} = 150\lambda$. The corresponding input beam radius required (assuming a paraxial beam) is $w_\mathrm{L} = w_0\sqrt{1+z_\mathrm{L}^2/z_\mathrm{R}^2} \simeq 20\lambda$. By selecting a lens radius of $R_\mathrm{L} = 90\lambda$, we ensure that the lens radius is much larger than the input beam (less than 10^{-12}% of the beam power is lost around the edge of the lens), whilst being of a realistic numerical aperture ($\mathrm{NA} \simeq 0.5$).

8.3.2 Limits on the paraxial approximation

If we assume that the Gaussian beam has been focussed by a lens a distance z_L upstream of the atom, in order for Eq. (8.2.3) to be valid, the paraxial approximation requires that $w_\mathrm{L}/z_\mathrm{L} \ll 1$. Assuming that the lens is in the far field of the atom and the beam ($z_\mathrm{L} \gg \lambda, z_\mathrm{R}$), this puts limits on the possible values of beam waist w_0 that can be considered under the

paraxial approximation:

$$\frac{w_\mathrm{L}}{z_\mathrm{L}} = \frac{w_0}{z_\mathrm{L}}\left(1+\frac{z_\mathrm{L}^2}{z_\mathrm{R}^2}\right)^{\frac{1}{2}} \ll 1, \tag{8.3.2a}$$

$$\left(1+\frac{z_\mathrm{L}^2\lambda^2}{\pi^2 w_0^4}\right) \ll \frac{z_\mathrm{L}^2}{w_0^2}, \tag{8.3.2b}$$

$$\frac{z_\mathrm{L}^2}{2} - \frac{z_\mathrm{L}^2}{2}\left(1-\frac{4\lambda^2}{\pi^2 z_\mathrm{L}^2}\right)^{\frac{1}{2}} \ll w_0^2 \ll \frac{z_\mathrm{L}^2}{2} + \frac{z_\mathrm{L}^2}{2}\left(1-\frac{4\lambda^2}{\pi^2 z_\mathrm{L}^2}\right)^{\frac{1}{2}}, \tag{8.3.2c}$$

$$\frac{\lambda}{\pi} \simeq 0.3\lambda \ll w_0 \ll z_\mathrm{L}\,. \tag{8.3.2d}$$

The optimised single-atom extinction in Sec. 8.2.3 occurred for $w_0 = 0.28\lambda$. This however is clearly outside the range in which the paraxial regime is valid. In Sec. 8.3.3 we shall go beyond the paraxial model and introduce a full vector treatment for the propagation of a focussed laser beam.

8.3.3 Vector field propagation

Let us consider a laser beam, propagating with wavevector $\mathbf{k} = k\hat{\mathbf{z}}$ and circularly polarised $\hat{\boldsymbol{\epsilon}}_+ = (\hat{\mathbf{x}} + \mathrm{i}\hat{\mathbf{y}})/\sqrt{2}$, incident on a focusing lens at position $z = -z_\mathrm{L}$, as shown in Fig. 8.1. The electric field beam profile across the lens is $\mathbf{E}_\mathrm{In} = \mathrm{i}E_\mathrm{L}\,\mathrm{e}^{-\rho^2/w_\mathrm{L}^2}\hat{\boldsymbol{\epsilon}}_+$, where w_L is the $1/\mathrm{e}$ beam radius at the lens.[c] As the field propagates through the lens, it acquires a phase and the wavevector $\hat{\mathbf{k}}$ changes direction. The change in $\hat{\mathbf{k}}$ introduces small contributions from the other two polarizations $\hat{\boldsymbol{\epsilon}}_- = (\hat{\mathbf{x}} - \mathrm{i}\hat{\mathbf{y}})/\sqrt{2}$ and $\hat{\mathbf{z}}$. The total field immediately after the lens is then

$$\mathbf{E}(\rho,\phi,z=-f) = \frac{E_\mathrm{L}\,\mathrm{e}^{-\rho^2/w_\mathrm{L}^2}}{\sqrt{|\cos\theta|}}\left(\frac{1+\cos\theta}{2}\hat{\epsilon}_+ + \frac{\sin\theta}{\sqrt{2}}\mathrm{e}^{\mathrm{i}\phi}\hat{\mathbf{z}} + \frac{\cos\theta-1}{2}\mathrm{e}^{2\mathrm{i}\phi}\hat{\epsilon}_-\right) \times \exp\left[-\mathrm{i}\left(k\sqrt{\rho^2+f^2}-\pi/2\right)\right], \tag{8.3.3}$$

[c] The factor of i is included so that the field in the focus will be approximately real, such as to match the Gaussian beam expression in Eq. (8.2.3).

where $\rho^2 = x^2 + y^2$, $\phi = \tan^{-1}(y/x)$ and $\theta = \tan^{-1}(\rho/f)$ is the angle between the $-z$ axis and a point on the lens. This expression can be calculated by rotating the $\mathbf{E}_{\rm In}$ such that the new wavevector points towards the focus. Equivalent expressions exist for incident polarisations of $\hat{\boldsymbol{\epsilon}}_-$ and $\hat{\mathbf{z}}$.

The total field can be decomposed into an orthogonal set of modes, $\mathbf{E} = \sum_\mu \kappa_\mu \mathbf{E}_\mu$, where $\mu = (k_t, s, m)$, $k_t = \sqrt{k^2 - k_z^2}$ is the transverse wavevector component, $s = \pm 1$ is the helicity and m is an angular momentum index. This decomposition now allows us to propagate the field to any point behind the lens. The expansion coefficients κ_μ are

$$\kappa_\mu = \delta_{m1}\pi k_t \int_0^\infty \mathrm{d}\rho_{\rm L}\,\rho_{\rm L}\frac{1}{\sqrt{\cos\theta_{\rm L}}}\left\{\frac{sk+k_z}{k}\left(\frac{1+\cos\theta_{\rm L}}{2}\right)J_0(k_t\rho_{\rm L}) + \mathrm{i}\frac{\sqrt{2}k_t}{k}\left(\frac{\sin\theta_{\rm L}}{\sqrt{2}}\right)J_1(k_t\rho_{\rm L})\right.$$
$$\left. + \frac{sk-k_z}{k}\left(\frac{\cos\theta_{\rm L}-1}{2}\right)J_2(k_t\rho_{\rm L})\right\}\exp\left[-\mathrm{i}\left(k\sqrt{\rho_{\rm L}^2+f^2}-\pi/2\right) - \frac{\rho_{\rm L}^2}{w_{\rm L}^2}\right], \tag{8.3.4}$$

where J_m is the mth order Bessel function, $\rho_{\rm L}$ is the radial position across the lens and $\theta_{\rm L} = \tan^{-1}(\rho_{\rm L}/f)$. The field components in the $\pm$ and z polarizations are then

$$\begin{aligned}
E_+(\rho,\phi,z) =& E_{\rm L}\sum_{s=\pm1}\int_0^k \mathrm{d}k_t \frac{1}{4\pi}\frac{sk+k_z}{k}J_0(k_t\rho)\,\mathrm{e}^{\mathrm{i}k_z(z+f)}\kappa_\mu,\\
E_z(\rho,\phi,z) =& E_{\rm L}\sum_{s=\pm1}\int_0^k \mathrm{d}k_t (-\mathrm{i})\frac{\sqrt{2}}{4\pi}\frac{k_t}{k}J_1(k_t\rho)\,\mathrm{e}^{\mathrm{i}k_z(z+f)}\,\mathrm{e}^{\mathrm{i}\phi}\kappa_\mu,\\
E_-(\rho,\phi,z) =& E_{\rm L}\sum_{s=\pm1}\int_0^k \mathrm{d}k_t \frac{1}{4\pi}\frac{sk-k_z}{k}J_2(k_t\rho)\,\mathrm{e}^{\mathrm{i}k_z(z+f)}\,\mathrm{e}^{2\mathrm{i}\phi}\kappa_\mu.
\end{aligned} \tag{8.3.5}$$

Using this method we calculate the electric field, $\mathbf{E} = E_+\hat{\boldsymbol{\epsilon}}_+ + E_-\hat{\boldsymbol{\epsilon}}_- + E_z\hat{\boldsymbol{\epsilon}}_z$, anywhere behind the focussing lens. Other methods, for example based the Rayleigh-Sommerfeld model, also exist [138, 139].

In Fig. 8.3(b–g) we plot the different polarisation components of the full vector propagated field in the focal and output lens planes for a focussing lens of radius $R_{\rm L} = 90\lambda$ and focal length $f = 150\lambda$. As suggested in Sec. 8.3.2, for $w_0 = 0.28\lambda$ in (b,e), the paraxial and vector models deviate significantly. Part of the reason for this is that the lens size does not cover the whole beam [as shown by the shaded region in Fig. 8.3(e)], and so some of the

power is lost. In addition to this, the finite size of the lens will have a significant diffractive contribution to the field in the focal plane, deforming the field.[d] However, even for a much less tightly focussed beam $w_0 = 2.5\lambda$ in Fig. 8.3(d,g), there is still a few percent contribution from the E_z polarisation component in both the focal and lens planes. Whilst the field experienced by the atom at the focus is well described by the paraxial model, once we have multiple atoms arranged across the focal plane, these additional polarisation components will affect the behaviour of the system. The field cancellation in the lens plane will also be affected. With these effects accounted for, the calculated extinction of the full vector field plotted with the red line in Fig. 8.3(a) is significantly weaker than the paraxial model prediction, peaking at around 40%.

Note that whilst we plot the transmission in Fig. 8.3(a) as a function of beam waist, what we mean by w_0 for the full vector model is not the measured beam waist in the focal plane, but rather w_0 is the effective beam waist that would be realised for the same input beam if it were calculated using the paraxial model (8.2.3). That is, for every value of w_0, we calculate the corresponding value of w_L for a paraxial beam, and then use that beam radius for the input field of the full vector model. For example, the measured $1/e$ waist of the $|E_+|$ field component in Fig. 8.3(d) is $w_0 \simeq 2.52\lambda$, which only differs slightly from the equivalent waist in the paraxial model ($w_0 = 2.5\lambda$).

The integral in Eq. (8.3.4) assumes a lens with infinite radius, although in practice for our choice of parameters the interval converges sufficiently (0.01%) by $\rho_L^{\max} \simeq 50\lambda$ and so to a good approximation we can assume that the input lens has the same radius as the output collection lens ($R_L = 90\lambda$).

8.4 Extinction from a random two-dimensional gas

8.4.1 Beer-Lambert model

Replacing the single atom with an ensemble of atoms is clearly going to affect the extinction of the beam. Trivially, one might assume that the total extinction or scattering of the

[d] The field in the focal plane of a lens is the Fourier transform of the field incident on the lens.

beam is just the sum of the extinction or scattering due to each individual atom. This is known as the Beer-Lambert model, which predicts that the transmission of an incident light beam through an ensemble of independent scatterers decays exponentially as the thickness, ℓ, and the 3D number density, N_{3D}, of the ensemble increase:

$$T_{BL} = \exp(-\sigma_{sc}^{(1)} N_{3D} \ell), \tag{8.4.1}$$

where $\sigma_{sc}^{(1)}$ is the single atom scattering cross-section from Eq. (4.4.14),

$$\sigma_{sc}^{(1)} = \frac{k}{\varepsilon_0}\mathrm{Im}(\alpha) = \frac{\sigma_{sc,0}^{(1)}}{1+(\Delta/\gamma_0)^2}, \tag{8.4.2}$$

and

$$\sigma_{sc,0}^{(1)} = \frac{6\pi}{k_0^2} = \frac{3\lambda_0^2}{2\pi}, \tag{8.4.3}$$

is the resonant ($\Delta = 0$) cross-section (4.4.15). For a 2D ensemble, we can define an equivalent 2D Beer-Lambert transmission

$$T_{BL} = \exp(-\sigma_{sc}^{(1)} N_{2D}), \tag{8.4.4}$$

where N_{2D} is the 2D number density. This exponential form can also be used to define the *optical depth* (OD):

$$\mathrm{T} \equiv \mathrm{e}^{-\mathrm{OD}}, \qquad \mathrm{OD} \equiv -\ln(T). \tag{8.4.5}$$

8.4.2 Deviation from the Beer-Lambert model

The Beer-Lambert model is a powerful tool in atomic physics, for example as a means of measuring the number density using the optical depth. However, recent experiments in cold (~ 100 μK) [18, 19, 141] and very hot (~ 100 K) [44] atomic vapours have demonstrated a deviation from the Beer-Lambert model at high number densities. This is manifested as an attenuation of the optical depth, i.e. the measured optical transmission is greater than predicted by (8.4.4). The reason for this is that the densities are now high enough that the interactions are not insignificant and the approximation that the atoms

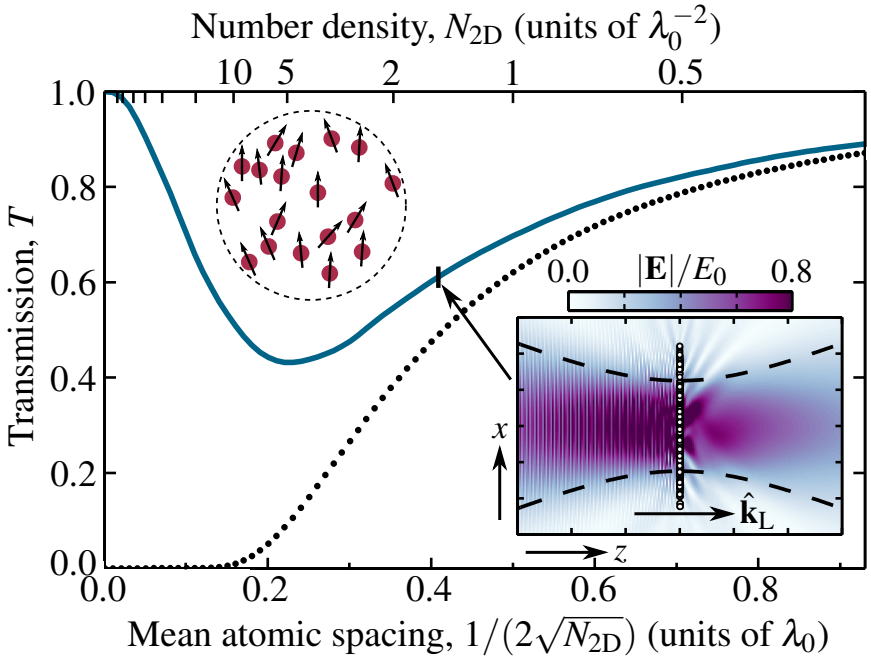

Figure 8.4: Resonant optical transmission of a Gaussian beam through a random 2D monolayer of $N = 100$ interacting dipoles as a function of mean atomic spacing $\langle R_{ij}\rangle = 1/(2\sqrt{N_{2D}})$ [140], where N_{2D} is the 2D number density. For decreasing mean atomic spacing, the interacting monolayer (blue solid line) deviates from T_{BL} [black dotted line - calculated from Eq. (8.4.4)], which assumes each dipole is a non-interacting opaque disk of cross sectional area $\sigma_{sc,0}^{(1)}$ (8.4.3). Each data point is averaged over 100 realisations. The beam waist is $w_0 \simeq 2.5\lambda$ and the collection lens has radius $R_L = 90\lambda_0$ and position $z_L = 150\lambda_0$. (Inset) Weak cancellation of the total electric field magnitude $|\mathbf{E}|$ in the xz plane downstream of the monolayer ($N_{2D} \simeq 1.5\lambda_0^{-2}$). x and z vary between $\pm 6\lambda_0$ and $\pm 30\lambda_0$ respectively. The beam is propagating in the $+z$ direction. The black dashed line shows the $1/e$ beam radius and the white circles the atom positions.

behave independently is no longer valid. As is the theme of this Thesis, the medium is behaving cooperatively, and this is being manifested as a reduced optical depth.

We can see the presence of this optical depth attenuation by calculating the transmission through a 2D gas of $N = 100$ cold atoms (i.e. ignoring atomic motion), where the atoms

are randomly and uniformly distributed in a 2D disk.[e] In Fig. 8.4 we plot this transmission as a function of 2D number density.

For low densities ($N_{2D} \ll \lambda_0^{-2}$, or $N_{3D} \ll \lambda_0^{-3}$ in 3D ensembles) the local field at each dipole is dominated by the external driving field since the scattered fields from neighbouring dipoles in the far field decay with $1/(k_0 R_{ij})$, where $R_{ij} = |\mathbf{R}_{ij}|$. The calculated transmission in Fig. 8.4 is therefore similar to that predicted by the non-interacting Beer-Lambert model.

However, as the density increases the transmission begins to deviate from the Beer-Lambert line. The extinction through the monolayer becomes increasingly attenuated as density increases until the infinitely dense limit where the medium becomes completely transparent. At first this may seem counterintuitive. As more and more atoms are placed within the focus of the beam, they radiate within the same mode and are driven by the strongest part of the beam. However, as we have seen in Sec. 5.2.3, the $1/R_{ij}^3$ near-field term of the dipole–dipole interaction results in each atom experiencing a divergent energy shift, which gets larger and larger for decreasing atom spacing. This results in a broadening and weakening of the extinction lineshape of the ensemble, eventually getting to the limit where the atoms are all completely shifted off resonance. However, unlike in the regular arrays of Chapters 6 and 7 where there were well defined eigenmodes which you could tune the driving field to, because we are averaging over many random configurations, the eigenmodes for each configuration are different and so become averaged out also, resulting in a broadening of the lineshape.

8.5 Extinction from a periodic two-dimensional array

8.5.1 Different lattice geometries

Our results from the previous Chapters would suggest that the behaviour of a structured array of atoms will be different to a random ensemble. Striking transmission phenomena have already been realised experimentally in arrays of scatterers, for example near

[e] We assume they are trapped in an infinitely deep potential well in z.

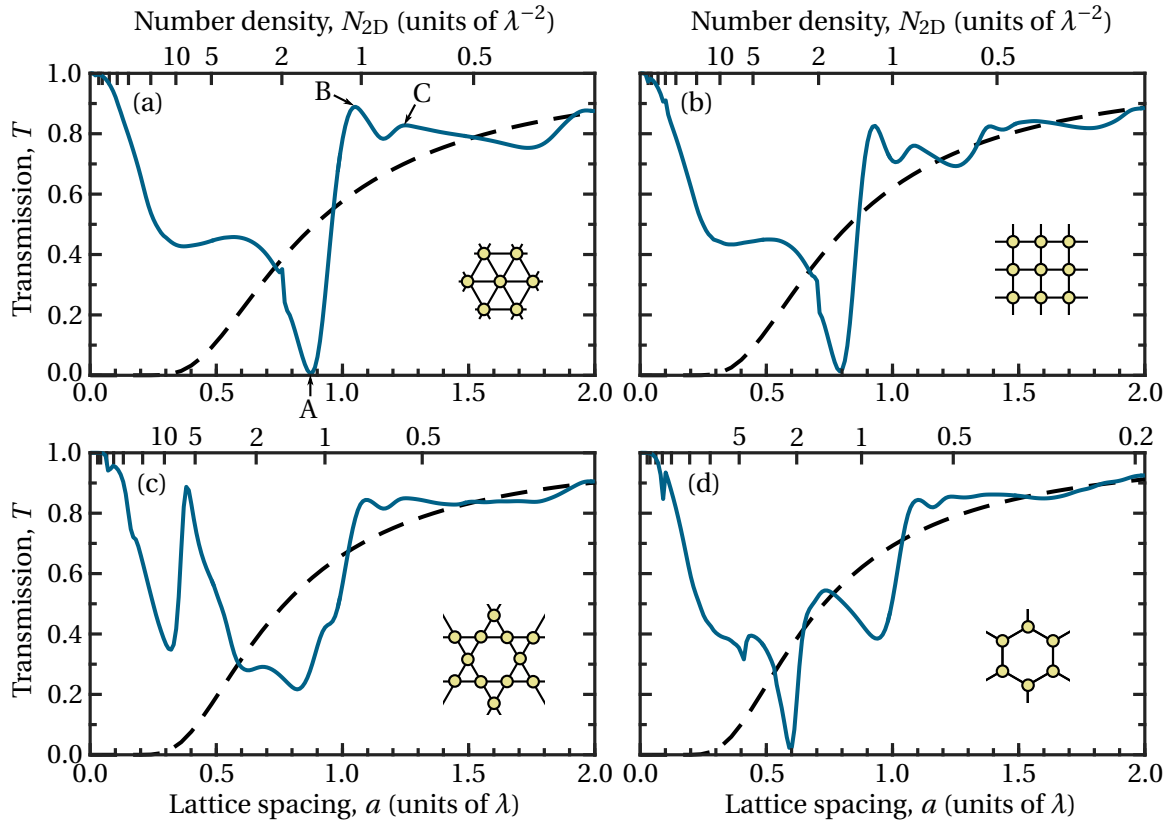

Figure 8.5: Resonant optical transmission of a Gaussian beam through periodic atomic array as a function of nearest-neighbour lattice spacing a. The lattice geometries and atom numbers are (a) triangular and $N = 102$, (b) square and $N = 100$, (c) kagome and $N = 97$, (d) hexagonal and $N = 96$. The transmission through each lattice (blue solid lines) exhibit strong deviation from the non-interacting Beer-Lambert transmission (black dashed lines). A, B and C in (a) correspond to the lattice spacings used in Fig. 8.7. The beam and lens parameters are the same as in Fig. 8.4.

perfect extinction and transmission through arrays of gold nanorods [142], linewidth narrowing in metamolecules [57], and extraordinary optical transmission (EOT) in hole arrays [143]. In addition to diffraction and interference effects, the coupling to collective and plasmonic modes plays a crucial role in explaining these phenomena [144, 145, 146]. The advantages of atomic systems over other plasmonic or diffractive systems include easy access to the quantum regime, much higher Q-factors, and significantly less non-

radiative decay (see Sec. 1.4).

In Fig. 8.5 we plot the transmission of a focussed Gaussian beam through atomic lattices of varying lattice spacing and lattice geometry. The driving field is resonant with the bare-atom transition frequency $\Delta = 0$. As in Fig. 8.4, we plot the non-interacting Beer-Lambert transmission for comparison. The deviation from this non-interacting model is now very different to the random monolayer in Fig. 8.4. Rather than seeing a gradual attenuation of the extinction for increasing number densities, the transmission now oscillates wildly above and below the non-interacting level. In fact, for the triangular (a), square (b) and hexagonal (d) lattices, there exists a *magic lattice spacing* for which the medium is almost completely opaque (triangular: $\epsilon_{\max} > 99\%$ at $a = 0.87\lambda$; square: $\epsilon_{\max} > 98\%$ at $a = 0.79\lambda$; hexagonal: $\epsilon_{\max} > 98\%$ at $a = 0.60\lambda$). The position of these magic lattice spacings appears to scale with packing efficiency: the triangular lattice has the largest packing efficiency (density for a given lattice spacing) and correspondingly the largest magic lattice spacing. The hexagonal has the lowest packing efficiency and the smallest magic lattice spacing. It is not immediately obvious why this should be, although we shall leave further investigation of this to future works.

Interestingly, whilst in Chap. 7 the kagome lattice was the most promising geometry in terms of realising strong mode interferences, those same mode interferences mean that the peak extinction is much less, and the other lattices now provide much better peak extinctions. Different lattices therefore have different advantages.

8.5.2 Eigenvalue behaviour

In Fig. 8.6 we plot the extinction as a function of lattice spacing and detuning for the triangular lattice from Fig. 8.5(a). Similar to the extinction cross-section plots in Fig. 7.3, the extinction lineshape appears to narrow and shift from blue to red over the range of lattice spacings considered. In Fig. 8.6(b) we plot the regions for which the extinction is greater than 98% (red) and 90% (dark blue). We see that rather than there being just a single magic lattice spacing, there is a range of lattice spacings and detunings for which a large extinction is possible. The black dashed line in Fig. 8.6(b) indicates that the location of the magic lattice spacing from Fig. 8.5(a) corresponds to where the peak of extinction

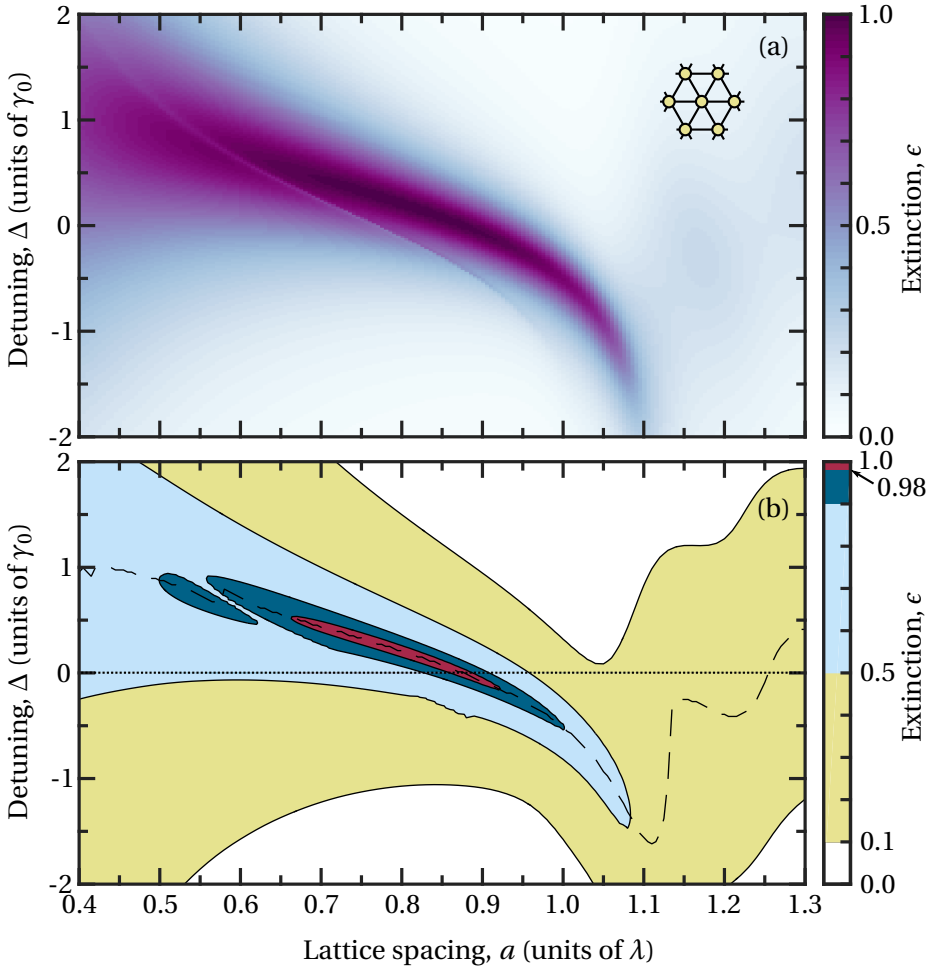

Figure 8.6: Optical extinction $\epsilon \equiv 1 - T$ as a function of lattice spacing a and detuning Δ through the same triangular two-dimensional lattices as in Fig. 8.5(a). The colormaps are (a) continuous and (b) discrete to highlight different ranges of extinction. The black dashed line in (b) shows the shifted linecentre of the extinction. The beam and lens parameters are the same as in Fig. 8.4.

lineshape moves through resonance with the driving field (which in Fig. 8.5 is $\Delta = 0$). Conversely, the peak in the transmission in Fig. 8.5(a) occurs around $a = 1.05\lambda$ at which point the extinction is now shifted off resonance and the driving field at $\Delta = 0$ is in the wings of the lineshape.

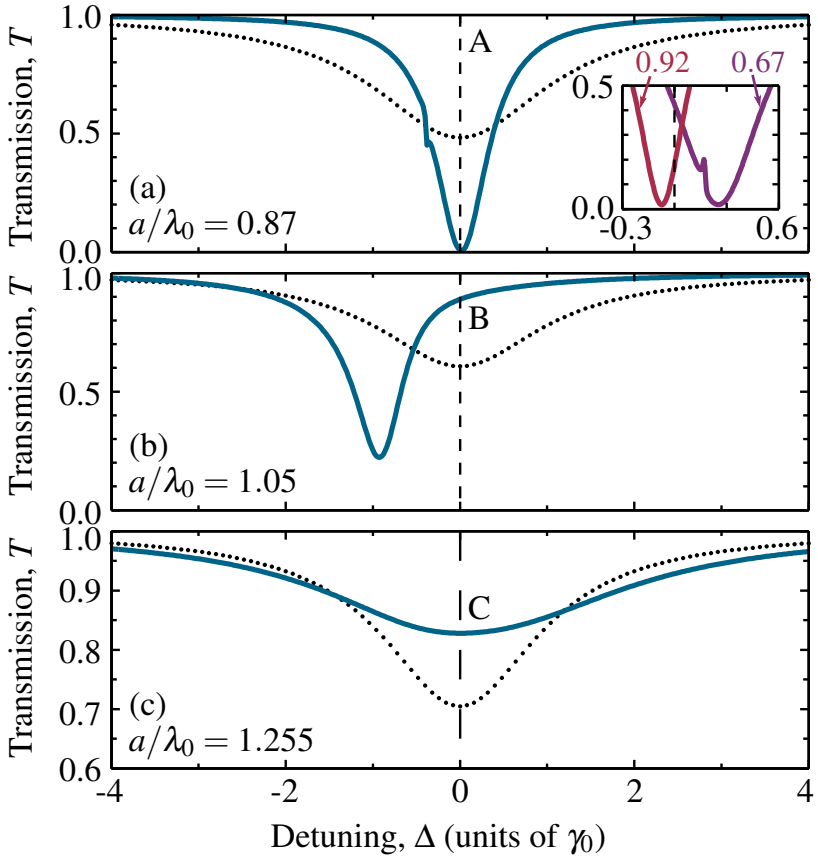

Figure 8.7: Transmission as a function of detuning (solid lines) through an $N = 102$ triangular lattice of interacting dipoles. The lattice spacings in (a–c) correspond to those labeled A, B and C in Fig. 8.5. The transmission at lattice spacings of $a = \{0.67, 0.92\}\lambda_0$ are also plotted in the inset of (a). The black dotted lines plot the Beer-Lambert non-interacting transmission (8.4.4). The beam and lens parameters are the same as in Fig. 8.4. The vertical dashed lines at $\Delta = 0$ have dash lengths $\Delta T = 0.05$.

To highlight this behaviour, in Fig. 8.7 we plot the transmission lineshapes from Fig. 8.6 at the magic lattice spacing $a = 0.87\lambda$ (a), the transmission maximum at $a = 1.05\lambda$ (b), and an additional local transmission maximum at $a = 1.255\lambda$ (c). The magic lattice spacing in (a) occurs because the lineshape is centred on $\Delta = 0$ and is strongly subradiant. The eigenmode behaviour here is dominated by two nearly degenerate eigenmodes with $\gamma_p \simeq 0.37\gamma_0$ with shifts $\Delta_p \simeq 0$. In Sec. 4.6.3 we showed how it is this subradiance that leads to

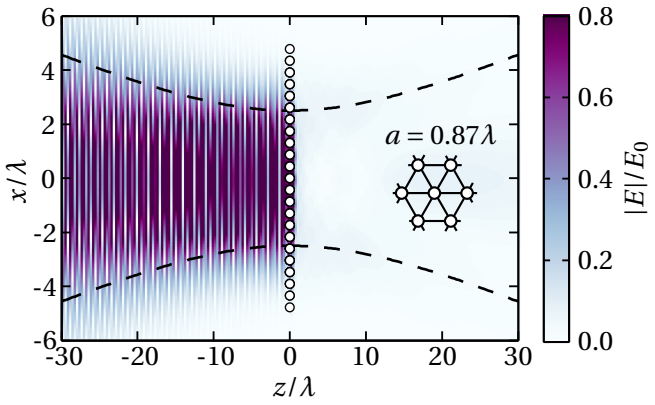

Figure 8.8: The total electric field magnitude for a (paraxial) Gaussian beam focussed on a triangular lattice with the magic lattice spacing $a = 0.87\lambda$ and driven on resonance $\Delta = 0$. The beam is polarised linearly in y and propagating with wavevector $\hat{\mathbf{k}} = \hat{\mathbf{z}}$. Efficient cancellation of the driving field by the scattered fields results in extinction and reflection of the beam. The dipole positions are indicated with white circles and the black dashed lines show the 1/e width of the beam.

an increase in the peak extinction. The lineshape in Fig. 8.7(b) is again subradiant and therefore exhibits a stronger extinction than the non-interacting model predicts, however it is now shifted off resonance and so the extinction at $\Delta = 0$ is much weaker, resulting in the transmission maximum in Fig. 8.5(a). In Fig. 8.7(c) the lineshape is again centred on $\Delta = 0$, although now it is superradiant ($\gamma_p \simeq 2\gamma_0$) which reduces the peak extinction.

8.5.3 Potential applications

The near-perfect extinction exhibited in the triangular, square and hexagonal lattices in Fig. 8.5(a,b,d) could provide a novel new way of realising strong atom–light coupling. Out of the three, the triangular lattice is perhaps the most promising as its magic lattice spacing is largest (and therefore perhaps the easiest to realise) and it exhibits the largest range in transmission ($< 1\%$ to $\simeq 90\%$) for a small change in lattice spacing ($a = 0.87\lambda_0 \rightarrow 1.05\lambda_0$). The transmission minimum at the magic lattice spacing also corresponds to a reflection maximum, observable in the inset to Fig. 8.8, as well as by calcu-

lating the power reflected back through the focusing lens at $z = -z_L$ (reflection $R \gg 98\%$ for the triangular lattice at $a = 0.87\lambda$). Consequently the monolayer can be switched between distinct transmission and reflection states, in the same spatial mode, which is the ideal starting point for a gate or all-optical transistor. A potential use for this in a Rydberg gate scheme is discussed in Sec. 9.3.

We found that changing the polarisation has little effect on the transmission behaviour. Furthermore, if we wanted to realise this extinction in a closed 2-level transition, such as in an alkali metal transition (see Sec. 3.2.2), where the dipoles are restricted to a single polarisation, the difference in transmission behaviour compared with the behaviours plotted here is only a few percent. This extinction should therefore be realisable in a number of different systems.

8.6 Imperfect trapping

8.6.1 Finite trapping depth

When considering a possible realization of this in an atomic experiment, it is necessary to consider how effects such as finite trapping depth [Fig. 8.9(a)] and imperfect filling [Fig. 8.9(b)] affect the extinction. Following the approach in [14], we assume the trapping potential confining the atoms in a square lattice has the form

$$V = V_0 \left[\sin^2\left(\frac{\pi x}{a}\right) + \sin^2\left(\frac{\pi y}{a}\right) \right], \tag{8.6.1}$$

where $V_0 = sE_R$ is the amplitude of the trapping potential, $E_R = \pi^2\hbar^2/2ma^2$ is the lattice recoil energy and m is the mass of the atom. We assume an infinitely deep trapping potential in the $z = 0$ plane. We assume the wavefunction of each atom has the form of a ground state harmonic oscillator:

$$\Psi_i(\mathbf{R}_i) = \frac{1}{(\pi^3 l^4 l_z^2)^{1/4}} \exp\left(-\frac{X_i^2 + Y_i^2}{2l^2} - \frac{Z_i^2}{2l_z^2} \right), \tag{8.6.2}$$

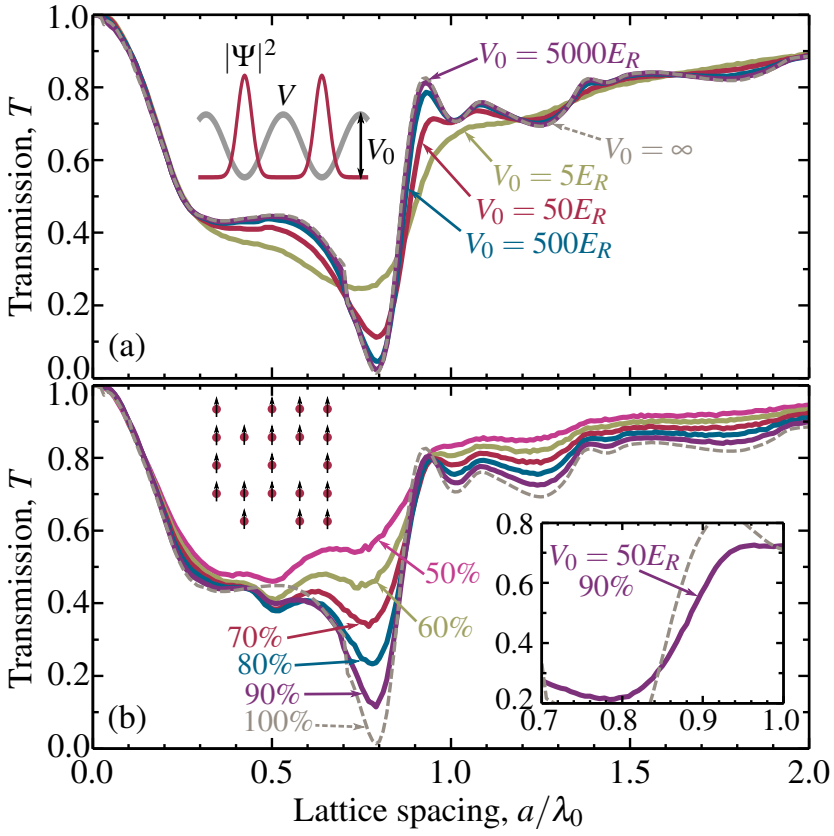

Figure 8.9: The effect of finite trap depth (a) and finite filling factors (b) on resonant optical transmission through a 10×10 square lattice. (a) The trap depths are $V_0 = \infty$ (grey dashed), $V_0 = 5000E_R$ (purple), $V_0 = 500E_R$ (blue), $V_0 = 50E_R$ (red), and $V_0 = 5E_R$ (green), where E_R is the recoil energy and the filling is 100%. (b) The lattice sites are randomly occupied with filling factors of 100% (grey dashed), 90% (purple), 80% (blue), 70% (red), 60% (green), and 50% (pink), with $V_0 = \infty$. The purple line in the inset is a combination of finite trap depth ($V_0 = 50E_R$) and 90% filling. Each line is an average of several hundred realizations. The same lens and beam parameters as in Fig. 8.4 are used.

where $\mathbf{R}_i = (X_i, Y_i, Z_i)$ is the separation of atom i from the ith lattice site, $l = as^{-1/4}/\pi$ and $l_z = \sqrt{\hbar/m\omega_z}$. The atomic positions are sampled at random using the probability distribution $\rho_i(\mathbf{r}) = |\Psi_i(\mathbf{R}_i)|^2$ which is a Gaussian with 1/e radius l in the xy plane.

Typical trap depths in Mott-Insulator experiments lie in the range $V_0 = (20-50)E_R$ [51, 83, 120, 147] (E_R is the recoil energy), although $V_0 \sim 10^3 E_R$ is also possible [51, 147]. The transmission for different trap depths is plotted in Fig. 8.9 (assuming 100% filling efficiency). Each line corresponds to the average of hundreds of realisations. Clearly, the magnitude of the range in extinction decreases as the atomic positions become less and less ordered, tending gradually towards the behaviour of a random monolayer as in Fig. 8.4.

8.6.2 Finite filling efficiency

In a real experiment not every lattice site will be occupied by an atom. We model this in Fig. 8.9 by randomly removing a proportion of the atoms. Filling efficiency greater than 90% can be achieved [119, 120, 147, 148], which when combined with a trap depth of $V_0 = 50E_R$ [Fig. 8.9(b), inset], still gives a significant range in transmission [(21 ± 5)% to (72 ± 2)% between $a \simeq 0.8\lambda_0$ and $a \simeq 0.95\lambda_0$]. The extinction is also robust to small changes in the direction of incidence of the laser: rotating the incident laser 10° from the normal of a 10×10 square lattice still produces a peak extinction of over 90%.

The number of lattice sites does not have to be large to observe strong extinction: a 4×4 perfect square lattice peaks at $\epsilon = 96\%$ (for $w_0 = \lambda$). With 100% filling, increasing the atom number increases the peak extinction. The optimal beamwidth for maximizing the extinction scales with $\sqrt{N}$ ($w_0 \simeq 2.5\lambda$ [f] optimizes the extinction for square and triangular lattices with $N \simeq 100$). However, for 50% filling as in Fig. 8.7(b), adding more lattice sites (e.g., 200 sites with 100 vacancies) makes little difference to the transmission, meaning high filling factors are essential for efficient extinction.

[f] The vector field propagation model results in a beam waist of $w_0 \simeq 2.52\lambda$.

Chapter Summary

- To maximise coupling between light and a single atom requires a very tightly focussed laser beam
- This condition can be significantly relaxed by replacing the single atom with a 2D square, triangular, or hexagonal atomic lattice
- For each lattice, a magic lattice spacing exists for which a resonant driving field is almost perfectly reflected by the lattice
- This near-perfect extinction is due to mode matching between the driving and scattered fields as well as subradiant behaviour of the atomic ensemble
- The extinction is robust to finite lattice depths and vacant lattice sites

Chapter 9

Conclusions and Outlook

9.1 Different geometries; different advantages

In this Thesis we have observed many interesting cooperative phenomena in different atomic lattice geometries. We have seen that different lattice structures have different advantages. For example, if we want to realise enhanced extinction, then regular lattices such as triangular, square, and hexagonal lattices are best (Chap. 8). If instead we want to observe interferences between different eigenmodes producing strong Fano resonances, then the semi-regular kagome lattice is better (Chap. 7). Hopefully this work will motivate further investigations into different structures and geometries, opening the door to many new and exciting phenomena with potentials for new applications and understanding. For example, preliminary investigations have shown that other semi-regular lattices (for example the Lieb lattice [117]) may also exhibit mode interferences like the ones observed in the kagome lattice (Chap. 7), further strengthening the theory that the semi-regular nature has something to do with these cooperative modes.

We began to investigate in Chaps. 5 and 6 how changing the driving field affects which eigenmodes are driven. Using a similar model to ours, Jenkins and Ruostekoski [14] showed that by tailoring the phase profile of the incident driving field, it is possible to selectively excite different cooperative eigenmodes of 2D atomic lattices, resulting in sub-

wavelength control of the excitation localisation across the lattice. For example, by tailoring the driving field to couple only to highly subradiant modes, it may be possible to increase even further the efficiency of the extinction in Chap. 8.

9.2 Strong driving

Whilst in this Thesis we limited our investigation to the weak driving limit for which finite excited state population is ignored, there exist several approaches for extending this to include stronger driving fields. Short of solving the full many-atom quantum master equation (3.3.25), we could investigate the many-atom optical Bloch equations (3.3.27) [35, 79], adding additional higher order correlation terms as necessary [37, 79]. For example, the problem of excitation hopping around a spin lattice [40, 50] has applications in areas such as quantum topological states [149, 150] and quantum simulation of phenomena such as photosynthesis [151, 152].

9.3 Rydberg gate schemes

One way of making use of the near-perfect extinction presented in Chap. 8 could be to incorporate it into a scheme for a Rydberg phase gate, for use in a quantum information circuit. For example, a setup similar to that described in [124] could be used. Consider an atom with three energy levels: a ground state $|g\rangle$, an excited state $|e\rangle$, and a further highly excited Rydberg state $|R\rangle$. Let there be two driving fields, one coupling the states $|g\rangle$ and $|e\rangle$ (Ω_{ge}), and the other coupling $|e\rangle$ and $|R\rangle$ (Ω_{eR}). Dipole–dipole interactions between two atoms both in the Rydberg state shift the $|e\rangle$ to $|R\rangle$ transition off resonance with Ω_{eR}, meaning that the atom in question cannot be excited to $|R\rangle$ if there already exists another Rydberg atom within a blockade radius of the first atom. The $|g\rangle$ to $|e\rangle$ transition is also affected by this, and so depending on whether the atom can be excited to $|R\rangle$ or not, the Ω_{ge} beam will or will not couple to these states. The presence of a second *control* Rydberg atom can therefore determine whether or not the Ω_{ge} laser beam is scattered by the atom or not. The fidelity of the gate operation is limited by how efficiently the atom can scatter

the light. If we arrayed the atoms in a lattice structure as in Chap. 8, then not only could we significantly increase the efficiency of the atom–light coupling, but the scattering also now happens into a single spatial mode rather than anywhere into the 4π solid angle surrounding the atom (this can be seen in Fig. 8.8). The light is either transmitted or reflected by the lattice; the amount of scattering into other modes is significantly reduced by the cooperative behaviour. Such a gate proposal will be the subject of future work.

9.4 Atomic crystallisation

Throughout this Thesis we have ignored the effect of radiation recoil when an atom radiates a photon. The dipole-dipole force can be used to crystallise an ensemble of atoms in particular structures [153]. Incorporating this with the various cooperative phenomena we have observed may provide a further avenue of interest.

9.5 Beyond atoms

By modifying the polarisability, we can apply our coupled equations to different types of electric (and magnetic) dipole lattices. There has also been recent interest in how different species of dipole (e.g., atoms and plasmonic nanostructures) couple with one another [105] and whether the creation of a hybrid system employing the advantages of both (e.g., long atomic lifetimes, precise nanoparticle localisation) might be possible. All of these things provide promising avenues for future investigations.

Appendix A

Solutions to the simple harmonic oscillator

A.1 Steady-state solution

The equation of motion describing the electron displacement s described in Sec. 2.5 is given by

$$\frac{\mathrm{d}^2 s^2}{\mathrm{d}t^2} + \Gamma \frac{\mathrm{d}s}{\mathrm{d}t} + \omega_0^2 s = \frac{2e}{m}\left[E_0^{\Re}(\mathbf{r}_0)\cos\omega t + E_0^{\Im}(\mathbf{r}_0)\sin\omega t\right]. \tag{A.1.1}$$

From the form of the electric field, an appropriate trial solution is $s(t) = A\cos\omega t + B\sin\omega t$. Substituting this into Eq. (A.1.1) gives and equating the cos and sin terms gives

$$\cos: \qquad -\omega^2 A + \omega\Gamma B + \omega_0^2 A = \frac{2e}{m}E_0^{\Re}, \tag{A.1.2a}$$

$$\sin: \qquad -\omega^2 B - \omega\Gamma A + \omega_0^2 B = \frac{2e}{m}E_0^{\Im}. \tag{A.1.2b}$$

Writing this equation as

$$\begin{pmatrix} \omega_0^2 - \omega^2 & \omega\Gamma \\ -\omega\Gamma & \omega_0^2 - \omega^2 \end{pmatrix}\begin{pmatrix} A \\ B \end{pmatrix} = \frac{2e}{m}\begin{pmatrix} E_0^{\Re} \\ E_0^{\Im} \end{pmatrix}, \tag{A.1.3}$$

the solution is

$$\begin{pmatrix} A \\ B \end{pmatrix} = \frac{2e}{m} \frac{1}{(\omega_0^2 - \omega^2)^2 + \omega^2\Gamma^2} \begin{pmatrix} \omega_0^2 - \omega^2 & -\omega\Gamma \\ \omega\Gamma & \omega_0^2 - \omega^2 \end{pmatrix} \begin{pmatrix} E_0^{\Re} \\ E_0^{\Im} \end{pmatrix}, \tag{A.1.4}$$

giving

$$A = \frac{2e}{m} \frac{(\omega_0^2 - \omega^2)E_0^{\Re} - \omega\Gamma E_0^{\Im}}{(\omega_0^2 - \omega^2)^2 + \omega^2\Gamma^2}, \tag{A.1.5a}$$

$$B = \frac{2e}{m} \frac{(\omega_0^2 - \omega^2)E_0^{\Im} + \omega\Gamma E_0^{\Re}}{(\omega_0^2 - \omega^2)^2 + \omega^2\Gamma^2}, \tag{A.1.5b}$$

where $A = 2s^{\Re}$ and $B = 2s^{\Im}$.

A.2 Transient single atom solution solution

The transient solution to

$$\frac{\mathrm{d}^2 s_t^2}{\mathrm{d}t} + \Gamma \frac{\mathrm{d}s_t}{\mathrm{d}t} + \omega_0^2 s_t = 0, \tag{A.2.1}$$

has the form $s_t(t) = C\mathrm{e}^{Dt}$. Substituting this in gives

$$D^2 C\mathrm{e}^{Dt} + D\Gamma C\mathrm{e}^{Dt} + \omega_0^2 C\mathrm{e}^{Dt} = 0, \tag{A.2.2a}$$

$$D^2 + D\Gamma + \omega_0^2 = 0, \tag{A.2.2b}$$

$$\begin{aligned} D &= -\frac{\Gamma}{2} \pm \frac{1}{2}\sqrt{\Gamma_0^2 - 4\omega_0^2} \\ &= -\gamma \pm \sqrt{\gamma^2 - \omega_0^2}, \end{aligned} \tag{A.2.2c}$$

where we have set $\gamma = (\Gamma/2)$. For atomic resonances, $\gamma \ll \omega_0$ and so the square root term in Eq. (A.2.2c) introduces a factor of $\mathrm{i} = \sqrt{-1}$,

$$D = -\gamma \pm \mathrm{i}\sqrt{\omega_0^2 - \gamma^2} \tag{A.2.3a}$$

$$\begin{aligned} s_t(t) =& C\,\mathrm{e}^{-\gamma t}\left(\mathrm{e}^{\mathrm{i}\sqrt{\omega_0^2-\gamma^2}\,t} + \mathrm{e}^{-\mathrm{i}\sqrt{\omega_0^2-\gamma^2}\,t}\right) \\ =& 2C\,\mathrm{e}^{-\gamma t}\cos\left(\sqrt{\omega_0^2-\gamma^2}\,t\right) \\ =& s_t(0)\,\mathrm{e}^{-\gamma t}\cos\left(\sqrt{\omega_0^2-\gamma^2}\,t\right). \end{aligned} \tag{A.2.3b}$$

This transient solution decays with lifetime $(1/\gamma)$, after which the behaviour is dominated by the steady-state solution.

Appendix B

Derivation of the cooperative decay Γ_{ij} and shift Ω_{ij}

In this Appendix we will derive the expressions for the cooperative decay Γ_{ij} and Ω_{ij} from Sec. 3.3.4. In doing so, we will also derive the single atom natural decay rate Γ_0 (see Sec. 2.3.3). This has been adapted from Sec. 14.1 of [70] to include three excited levels rather than just one.

B.1 Single photon, double time integral

In order to do this, we need to calculate the single photon term from (2.3.7),

$$\int_0^{\Delta t} \mathrm{d}t_1 \int_0^{t_1} \mathrm{d}t_2 \, \gamma_{ij}^{\alpha\beta}(t_1 - t_2) \equiv \left(\frac{1}{2}\Gamma_{ij}^{\alpha\beta} + \mathrm{i}\Omega_{ij}^{\alpha\beta} \right), \tag{B.1.1}$$

where from (3.3.15)

$$\gamma_{ij}^{\alpha\beta}(\tau) = \sum_{|\omega_k - \omega_0| < \vartheta} \left(\kappa_{k\alpha} \kappa_{j\beta}^* \right) \mathrm{e}^{-\mathrm{i}(\omega_k - \omega_0)\tau + \mathrm{i}\mathbf{k}\cdot(\mathbf{r}_i - \mathbf{r}_j)}. \tag{B.1.2}$$

This sum is the sum over modes Λ which includes a sum over the frequencies, as shown, and also a sum over the two polarisations of the mode $\hat{\boldsymbol{\epsilon}}_m$ and $\hat{\boldsymbol{\epsilon}}_n$, where $\hat{\boldsymbol{\epsilon}}_m \cdot \hat{\boldsymbol{\epsilon}}_n = \delta_{mn}$ and

$\hat{\boldsymbol{\epsilon}}_m \cdot \mathbf{k} = 0$. From the definition of $\kappa_{j\alpha}$ (3.3.12) and $\mathbf{u}_k(\mathbf{r})$ (2.2.12), we have

$$\sum_{m,n} \kappa_{k\alpha}\kappa^*_{k\beta} \equiv \frac{\omega_k}{2\hbar\varepsilon_0 V}\Big[\big(\mathbf{d}_{\alpha g}\cdot\hat{\boldsymbol{\epsilon}}_m\big)\big(\mathbf{d}^*_{\beta g}\cdot\hat{\boldsymbol{\epsilon}}_m\big) + \big(\mathbf{d}_{\alpha g}\cdot\hat{\boldsymbol{\epsilon}}_n\big)\big(\mathbf{d}^*_{\beta g}\cdot\hat{\boldsymbol{\epsilon}}_n\big)\Big]. \tag{B.1.3}$$

Let us first write that $\mathbf{d}_{\alpha g} = d_{\alpha g}\hat{\mathbf{d}}_{\alpha g}$ and assuming that $d_{\alpha g} = d_{eg}$ for all possible directions α, then

$$\begin{aligned}
&\big(\mathbf{d}_{\alpha g}\cdot\hat{\boldsymbol{\epsilon}}_m\big)\big(\mathbf{d}^*_{\beta g}\cdot\hat{\boldsymbol{\epsilon}}_m\big) + \big(\mathbf{d}_{\alpha g}\cdot\hat{\boldsymbol{\epsilon}}_n\big)\big(\mathbf{d}^*_{\beta g}\cdot\hat{\boldsymbol{\epsilon}}_n\big) \\
&\qquad = |d_{eg}|^2\Big[\big(\hat{\mathbf{d}}_{\alpha g}\cdot\hat{\boldsymbol{\epsilon}}_m\big)\big(\hat{\mathbf{d}}^*_{\beta g}\cdot\hat{\boldsymbol{\epsilon}}_m\big) + \big(\hat{\mathbf{d}}_{\alpha g}\cdot\hat{\boldsymbol{\epsilon}}_n\big)\big(\hat{\mathbf{d}}^*_{\beta g}\cdot\hat{\boldsymbol{\epsilon}}_n\big)\Big] \\
&\qquad = |d_{eg}|^2\Big[\delta_{\alpha\beta} - \big(\hat{\mathbf{d}}_{\alpha g}\cdot\hat{\mathbf{k}}\big)\big(\hat{\mathbf{d}}^*_{\beta g}\cdot\hat{\mathbf{k}}\big)\Big]
\end{aligned} \tag{B.1.4}$$

where $\hat{\mathbf{k}}$ is the unit vector in the direction $\mathbf{k}$.

The sum over the mode vectors $\mathbf{k}$ can be converted to a continuous integral

$$\frac{1}{V}\sum_{\mathbf{k}} \to \frac{1}{(2\pi)^3}\int \mathrm{d}^3\mathbf{k} \to \frac{1}{(2\pi c)^3}\int_{\omega_0-\vartheta}^{\omega_0+\vartheta} {\omega_k}^2 \mathrm{d}\omega_k \int \mathrm{d}\omega_k, \tag{B.1.5}$$

where $\mathrm{d}\omega_k$ is the differential solid angle. The angular integral becomes

$$\int \mathrm{d}\omega_k \Big[\delta_{\alpha\beta} - \big(\hat{\mathbf{d}}_{\alpha g}\cdot\hat{\mathbf{k}}\big)\big(\hat{\mathbf{d}}^*_{\beta g}\cdot\hat{\mathbf{k}}\big)\Big]\, \mathrm{e}^{\mathrm{i}(kr_{ij})(\hat{\mathbf{k}}\cdot\hat{\mathbf{r}}_{ij})}, \tag{B.1.6}$$

where $\mathbf{r}_{ij} \equiv \mathbf{r}_i - \mathbf{r}_j = r_{ij}\hat{\mathbf{r}}_{ij}$. The exponential plane wave can be expanded in terms of Legendre polynomials $P_\ell(\cos\theta)$,

$$\mathrm{e}^{\mathrm{i}(kr_{ij})(\hat{\mathbf{k}}\cdot\hat{\mathbf{r}}_{ij})} = \sum_{\ell=0}^{\infty}(2\ell+1)\,\mathrm{i}^\ell\, j_\ell(kr_{ij})\, P_\ell\big(\hat{\mathbf{k}}\cdot\hat{\mathbf{r}}_{ij}\big), \tag{B.1.7}$$

where $j_\ell(x)$ is a spherical Bessel function. To solve (B.1.6), let us consider separately the cases where $\alpha = \beta$ and $\alpha \neq \beta$.

B.1.1 $\alpha = \beta$

Using the definitions $P_0(x) = 1$ and $P_2(x) = (3x^2 - 1)/2$, we can rewrite

$$1 - |\hat{\mathbf{d}}_{\alpha g} \cdot \hat{\mathbf{k}}|^2 \;=\; \frac{2}{3}\Big(P_0\left(\hat{\mathbf{d}}_{\alpha g} \cdot \hat{\mathbf{k}}\right) - P_2\left(\hat{\mathbf{d}}_{\alpha g} \cdot \hat{\mathbf{k}}\right)\Big). \tag{B.1.8}$$

This makes the angular integral (B.1.6)

$$\int \mathrm{d}\omega_k \frac{2}{3}\Big[P_0\left(\hat{\mathbf{d}}_{\alpha g} \cdot \hat{\mathbf{k}}\right) - P_2\left(\hat{\mathbf{d}}_{\alpha g} \cdot \hat{\mathbf{k}}\right)\Big] \sum_{\ell=0}^{\infty} (2\ell+1)\,\mathrm{i}^{\ell}\, j_{\ell}(kr_{ij})\, P_{\ell}\left(\hat{\mathbf{k}} \cdot \hat{\mathbf{r}}_{ij}\right). \tag{B.1.9}$$

The Legendre polynomials are related to the spherical harmonics $Y_{\ell m}$ via the spherical harmonic addition theorem

$$P_{\ell}(\mathbf{u} \cdot \mathbf{v}) = \frac{4\pi}{2\ell+1} \sum_{m=-\ell}^{\ell} Y_{\ell m}\left(\theta_u, \phi_u\right) Y^*_{\ell m}\left(\theta_v, \phi_v\right), \tag{B.1.10}$$

where the vector $\mathbf{u}(\mathbf{v})$ has coordinates $\theta_{u(v)}$ and $\phi_{u(v)}$. This relation comes from the double angle formulae $\cos(\theta + \theta')$. The spherical harmonics are orthogonal

$$\int \mathrm{d}\Omega Y_{\ell m}(\theta, \phi)\, Y^*_{\ell' m'}(\theta, \phi) = \delta_{\ell \ell'} \delta_{m m'}. \tag{B.1.11}$$

The product of two Legendre polynomials, as in (B.1.9), is therefore

$$
\begin{aligned}
&\int \mathrm{d}\omega_k P_\ell(\hat{\mathbf{k}}\cdot\hat{\mathbf{r}}_{ij})\, P_{\ell'}(\hat{\mathbf{d}}_{\alpha g}\cdot\hat{\mathbf{k}}) \\
&= \int \mathrm{d}\omega_k \left(\frac{4\pi}{2\ell+1}\right)\left(\frac{4\pi}{2\ell'+1}\right) \sum_{m=-\ell}^{\ell} Y_{\ell m}(\theta_k,\phi_k)\, Y^*_{\ell m}(\theta_r,\phi_r) \sum_{m'=-\ell'}^{\ell'} Y_{\ell' m'}(\theta_\alpha,\phi_\alpha)\, Y^*_{\ell' m'}(\theta_k,\phi_k) \\
&= \left(\frac{4\pi}{2\ell+1}\right)\left(\frac{4\pi}{2\ell'+1}\right) \sum_{m=-\ell}^{\ell} \sum_{m'=-\ell'}^{\ell'} Y_{\ell' m'}(\theta_\alpha,\phi_\alpha)\, Y^*_{\ell m}(\theta_r,\phi_r) \int \mathrm{d}\omega_k \Big[Y_{\ell m}(\theta_k,\phi_k)\, Y^*_{\ell' m'}(\theta_k,\phi_k) \Big] \\
&= \left(\frac{4\pi}{2\ell+1}\right)^2 \sum_{m=-\ell}^{\ell} Y_{\ell m}(\theta_\alpha,\phi_\alpha)\, \delta_{\ell\ell'}\, Y^*_{\ell m}(\theta_r,\phi_r) \\
&= \left(\frac{4\pi}{2\ell+1}\right) P_\ell\left(\hat{\mathbf{d}}_{\alpha g}\cdot\hat{\mathbf{r}}_{ij}\right) \delta_{\ell\ell'}
\end{aligned}
\tag{B.1.12}
$$

(B.1.6) then becomes

$$
\begin{aligned}
&\int \mathrm{d}\omega_k \frac{2}{3}\Big[P_0\left(\hat{\mathbf{d}}_{\alpha g}\cdot\hat{\mathbf{k}}\right) - P_2\left(\hat{\mathbf{d}}_{\alpha g}\cdot\hat{\mathbf{k}}\right) \Big] \sum_{\ell=0}^{\infty} (2\ell+1)\, \mathrm{i}^\ell\, j_\ell(kr_{ij})\, P_\ell\left(\hat{\mathbf{k}}\cdot\hat{\mathbf{r}}_{ij}\right) \\
&\qquad = \frac{8\pi}{3}\Big[j_0(kr_{ij}) P_0\left(\hat{\mathbf{r}}\cdot\hat{\mathbf{d}}_{\alpha g}\right) + j_2(kr_{ij}) P_2\left(\hat{\mathbf{r}}\cdot\hat{\mathbf{d}}_{\alpha g}\right) \Big].
\end{aligned}
\tag{B.1.13}
$$

B.1.2 $\alpha \neq \beta$

The $\alpha \neq \beta$ terms in (B.1.6) can be written (using $\mathbf{d}^*_{\beta g} = \mathbf{d}_{g\beta}$)

$$
\begin{aligned}
&-\int \mathrm{d}\omega_k \big(\hat{\mathbf{d}}_{\alpha g}\cdot\hat{\mathbf{k}}\big)\big(\hat{\mathbf{d}}_{g\beta}\cdot\hat{\mathbf{k}}\big) \sum_{\ell=0}^{\infty} (2\ell+1)\, \mathrm{i}^\ell\, j_\ell(kr_{ij})\, P_\ell\left(\hat{\mathbf{k}}\cdot\hat{\mathbf{r}}_{ij}\right) \\
&= -\sum_{\ell=0}^{\infty} (2\ell+1)\, \mathrm{i}^\ell\, j_\ell(kr_{ij}) \int \mathrm{d}\omega_k P_1\big(\hat{\mathbf{d}}_{\alpha g}\cdot\hat{\mathbf{k}}\big) P_1\big(\hat{\mathbf{d}}_{g\beta}\cdot\hat{\mathbf{k}}\big) P_\ell\left(\hat{\mathbf{k}}\cdot\hat{\mathbf{r}}_{ij}\right)
\end{aligned}
\tag{B.1.14}
$$

assuming that $\hat{\mathbf{d}}_{\alpha g}$ is real. A product of three Legendre polynomials can again be expanded using the spherical harmonic addition theorem (B.1.10),

$$\begin{aligned}
&\int \mathrm{d}\omega_k P_\ell\big(\hat{\mathbf{d}}_{\alpha g}\cdot\hat{\mathbf{k}}\big) P_{\ell'}\big(\hat{\mathbf{d}}_{g\beta}\cdot\hat{\mathbf{k}}\big) P_{\ell''}\big(\hat{\mathbf{k}}\cdot\hat{\mathbf{r}}_{ij}\big) \\
&\quad = \int \mathrm{d}\omega_k \left(\frac{4\pi}{2\ell+1}\right)\left(\frac{4\pi}{2\ell'+1}\right)\left(\frac{4\pi}{2\ell''+1}\right) \sum_{m=-\ell}^{\ell} Y_{\ell m}\left(\theta_k,\phi_k\right) Y^*_{\ell m}\left(\theta_\alpha,\phi_\alpha\right) \\
&\qquad \sum_{m'=-\ell'}^{\ell'} Y_{\ell' m'}\left(\theta_k,\phi_k\right) Y^*_{\ell' m'}\left(\theta_\beta,\phi_\beta\right) \sum_{m''=-\ell''}^{\ell''} Y_{\ell'' m''}\left(\theta_k,\phi_k\right) Y^*_{\ell'' m''}\left(\theta_r,\phi_r\right). \qquad \text{(B.1.15)}
\end{aligned}$$

The product of three spherical harmonics is described by Clebsch-Gordan coefficients,

$$\begin{aligned}
&\int \mathrm{d}\omega_k Y_{\ell m}\left(\theta_k,\phi_k\right) Y_{\ell' m'}\left(\theta_k,\phi_k\right) Y_{\ell'' m''}\left(\theta_k,\phi_k\right) \\
&\qquad = \sqrt{\frac{(2\ell+1)(2\ell'+1)}{4\pi(2\ell''+1)}}\, \langle \ell\, m;\, \ell'\, m' \,|\, \ell''\, m''\rangle \,\langle \ell\, 0;\, \ell'\, 0 \,|\, \ell''\, 0\rangle\,. \qquad \text{(B.1.16)}
\end{aligned}$$

If ℓ'' sits outside the region $|\ell-\ell'| \le \ell'' \le (\ell+\ell')$ and/or $\ell+\ell'+\ell''$ is an odd integer, the Clebsch-Gordon coefficient $\langle \ell\, 0;\, \ell'\, 0 \,|\, \ell''\, 0\rangle = 0$. So for our case where ($\ell = 1$, $\ell' = 1$), the only possible non-zero values of ℓ'' will be 0 or 2.

Rather than calculate the Clebsch-Gordon coefficients for each term in the sums in (B.1.15), we will calculate the terms for $\ell'' = 0$ and $\ell'' = 2$ directly, without expressing them in spherical harmonics. To make the angular integrals more convenient, we will first make a frame transformation such that $\hat{\mathbf{d}}_{\alpha g} = \hat{\mathbf{x}}$ and $\hat{\mathbf{d}}_{g\beta} = \hat{\mathbf{y}}$. Using spherical polar coordinates

$$x = r\sin\theta\cos\phi, \qquad y = r\sin\theta\sin\phi, \qquad z = r\cos\theta, \qquad \text{(B.1.17)}$$

we can then express $\hat{\mathbf{k}}$ and $\hat{\mathbf{r}}$ as

$$\begin{aligned}
\hat{\mathbf{k}} &= \sin\theta_k\cos\phi_k\hat{\mathbf{x}} + \sin\theta_k\sin\phi_k\hat{\mathbf{y}} + \cos\theta_k\hat{\mathbf{z}}\,, \\
\hat{\mathbf{r}} &= \sin\theta_r\cos\phi_r\hat{\mathbf{x}} + \sin\theta_r\sin\phi_r\hat{\mathbf{y}} + \cos\theta_r\hat{\mathbf{z}}\,. \qquad \text{(B.1.18)}
\end{aligned}$$

The angular integral (B.1.6) now has the form

$$
\begin{aligned}
&-\int \mathrm{d}\omega_k \big(\hat{\mathbf{d}}_{\alpha g}\cdot\hat{\mathbf{k}}\big)\big(\hat{\mathbf{d}}^*_{g\beta}\cdot\hat{\mathbf{k}}\big)\sum_{\ell''=0,2}(2\ell''+1)\,\mathrm{i}^{\ell''}\,j_{\ell''}(kr_{ij})\,P_{\ell''}\big(\hat{\mathbf{k}}\cdot\hat{\mathbf{r}}_{ij}\big)\\
&=-\sum_{\ell''=0,2}(2\ell''+1)\,\mathrm{i}^{\ell''}\,j_{\ell''}(kr_{ij})\int_{\phi_k=0}^{2\pi}\mathrm{d}\phi_k\int_{\theta_k=0}^{\pi}\mathrm{d}\theta_k\sin\theta_k\big(\sin\theta_k\cos\phi_k\big)\big(\sin\theta_k\sin\phi_k\big)\\
&\quad P_{\ell''}\big(\sin\theta_k\cos\phi_k\sin\theta_r\cos\phi_r+\sin\theta_k\sin\phi_k\sin\theta_r\sin\phi_r+\cos\theta_k\cos\theta_r\big)\\
&=0\;+\;5\,j_2(kr_{ij})\left[\frac{4\pi}{5}\big(\hat{\mathbf{d}}_{\alpha g}\cdot\hat{\mathbf{r}}_{ij}\big)\big(\hat{\mathbf{d}}_{g\beta}\cdot\hat{\mathbf{r}}_{ij}\big)\right].
\end{aligned}
\tag{B.1.19}
$$

B.2 Solution

Combining the solutions for the angular integrals from (B.1.13) (B.1.19) into (B.1.2) gives

$$
\begin{aligned}
\gamma_{ij}^{\alpha\beta}=\frac{|d_{eg}|^2}{(2\pi c)^3}\int_{\omega_0-\vartheta}^{\omega_0+\vartheta}\mathrm{d}\omega_k\frac{\omega_k^3}{2\hbar\varepsilon_0}\Big\{\delta_{\alpha\beta}\frac{8\pi}{3}\Big[j_0(kr_{ij})+j_2(kr_{ij})P_2\big(\hat{\mathbf{r}}_{ij}\cdot\hat{\mathbf{d}}_{\alpha g}\big)\Big]\\
+(1-\delta_{\alpha\beta})\,4\pi\,j_2(kr_{ij})\big(\hat{\mathbf{d}}_{\alpha g}\cdot\hat{\mathbf{r}}_{ij}\big)\big(\hat{\mathbf{d}}_{g\beta}\cdot\hat{\mathbf{r}}_{ij}\big)\Big\}.
\end{aligned}
\tag{B.2.1}
$$

The time integral (B.1.1) can be approximated using the Born-Markov approximations as we did in Sec. 2.3.3,

$$
\int_0^{\Delta t}\mathrm{d}t_1\int_0^{t_1}\mathrm{d}t_2\,\mathrm{e}^{-\mathrm{i}(\omega_k-\omega_0)(t_1-t_2)}\simeq\left(\pi\,\delta(\omega_k-\omega_0)-\frac{\mathrm{iP}}{\omega_k-\omega_0}\right)\Delta t,
\tag{B.2.2}
$$

where P is the principal value integral (see Eq. (12.2.21) of [69] and Eq. B.2.7).

B.2.1 Cooperative decay Γ_{ij}

Comparing (B.2.2) with (B.1.1)

$$
\int_0^{\Delta t}\mathrm{d}t_1\int_0^{t_1}\mathrm{d}t_2\,\gamma_{ij}^{\alpha\beta}(t_1-t_2)\equiv\left(\frac{1}{2}\Gamma_{ij}^{\alpha\beta}+\mathrm{i}\Omega_{ij}^{\alpha\beta}\right),
\tag{B.2.3}
$$

we can extract the cooperative decay Γ_{ij},

$$\begin{aligned}
\Gamma_{ij}^{\alpha\beta} =& \frac{|d_{eg}|^2 k_0^3}{3\pi\varepsilon_0\hbar}\Big\{\delta_{\alpha\beta}\left[j_0(k_0 r_{ij}) + \frac{1}{2}\left(3|\hat{\mathbf{r}}_{ij}\cdot\hat{\mathbf{d}}_{\alpha g}|^2 - 1\right) j_2(k_0 r_{ij})\right] \\
&+ \frac{3}{2}(1-\delta_{\alpha\beta})\, j_2(k_0 r_{ij})\left(\hat{\mathbf{d}}_{\alpha g}\cdot\hat{\mathbf{r}}_{ij}\right)\left(\hat{\mathbf{d}}_{g\beta}\cdot\hat{\mathbf{r}}_{ij}\right)\Big\}, \\
=& \frac{k_0^3}{4\pi\varepsilon\hbar}\mathbf{d}_{\alpha g}\cdot\Big\{\mathbf{d}_{g\beta}\left[\frac{\sin(k_0 r_{ij})}{k_0 r_{ij}} + \frac{\cos(k_0 r_{ij})}{(k_0 r_{ij})^2} - \frac{\sin(k_0 r_{ij})}{(k_0 r_{ij})^3}\right] \\
&+ \left(\hat{\mathbf{r}}_{ij}\cdot\mathbf{d}_{g\beta}\right)\hat{\mathbf{r}}_{ij}\left[-\frac{\sin(k_0 r_{ij})}{k_0 r_{ij}} - \frac{3\cos(k_0 r_{ij})}{(k_0 r_{ij})^2} + \frac{3\sin(k_0 r_{ij})}{(k_0 r_{ij})^3}\right]\Big\} \\
=& \frac{1}{\hbar}\mathbf{d}_{\alpha g}\cdot\mathrm{Im}\left[\mathrm{G}(\mathbf{r}_i - \mathbf{r}_j)\mathbf{d}_{g\beta}\right]
\end{aligned} \tag{B.2.4}$$

where we have used $k_0 = \omega_0/c$. The $\delta_{\alpha\beta}$ term is equivalent to Eq. (14.1.17) in [70] which is the result for multiple 2-level atoms. The additional $(1-\delta_{\alpha\beta})$ term appears because of the possibility of interactions between atoms coupling to different excited states. In the last line of this equation, we can see that the cooperative decay $\Gamma_{ij}^{\alpha\beta}$ is actually equivalent to the imaginary part of the interaction between a dipole moment $\mathbf{d}_{\alpha g}$ and the imaginary part of the field scattered from a second (assumed real) dipole moment $\mathbf{d}_{g\beta}$. We will discuss this further in Sec. B.2.3.

The spherical Bessel functions have the form

$$\begin{aligned}
j_0(x) &= \frac{\sin x}{x} \quad \xrightarrow{x\to 0} \quad 1\,, \\
j_2(x) &= -\frac{\sin x}{x} - \frac{3\cos x}{x^2} + \frac{3\sin x}{x^3} \quad \xrightarrow{x\to 0} \quad 0\,.
\end{aligned} \tag{B.2.5}$$

Taking the limit $r_{ij} \to 0$, Γ_{ii} becomes the natural spontaneous decay rate for a single atom,

$$\Gamma_{ii}^{\alpha\alpha} = \Gamma_0 \equiv \frac{|d_{eg}|^2 k_0^3}{3\pi\varepsilon_0\hbar}. \tag{B.2.6}$$

B.2.2 Cooperative shift Ω_{ij}

The principal value integral in (B.2.2) can be expressed as

$$\mathrm{P}\int_{-a}^{b}\mathrm{d}z\frac{f(z)}{z}\equiv\lim_{\delta\to 0+}\left[\int_{-a}^{-\delta}\mathrm{d}z\frac{f(z)}{z}+\int_{\delta}^{b}\mathrm{d}z\frac{f(z)}{z}\right]. \tag{B.2.7}$$

The integral in (B.2.2) has terms of the form

$$\mathrm{P}\int_{\omega_0-\vartheta}^{\omega_0+\vartheta}\mathrm{d}\omega_k\frac{\cos(\omega_k r_{ij}/c)}{\omega_k-\omega_0}=-2\,\mathrm{Si}(\vartheta r_{ij}/c)\sin(k_0 r_{ij})\simeq-\pi\sin(k_0 r_{ij}), \tag{B.2.8a}$$

$$\mathrm{P}\int_{\omega_0-\vartheta}^{\omega_0+\vartheta}\mathrm{d}\omega_k\frac{\sin(\omega_k r_{ij}/c)}{\omega_k-\omega_0}=2\,\mathrm{Si}(\vartheta r_{ij}/c)\cos(k_0 r_{ij})\simeq\pi\cos(k_0 r_{ij}), \tag{B.2.8b}$$

where

$$\mathrm{Si}(x)=\int_0^x\mathrm{d}z\frac{\sin z}{z}\simeq\frac{\pi}{2}\quad\text{when } x>2. \tag{B.2.9}$$

As already mentioned, Ω_{ii} is the Lamb shift which we shall assume has been included into the definition of ω_0 and so can be ignored. For $i\neq j$ however, the resulting expression is essentially the same as that of the cooperative decay (B.2.10), albeit having exchanged $j_0(x)\to y_0(x)$ and $j_2(x)\to y_2(x)$,

$$\begin{aligned}
\Omega_{ij}^{\alpha\beta}=&\frac{\Gamma_0}{2}\Big\{\delta_{\alpha\beta}\left[y_0(k_0r_{ij})+\frac{1}{2}\left(3\,|\hat{\mathbf{r}}_{ij}\cdot\hat{\mathbf{d}}_{\alpha g}|^2-1\right)y_2(k_0r_{ij})\right]\\
&\qquad+\frac{3}{2}(1-\delta_{\alpha\beta})\,y_2(k_0r_{ij})\left(\hat{\mathbf{d}}_{\alpha g}\cdot\hat{\mathbf{r}}_{ij}\right)\left(\hat{\mathbf{d}}_{g\beta}\cdot\hat{\mathbf{r}}_{ij}\right)\Big\},\\
=&\frac{k_0^3}{4\pi\varepsilon\hbar}\mathbf{d}_{\alpha g}\cdot\Big\{\mathbf{d}_{g\beta}\left[-\frac{\cos(k_0r_{ij})}{k_0r_{ij}}+\frac{\sin(k_0r_{ij})}{(k_0r_{ij})^2}+\frac{\cos(k_0r_{ij})}{(k_0r_{ij})^3}\right]\\
&\qquad+\left(\hat{\mathbf{r}}_{ij}\cdot\mathbf{d}_{g\beta}\right)\hat{\mathbf{r}}_{ij}\left[\frac{\cos(k_0r_{ij})}{k_0r_{ij}}-\frac{3\sin(k_0r_{ij})}{(k_0r_{ij})^2}-\frac{3\cos(k_0r_{ij})}{(k_0r_{ij})^3}\right]\Big\}\\
=&-\frac{1}{\hbar}\mathbf{d}_{\alpha g}\cdot\mathrm{Re}\left[\mathsf{G}(\mathbf{r}_i-\mathbf{r}_j)\mathbf{d}_{g\beta}\right]
\end{aligned} \tag{B.2.10}$$

where $y_\ell(x)$ are the spherical Neumann functions,

$$y_0(x) = -\frac{\cos x}{x}, \qquad y_2(x) = \frac{\cos x}{x} - \frac{3\sin x}{x^2} - \frac{3\cos x}{x^3}. \tag{B.2.11}$$

As with the cooperative decay, we have been ale to express $\Omega_{ij}^{\alpha\beta}$ in terms of the interaction between a dipole moment $\mathbf{d}_{\alpha g}$ and the real part of the electric field scattered from a (real) classical dipole $\mathbf{d}_{g\beta}$. We shall now look at this in more detail.

B.2.3 Scattered dipole field

From classical electromagnetism (Maxwell's equations), the electric field scattered from a single classical dipole $\mathbf{d}_j$ is (4.2.4)

$$\begin{aligned}\mathbf{E}_j(\mathbf{r}) =& \mathsf{G}(\mathbf{R}_j)\,\mathbf{d}_j \\ =& \frac{k^3}{4\pi\varepsilon_0} \mathrm{e}^{\mathrm{i}kR_j} \left\{ \left[\frac{1}{kR_j} + \frac{\mathrm{i}}{(kR_j)^2} - \frac{1}{(kR_j)^3} \right] \mathbf{d}_j + \left[-\frac{1}{kR_j} - \frac{3\mathrm{i}}{(kR_j)^2} + \frac{3}{(kR_j)^3} \right] (\hat{\mathbf{R}}_j \cdot \mathbf{d}_j)\,\hat{\mathbf{R}}_j \right\},\end{aligned} \tag{B.2.12}$$

where $\mathbf{R}_j \equiv \mathbf{r} - \mathbf{r}_j$. Assuming that $\mathbf{d}_j$ is real, we were able to show in the previous two sections that $\Omega_{ij}^{\alpha\beta}$ and $\Gamma_{ij}^{\alpha\beta}$ are just the interaction of a dipole $\mathbf{d}_i$ with the real and imaginary parts of $\mathbf{E}_j(\mathbf{r})$ respectively,

$$\hbar\Omega_{ij}^{\alpha\beta} - \frac{\mathrm{i}}{2}\hbar\Gamma_{ij}^{\alpha\beta} \quad = \quad -\mathbf{d}_{\alpha g} \cdot \mathsf{G}(\mathbf{r}_i - \mathbf{r}_j)\,\mathbf{d}_{g\beta} \quad = \quad \mathsf{H}_{\text{int}}. \tag{B.2.13}$$

In Sec. 2.3.5 we showed that a coherent state in the field modes could be treated as a classical electric driving field. What we have seen here is that the interaction between two atomic electric dipoles is also equivalent to the scattering of classical electric fields between the dipoles.

Appendix C

Many-atom four-level optical Bloch equations

C.1 Many-atom master equation

The master equation governing the dynamics of the N-atom master equation for 4-level atoms is given by (3.3.25),

$$\dot{\rho}_N(t) = -\frac{\mathrm{i}}{\hbar}\Big[\sum_i \mathsf{H}_{\mathrm{sys},i} + \sum_{\substack{i,j \\ i\neq j}} \sum_{\alpha,\beta}^{\{x,y,z\}} \hbar\Omega_{ij}^{\alpha\beta}\sigma_{i\alpha}^{+}\sigma_{j\beta}^{-}\,,\ \rho_N(t)\Big] + \frac{1}{2}\sum_{i,j}\sum_{\alpha,\beta}^{\{x,y,z\}} \Gamma_{ij}^{\alpha\beta}\Big(2\sigma_{i\alpha}^{-}\rho_N(t)\sigma_{j\beta}^{+} - \sigma_{j\beta}^{+}\sigma_{i\alpha}^{-}\rho_N(t) - \rho_N(t)\sigma_{j\beta}^{+}\sigma_{i\alpha}^{-}\Big), \tag{C.1.1}$$

where

$$H_{\mathrm{sys},i} = \frac{\hbar\omega_0}{2}\left(-|g_i\rangle\langle g_i| + |x_i\rangle\langle x_i| + |y_i\rangle\langle y_i| + |z_i\rangle\langle z_i|\right) - \sum_{\alpha}^{\{x,y,z\}}\left[\mathbf{d}_{\alpha g}\cdot\mathbf{E}_0(\mathbf{r}_i)\mathrm{e}^{-\mathrm{i}\omega t}\sigma_{i\alpha}^{+} + \mathbf{d}_{g\alpha}\cdot\mathbf{E}_0^{*}(\mathbf{r}_i)\mathrm{e}^{\mathrm{i}\omega t}\sigma_{i\alpha}^{-}\right]. \tag{C.1.2}$$

To reduce the complexity of the problem, we have made the mean-field approximation $\rho_N = \bigotimes_\ell \rho_\ell$, where the single-atom density matrix for the ℓth atom, ρ_ℓ, has the form (see Sec. 3.3.1)

$$\rho_\ell = \sum_{\mu,\nu} \rho_{\mu\nu}^{(\ell)} \left|\mu_\ell\right\rangle \left\langle\nu_\ell\right|, \tag{C.1.3}$$

for $\{\mu,\nu\} \in \{g,x,y,z\}$. The density matrix element $\rho_{\mu\nu}^{(\ell)}$ can be extracted from the complete density matrix ρ_N by calculating the trace of $\left|\nu_\ell\right\rangle \left\langle\mu_\ell\right|$,

$$\begin{aligned}
\mathrm{Tr}\left(\rho_N \left|\nu_\ell\right\rangle \left\langle\mu_\ell\right|\right) =& \mathrm{Tr}\left(\sum_{\mu'\nu'} \rho_{\mu'\nu'}^{(\ell)} \left|\nu_\ell\right\rangle \left\langle\mu_\ell\right| \bigotimes_{i\neq\ell} \rho_i\right) \\
=& \mathrm{Tr}\left(\sum_{\mu'\nu'} \rho_{\mu'\nu'}^{(\ell)} \left|\nu_\ell\right\rangle \left\langle\mu_\ell\right|\right) \Pi_{i\neq\ell} \mathrm{Tr}\left(\rho_i\right) \\
=& \rho_{\mu\nu}^{(\ell)}.
\end{aligned} \tag{C.1.4}$$

In showing this we have made use of the trace product rule

$$\mathrm{Tr}\left(\rho_i \otimes \rho_j\right) = \mathrm{Tr}\left(\rho_i\right)\ \mathrm{Tr}\left(\rho_j\right), \tag{C.1.5}$$

and that the trace of ρ_i is 1.

In the following Sections, we shall go through each of the different terms in the master equation (C.1.1), term by term, calculating their contribution to $\dot{\rho}_{\mu\nu}^{(\ell)}$,

$$\dot{\rho}_{\mu\nu}^{(\ell)} = \mathrm{Tr}\left(\dot{\rho}_N \left|\nu_\ell\right\rangle \left\langle\mu_\ell\right|\right). \tag{C.1.6}$$

C.2 $\sum_i \mathsf{H}_{\mathbf{sys},i}$

The operators in $\mathsf{H}_{\mathrm{sys},i}$ are all single-body terms of the form $\left|\alpha_i\right\rangle \left\langle\beta_i\right|$, where $\{\alpha,\beta\} \in \{g,x,y,z\}$. The Hamiltonian $\mathsf{H}_{\mathrm{sys},i}$ interacts with the density matrix inside the commutator $[\mathsf{H}_{\mathrm{sys},i}, \rho_N]$. The contribution of each of these operators to $\dot{\rho}_{\mu\nu}^{(\ell)}$ (C.5.7) is therefore

proportional to

$$
\begin{aligned}
&\mathrm{Tr}\Big[\Big(|\alpha_i\rangle\langle\beta_i|,\rho_N\Big)|\nu_\ell\rangle\langle\mu_\ell|\Big] \\
&\quad= \mathrm{Tr}\Big(|\alpha_i\rangle\langle\beta_i|\,\rho_N\,|\nu_\ell\rangle\langle\mu_\ell| - \rho_N\,|\alpha_i\rangle\langle\beta_i|\,|\nu_\ell\rangle\langle\mu_\ell|\Big) \\
&\quad= \delta_{i\ell}\,\mathrm{Tr}\Big(|\alpha_\ell\rangle\langle\beta_\ell|\sum_{\mu'\nu'}^{\{g,x,y,z\}}\rho^{(\ell)}_{\mu'\nu'}\,|\mu'_\ell\rangle\langle\nu'_\ell|\nu_\ell\rangle\langle\nu_\ell| \\
&\qquad\qquad - \sum_{\mu'\nu'}^{\{g,x,y,z\}}\rho^{(\ell)}_{\mu'\nu'}\,|\mu'_\ell\rangle\langle\nu'_\ell|\alpha_\ell\rangle\langle\beta_\ell|\nu_\ell\rangle\langle\mu_\ell|\Big)\,\Pi_{j\neq\ell}\mathrm{Tr}\left(\rho_j\right) \\
&\qquad + (1-\delta_{i\ell})\,\mathrm{Tr}\Big(|\alpha_i\rangle\langle\beta_i|\sum_{\mu'\nu'}^{\{g,x,y,z\}}\rho^{(i)}_{\mu'\nu'}\,|\mu'_i\rangle\langle\nu'_i| - \sum_{\mu'\nu'}^{\{g,x,y,z\}}\rho^{(i)}_{\mu'\nu'}\,|\mu'_i\rangle\langle\nu'_i|\alpha_i\rangle\langle\beta_i|\Big) \\
&\qquad\qquad \times\mathrm{Tr}\Big(\sum_{\mu'\nu'}^{\{g,x,y,z\}}\rho^{(\ell)}_{\mu'\nu'}\,|\mu'_\ell\rangle\langle\nu'_\ell|\nu_\ell\rangle\langle\mu_\ell|\Big)\,\Pi_{j\neq\ell}\mathrm{Tr}\left(\rho_j\right) \\
&\quad= \delta_{i\ell}\left(\delta_{\alpha\mu}\rho^{(\ell)}_{\beta\nu} - \delta_{\beta\nu}\rho^{(\ell)}_{\mu\alpha}\right) + (1-\delta_{i\ell})\left(\rho^{(i)}_{\beta\alpha} - \rho^{(i)}_{\beta\alpha}\right)\left(\rho^{(\ell)}_{\mu\nu}\right) \\
&\quad= \delta_{i\ell}\left(\delta_{\alpha\mu}\rho^{(\ell)}_{\beta\nu} - \delta_{\beta\nu}\rho^{(\ell)}_{\mu\alpha}\right). \qquad \text{(C.2.1)}
\end{aligned}
$$

Substituting this into $\mathsf{H}_{\mathrm{sys},i}$, the trace of the Hamiltonian is then

$$\begin{aligned}
&\mathrm{Tr}\Big[-\frac{\mathrm{i}}{\hbar}\Big(\sum_i \mathsf{H}_{\mathrm{sys},i},\rho_N\Big)|\nu_\ell\rangle\langle\mu_\ell|\Big] \\
&\quad= -\frac{\mathrm{i}}{\hbar}\sum_i \mathrm{Tr}\Big\{\Big[\frac{\hbar\omega_0}{2}\Big(-|g_i\rangle\langle g_i| + \sum_\alpha^{\{x,y,z\}}|\alpha_i\rangle\langle\alpha_i|\Big) \\
&\qquad - \sum_\alpha^{\{x,y,z\}}\Big(\mathbf{d}_{\alpha g}\cdot\mathbf{E}_{0,i}^{(+)}|\alpha_i\rangle\langle g_i| + \mathbf{d}_{g\alpha}\cdot\mathbf{E}_{0,i}^{(-)}|g_i\rangle\langle\alpha_i|\Big)\ ,\ \rho_N\Big]|\nu_\ell\rangle\langle\mu_\ell|\Big\} \\
&\quad= -\mathrm{i}\frac{\omega_0}{2}\Big[-\Big(\delta_{g\mu}\rho_{g\nu}^{(\ell)} - \delta_{g\nu}\rho_{\mu g}^{(\ell)}\Big) + \Big(\delta_{\mu\neq g}\rho_{\mu\nu}^{(\ell)} - \delta_{\nu\neq g}\rho_{\mu\nu}^{(\ell)}\Big)\Big] \\
&\qquad + \frac{\mathrm{i}}{\hbar}\Big(\delta_{\mu\neq g}\mathbf{d}_{\mu g}\cdot\mathbf{E}_{0,\ell}^{(+)}\rho_{g\nu}^{(\ell)} - \delta_{\nu\neq g}\mathbf{d}_{g\nu}\cdot\mathbf{E}_{0,\ell}^{(-)}\rho_{\mu g}^{(\ell)}\Big) \\
&\qquad - \frac{\mathrm{i}}{\hbar}\sum_\alpha^{\{x,y,z\}}\Big(\delta_{g\nu}\mathbf{d}_{\alpha g}\cdot\mathbf{E}_{0,\ell}^{(+)}\rho_{\mu\alpha}^{(\ell)} - \delta_{g\mu}\mathbf{d}_{g\alpha}\cdot\mathbf{E}_{0,\ell}^{(-)}\rho_{\alpha\nu}^{(\ell)}\Big), \qquad \text{(C.2.2)}
\end{aligned}$$

where we have used $\mathbf{E}_{0,i}^{(+)} = \big(\mathbf{E}_{0,i}^{(-)}\big)^* = \mathbf{E}_0(\mathbf{r}_i)\mathrm{e}^{-\mathrm{i}\omega t}$.

C.3 $\Omega_{ij}^{\alpha\beta}$

The first of the two-body terms is the cooperative shift $\hbar\Omega_{ij}^{\alpha\beta}\sigma_{i\alpha}^{+}\sigma_{j\beta}^{-}$. The trace of the $\sigma_{i\alpha}^{+}\sigma_{j\beta}^{-}$ commutator is

$$\begin{aligned}
&\mathrm{Tr}\Big(\Big[\sigma_{i\alpha}^{+}\sigma_{j\beta}^{-},\rho_N\Big]|\nu_\ell\rangle\langle\mu_\ell|\Big) \\
&= \mathrm{Tr}\Big(|\alpha_i\rangle\langle g_i|g_j\rangle\langle\beta_j|\rho_N|\nu_\ell\rangle\langle\mu_\ell| - \rho_N|\alpha_i\rangle\langle g_i|g_j\rangle\langle\beta_j|\nu_\ell\rangle\langle\mu_\ell|\Big) \\
&= \delta_{i=j=\ell}\Big(\delta_{\alpha\mu}\rho_{\beta\nu}^{(\ell)} - \delta_{\beta\nu}\rho_{\mu\alpha}^{(\ell)}\Big) \\
&\quad + \delta_{(i=\ell)\neq j}\Big(\delta_{\alpha\mu}\rho_{g\nu}^{(\ell)}\rho_{\beta g}^{(j)} - \delta_{g\nu}\rho_{\mu\alpha}^{(\ell)}\rho_{\beta g}^{(j)}\Big) + \delta_{(j=\ell)\neq i}\Big(\delta_{g\mu}\rho_{\beta\nu}^{(\ell)}\rho_{g\alpha}^{(i)} - \delta_{\beta\nu}\rho_{\mu g}^{(\ell)}\rho_{g\alpha}^{(i)}\Big) \\
&\quad + \delta_{(i=j)\neq\ell}\Big(\rho_{\beta\alpha}^{(i)} - \rho_{\beta\alpha}^{(i)}\Big)\rho_{\mu\nu}^{(\ell)} + \delta_{i\neq j\neq\ell}\Big(\rho_{g\alpha}^{(i)}\rho_{\beta g}^{(j)}\rho_{\mu\nu}^{(\ell)} - \rho_{g\alpha}^{(i)}\rho_{\beta g}^{(j)}\rho_{\mu\nu}^{(\ell)}\Big). \qquad \text{(C.3.1)}
\end{aligned}$$

The terms on the last line of this equation are both zero. We have furthermore assumed that the Lamb shift $\Omega_{\ell\ell}$ has already been included in the definition of ω_0 and can be ignored. We therefore only need consider the terms where $(i = \ell \neq j)$ or $(j = \ell \neq i)$. The contribution to $\dot{\rho}^{(\ell)}_{\mu\nu}$ is therefore

$$\begin{aligned}
&\mathrm{Tr}\Big\{ -\frac{\mathrm{i}}{\hbar}\Big[\sum_{\substack{i,j \\ i\neq j}} \sum_{\alpha,\beta}^{\{x,y,z\}} \hbar\Omega^{\alpha\beta}_{ij}\sigma^{+}_{i\alpha}\sigma^{-}_{j\beta}\,,\,\rho_N(t)\Big]\,|\nu_\ell\rangle\langle\mu_\ell|\Big\} \\
&\qquad = \mathrm{i}\sum_{i\neq\ell}\sum_{\alpha}^{\{x,y,z\}}\Big(\delta_{\nu\neq g}\,\Omega^{\alpha\nu}_{i\ell}\,\rho^{(\ell)}_{\mu g}\,\rho^{(i)}_{g\alpha} - \delta_{\mu\neq g}\,\Omega^{\mu\alpha}_{\ell i}\,\rho^{(\ell)}_{g\nu}\,\rho^{(i)}_{\alpha g}\Big) \\
&\qquad\quad + \mathrm{i}\sum_{i\neq\ell}\sum_{\alpha,\beta}^{\{x,y,z\}}\Omega^{\alpha\beta}_{i\ell}\Big(\delta_{g\nu}\,\rho^{(\ell)}_{\mu\alpha}\,\rho^{(i)}_{\beta g} - \delta_{g\mu}\,\rho^{(\ell)}_{\beta\nu}\,\rho^{(i)}_{g\alpha}\Big) \qquad \text{(C.3.2)}
\end{aligned}$$

where we have used $\omega_{ij} = \omega_{ji}$ (and equivalently $\omega^{\alpha\beta} = \omega^{\beta\alpha}$).

C.4 $\Gamma_{ij}^{\alpha\beta}$

The final terms we need to consider are the cooperative decay terms $\Gamma_{ij}^{\alpha\beta}$,

$$
\begin{aligned}
&\mathrm{Tr}\left[\left(2\sigma_{i\alpha}^{-}\rho_N\sigma_{j\beta}^{+}-\sigma_{j\beta}^{+}\sigma_{i\alpha}^{-}\rho_N-\rho_N\sigma_{j\beta}^{+}\sigma_{i\alpha}^{-}\right)|\nu_\ell\rangle\langle\mu_\ell|\right]\\
&= \mathrm{Tr}\Big(2|g_i\rangle\langle\alpha_i|\rho_N|\beta_j\rangle\langle g_j||\nu_\ell\rangle\langle\mu_\ell| - |\beta_j\rangle\langle g_j||g_i\rangle\langle\alpha_i|\rho_N|\nu_\ell\rangle\langle\mu_\ell|\\
&\quad - \rho_N|\beta_j\rangle\langle g_j||g_i\rangle\langle\alpha_i||\nu_\ell\rangle\langle\mu_\ell|\Big)\\
&= \delta_{i=j=\ell}\left(2\delta_{g\mu}\delta_{g\nu}\rho_{\alpha\beta}^{(\ell)} - \delta_{\beta\mu}\rho_{\alpha\nu}^{(\ell)} - \delta_{\alpha\nu}\rho_{\mu\beta}^{(\ell)}\right)\\
&\quad + \delta_{(i=\ell)\neq j}\left(2\delta_{g\mu}\rho_{\alpha\nu}^{(\ell)}\rho_{g\beta}^{(j)} - \delta_{g\mu}\rho_{\alpha\nu}^{(\ell)}\rho_{g\beta}^{(j)} - \delta_{\alpha\nu}\rho_{\mu g}^{(\ell)}\rho_{g\beta}^{(j)}\right)\\
&\quad + \delta_{(j=\ell)\neq i}\left(2\delta_{g\nu}\rho_{\mu\beta}^{(\ell)}\rho_{\alpha g}^{(i)} - \delta_{\beta\mu}\rho_{g\nu}^{(\ell)}\rho_{\alpha g}^{(i)} - \delta_{g\nu}\rho_{\mu\beta}^{(\ell)}\rho_{\alpha g}^{(i)}\right)\\
&\quad + \delta_{(i=j)\neq\ell}\left(2\rho_{\alpha\beta}^{(i)} - \rho_{\alpha\beta}^{(i)} - \rho_{\alpha\beta}^{(i)}\right)\rho_{\mu\nu}^{(\ell)}\\
&\quad + \delta_{i\neq j\neq\ell}\left(2\rho_{\alpha g}^{(i)}\rho_{g\beta}^{(j)}\rho_{\mu\nu}^{(\ell)} - \rho_{\alpha g}^{(i)}\rho_{g\beta}^{(j)}\rho_{\mu\nu}^{(\ell)} - \rho_{\alpha g}^{(i)}\rho_{g\beta}^{(j)}\rho_{\mu\nu}^{(\ell)}\right)\\
&= \delta_{i=j=\ell}\left(2\delta_{g\mu}\delta_{g\nu}\rho_{\alpha\beta}^{(\ell)} - \delta_{\beta\mu}\rho_{\alpha\nu}^{(\ell)} - \delta_{\alpha\nu}\rho_{\mu\beta}^{(\ell)}\right)\\
&\quad + \delta_{(i=\ell)\neq j}\left(\delta_{g\mu}\rho_{\alpha\nu}^{(\ell)} - \delta_{\alpha\nu}\rho_{\mu g}^{(\ell)}\right)\rho_{g\beta}^{(j)}\\
&\quad + \delta_{(j=\ell)\neq i}\left(\delta_{g\nu}\rho_{\mu\beta}^{(\ell)} - \delta_{\beta\mu}\rho_{g\nu}^{(\ell)}\right)\rho_{\alpha g}^{(i)}.
\end{aligned}
\tag{C.4.1}
$$

Substituting this into the master equation, this becomes[a]

$$\begin{aligned}
\mathrm{Tr}\Big[\frac{1}{2}\sum_{i,j}\sum_{\alpha,\beta}^{\{x,y,z\}}\Gamma_{ij}^{\alpha\beta}\Big(2\sigma_{i\alpha}^{-}\rho_N(t)\sigma_{j\beta}^{+}-\sigma_{j\beta}^{+}\sigma_{i\alpha}^{-}\rho_N(t)-\rho_N(t)\sigma_{j\beta}^{+}\sigma_{i\alpha}^{-}\Big)|\nu_\ell\rangle\langle\mu_\ell|\Big] \\
= \sum_{\alpha}^{\{x,y,z\}}\Gamma_0\delta_{g\mu}\delta_{g\nu}\rho_{\alpha\alpha}^{(\ell)} - \frac{1}{2}\Gamma_0\rho_{\mu\nu}^{(\ell)}\big(\delta_{\mu\neq g}+\delta_{\nu\neq g}\big) \\
- \frac{1}{2}\sum_{\alpha}^{\{x,y,z\}}\sum_{i\neq\ell}\Big(\Gamma_{i\ell}^{\nu\alpha}\delta_{\nu\neq g}\rho_{\mu g}^{(\ell)}\rho_{g\alpha}^{(i)}+\Gamma_{i\ell}^{\alpha\mu}\delta_{\mu\neq g}\rho_{g\nu}^{(\ell)}\rho_{\alpha g}^{(i)}\Big) \\
+ \frac{1}{2}\sum_{\alpha\beta}^{\{x,y,z\}}\sum_{i\neq\ell}\Gamma_{i\ell}^{\alpha\beta}\Big(\delta_{g\mu}\rho_{\alpha\nu}^{(\ell)}\rho_{g\beta}^{(i)}+\delta_{g\nu}\rho_{\mu\beta}^{(\ell)}\rho_{\alpha g}^{(i)}\Big) \qquad \text{(C.4.2)}
\end{aligned}$$

C.5 Optical Bloch equations, $\dot{\rho}_\ell$

We can now combine the results in (C.2.2), (C.3.2), and (C.4.2) to determine the total time dynamics of the density matrix $\dot{\rho}_\ell$ (the many atom optical Bloch equations),

$$\dot{\rho}_{\mu\nu}^{(\ell)} = (C.2.2) + (C.3.2) + (C.4.2). \qquad \text{(C.5.1)}$$

Using the relations $\mathrm{Tr}(\rho_\ell)=1$ and $\rho_{\mu\nu}^{(\ell)}=(\rho_{\nu\mu}^{(\ell)})^*$, we therefore only need to consider three different terms,

$$\begin{aligned}
\dot{\rho}_{\mu\mu}^{(\ell)}\Big|_{\mu\neq g} =& \frac{\mathrm{i}}{\hbar}\Big(\mathbf{d}_{\mu g}\cdot\mathbf{E}_{0,\ell}^{(+)}\rho_{g\mu}^{(\ell)} - \mathbf{d}_{g\mu}\cdot\mathbf{E}_{0,\ell}^{(-)}\rho_{\mu g}^{(\ell)}\Big) \\
&+ \mathrm{i}\sum_{i\neq\ell}\sum_{\alpha}^{\{x,y,z\}}\Omega_{i\ell}^{\alpha\mu}\Big(\rho_{\mu g}^{(\ell)}\rho_{g\alpha}^{(i)} - \rho_{g\mu}^{(\ell)}\rho_{\alpha g}^{(i)}\Big) \\
&- \Gamma_0\rho_{\mu\mu}^{(\ell)} - \sum_{i\neq\ell}\sum_{\alpha}^{\{x,y,z\}}\frac{\Gamma_{i\ell}^{\alpha\mu}}{2}\Big(\rho_{\mu g}^{(\ell)}\rho_{g\alpha}^{(i)}+\rho_{g\mu}^{(\ell)}\rho_{\alpha g}^{(i)}\Big). \qquad \text{(C.5.2)}
\end{aligned}$$

[a] Note that $\Gamma_{\ell\ell}^{\alpha\beta}=\Gamma_0\delta_{\alpha\beta}$

In Sec. B.2.3 we showed that $\Omega_{ij}^{\alpha\beta}$ and $\Gamma_{ij}^{\alpha\beta}$ are related to the interaction of a dipole $\mathbf{d}_{\alpha g}$ with the classical electric field scattered from a dipole $\mathbf{d}_{g\beta}$,

$$-\Omega_{ij}^{\alpha\beta}+\frac{\mathrm{i}}{2}\Gamma_{ij}^{\alpha\beta} \quad = \quad \frac{1}{\hbar}\mathbf{d}_{\alpha g}\cdot \mathsf{G}(\mathbf{r}_i-\mathbf{r}_j)\,\mathbf{d}_{g\beta} \quad \equiv \quad \frac{1}{\hbar}\mathbf{d}_{\alpha g}\cdot\mathbf{E}_{j\beta}(\mathbf{r}_i). \tag{C.5.3}$$

Substituting this into (C.5.2) and using the notation $\mathsf{G}(\mathbf{r}_i-\mathbf{r}_j)\equiv \mathsf{G}_{ij}$ gives[b]

$$\begin{aligned}\dot{\rho}_{\mu\mu}^{(\ell)}\Big|_{\mu\neq g} =& -\Gamma_0\,\rho_{\mu\mu}^{(\ell)} + \frac{\mathrm{i}}{\hbar}\rho_{g\mu}^{(\ell)}\mathbf{d}_{\mu g}\cdot\left(\mathbf{E}_{0,\ell}^{(+)}+\sum_{i\neq\ell}\sum_{\alpha}^{\{x,y,z\}}\rho_{\alpha g}^{(i)}\,\mathsf{G}_{i\ell}\,\mathbf{d}_{g\alpha}\right)\\ &-\frac{\mathrm{i}}{\hbar}\rho_{\mu g}^{(\ell)}\mathbf{d}_{g\mu}\cdot\left(\mathbf{E}_{0,\ell}^{(-)}+\sum_{i\neq\ell}\sum_{\alpha}^{\{x,y,z\}}\rho_{g\alpha}^{(i)}\,\mathsf{G}_{i\ell}^{*}\,\mathbf{d}_{\alpha g}\right)\\ =& -\Gamma_0\,\rho_{\mu\mu}^{(\ell)} - \frac{2}{\hbar}\mathrm{Im}\left[\rho_{g\mu}^{(\ell)}\mathbf{d}_{\mu g}\cdot\left(\mathbf{E}_{0,\ell}^{(+)}+\sum_{i\neq\ell}\sum_{\alpha}^{\{x,y,z\}}\rho_{\alpha g}^{(i)}\,\mathsf{G}_{i\ell}\,\mathbf{d}_{g\alpha}\right)\right].\end{aligned} \tag{C.5.4}$$

From this we can see, as we did in Sec. B.2.3, that the interaction between the multiple atoms can be treated as a pair-wise sum of classical electric fields scattered between the dipoles. The new effective local field felt by dipole ℓ is now a sum of the driving field and the field scattered from every other dipole $i\neq\ell$. We can calculate $\dot{\rho}_{gg}^{(\ell)}$ by using

$$\dot{\rho}_{gg}^{(\ell)} = -\sum_{\mu\neq g}\dot{\rho}_{\mu\mu}^{(\ell)}. \tag{C.5.5}$$

Next let us consider a lowering operator $|\nu=g\rangle\langle\mu\neq g|$,

[b] We have also used the fact that $\mathbf{d}_{\alpha g}\cdot\mathsf{G}\mathbf{d}_{g\mu}=\mathbf{d}_{\mu g}\cdot\mathsf{G}\mathbf{d}_{g\alpha}$.

$$
\begin{aligned}
\dot{\rho}^{(\ell)}_{\mu g} =& -\left(\mathrm{i}\omega_0 + \frac{\Gamma_0}{2}\right)\rho^{(\ell)}_{\mu g} + \frac{\mathrm{i}}{\hbar}\left(\mathbf{d}_{\mu g}\cdot\mathbf{E}^{(+)}_{0,\ell}\,\rho^{(\ell)}_{gg} - \sum_{\alpha}^{\{x,y,z\}}\mathbf{d}_{\alpha g}\cdot\mathbf{E}^{(+)}_{0,\ell}\,\rho^{(\ell)}_{\mu\alpha}\right) \\
&- \mathrm{i}\sum_{i\neq\ell}\sum_{\alpha}^{\{x,y,z\}}\Omega^{\mu\alpha}_{\ell i}\,\rho^{(\ell)}_{gg}\rho^{(i)}_{\alpha g} + \mathrm{i}\sum_{i\neq\ell}\sum_{\alpha\beta}^{\{x,y,z\}}\Omega^{\alpha\beta}_{i\ell}\,\rho^{(\ell)}_{\mu\alpha}\rho^{(i)}_{\beta g} \\
&- \frac{1}{2}\sum_{i\neq\ell}\sum_{\alpha}^{\{x,y,z\}}\Gamma^{\alpha\mu}_{i\ell}\,\rho^{(\ell)}_{gg}\rho^{(i)}_{\alpha g} + \frac{1}{2}\sum_{i\neq\ell}\sum_{\alpha\beta}^{\{x,y,z\}}\Gamma^{\alpha\beta}_{i\ell}\,\rho^{(\ell)}_{\mu\beta}\rho^{(i)}_{\alpha g} \\
=& -\left(\mathrm{i}\omega_0 + \frac{\Gamma_0}{2}\right)\rho^{(\ell)}_{\mu g} \\
&+ \frac{\mathrm{i}}{\hbar}\left(\rho^{(\ell)}_{gg}\mathbf{d}_{\mu g} - \sum_{\alpha}^{\{x,y,z\}}\rho^{(\ell)}_{\mu\alpha}\,\mathbf{d}_{\alpha g}\right)\cdot\left(\mathbf{E}^{(+)}_{0,\ell} + \sum_{i\neq\ell}\sum_{\beta}^{\{x,y,z\}}\rho^{(i)}_{\beta g}\,\mathsf{G}_{i\ell}\,\mathbf{d}_{g\beta}\right).
\end{aligned}
\tag{C.5.6}
$$

Finally, let us consider a coherence term between two excited states $|\nu \neq g\rangle\langle\mu \neq g \neq \nu|$,

$$
\begin{aligned}
\dot{\rho}^{(\ell)}_{\mu\nu} =& \frac{\mathrm{i}}{\hbar}\left(\rho^{(\ell)}_{g\nu}\,\mathbf{d}_{\mu g}\cdot\mathbf{E}^{(+)}_{0,\ell} - \rho^{(\ell)}_{\mu g}\,\mathbf{d}_{g\nu}\cdot\mathbf{E}^{(-)}_{0,\ell}\right) \\
&+ \mathrm{i}\sum_{i\neq\ell}\sum_{\alpha}^{\{x,y,z\}}\left(\Omega^{\alpha\nu}_{i\ell}\rho^{(\ell)}_{\mu g}\rho^{(i)}_{g\alpha} - \Omega^{\mu\alpha}_{i\ell}\rho^{(\ell)}_{g\nu}\rho^{(i)}_{\alpha g}\right) \\
&- \Gamma_0\,\rho^{(\ell)}_{\mu\nu} - \frac{1}{2}\sum_{i\neq\ell}\sum_{\alpha}^{\{x,y,z\}}\left(\Gamma^{\nu\alpha}_{i\ell}\rho^{(\ell)}_{\mu g}\rho^{(i)}_{g\alpha} + \Gamma^{\alpha\mu}_{i\ell}\rho^{(\ell)}_{g\nu}\rho^{(i)}_{\alpha g}\right) \\
=& -\Gamma_0\,\rho^{(\ell)}_{\mu\nu} + \frac{\mathrm{i}}{\hbar}\rho^{(\ell)}_{g\nu}\mathbf{d}_{\mu g}\cdot\left(\mathbf{E}^{(+)}_{0,\ell} + \sum_{i\neq\ell}\sum_{\alpha}^{\{x,y,z\}}\rho^{(i)}_{\alpha g}\,\mathsf{G}_{i\ell}\,\mathbf{d}_{g\alpha}\right) \\
&- \frac{\mathrm{i}}{\hbar}\rho^{(\ell)}_{\mu g}\mathbf{d}_{g\nu}\cdot\left(\mathbf{E}^{(-)}_{0,\ell} + \sum_{i\neq\ell}\sum_{\alpha}^{\{x,y,z\}}\rho^{(i)}_{g\alpha}\,\mathsf{G}^{*}_{i\ell}\,\mathbf{d}_{\alpha g}\right).
\end{aligned}
\tag{C.5.7}
$$

This is similar in form to the populations in (C.5.4) and so $\rho_{\mu\neq}$ behaves like a population rather than a coherence. This is because the states $|\mu\rangle$ and $|\nu\rangle$ are not coupled in the same

way as the ground and excited states are.

If we ignore the multiple atom terms, then these equations give us the single-atom optical Bloch equations (2.3.29).

Appendix D

Light–matter coupling experiments

System	Group	Year	Result	Notes
Single atom, high numerical aperture (NA) lens	Kurtsiefer [101]	2009	$\epsilon = 10.4\%$	Predict $\epsilon = 92\%$ for $u = w_L/f = 2.24$
	Kurtsiefer [154]	2009	$\theta = 0.97°$	Predict $\theta \simeq 30°$ for $u = 2.24$
	Kurtsiefer [155]	2011	$R = 0.16\%$, $T = 92\%$	
Single ion, high NA lens	Blatt [156, 157]	2010 & 2011	$\epsilon = 1.35\%$	Use atom as a mirror forming a Fabry Perot cavity with a real mirror, causing a 0.8% oscillation in reflection and transmission depending on atom-mirror spacing.
	Eschner [158]	2011	$A = 3\%$	
	Kielpinski [159]	2012	$\epsilon = 3\%$	
	Blatt [160]	2013	$\theta = 0.3°$	Use EIT to measure θ, limited by finite NA
	Eschner [161]	2014		Measure quantum beats of a single ion and single photons
Single molecule, high NA lens	Sandoghdar [126]	2008	$\epsilon = 11.5\%$	By postselecting the polarization they can exclude the incoherent radiation and just include the coherent radiation, measuring $\epsilon = 22\%$.
	Sandoghdar [127]	2011	$\epsilon = 19\%$, $\theta = 3°$	
Quantum dot, high NA lens	Atatüre [162]	2007	$\epsilon = 12\%$	

Table D.1: A list of recent experiments involving the coupling of light and a single quantum emitter. Key: ϵ = extinction, R = reflectivity, θ = phase shift, A = absorption, G = coupling efficiency; see individual references for exact definitions. This table is copied and extended from [1]. Table continues on next page.

System	Group	Year	Result	Notes
Single atom, cavity	Rempe [163]	2007		Create entangled Bell state between single atom and single photon with fidelity 86%.
	Rempe [164]	2010	$\Delta T = 20\%$	Contrast on the EIT transmission
	Lukin [165]	2013	$\epsilon = 2\%$	
	Lukin [125]	2014	$\theta = (1.1 \pm 0.1)\pi$	
	Rempe [129]	2014	$\theta = 140^\circ$	
Single ion, parabolic mirror	Sondermann [128]	2014	$G = 7.2\%$	
Single atom, waveguide	Kimble [130]	2014	$\Delta R = 25\%$	Measure a dip in reflectivity of 25% for an average of $\overline{N} = 1$
Single molecule, waveguide	Sandoghdar [166]	2014	$\epsilon = 6.5\%$	
Artificial superconducting atom	Delsing [131]	2012	$\epsilon > 99\%$	Couple through 1D open channel rather than free space

Table D.2: Continuation of Table D.1.

Bibliography

[1] G. Leuchs and M. Sondermann. *Light–matter interaction in free space.* J. Mod. Opt. **60**, 36 (2013). 11, 195

[2] M. Scheibner, T. Schmidt, L. Worschech, A. Forchel, G. Bacher, T. Passow, and D. Hommel. *Superradiance of quantum dots.* Nat. Phys. **3**, 106 (2007). 17

[3] R. Röhlsberger, K. Schlage, B. Sahoo, S. Couet, and R. Rüffer. *Collective Lamb shift in single-photon superradiance.* Science **328**, 1248 (2010). 17, 20

[4] R. G. DeVoe and R. G. Brewer. *Observation of superradiant and subradiant spontaneous emission of two trapped ions.* Phys. Rev. Lett. **76**, 2049 (1996). 17, 99, 105

[5] Z. Meir, O. Schwartz, E. Shahmoon, D. Oron, and R. Ozeri. *Cooperative Lamb Shift in a Mesoscopic Atomic Array.* Phys. Rev. Lett. **113**, 193002 (2014). 17, 22, 99, 105

[6] B. Casabone, K. Friebe, B. Brandstätter, K. Schüppert, R. Blatt, and T. E. Northup. *Enhanced Quantum Interface with Collective Ion-Cavity Coupling.* Phys. Rev. Lett. **114**, 023602 (2015). 17

[7] S. Inouye, A. P. Chikkatur, D. M. Stamper-Kurn, J. Stenger, D. E. Pritchard, and W. Ketterle. *Superradiant Rayleigh scattering from a Bose-Einstein condensate.* Science **285**, 571 (1999). 17

[8] Y. Yoshikawa, Y. Torii, and T. Kuga. *Superradiant Light Scattering from Thermal Atomic Vapors.* Phys. Rev. Lett. **94**, 083602 (2005). 17

[9] J. A. Greenberg and D. J. Gauthier. *Steady-state, cavityless, multimode superradiance in a cold vapor.* Phys. Rev. A **86**, 013823 (2012). 17

[10] A. Goban, C.-L. Hung, J. D. Hood, S.-P. Yu, J. A. Muniz, O. Painter, and H. J. Kimble. *Superradiance for Atoms Trapped along a Photonic Crystal Waveguide*. Phys. Rev. Lett. **115**, 063601 (2015). 17, 99

[11] W. Guerin, M. O. Araújo, and R. Kaiser. *Subradiance in a Large Cloud of Cold Atoms*. Phys. Rev. Lett. **116**, 083601 (2016). 17

[12] J. Keaveney, A. Sargsyan, U. Krohn, I. G. Hughes, D. Sarkisyan, and C. S. Adams. *Cooperative Lamb Shift in an Atomic Vapor Layer of Nanometer Thickness*. Phys. Rev. Lett. **108**, 173601 (2012). 17, 20, 21

[13] M. T. Rouabah, M. Samoylova, R. Bachelard, P. W. Courteille, R. Kaiser, and N. Piovella. *Coherence effects in scattering order expansion of light by atomic clouds*. J. Opt. Soc. Am. A **31**, 1031 (2014). 17

[14] S. D. Jenkins and J. Ruostekoski. *Controlled manipulation of light by cooperative response of atoms in an optical lattice*. Phys. Rev. A **86**, 031602 (2012). 17, 22, 58, 165, 169

[15] E. Akkermans, A. Gero, and R. Kaiser. *Photon Localization and Dicke Superradiance in Atomic Gases*. Phys. Rev. Lett. **101**, 103602 (2008). 17

[16] S. E. Skipetrov and I. M. Sokolov. *Magnetic-Field-Driven Localization of Light in a Cold-Atom Gas*. Phys. Rev. Lett. **114**, 053902 (2015). 17

[17] L. Chomaz, L. Corman, T. Yefsah, R. Desbuquois, and J. Dalibard. *Absorption imaging of a quasi-two-dimensional gas: a multiple scattering analysis*. New J. Phys. **14**, 055001 (2012). 17, 20, 25, 69, 70, 71, 82

[18] J. Pellegrino, R. Bourgain, S. Jennewein, Y. R. P. Sortais, A. Browaeys, S. D. Jenkins, and J. Ruostekoski. *Observation of Suppression of Light Scattering Induced by Dipole-Dipole Interactions in a Cold-Atom Ensemble*. Phys. Rev. Lett. **113**, 133602 (2014). 17, 20, 21, 157

[19] K. Kemp, S. J. Roof, M. D. Havey, I. M. Sokolov, and D. V. Kupriyanov. *Cooperatively enhanced light transmission in cold atomic matter*. arxiv.org:1410.2497 (2014). 17, 157

[20] R. Dicke. *Coherence in Spontaneous Radiation Processes.* Phys. Rev. **93**, 99 (1954). 18, 19, 105, 124

[21] A. V. Andreev, V. I. Emel'yanov, and Y. A. Il'inskii. *Collective spontaneous emission (Dicke superradiance).* Sov. Phys. Uspekhi **23**, 493 (1980). 18, 19

[22] N. E. Rehler and J. H. Eberly. *Superradiance.* Phys. Rev. A **3**, 1735 (1971). 19

[23] R. H. Lehmberg. *Radiation from an N-atom system. I. General formalism.* Phys. Rev. A **2**, 883 (1970). 19

[24] R. Friedberg, S. R. Hartmann, and J. T. Manassah. *Frequency shifts in emission and absorption by resonant systems ot two-level atoms.* Phys. Rep. **7**, 101 (1973). 19, 20

[25] M. Gross and S. Haroche. *Superradiance: An essay on the theory of collective spontaneous emission.* Phys. Rep. **93**, 301 (1982). 19

[26] D. James. *Frequency shifts in spontaneous emision from two interacting atoms.* Phys. Rev. A **47**, 1336 (1993). 19, 55, 56, 65

[27] M. J. Stephen. *First-Order Dispersion Forces.* J. Chem. Phys. **40**, 669 (1964). 19

[28] J. Eschner, C. Raab, F. Schmidt-Kaler, and R. Blatt. *Light interference from single atoms and their mirror images.* Nature **413**, 495 (2001). 19

[29] R. J. Thompson, G. Rempe, and H. J. Kimble. *Observation of normal-mode splitting for an atom in an optical cavity.* Phys. Rev. Lett. **68**, 1132 (1992). 19

[30] M. Brune, F. Schmidt-Kaler, A. Maali, J. Dreyer, E. Hagley, J. M. Raimond, and S. Haroche. *Quantum Rabi Oscillation: A Direct Test of Field Quantization in a Cavity.* Phys. Rev. Lett. **76**, 1800 (1996). 20

[31] A. A. Svidzinsky, L. Yuan, and M. O. Scully. *Quantum Amplification by Superradiant Emission of Radiation.* Phys. Rev. X **3**, 041001 (2013). 20

[32] J. Javanainen, J. Ruostekoski, Y. Li, and S. M. Yoo. *Shifts of a Resonance Line in a Dense Atomic Sample.* Phys. Rev. Lett. **112**, 113603 (2014). 20, 70, 71, 101

[33] J. Javanainen and J. Ruostekoski. *Light propagation beyond the mean-field theory of standard optics.* Opt. Express **24**, 993 (2016). 20

[34] S. Jennewein, M. Besbes, N. J. Schilder, S. D. Jenkins, C. Sauvan, J. Ruostekoski, J. J. Greffet, Y. R. P. Sortais, and A. Browaeys. *Observation of the Failure of Lorentz Local field Theory in the Optical Response of Dense and Cold Atomic Systems.* arXiv:1510.08041 (2015). 20, 21

[35] S. L. Bromley, B. Zhu, M. Bishof, X. Zhang, T. Bothwell, J. Schachenmayer, T. L. Nicholson, R. Kaiser, S. F. Yelin, M. D. Lukin, A. M. Rey, and J. Ye. *Collective atomic scattering and motional effects in a dense coherent medium.* Nat. Commun. **7**, 11039 (2016). 20, 21, 55, 65, 66, 170

[36] O. Morice, Y. Castin, and J. Dalibard. *Refractive index of a dilute Bose gas.* Phys. Rev. A **51**, 3896 (1995). 20, 25

[37] J. Ruostekoski and J. Javanainen. *Quantum field theory of cooperative atom response: Low light intensity.* Phys. Rev. A **55**, 513 (1997). 20, 25, 67, 170

[38] J. Javanainen, J. Ruostekoski, B. Vestergaard, and M. R. Francis. *One-dimensional modeling of light propagation in dense and degenerate samples.* Phys. Rev. A **59**, 649 (1999). 20, 25

[39] A. A. Svidzinsky, J. T. Chang, and M. O. Scully. *Cooperative spontaneous emission of N atoms: Many-body eigenstates, the effect of virtual Lamb shift processes, and analogy with radiation of N classical oscillators.* Phys. Rev. A **81**, 053821 (2010). 20, 25, 26, 51, 71, 77

[40] B. Olmos, D. Yu, Y. Singh, F. Schreck, K. Bongs, and I. Lesanovsky. *Long-Range Interacting Many-Body Systems with Alkaline-Earth-Metal Atoms.* Phys. Rev. Lett. **110**, 143602 (2013). 20, 22, 55, 58, 65, 99, 170

[41] S. D. Jenkins and J. Ruostekoski. *Theoretical formalism for collective electromagnetic response of discrete metamaterial systems.* Phys. Rev. B **86**, 085116 (2012). 21

[42] B. Hopkins, A. N. Poddubny, A. E. Miroshnichenko, and Y. S. Kivshar. *Revisiting the physics of Fano resonances for nanoparticle oligomers.* Phys. Rev. A **88**, 053819 (2013). 21, 95, 117

[43] S. D. Emami, M. R. K. Soltanian, A. Attaran, H. A. Abdul-Rashid, R. Penny, M. Moghavvemi, S. W. Harun, H. Ahmad, and W. S. Mohammed. *Application of Fano resonance effects in optical antennas formed by regular clusters of nanospheres.* Appl. Phys. A **118**, 139 (2014). 21, 117

[44] J. Keaveney, A. Sargsyan, U. Krohn, J. Gontcharov, I. G. Hughes, D. Sarkisyan, and C. S. Adams. *Optical transmission through a dipolar layer* . arXiv:1109.3669 (2011). 21, 157

[45] M. Greiner, O. Mandel, T. Esslinger, T. W. Hänsch, and I. Bloch. *Quantum phase transition from a superfluid to a Mott insulator in a gas of ultracold atoms.* Nature **415**, 39 (2002). 21

[46] P. Windpassinger and K. Sengstock. *Engineering novel optical lattices.* Rep. Prog. Phys. **76**, 086401 (2013). 21

[47] F. Nogrette, H. Labuhn, S. Ravets, D. Barredo, L. Béguin, A. Vernier, T. Lahaye, and A. Browaeys. *Single-Atom Trapping in Holographic 2D Arrays of Microtraps with Arbitrary Geometries.* Phys. Rev. X **4**, 021034 (2014). 21, 22

[48] D. Peter, S. Müller, S. Wessel, and H. P. Büchler. *Anomalous Behavior of Spin Systems with Dipolar Interactions.* Phys. Rev. Lett. **109**, 025303 (2012). 21

[49] B. Yan, S. A. Moses, B. Gadway, J. P. Covey, K. R. A. Hazzard, A. M. Rey, D. S. Jin, and J. Ye. *Observation of dipolar spin-exchange interactions with lattice-confined polar molecules.* Nature **501**, 521 (2013). 21, 22

[50] D. Barredo, H. Labuhn, S. Ravets, T. Lahaye, A. Browaeys, and C. S. Adams. *Coherent Excitation Transfer in a Spin Chain of Three Rydberg Atoms.* Phys. Rev. Lett. **114**, 113002 (2015). 21, 99, 170

[51] W. S. Bakr, J. I. Gillen, A. Peng, S. Fölling, and M. Greiner. *A quantum gas microscope for detecting single atoms in a Hubbard-regime optical lattice.* Nature **462**, 74 (2009). 22, 144, 167

[52] C. Weitenberg, M. Endres, J. F. Sherson, M. Cheneau, P. Schauß, T. Fukuhara, I. Bloch, and S. Kuhr. *Single-spin addressing in an atomic Mott insulator.* Nature **471**, 319 (2011). 22

[53] A. Micheli, G. K. Brennen, and P. Zoller. *A toolbox for lattice-spin models with polar molecules.* Nat. Phys. **2**, 341 (2006). 22

[54] A. González-Tudela, C. L. Hung, D. E. Chang, J. I. Cirac, and H. J. Kimble. *Subwavelength vacuum lattices and atomâĂŞatom interactions in two-dimensional photonic crystals.* Nat. Photonics **9**, 320 (2015). 22

[55] N. Liu, L. Langguth, T. Weiss, J. Kästel, M. Fleischhauer, T. Pfau, and H. Giessen. *Plasmonic analogue of electromagnetically induced transparency at the Drude damping limit.* Nat. Mater. **8**, 758 (2009). 22, 138

[56] B. Luk'yanchuk, N. I. Zheludev, S. A. Maier, N. J. Halas, P. Nordlander, H. Giessen, and C. T. Chong. *The Fano resonance in plasmonic nanostructures and metamaterials.* Nat. Mater. **9**, 707 (2010). 22, 117

[57] V. A. Fedotov, N. Papasimakis, E. Plum, A. Bitzer, M. Walther, P. Kuo, D. P. Tsai, and N. I. Zheludev. *Spectral collapse in ensembles of metamolecules.* Phys. Rev. Lett. **104**, 223901 (2010). 22, 160

[58] N. Rougemaille, F. Montaigne, B. Canals, A. Duluard, D. Lacour, M. Hehn, R. Belkhou, O. Fruchart, S. El Moussaoui, A. Bendounan, and F. Maccherozzi. *Artificial Kagome Arrays of Nanomagnets: A Frozen Dipolar Spin Ice.* Phys. Rev. Lett. **106**, 057209 (2011). 22

[59] S. Krämer, L. Ostermann, and H. Ritsch. *Optimized geometries for future generation optical lattice clocks.* arXiv:1506.09079 (2015). 22, 129

[60] J. G. Bohnet, Z. Chen, J. M. Weiner, D. Meiser, M. J. Holland, and J. K. Thompson. *A steady-state superradiant laser with less than one intracavity photon.* Nature **484**, 78 (2012). 22

[61] A. D. Ludlow, M. M. Boyd, J. Ye, E. Peik, and P. Schmidt. *Optical atomic clocks.* Rev. Mod. Phys. **87**, 637 (2015). 22

[62] R. Moessner and A. P. Ramirez. *Geometrical frustration.* Phys. Today **59**, 24 (2006). 22, 142

[63] M. Maksymenko, V. R. Chandra, and R. Moessner. *Classical dipoles on the kagome lattice.* Phys. Rev. B **91**, 184407 (2015). 22, 141, 142

[64] G. Nienhuis and F. Schuller. *Spontaneous emission and light scattering by atomic lattice models.* J. Phys. B At. Mol. Phys. **20**, 23 (1987). 22

[65] D. E. Chang, L. Jiang, A. V. Gorshkov, and H. J. Kimble. *Cavity QED with atomic mirrors.* New J. Phys. **14**, 063003 (2012). 22

[66] R. J. Bettles, S. A. Gardiner, and C. S. Adams. *Cooperative ordering in lattices of interacting two-level dipoles.* Phys. Rev. A **92**, 063822 (2015). 23, 132, 133

[67] R. J. Bettles, S. A. Gardiner, and C. S. Adams. *Enhanced Optical Cross Section via Collective Coupling of Atomic Dipoles in a 2D Array.* Phys. Rev. Lett. **116**, 103602 (2016). 23, 132, 146, 151

[68] O. Morice. *Atomes Redroidis Par Laser: Du Refroidissement Sub-Recul À La Recherche D'effets Quantiques Collectifs.* Ph.D. thesis, École Normale Supérieure, Université Paris (1995). 25

[69] C. Gardiner and P. Zoller. *The Quantum World of Ultra-Cold Atoms and Light: Book 1 Foundations of Quantum Optics.* 1st ed., (Imperial College Press, London 2014). 25, 26, 27, 29, 31, 33, 37, 40, 41, 55, 180

[70] C. Gardiner and P. Zoller. *The Quantum World of Ultra-Cold Atoms and Light: Book 2 The Physics of Quantum-Optical Devices.* 1st ed., (Imperial College Press, London 2015). 25, 26, 27, 28, 29, 37, 40, 42, 44, 55, 81, 175, 181

[71] M. A. Kovaleva and L. I. Manevich. *Superradiant transition and its classical analogue.* Russ. J. Phys. Chem. B **7**, 534 (2013). 26

[72] C. Cohen-Tannoudji and J. D.-R. Gilbert Grynberg. *Atom-Photon Interactions,* (John Wiley & Sons, Inc. 2004). 29, 32

[73] J. D. Jackson. *Classical Electrodynamics,* (John Wiley & Sons, Inc., New York, London 1963). 32, 80, 81, 83, 85, 86, 90, 94, 127

[74] T. Werlang, A. Dodonov, E. Duzzioni, and C. Villas-Bôas. *Rabi model beyond the rotating-wave approximation: Generation of photons from vacuum through decoherence.* Phys. Rev. A **78**, 053805 (2008). 37

[75] R. Friedberg and J. T. Manassah. *Effects of including the counterrotating term and virtual photons on the eigenfunctions and eigenvalues of a scalar photon collective emission theory.* Phys. Lett. A **372**, 2514 (2008). 37, 77

[76] Y. Li, J. Evers, W. Feng, and S. Y. Zhu. *Spectrum of collective spontaneous emission beyond the rotating-wave approximation.* Phys. Rev. A **87**, 053837 (2013). 37

[77] J. Dalibard, Y. Castin, and K. Mølmer. *Wave-Function Approach to Dissipative Processes in Quantum Optics.* Phys. Rev. Lett. **68**, 580 (1992). 41

[78] D. C. Burnham and R. Y. Chiao. *Coherent Resonance Fluorescence Excited by Short Light Pulses.* Phys. Rev. **188**, 667 (1969). 51

[79] S. Krämer and H. Ritsch. *Generalized mean-field approach to simulate the dynamics of large open spin ensembles with long range interactions.* Eur. Phys. J. D **69**, 282 (2015). 55, 60, 65, 66, 67, 170

[80] B. H. Bransden and C. J. Joachain. *Physics of Atoms and Molecules.* 2nd ed., (Dorling Kindersley, New Delhi 2003). 56

[81] X. Zhou, X. Xu, X. Chen, and J. Chen. *Magic wavelengths for terahertz clock transitions.* Phys. Rev. A **81**, 012115 (2010). 58

[82] Z. Barber, J. Stalnaker, N. Lemke, N. Poli, C. Oates, T. Fortier, S. Diddams, L. Hollberg, C. Hoyt, A. Taichenachev, and V. Yudin. *Optical Lattice Induced Light Shifts in an Yb Atomic Clock.* Phys. Rev. Lett. **100**, 103002 (2008). 58

[83] T. Fukuhara, S. Sugawa, M. Sugimoto, S. Taie, and Y. Takahashi. *Mott insulator of ultracold alkaline-earth-metal-like atoms.* Phys. Rev. A **79**, 041604 (2009). 58, 167

[84] S. Stellmer, B. Pasquiou, R. Grimm, and F. Schreck. *Creation of Ultracold Sr2 Molecules in the Electronic Ground State.* Phys. Rev. Lett. **109**, 115302 (2012). 58

[85] J. R. Ott, M. Wubs, P. Lodahl, N. A. Mortensen, and R. Kaiser. *Cooperative fluorescence from a strongly driven dilute cloud of atoms.* Phys. Rev. A **87**, 061801 (2013). 61

[86] M. Samoylova, N. Piovella, R. Bachelard, and P. W. Courteille. *Microscopic theory of photonic band gaps in optical lattices.* Opt. Commun. **312**, 94 (2014). 70, 71

[87] Z. Bai, J. Demmel, J. Dongarra, A. Ruhe, and H. van der Vorst (editors). *Templates for the Solution of Algebraic Eigenvalue Problems*, (Society for Industrial and Applied Mathematics 2000). 71

[88] A. Goetschy and S. E. Skipetrov. *Non-Hermitian Euclidean random matrix theory.* Phys. Rev. E **84**, 011150 (2011). 71

[89] M. Rusek, J. Mostowski, and A. OrÅĆowski. *Random Green matrices: From proximity resonances to Anderson localization.* Phys. Rev. A **61**, 022704 (2000). 71

[90] M. Antezza, Y. Castin, and D. A. W. Hutchinson. *Quantitative study of two- and three-dimensional strong localization of matter waves by atomic scatterers.* Phys. Rev. A - At. Mol. Opt. Phys. **82**, 1 (2010). 71

[91] B. Grémaud and T. Wellens. *Speckle Instability: Coherent Effects in Nonlinear Disordered Media.* Phys. Rev. Lett. **104**, 133901 (2010). 71

[92] L. Bellando, A. Gero, E. Akkermans, and R. Kaiser. *Cooperative effects and disorder: A scaling analysis of the spectrum of the effective atomic Hamiltonian.* Phys. Rev. A **90**, 063822 (2014). 71, 126

[93] C. J. Joachain, N. J. Kylstra, and R. M. Potvliege. *Atoms in Intense Laser Fields*, (Cambridge University Press, Cambridge 2011). 72

[94] R. A. Horn and C. R. Johnson. *Matrix analysis.* 2nd ed., (Cambridge University Press, Cambridge 1985). 76

[95] R. Bronson. *Matrix Methods: An Introduction*, (Academic Press, New York 1970). 76

[96] A. A. Svidzinsky and J. T. Chang. *Cooperative spontaneous emission as a many-body eigenvalue problem.* Phys. Rev. A **77**, 043833 (2008). 77

[97] W. D. Heiss. *The physics of exceptional points.* J. Phys. A Math. Theor. **45**, 444016 (2012). 77

[98] B. T. Draine. *The discrete-dipole approximation and its application to interstellar graphite grains.* Astrophys. J. **333**, 848 (1988). 83

[99] R. Messina, M. Tschikin, S.-A. Biehs, and P. Ben-Abdallah. *Fluctuation-electrodynamic theory and dynamics of heat transfer in systems of multiple dipoles.* Phys. Rev. B **88**, 104307 (2013). 83, 85

[100] J.-P. Hugonin, M. Besbes, and P. Ben-Abdallah. *Fundamental limits for light absorption and scattering induced by cooperative electromagnetic interactions.* Phys. Rev. B **91**, 180202 (2015). 85, 92

[101] M. K. Tey, G. Maslennikov, T. C. H. Liew, S. A. Aljunid, F. Huber, B. Chng, Z. Chen, V. Scarani, and C. Kurtsiefer. *Interfacing light and single atoms with a lens.* New J. Phys. **11**, 043011 (2009). 92, 148, 151, 195

[102] S. DâĂŹAgostino, F. Della Sala, and L. C. Andreani. *Dipole-excited surface plasmons in metallic nanoparticles: Engineering decay dynamics within the discrete-dipole approximation.* Phys. Rev. B **87**, 205413 (2013). 92

[103] U. Fano. *Effects of Configuration Interaction on Intensities and Phase Shifts.* Phys. Rev. **124**, 1866 (1961). 115, 117

[104] V. Giannini, Y. Francescato, H. Amrania, C. C. Phillips, and S. a. Maier. *Fano resonances in nanoscale plasmonic systems: a parameter-free modeling approach.* Nano Lett. **11**, 2835 (2011). 117

[105] C. Stehle, C. Zimmermann, and S. Slama. *Cooperative coupling of ultracold atoms and surface plasmons.* Nat. Phys. **10**, 937 (2014). 117, 171

[106] R. T. Sutherland and F. Robicheaux. *Collective Dipole-Dipole Interactions in an Atomic Array.* arXiv:1605.00292 (2016). 120

[107] S. E. Skipetrov and A. Goetschy. *Eigenvalue distributions of large Euclidean random matrices for waves in random media.* J. Phys. A Math. Theor. **44**, 065102 (2011). 126

[108] P. W. Milonni and P. L. Knight. *Spontaneous Emission Between Mirrors.* Opt. Commun. **9**, 119 (1973). 127

[109] G.-W. Chern, P. Mellado, and O. Tchernyshyov. *Two-Stage Ordering of Spins in Dipolar Spin Ice on the Kagome Lattice.* Phys. Rev. Lett. **106**, 207202 (2011). 136

[110] E. Waks and J. Vuckovic. *Dipole Induced Transparency in Drop-Filter Cavity-Waveguide Systems.* Phys. Rev. Lett. **96**, 153601 (2006). 138

[111] S. Zhang, D. A. Genov, Y. Wang, M. Liu, and X. Zhang. *Plasmon-Induced Transparency in Metamaterials.* Phys. Rev. Lett. **101**, 047401 (2008). 138

[112] S. D. Jenkins and J. Ruostekoski. *Metamaterial Transparency Induced by Cooperative Electromagnetic Interactions.* Phys. Rev. Lett. **111**, 147401 (2013). 138

[113] R. Puthumpally-Joseph, M. Sukharev, O. Atabek, and E. Charron. *Dipole-Induced Electromagnetic Transparency.* Phys. Rev. Lett. **113**, 163603 (2014). 138

[114] S.-M. Yoo and S. M. Paik. *Cooperative optical response of 2D dense lattices with strongly correlated dipoles.* Opt. Express **24**, 2156 (2016). 138

[115] G. B. Jo, J. Guzman, C. K. Thomas, P. Hosur, A. Vishwanath, and D. M. Stamper-Kurn. *Ultracold Atoms in a Tunable Optical Kagome Lattice.* Phys. Rev. Lett. **108**, 045305 (2012). 142

[116] R. A. Vicencio and C. Mejía-Cortés. *Diffraction-free image transmission in kagome photonic lattices.* J. Opt. **16**, 015706 (2014). 142

[117] R. A. Vicencio, C. Cantillano, L. Morales-Inostroza, B. Real, C. Mejía-Cortés, S. Weimann, A. Szameit, and M. I. Molina. *Observation of Localized States in Lieb Photonic Lattices.* Phys. Rev. Lett. **114**, 245503 (2015). 142, 169

[118] S. Mukherjee, A. Spracklen, D. Choudhury, N. Goldman, P. Öhberg, E. Andersson, and R. R. Thomson. *Observation of a Localized Flat-Band State in a Photonic Lieb Lattice.* Phys. Rev. Lett. **114**, 245504 (2015). 142

[119] B. J. Lester, N. Luick, A. M. Kaufman, C. M. Reynolds, and C. A. Regal. *Rapid Production of Uniformly Filled Arrays of Neutral Atoms.* Phys. Rev. Lett. **115**, 073003 (2015). 144, 167

[120] W. S. Bakr, P. M. Preiss, M. E. Tai, R. Ma, J. Simon, and M. Greiner. *Orbital excitation blockade and algorithmic cooling in quantum gases.* Nature **480**, 500 (2011). 144, 167

[121] D. Tiarks, S. Baur, K. Schneider, S. Dürr, and G. Rempe. *Single-Photon Transistor Using a Förster Resonance.* Phys. Rev. Lett. **113**, 053602 (2014). 147

[122] H. Gorniaczyk, C. Tresp, J. Schmidt, H. Fedder, and S. Hofferberth. *Single-Photon Transistor Mediated by Interstate Rydberg Interactions.* Phys. Rev. Lett. **113**, 053601 (2014). 147

[123] D. Maxwell, D. Szwer, D. Paredes-Barato, H. Busche, J. D. Pritchard, A. Gauguet, K. Weatherill, M. Jones, and C. S. Adams. *Storage and Control of Optical Photons Using Rydberg Polaritons.* Phys. Rev. Lett. **110**, 103001 (2013). 147

[124] D. Paredes-Barato and C. S. Adams. *All-Optical Quantum Information Processing Using Rydberg Gates.* Phys. Rev. Lett. **112**, 040501 (2014). 147, 170

[125] T. G. Tiecke, J. D. Thompson, N. P. de Leon, L. R. Liu, V. Vuletić, and M. D. Lukin. *Nanophotonic quantum phase switch with a single atom.* Nature **508**, 241 (2014). 147, 196

[126] G. Wrigge, I. Gerhardt, J. Hwang, G. Zumofen, and V. Sandoghdar. *Efficient coupling of photons to a single molecule and the observation of its resonance fluorescence.* Nat. Phys. **4**, 60 (2008). 147, 153, 195

[127] M. Pototschnig, Y. Chassagneux, J. Hwang, G. Zumofen, A. Renn, and V. Sandoghdar. *Controlling the phase of a light beam with a single molecule.* Phys. Rev. Lett. **107**, 063001 (2011). 147, 195

[128] M. Fischer, M. Bader, R. Maiwald, A. Golla, M. Sondermann, and G. Leuchs. *Efficient saturation of an ion in free space.* Appl. Phys. B **117**, 797 (2014). 147, 148, 196

[129] C. Sames, H. Chibani, C. Hamsen, P. A. Altin, T. Wilk, and G. Rempe. *Antiresonance Phase Shift in Strongly Coupled Cavity QED.* Phys. Rev. Lett. **112**, 043601 (2014). 147, 196

[130] A. Goban, C.-L. Hung, S.-P. Yu, J. D. Hood, J. A. Muniz, J. H. Lee, M. J. Martin, A. C. McClung, K. S. Choi, D. E. Chang, O. Painter, and H. J. Kimble. *Atom-light interactions in photonic crystals.* Nat. Commun. **5**, 3808 (2014). 148, 196

[131] I. C. Hoi, T. Palomaki, J. Lindkvist, G. Johansson, P. Delsing, and C. M. Wilson. *Generation of nonclassical microwave states using an artificial atom in 1D open space.* Phys. Rev. Lett. **108**, 263601 (2012). 148, 196

[132] G. Zumofen, N. M. Mojarad, V. Sandoghdar, and M. Agio. *Perfect Reflection of Light by an Oscillating Dipole.* Phys. Rev. Lett. **101**, 180404 (2008). 148

[133] S. A. Aljunid, G. Maslennikov, Y. Wang, H. L. Dao, V. Scarani, and C. Kurtsiefer. *Excitation of a Single Atom with Exponentially Rising Light Pulses.* Phys. Rev. Lett. **111**, 103001 (2013). 148

[134] S. Van Enk and H. J. Kimble. *Strongly focused light beams interacting with single atoms in free space.* Phys. Rev. A **63**, 023809 (2001). 151

[135] K. G. Lee, X. W. Chen, H. Eghlidi, P. Kukura, R. Lettow, A. Renn, V. Sandoghdar, and S. Götzinger. *A planar dielectric antenna for directional single-photon emission and near-unity collection efficiency.* Nat. Photonics **5**, 166 (2011). 153

[136] M. Celebrano, P. Kukura, A. Renn, and V. Sandoghdar. *Single-molecule imaging by optical absorption.* Nat. Photonics **5**, 95 (2011). 153

[137] A. Arbabi, Y. Horie, A. J. Ball, M. Bagheri, and A. Faraon. *Subwavelength-thick Lenses with High Numerical Apertures and Large Efficiency Based on High Contrast Transmitarrays.* Nat. Commun. **6**, 1 (2015). 153

[138] M. Hillenbrand, A. Hoffmann, D. P. Kelly, and S. Sinzinger. *Fast nonparaxial scalar focal field calculations.* J. Opt. Soc. Am. A **31**, 1206 (2014). 155

[139] M. Hillenbrand, D. P. Kelly, and S. Sinzinger. *Numerical solution of nonparaxial scalar diffraction integrals for focused fields.* J. Opt. Soc. Am. A **31**, 1832 (2014). 155

[140] P. P. Bansal and A. J. Ardell. *Average nearest-neighbor distances between uniformly distributed finite particles.* Metallography **5**, 97 (1972). 158

[141] S. P. Rath, T. Yefsah, K. J. Günter, M. Cheneau, R. Desbuquois, M. Holzmann, W. Krauth, and J. Dalibard. *Equilibrium state of a trapped two-dimensional Bose gas.* Phys. Rev. A **82**, 013609 (2010). 157

[142] P. Ghenuche, G. Vincent, M. Laroche, N. Bardou, R. Haïdar, J.-L. Pelouard, and S. Collin. *Optical Extinction in a Single Layer of Nanorods.* Phys. Rev. Lett. **109**, 143903 (2012). 160

[143] T. Ebbesen, H. J. Lezec, H. F. Ghaemi, T. Thio, and P. A. Wolff. *Extraordinary optical transmission through sub-wavelength hole arrays.* Nature **391**, 667 (1998). 160

[144] S. D. Jenkins and J. Ruostekoski. *Cooperative resonance linewidth narrowing in a planar metamaterial.* New J. Phys. **14**, 103003 (2012). 160

[145] L. Martín-Moreno, F. J. García-Vidal, H. J. Lezec, K. M. Pellerin, T. Thio, J. B. Pendry, and T. W. Ebbesen. *Theory of Extraordinary Optical Transmission through Subwavelength Hole Arrays.* Phys. Rev. Lett. **86**, 1114 (2001). 160

[146] F. J. García de Abajo. *Colloquium: Light scattering by particle and hole arrays.* Rev. Mod. Phys. **79**, 1267 (2007). 160

[147] J. F. Sherson, C. Weitenberg, M. Endres, M. Cheneau, I. Bloch, and S. Kuhr. *Single-atom-resolved fluorescence imaging of an atomic Mott insulator.* Nature **467**, 68 (2010). 167

[148] W. S. Bakr, A. Peng, M. E. Tai, R. Ma, J. Simon, J. I. Gillen, S. Folling, L. Pollet, and M. Greiner. *Probing the Superfluid-to-Mott Insulator Transition at the Single-Atom Level.* Science **329**, 547 (2010). 167

[149] M. Hafezi, S. Mittal, J. Fan, A. Migdall, and J. M. Taylor. *Imaging topological edge states in silicon photonics.* Nat. Photonics **7**, 1001 (2013). 170

[150] D. Peter, N. Y. Yao, N. Lang, S. D. Huber, M. D. Lukin, and H. P. Büchler. *Topological bands with a Chern number C = 2 by dipolar exchange interactions.* Phys. Rev. A **91**, 053617 (2015). 170

[151] R. Monshouwer, M. Abrahamsson, F. van Mourik, and R. van Grondelle. *Superradiance and Exciton Delocalization in Bacterial Photosynthetic Light-Harvesting Systems.* J. Phys. Chem. B **101**, 7241 (1997). 170

[152] J. L. Herek, W. Wohlleben, R. J. Cogdell, D. Zeidler, and M. Motzkus. *Quantum control of energy flow in light harvesting.* Nature **417**, 533 (2002). 170

[153] T. Grieß er and H. Ritsch. *Light-Induced Crystallization of Cold Atoms in a 1D Optical Trap.* Phys. Rev. Lett. **111**, 055702 (2013). 171

[154] S. A. Aljunid, M. K. Tey, B. Chng, T. Liew, G. Maslennikov, V. Scarani, and C. Kurtsiefer. *Phase Shift of a Weak Coherent Beam Induced by a Single Atom.* Phys. Rev. Lett. **103**, 153601 (2009). 195

[155] S. A. Aljunid, B. Chng, J. Lee, M. Paesold, G. Maslennikov, and C. Kurtsiefer. *Interaction of light with a single atom in the strong focusing regime.* J. Mod. Opt. **58**, 299 (2011). 195

[156] L. Slodička, G. Hétet, S. Gerber, M. Hennrich, and R. Blatt. *Electromagnetically Induced Transparency from a Single Atom in Free Space.* Phys. Rev. Lett. **105**, 153604 (2010). 195

[157] G. Hétet, L. Slodička, M. Hennrich, and R. Blatt. *Single Atom as a Mirror of an Optical Cavity.* Phys. Rev. Lett. **107**, 133002 (2011). 195

[158] N. Piro, F. Rohde, C. Schuck, M. Almendros, J. Huwer, J. Ghosh, A. Haase, M. Hennrich, F. Dubin, and J. Eschner. *Heralded single-photon absorption by a single atom.* Nat. Phys. **7**, 17 (2011). 195

[159] E. W. Streed, A. Jechow, B. G. Norton, and D. Kielpinski. *Absorption imaging of a single atom.* Nat. Commun. **3**, 933 (2012). 195

[160] G. Hétet, L. Slodička, N. Röck, and R. Blatt. *Free-space read-out and control of single-ion dispersion using quantum interference.* Phys. Rev. A **88**, 041804 (2013). 195

[161] M. Schug, C. Kurz, P. Eich, J. Huwer, P. Müller, and J. Eschner. *Quantum interference in the absorption and emission of single photons by a single ion.* Phys. Rev. A **90**, 023829 (2014). 195

[162] A. N. Vamivakas, M. Atatüre, J. Dreiser, S. T. Yilmaz, A. Badolato, A. K. Swan, B. B. Goldberg, A. Imamoglu, and M. S. Ünlü. *Strong Extinction of a Far-Field Laser Beam by a Single Quantum Dot.* Nano Lett. **7**, 2892 (2007). 195

[163] T. Wilk, S. C. Webster, A. Kuhn, and G. Rempe. *Single-atom single-photon quantum interface.* Science **317**, 488 (2007). 196

[164] M. Mücke, E. Figueroa, J. Bochmann, C. Hahn, K. Murr, S. Ritter, C. J. Villas-Boas, and G. Rempe. *Electromagnetically induced transparency with single atoms in a cavity.* Nature **465**, 755 (2010). 196

[165] J. D. Thompson, T. Tiecke, N. P. de Leon, J. Feist, A. V. Akimov, M. Gullans, A. S. Zibrov, V. Vuletić, and M. D. Lukin. *Coupling a single trapped atom to a nanoscale optical cavity.* Science **340**, 1202 (2013). 196

[166] S. Faez, P. Türschmann, H. R. Haakh, S. Götzinger, and V. Sandoghdar. *Coherent Interaction of Light and Single Molecules in a Dielectric Nanoguide.* Phys. Rev. Lett. **113**, 213601 (2014). 196